

University of South Wales



2053100

 *Bound by*
Abbey
Bookbinding Co.

116 Cathays Terrace, Cardiff CF24 4HY
South Wales, U.K. Tel: (029) 20395882
www.bookbindersuk.com

Development and Clinical Application of Techniques for the Image Processing and Registration of Serially Acquired Medical Images

Glenda Patricia Williams

A submission presented in partial fulfilment of the requirements
of the University of Glamorgan/Prifysgol Morgannwg for the
degree of Doctor of Philosophy

This research programme was carried out in collaboration with
the University Hospital of Wales

October 2000

To my parents

*To everything there is a season,
A time for every purpose under heaven:
A time to be born, and a time to die;
A time to plant, and a time to pluck what is planted;
A time to kill, and a time to heal;
A time to break down, and a time to build up;
A time to weep, and a time to laugh;
A time to mourn, and a time to dance;
A time to cast away stones, and a time to gather stones;
A time to embrace, and a time to refrain from embracing;
A time to gain, and a time to lose;
A time to keep, and a time to throw away;
A time to tear, and a time to sew;
A time to keep silence, and a time to speak;
A time to love, and a time to hate;
A time to war, and a time of peace.*

Ecclesiastes 3:1-8

R10

Certificate of Research

This is to certify that, except where specific reference is made, the work described in this thesis is the result of the candidate. Neither this thesis, nor any part of it, has been presented, or is currently submitted, in candidature for any degree at any other University.

Signed

...Glenda P. Williams...
Candidate

Signed

...Paul Roach...
Director of Studies

Date

...19th October, 2000...

Abstract

In many magnetic resonance imaging (MRI) applications, it is necessary to compare regions of interest (ROIs) on different images of the same patient. This comparison is often made difficult when the scanned tissue volume is not in exactly the same three-dimensional location each time. Registration, the accurate alignment of the images through the determination of a transformation from one image space to another, is necessary so that ROIs may be compared correctly.

This thesis presents an implemented software system for the image processing and registration of MRI finger images. The particular application of this system is for patients suffering from rheumatoid arthritis. Firstly, features are derived from the images that will aid the registration process. The finger bones are considered to be the most reliable structures within MRI finger images and therefore, various image processing algorithms are applied to the images to create boundaries that are characteristic of the finger bones. In addition, a novel algorithm is presented which combines boundaries from many slices into a single image. Secondly, the rotational and translational offset between two images of the same finger is calculated. The Hough Transform is used to fit ellipses to the joint side of the two bones in the combined slice image. The displacement between the best-fit ellipse on images of the same finger provides the rotation and translation required to register the images. Finally, the calculated rotational and translational offset is applied to one of the images to register it to the other image. The system is applied to various data sets supplied by the University Hospital of Wales and is tested through fully worked examples. An analysis of the results is given.

Acknowledgements

I would like to take this opportunity to give my sincere thanks to my Director of Studies, Dr. Paul Roach and my Supervisor Dr. Sherrienne Lloyd, for their guidance, patience and encouragement throughout my Ph.D. and also for their constructive comments over the writing of this thesis.

This Ph.D. is a collaboration between the University of Glamorgan and the University Hospital of Wales (UHW). I would like to express my thanks to my Supervisor at UHW, Mr. Bill Stewart, for his involvement in this Ph.D., for the supply of data and for the helpful comments on this thesis. I would also like to thank the Rheumatologists I have worked with at UHW, Dr. Mike Plant and Dr. Jim Martin for their medical expertise and assistance in this research.

I would also like to thank my office mates, friends and colleagues within the Mathematics Department for all their help, support and encouragement in so many different ways.

Finally, my heartfelt gratitude to my parents, my family and close friends for all their love, support and encouragement during this Ph.D.

This research was partly sponsored by the University of Glamorgan.

Contents

1	Introduction	1
1.1	Background	4
1.1.1	A Brief Introduction to Magnetic Resonance Imaging	4
1.1.2	MRI Finger Images	6
1.1.3	Imaging Protocols	8
1.2	Registration	10
1.2.1	The Need for Registration	10
1.2.2	The Meaning and Purpose of Registration	13
1.3	An Overview of the Thesis	15
2	Literature Review	17
2.1	Applications of Registration	18
2.2	Medical Image Registration Methods	19
2.2.1	Dimensionality	21
2.2.2	Nature of registration basis	23
2.2.3	Nature of transformation	25
2.2.4	Domain of transformation	26
2.2.5	Interaction	26
2.2.6	Optimization procedure	27
2.2.7	Modalities involved	27
2.2.8	Subject	31

2.2.9	Object	32
2.3	Conclusions	33
3	Defining and Storing ROI Boundaries	35
3.1	A Set of Criteria for Drawing Region of Interest Boundaries	37
3.1.1	Assessment of Previous Image Analysis	38
3.1.2	Criteria for Drawing ROIs	41
3.1.3	Analysis of Data	44
3.1.4	Further Image Analysis to Enhance the Criteria	46
3.1.5	Establishing a Coefficient of Variation	49
3.1.6	Conclusions	51
3.2	The Region of Interest Drawtool	52
3.2.1	Interior Points of a Polygon	52
3.2.2	Bresenham's Algorithm	56
3.2.3	Implementation of Bresenham's Algorithm	57
3.2.4	Polygon Complexities	59
3.2.5	Region of Interest Statistics	65
3.2.6	The Region of Interest Path Structure	66
3.3	Summary	72
4	Processing of Raw Image Data	73
4.1	Locating Features By Pixel Intensities	74
4.1.1	Contrast Stretching	75
4.1.2	Standardization	77
4.1.3	Grey Level Thresholding	80
4.1.4	Reducing the number of grey levels	81
4.2	Locating Structural Features	82
4.2.1	Edge Detection and Gradient Operators	83
4.2.2	Laplacian and Zero Crossings	86

4.2.3	Bone Boundaries	88
4.3	Frequency Domain Techniques	91
4.3.1	The Fourier Transform	92
4.3.2	The Convolution Theorem	94
4.3.3	Filters	95
4.3.4	Fourier Descriptors	99
4.4	Conclusions	104
5	Registration Methods	106
5.1	Similarity Detection	107
5.2	Superimposition	109
5.3	Hough Transform Approaches to Registration	112
5.3.1	The Hough Transform	112
5.3.2	Hough Transform Results on Test Images	117
5.3.3	Hough Transform Results on Finger Images	120
5.3.4	The Generalised Hough Transform	122
5.3.5	Generalised Hough Transform Results	125
5.4	Combining the Slices	128
5.5	Moments	146
5.6	Conclusions	148
6	Analysis of the Proposed System	151
6.1	The System	152
6.2	Results of the Proposed System	154
6.2.1	Step 1 - Standardise	155
6.2.2	Step 2 - Derive Bone Boundaries	159
6.2.3	Step 3 - Segment	159
6.2.4	Step 4 - Combine the Slices	164
6.2.5	Step 5 - Determine the Registration Parameters	165

6.2.6	Step 6 - Actual Registration	166
6.3	Analysis of the Registration System and Results	168
6.3.1	Analysis of Assumptions	181
6.4	Conclusions of Thesis	185
6.5	Future Work	193
A	Inter Observer Variability Graphs	194
B	Polygon Complexities	204
B.1	Edge Equivalent Vertices	206
B.2	Peaks / Troughs	207
B.3	Horizontal edges	208
C	Interior Points of a Polygon Pseudocode	213
D	Generalised Hough Transform Results	218
D.1	PD-Weighted	220
D.1.1	Data set 1	220
D.2	T1-Weighted, Gadolinium Enhanced	224
D.2.1	Data set 2	224
D.2.2	Data set 3	228
D.2.3	Data set 4	232
D.3	Different weights	237
D.3.1	Data set 5	237
D.4	Inter Patient Analysis	243
D.4.1	Data set 6	243
E	Poster Abstract	245
F	IMA paper	246
G	Glossary	247

List of Figures

1.1	The general structure of the registration procedure.	3
1.2	Two dimensional cross-section of a finger.	7
1.3	MRI scan of an RA patient.	7
1.4	(a) MRI scanner (b) jig that holds the finger for scanning.	12
1.5	The final registration system.	14
3.1	Inter Observer Variability.	44
3.2	Bounding box examples.	53
3.3	Aliasing example.	57
3.4	Consecutive pixels from shallow lines.	58
3.5	Anticlockwise cycle of vertices.	58
3.6	Edge equivalent vertices (a) vertices A & C treated as non-vertex edge co-ordinates (b) vertex A treated as a non-vertex edge co-ordinate. . .	60
3.7	Vertices as peaks/troughs.	61
3.8	Independent horizontal edges.	61
3.9	Horizontal edges, (a) example 1 (b) example 2.	62
3.10	Horizontal edges, example 3.	62
3.11	Horizontal edges, example 4.	62
3.12	RIFF file hierarchy of chunks.	71
4.1	(a) PD-weighted image (b) T2-weighted image (c) T1-weighted image. .	75

4.2	(a) PD-weighted image contrast stretched (b) T2-weighted image contrast stretched (c) T1-weighted image contrast stretched.	76
4.3	(a) PD-weighted image standardized and contrast stretched (b) T2-weighted image standardized and contrast stretched (c) T1-weighted image standardized and contrast stretched.	78
4.4	(a) PD-weighted image (b) T2-weighted image, new standardizing method (c) T1-weighted image, new standardizing method.	79
4.5	MRI finger scan with rectangles drawn in the proximal phalanx, middle phalanx, tendon, hole, joint space, synovium dorsal and synovium palmar.	80
4.6	Average grey level plus or minus one standard deviation for each rectangle in Fig. 4.5.	81
4.7	Number of grey levels of Fig. 4.5 reduced to (a) 64 (b) 32 (c) 16 (d) 8 (e) 4 (f) 2.	82
4.8	(a) MRI finger scan (b) Sobel Edge Detector (c) Prewitt Edge Detector.	85
4.9	Sobel Edge Detector, with binary threshold and minimum pixel length straight line reduction.	85
4.10	(a) MRI finger scan (b) zero crossings of image showing clear boundaries.	87
4.11	(a) MRI finger scan (b) zero crossings of image showing relatively unclear boundaries.	88
4.12	The boundary sequence.	89
4.13	Boundary sequence on different weighted images.	91
4.14	Radial cross-section of the Ideal highpass filter.	96
4.15	Radial cross-section of the Butterworth highpass filter for $n = 1$	97
4.16	Radial cross-section of the Exponential highpass filter.	98
4.17	Effect of highpass filters with $D_0 = 50$ (a) ideal (b) Butterworth (c) exponential.	99
5.1	SSDA.	108

5.2	Lines in xy and mc space.	113
5.3	Ellipse parameters.	115
5.4	Orientations of ellipses.	118
5.5	Test Ellipses.	118
5.6	Open curves (a) first occasion middle phalanx (b) first occasion proximal phalanx (c) second occasion middle phalanx (d) second occasion proximal phalanx.	121
5.7	Geometry for R-Table entries.	123
5.8	Closed boundaries of two MRI scans of a PIP joint.	125
5.9	Combining the slices from Subject 1 (a) Merged image (b) Filled image (c) Detected boundary.	128
5.10	Open curves on combined slice boundaries for Subject 1 (a) first occasion T2-weighted (b) first occasion PD-weighted (c) first occasion T1-weighted (d) second occasion T2-weighted (e) second occasion PD-weighted (f) second occasion T1-weighted.	130
5.11	Open curves on combined slice boundaries for Subject 2 (a) first occasion T2-weighted (b) first occasion PD-weighted (c) first occasion T1-weighted (d) second occasion T2-weighted (e) second occasion PD-weighted (f) second occasion T1-weighted.	131
5.12	Open curves on combined slice boundaries for Subject 3 (a) first occasion T2-weighted (b) first occasion PD-weighted (c) first occasion T1-weighted (d) second occasion T2-weighted (e) second occasion PD-weighted (f) second occasion T1-weighted.	132
5.13	Open curves on combined slice boundaries for Subject 4 (a) first occasion T2-weighted (b) first occasion PD-weighted (c) first occasion T1-weighted (d) second occasion T2-weighted (e) second occasion PD-weighted (f) second occasion T1-weighted.	133

5.14	Open curves on combined slice boundaries for Subject 5 (a) first occasion T2-weighted (b) first occasion PD-weighted (c) first occasion T1-weighted (d) second occasion T2-weighted (e) second occasion PD-weighted (f) second occasion T1-weighted.	134
5.15	Narrower open curves on combined slice boundaries: Subject 1 (a) first occasion T2-weighted proximal phalanx (b) first occasion PD-weighted proximal phalanx (c) first occasion T1-weighted proximal phalanx (d) second occasion T2-weighted proximal phalanx (e) second occasion PD-weighted proximal phalanx (f) second occasion T1-weighted proximal phalanx.	141
5.16	Narrower open curves on combined slice boundaries: Subject 2 (a) first occasion T2-weighted proximal phalanx (b) first occasion PD-weighted proximal phalanx (c) first occasion T1-weighted proximal phalanx (d) second occasion T2-weighted proximal phalanx (e) second occasion PD-weighted proximal phalanx (f) second occasion T1-weighted proximal phalanx.	142
5.17	Narrower open curves on combined slice boundaries: Subject 3 (a) first occasion T2-weighted proximal phalanx (b) first occasion PD-weighted proximal phalanx (c) first occasion T1-weighted proximal phalanx (d) second occasion T2-weighted proximal phalanx (e) second occasion PD-weighted proximal phalanx (f) second occasion T1-weighted proximal phalanx.	143

5.18	Narrower open curves on combined slice boundaries: Subject 4 (a) first occasion T2-weighted proximal phalanx (b) first occasion PD-weighted proximal phalanx (c) first occasion T1-weighted proximal phalanx (d) second occasion T2-weighted proximal phalanx (e) second occasion PD-weighted proximal phalanx (f) second occasion T1-weighted proximal phalanx.	144
5.19	Narrower open curves on combined slice boundaries: Subject 5 (a) first occasion T2-weighted proximal phalanx (b) first occasion PD-weighted proximal phalanx (c) first occasion T1-weighted proximal phalanx (d) second occasion T2-weighted proximal phalanx (e) second occasion PD-weighted proximal phalanx (f) second occasion T1-weighted proximal phalanx.	145
5.20	A combined slice filled image.	147
5.21	(a) & (b) Location of centroid on two images of the same finger (c) mis-registration of the two images.	147
6.1	The final registration system.	154
6.2	(a) to (d) Subject 1 reference (first occasion T2-weighted) image slices 1 to 4 respectively.	156
6.3	(a) to (d) Subject 1 second occasion T2-weighted image slices 1 to 4 respectively.	157
6.4	(a) to (d) Subject 1 standardised second occasion T2-weighted image slices 1 to 4 respectively.	158
6.5	(a) to (d) Subject 1 boundaries derived from reference image slices 1 to 4 respectively.	160
6.6	(a) to (d) Subject 1 boundaries derived from second occasion T2-weighted image slices 1 to 4 respectively.	161

6.7	(a) to (d) Subject 1 segmented boundaries derived from reference image slices 1 to 4 respectively.	162
6.8	(a) to (d) Subject 1 segmented boundaries derived from second occasion T2-weighted image slices 1 to 4 respectively.	163
6.9	Subject 1 (a) combined slice reference image (b) second occasion combined slice image.	164
6.10	Subject 1 open curves on combined slice images (a) reference image (b) second occasion image.	166
6.11	Applying the registration parameters to subject 1 second occasion images (a) to (d) slices 1 to 4 respectively.	167
6.12	Subject 1 T2-weighted images (a) first occasion open curves (b) second occasion open curves (c) first occasion middle phalanx best-fit ellipse (d) first occasion proximal phalanx best-fit ellipse (e) second occasion middle phalanx best-fit ellipse (f) second occasion proximal phalanx best-fit ellipse.	170
6.13	Subject 2 T2-weighted images (a) first occasion open curves (b) second occasion open curves (c) first occasion middle phalanx best-fit ellipse (d) first occasion proximal phalanx best-fit ellipse (e) second occasion middle phalanx best-fit ellipse (f) second occasion proximal phalanx best-fit ellipse.	171
6.14	Subject 3 T2-weighted images (a) first occasion open curves (b) second occasion open curves (c) first occasion middle phalanx best-fit ellipse (d) first occasion proximal phalanx best-fit ellipse (e) second occasion middle phalanx best-fit ellipse (f) second occasion proximal phalanx best-fit ellipse.	172

6.15 Subject 4 T2-weighted images (a) first occasion open curves (b) second occasion open curves (c) first occasion middle phalanx best-fit ellipse (d) first occasion proximal phalanx best-fit ellipse (e) second occasion middle phalanx best-fit ellipse (f) second occasion proximal phalanx best-fit ellipse.	173
6.16 Subject 5 T2-weighted images (a) first occasion open curves (b) second occasion open curves (c) first occasion middle phalanx best-fit ellipse (d) first occasion proximal phalanx best-fit ellipse (e) second occasion middle phalanx best-fit ellipse (f) second occasion proximal phalanx best-fit ellipse.	174
6.17 Superimposition of registration of combined slice boundaries, subject 1 (a) middle phalanx (b) proximal phalanx.	175
6.18 Superimposition of registration of combined slice boundaries, subject 2 (a) middle phalanx (b) proximal phalanx.	175
6.19 Superimposition of registration of combined slice boundaries, subject 3 (a) middle phalanx (b) proximal phalanx.	176
6.20 Superimposition of registration of combined slice boundaries, subject 4 (a) middle phalanx (b) proximal phalanx.	176
6.21 Superimposition of registration of combined slice boundaries, subject 5 (a) middle phalanx (b) proximal phalanx.	177
6.22 Narrower open curves on combined slice boundaries: Subject 1 T2-weighted images (a) first occasion proximal phalanx (b) second occasion proximal phalanx.	178
6.23 Narrower open curves on combined slice boundaries: Subject 2 T2-weighted images (a) first occasion proximal phalanx (b) second occasion proximal phalanx.	178

6.24	Narrower open curves on combined slice boundaries: Subject 3 T2-weighted images (a) first occasion proximal phalanx (b) second occasion proximal phalanx.	179
6.25	Narrower open curves on combined slice boundaries: Subject 4 T2-weighted images (a) first occasion proximal phalanx (b) second occasion proximal phalanx.	179
6.26	Narrower open curves on combined slice boundaries: Subject 5 T2-weighted images (a) first occasion proximal phalanx (b) second occasion proximal phalanx.	180
6.27	Merged boundaries from Subject 3, first occasion T2-weighted images.	181
6.28	Superimposition of combined slice boundaries for subject 1 occasion 1 (a) PD-weighted combined slice boundaries superimposed onto T2-weighted combined slice boundaries (b) T1-weighted combined slice boundaries superimposed onto T2-weighted combined slice boundaries.	182
6.29	Narrower open curves on combined slice boundaries for Subject 1 (a) T2-weighted images (b) PD-weighted images (c) T1-weighted images. .	185
A.1	Synovium Dorsal Mean Pixel Intensity.	195
A.2	Synovium Dorsal Area.	195
A.3	Synovium Palmar Mean Pixel Intensity.	196
A.4	Synovium Palmar Area.	196
A.5	Proximal Phalanx Mean Pixel Intensity.	197
A.6	Middle Phalanx Mean Pixel Intensity.	197
A.7	Cartilage Mean Pixel Intensity.	198
A.8	Tendon Mean Pixel Intensity.	198
A.9	Synovium Dorsal Method 1 Mean Pixel Intensity.	199
A.10	Synovium Dorsal Method 1 Area.	199
A.11	Synovium Palmar Method 1 Mean Pixel Intensity.	200

A.12 Synovium Palmar Method 1 Area.	200
A.13 Joint Space Method 1 Area.	201
A.14 Joint Space Method 1 Area.	201
A.15 Synovium Dorsal Method 2 Mean Pixel Intensity.	202
A.16 Synovium Dorsal Method 2 Area.	202
A.17 Synovium Palmar Method 2 Mean Pixel Intensity.	203
A.18 Synovium Palmar Method 2 Area.	203
B.1 Edge equivalent vertices (a) vertices A & C treated as non-vertex edge co-ordinates (b) vertex A treated as a non-vertex edge co-ordinate. . .	206
B.2 Vertices as peaks/troughs.	207
B.3 Edge equivalent vertices on a horizontal edge.	209
B.4 Horizontal edges at the (a) start (b) end of a scan-line.	210
B.5 Horizontal edge in the middle of a scan-line. Scan-line j intersecting at vertex F is exiting the polygon.	210
B.6 Horizontal edge in the middle of a scan-line. Scan-line j intersecting at vertex D is not exiting the polygon.	211
B.7 Horizontal edge in the middle of a scan-line. Scan-line j intersecting at vertex D is exiting the polygon.	212
D.1 Bone contours derived from two MRI scans of a PIP joint.	220
D.2 Bone contours derived from two MRI scan of a PIP joint.	224
D.3 Bone contours derived from an MRI scan of a PIP joint.	228
D.4 Slice 2 of a pre- and post-Gadolinium T1-weighted scan.	232
D.5 Slice 3 of a pre- and post-Gadolinium T1-weighted scan.	233
D.6 Bone contours derived from a PD-weighted image.	237
D.7 PD-weighted, normalised and contrast stretched.	240
D.8 Bone contours derived from a 2nd MRI scan of a PIP joint.	243

List of Tables

3.1	Comparison of the second post-injection scan with the pre-injection scan.	47
3.2	Summary of the observer variability and bias studies.	50
3.3	Region of interest path structure.	68
3.4	Path structure example of a red rectangle.	69
3.5	Path structure example of a blue polygon.	69
4.1	Means and standard deviations for Figs. 4.1 & 4.2.	76
4.2	Means and standard deviations for Figs. 4.1 and 4.4.	79
5.1	Test Ellipses.	119
5.2	Best fit ellipses indicated by a maximum in the accumulator array. . . .	119
5.3	Consequence of rounding in calculations for Equation 5.4.	119
5.4	Numbers of boundary pixels on an open boundary of finger bone. . . .	120
5.5	Best fit ellipses indicated by a maximum in the accumulator array. . .	121
5.6	R-Table Example.	123
5.7	Generalised Hough Transform results for Figs. 5.8(a) & 5.8(b).	126
5.8	Generalised Hough Transform results for Fig. 5.6.	127
5.9	Hough Transform best fit ellipses for 5 subjects.	135
5.10	Subject 1 Hough Transform results.	136
5.11	Subject 2 Hough Transform results.	137
5.12	Subject 3 Hough Transform results.	138
5.13	Subject 4 Hough Transform results.	139

5.14 Subject 5 Hough Transform results.	140
6.1 Subject 1 fitting the best fit ellipses.	166
6.2 Registration parameters obtained from fitting the best fit ellipses for five subjects.	168
6.3 Subject 1 fitting the best fit ellipses to different weighted image combined slice boundaries.	183
D.1 Generalised Hough Transform results for Figs. D.1(a) & D.1(b).	220
D.2 Generalised Hough Transform results for Fig. D.1.	221
D.3 Generalised Hough Transform closed curve orientation results for Fig. D.1.	222
D.4 Generalised Hough Transform open curve orientation results for Fig. D.1.	223
D.5 Generalised Hough Transform results for Fig. D.2.	224
D.6 Generalised Hough Transform results for Fig. D.2.	225
D.7 Generalised Hough Transform closed curve orientation results for Fig. D.2.	226
D.8 Generalised Hough Transform open curve orientation results for Fig. D.2.	227
D.9 Generalised Hough Transform results for Fig. D.3.	228
D.10 Generalised Hough Transform results for Fig. D.3.	229
D.11 Generalised Hough Transform closed curve orientation results for Fig. D.3.	230
D.12 Generalised Hough Transform open curve orientation results for Fig. D.3.	231
D.13 Generalised Hough Transform results for Fig. D.4.	234
D.14 Generalised Hough Transform results for Fig. D.5.	235
D.15 Generalised Hough Transform results for Fig. D.4.	236
D.16 Generalised Hough Transform results for Fig. D.6(a), (b), (c).	238
D.17 Generalised Hough Transform results for Fig. D.6(d), (b), (c).	239

D.18 Generalised Hough Transform results for Fig. D.7.	241
D.19 Generalised Hough Transform results for Fig. D.7.	242
D.20 Generalised Hough Transform results for Fig. D.7.	242
D.21 Generalised Hough Transform results for Figs. D.4(a) & D.3(a).	243
D.22 Generalised Hough Transform results for Figs. D.8 & D.2(a).	244
D.23 Generalised Hough Transform results for Figs. D.4(a) & D.3(a).	244
D.24 Generalised Hough Transform results for Figs. D.8 & D.2(a).	244

Chapter 1

Introduction

This thesis documents the creation of a novel system for the image processing and registration of human finger images obtained by Magnetic Resonance Imaging (MRI). The purpose of the system is to aid clinicians' understanding of finger disease, in particular rheumatoid arthritis (RA). The system has been developed through collaboration between the University of Glamorgan and the University Hospital of Wales (UHW).

The system contains image processing tools that are used to extract features from the finger images. These features provide necessary information for image registration. The finger image has unique features and problem areas that require a systematic approach different from methods used for other parts of the body. The literature review detailed in Chapter 2 shows that such a system does not appear to already exist.

The developed system incorporates established image processing techniques and also new techniques, investigated and designed to meet the specific requirements of this application. All the techniques are interlinked to provide a working system.

At UHW, a small bore MRI scanner is used to acquire finger images of patients suffering from RA and also images of fingers of people not affected. The images are two-dimensional cross-sections of finger joints. All the images are stored on a computer.

The images are displayed by a viewer, created at UHW from complementary research [OConnor98b]. The image processing and registration system is incorporated into the viewer to detect features in the MR images that can be used for registration. The difficulties which arise in the initial study of registration are:

- it is not known what constitutes a useful registration feature in an MRI finger image;
- there could be more than one such useful feature in an MRI finger image;
- the locations of useful features in an MRI finger image are unknown.

When features are located in an image they are fed into the registration process. Particular difficulties here are:

- image features may be derived from different cross-sections of the finger;
- anatomical changes to the finger over time could affect the derived features;
- small changes in the position of the finger lead to large changes in the registration process - it is ill-conditioned.

Ideally the final registration algorithm must take all these points into account and give a measure of accuracy of the registration achieved.

The general structure of the registration procedure is shown in Fig. 1.1.

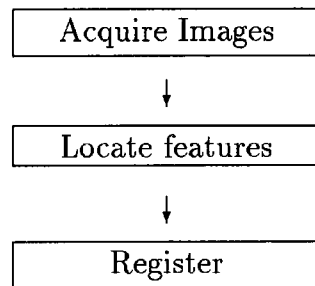


Figure 1.1: The general structure of the registration procedure.

This chapter introduces the reader to the background to this research - the basic concepts of MRI and the particular images used in this specific application. The issue of registration is introduced in Section 1.2 before an overview of the thesis is outlined.

1.1 Background

In this section, a brief introduction to Magnetic Resonance Imaging (MRI) is given. The resulting MRI images acquired for this project are described, followed by an explanation of the different imaging protocols used at UHW.

1.1.1 A Brief Introduction to Magnetic Resonance Imaging

The main source of information concerning the medical application in general and Magnetic Resonance Imaging (MRI) and Rheumatoid Arthritis (RA) in particular, came from staff at the University Hospital of Wales, whose help and expertise is acknowledged here and appreciated. Further information was obtained from selected texts and journals.

One of the earliest articles on MRI came from the Nottingham University research group and was published in the British Journal of Radiology in 1978 [Hinshaw78].

The basis of the use of MRI is provided in “Magnetic Resonance in Medicine” [Rinck93]. This starts with a historical section on the foundation of MRI, explains the basics of MRI, equipment and images and gives examples of specific applications. Further information is provided by Christensen’s Physics of Diagnostic Radiology [Curry90], which deals with imaging techniques explained from the perspective of the Physicist.

Atomic nuclei are known to have magnetic properties. This forms the basis of magnetic resonance imaging. Whereas x-ray images stem from interactions between the high frequency electromagnetic radiation and the electron clouds of atoms, the Nuclear Magnetic Resonance (NMR) signal stems from the interaction of radiowaves with the atomic nucleus itself. Hence there is a completely different contrast behaviour of MRI compared to other medical imaging techniques [Rinck93]. Contrast resolution is the principal advantage of MRI [Curry90].

Clearly, hydrogen (H1) nuclei occur naturally in the human body principally in water and fat. In the presence of a magnetic field a single energy level splits into two distinct energy levels. At equilibrium there is a slightly larger population in the lower, more stable, energy level than in the higher, excited level. By introducing a radio frequency (RF) pulse into the magnetic field, some nuclei will jump to the higher energy level. Once the RF pulse has been switched off, the nuclei return to the lower level, emitting a signal [Rinck93].

The frequency components of the emitted signal are analysed using Fourier Transforms in order to measure the intensity of each frequency. Magnetic Resonance signals are sine and cosine waves and can be defined by amplitude, frequency and phase. The amplitude is also called the signal strength and reflects the brightness of a picture element (pixel) of an MRI image [Rinck93].

The MRI signal can often have a very low intensity and therefore can be severely affected by background noise. To improve the signal-to-noise (S/N) ratio, the images are taken more than once and the data from each image are averaged to produce the final image [Rinck93]. In this study, the images usually result from the average of two acquisitions.

The three dominant factors which affect the contrast of an MRI image are the T1 and T2 relaxation times and the proton density [Rinck93]. “The T1 relaxation time characterises the process of returning to a state of equilibrium from an excited state, the T2 relaxation time characterises the dephasing of the spins and the proton density reflects the water content” [*ibid.*], more particularly, the number of hydrogen nuclei present per unit volume [Stewart2000]. Adjusting the relaxation times will create proton density-weighted, T1-weighted or T2-weighted images. The weighted images have differing contrast.

MRI is believed to be safe as there are no known side effects. However, patients with cardiac pace-makers or any internal metal prostheses are not scanned as a precaution, because of the strong magnetic field. The disadvantages of MRI are that it is expensive and not widely available. However, this does not affect this project as adequate time is provided by the project collaborator, UHW. For more detailed information on MRI the reader is referred to texts such as [Curry90] and [Rinck93].

1.1.2 MRI Finger Images

The MRI signal is reconstructed into a 256×256 grey-level image using Surrey Medical Instruments (SMIS) software. In the image, an intensity value of 0 is mapped to black and 4095 is mapped to white.

By convention, the letters x , y and z are used to indicate directions in three dimensions. In this study, the finger to be scanned is placed with its long axis along the z direction and its short axis along the y direction (illustrated in Fig. 1.2). The x direction is the vertical axis. The MRI images in this project are cross-sections (slices) of finger joints. These images are acquired in the y direction and are known as sagittal slices [Rinck93].

For this project, the proximal interphalangeal (PIP) joint, usually on the middle finger, is the object being imaged. An example MRI finger image is shown in Fig. 1.3. The two bones in the joint are labelled as the proximal phalanx and the middle phalanx, the former being nearer the hand and the latter nearer the finger tip. “Two types of bone tissue can be discerned. Cortical bone has a dense structure, while trabecular bone has a spongy appearance. The long bones have a thick outer layer of cortical bone with a thin inner layer of trabecular bone. The short bones, on the other hand, are composed of mainly trabecular bone with a thin layer of cortical bone” [MedSci98]. Cortical bone appears very dark on an MRI image, but trabecular bone appears much lighter.

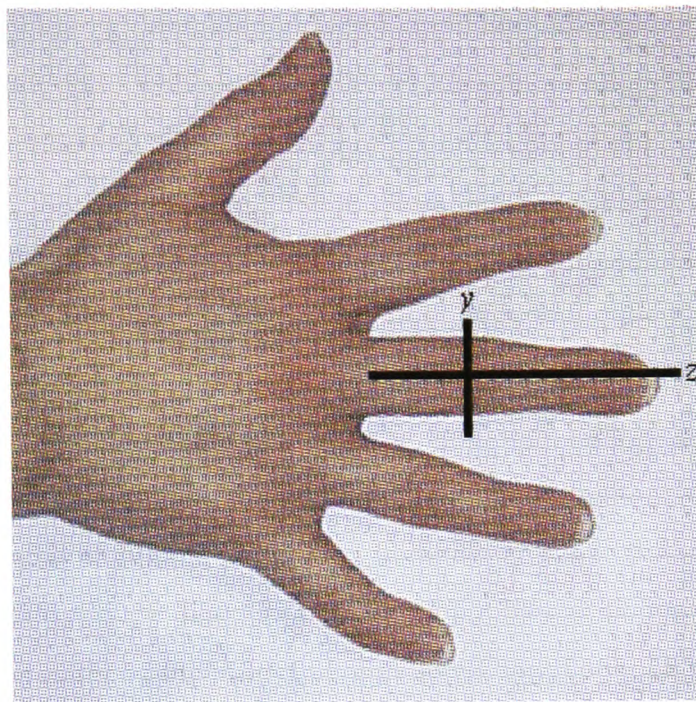


Figure 1.2: Two dimensional cross-section of a finger.

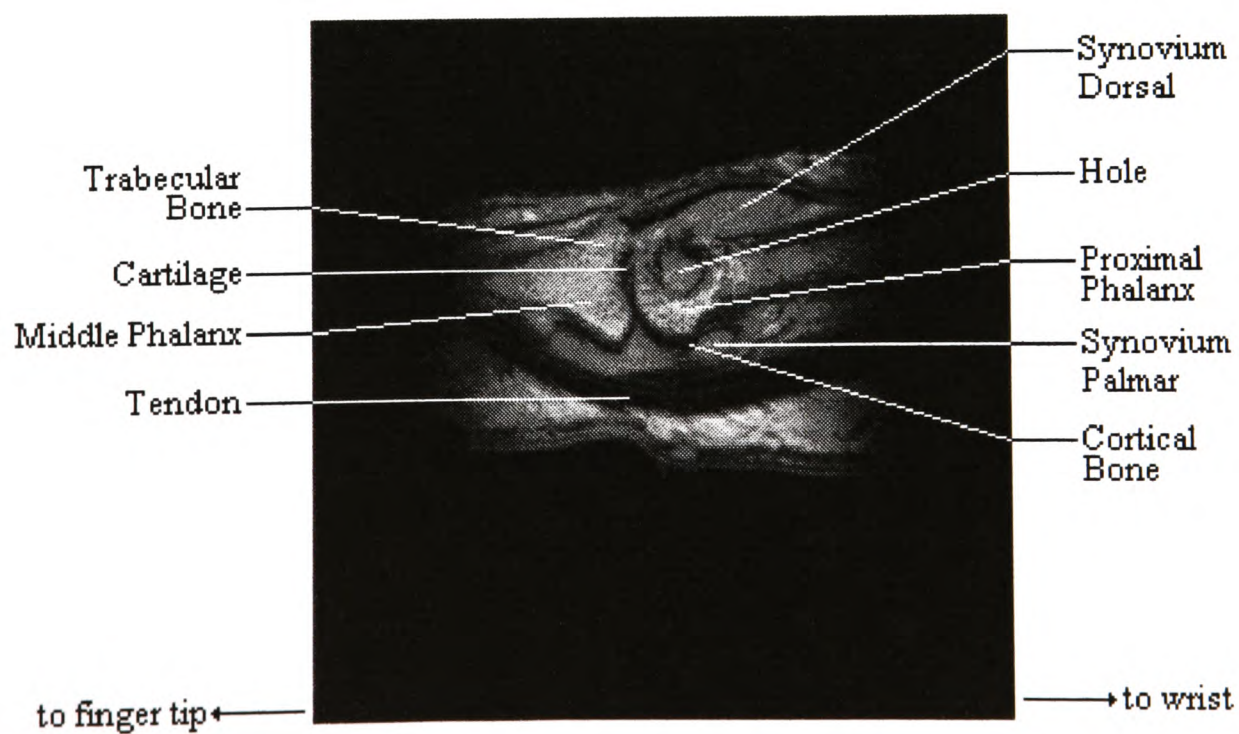


Figure 1.3: MRI scan of an RA patient.

Between the bones are narrow stripes of cartilage. The flexor tendon can be seen running below the finger. The joint capsule, which is more easily seen below the middle phalanx, contains synovial tissue, a normally thin lining of the joint. This is labelled above and below the bones as synovium dorsal and synovium palmar respectively. There is also a clearly visible “hole” (bone erosion) in this patient’s finger.

RA has a destructive effect on the finger joint. The normally thin lining of synovial tissue swells and may erode the bones and thin the cartilage. Added to the discomfort of the swelling, RA finger joints can become very stiff and painful [Plant95b]. The speed at which the disease affects the joint varies from patient to patient and is not dependent on length of illness. There is, however, a level of disease activity. With treatment the activity of the disease can be reduced. The activity of the diseased tissue is distinguished as *active synovium* and *non-active synovium*. Gadolinium-enhanced finger images (explained in the next section) can clearly show the activity of the diseased tissue [Plant95a].

MRI has the potential to image synovial tissue directly in RA patients, which is not possible by x-ray imaging [Plant95b]. Scanning the progress of the disease allows monitoring with the prospect of improving drug therapy and also of early secure diagnosis. Early secure diagnosis can justify the use of aggressive therapies.

1.1.3 Imaging Protocols

Different clinical trials require the use of different sequences of scans, depending on the nature of the trial. At UHW, three imaging protocols have been tried and tested.

The first imaging protocol acquires PD-weighted, T2-weighted and T1-weighted sequences consecutively. The total acquisition time for this protocol is slightly more than seventeen minutes. Consequently, it is difficult for a patient to keep perfectly still during this time and the latter images can show movement.

The second imaging protocol is a series of consecutive T1-weighted scans, with the contrast agent, Gadolinium, intravenously injected after the first scan. This protocol is known, at UHW, as the Gadolinium-protocol and will be referred to as such throughout the thesis.

Each T1-weighted scan is approximately three minutes in duration. A series of 9 or 10 scans are taken in all making a total acquisition time of approximately 30 minutes. Again, it is difficult for a patient to remain perfectly still during this time. Consequently movement may be observed in the images particularly between the first scan and the later ones.

The Gadolinium-protocol is used at UHW to assess disease activity in RA patients. Results [Plant95a] show that Gadolinium does enhance active synovial tissue and fluid in images of RA patients. In fact, Gadolinium enhances all regions of the entire image to varying degrees. We found that the enhancement is minimal in non-synovium regions, but active synovium is enhanced greatly. Inactive synovium is only minimally enhanced, as with the other regions. In some active cases, over 100% increase in synovium pixel intensity was obtained, resulting in much improved clarity. Results of the analysis of Gadolinium enhancement were presented as a poster at the American Conference of Rheumatology [Plant95a] (listed in Appendix E).

The third imaging protocol developed at UHW acquires all three weighted scans simultaneously. If required, Gadolinium is then injected into the patient and two more T1-weighted scans taken to show the peak and decay of the contrast agent. This latter protocol has a valuable advantage over the other protocols in that each of the first three images acquired are subject to the same movement of the finger. This advantage removes some of the registration problems, which are discussed in the next section.

To monitor the course of rheumatic disease, a patient must be scanned on successive occasions and the images analysed and compared. This immediately raises the issue of registration which is introduced in the next section.

1.2 Registration

In many magnetic resonance applications, it is necessary to compare regions of interest (ROIs) on different images. This comparison may be difficult as it is unlikely that the area being scanned is in exactly the same three-dimensional location every time. For example, a clinical trial may test the success of a certain drug by periodic scanning of the same tissue area. The slices taken in each set of scans will not exactly match across all sets. Another example of the difficulty of comparison is when a patient is unable to keep perfectly still during a series of scans. Hence, the later scans show some movement when compared to the earlier scans. The movement may affect which cross-sections are imaged for each slice.

Accurate alignment of the images is necessary, so that ROIs may be compared correctly. This is known as *registration* [Elsen93, Maguire91, Maintz98, Maurer93, West96, West99].

This section introduces the reader to the problem of registration. The application of registration presented in this thesis is specifically the registration of MRI finger images.

1.2.1 The Need for Registration

Repeated scanning of patients' fingers to monitor disease immediately creates registration problems. The problems can be broadly categorised as:

- incorrect positioning for scanning;
- finger movement;
- changes within the finger.

Each of these types of problems are now explained in the context of the specific application of this research to MRI finger images.

Incorrect Positioning for Scanning between Serial Examinations

To monitor, for example, the course of rheumatic disease, repeated scans of patients' joints must be taken on successive occasions. To assess treatment progress, in an ideal situation the same cross-sections of the finger would be compared. Ensuring that comparisons are made of the same cross-sections requires identical re-positioning of the finger for scanning, assuming that the finger has not altered physically.

At UHW, the patient's finger is positioned in the MRI scanner with the aid of a plastic syringe. The syringe is fitted to the finger and excess space packed prior to scanning. There is currently no method at UHW of ensuring that a patient's finger is in exactly the same three-dimensional location every time it is scanned. Hence, it is very likely that the finger is not re-positioned in the same way. The position can differ in any, or all axes, rotationally and in relative angles of articulated joints. Here is an immediate need for registration.

MRI scans of rheumatoid arthritis (RA) patients require the measurement of synovial tissue around the joint. As many RA patients have swollen fingers, small female patients find it easier to insert their hand into the scanner. Conversely, small female patients tend to have short arms and sometimes struggle to position their finger far enough forwards in the scanner. Thus, the cross-sections taken may not contain all of the synovial tissue in the joint. Fig. 1.4(a) illustrates the MRI scanner and Fig. 1.4(b) illustrates the positioning of a finger in the jig that is inserted into the scanner.

It is unlikely that any method will be found of ensuring that exactly the same cross-sections of the finger are taken each time. Even moulds made of the finger would be inadequate, as the physiology of the treated joint will often change between scan sessions. Sufficient clamping of the finger is necessary to reduce the number of registration problems.



Figure 1.4: (a) MRI scanner (b) jig that holds the finger for scanning.

Finger Movement

The syringe used for positioning the finger in the MRI scanner restricts considerable amounts of, although not all, movement. Finger movement can occur in many directions: forwards, backwards, rotational or bending at articulated joints. In obtaining the results for a conference poster [Plant95a] it was found that very slight movements during scanning have a great effect on the images.

For simple motion, such as forwards and backwards movement, registration is very straightforward, requiring only a simple shift to match up the images. Rotational movement and bending at articulated joints have more severe consequences and may require a combined slice approach (explained in Section 5.4).

Slippage can also occur. When the finger is inserted into the scanner, this gives a forwards thrust. If the patient later relaxes then the constant pressure on the skin holds the skin in place while the internal joint relaxes back (slippage).

Changes within the Finger

There are a number of different physiological changes that can occur inside the finger. Over time, and with treatment, the shape and size of the synovium may change. Further, RA has a destructive effect on the joint in that bone erosion and cartilage thinning may occur [Plant95b].

Digital arterioles have a pump flow of blood through them, whereas the veins and capillaries around the joint have a constant flow. The blood flow through these arteries could cause small amounts of movement within tissue regions during scanning [*ibid.*]. Also, the tendon below the joint could relax [*ibid.*].

1.2.2 The Meaning and Purpose of Registration

Registration, or image matching, is a growing area of research in medical research. The term registration is often used broadly to cover a wide variety of matching methods. Maurer and Fitzpatrick [Maurer93] define registration as the determination of a one-to-one mapping between the co-ordinates in one space and those in another, such that points in the two spaces that correspond to the same anatomic point are mapped to each other. They classify the mappings, which are also called transformations, as two dimensional for 2D spaces and three dimensional for 3D spaces.

Van den Elsen *et al.* [Elsen93] define a transformation as a set of equations that will map the co-ordinates of each point in one image into the co-ordinates of the physically corresponding point in the other image.

Thus, the registration procedure required is twofold. Firstly, points suitable for registration must be located in the image. Secondly, a transformation must be determined that maps the points in one image onto the points in the second image. This general structure is illustrated in Fig. 1.1.

This research determines what the author considers to be the best features in MRI finger images to be used for registration. These features are boundaries that are assumed to represent the bones in the finger joint being imaged. As such, these features are reliable structures for the registration process. The features are located using a combination of standard and new image processing techniques. Derived images containing such features have the Hough transform applied to them to locate the best-fit ellipses to the boundaries in the image. The displacement of the best-fit ellipse between images of the same finger taken over time provide the relative rotation and translation required to register the images.

The final registration procedure is illustrated in Fig. 1.5.

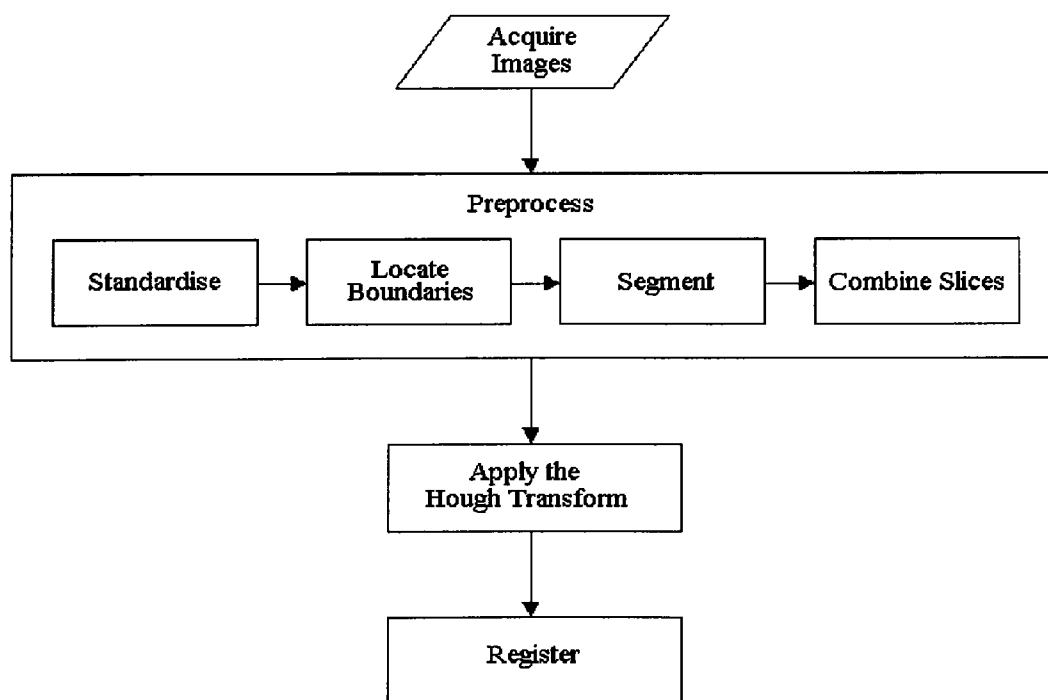


Figure 1.5: The final registration system.

1.3 An Overview of the Thesis

In Chapter 2 a review of the literature is given. That review starts by discussing Magnetic Resonance Imaging (MRI) and then concentrates on the more specific area of registration.

Chapter 3 is split into two parts. In the first part, a set of criteria for drawing ROI boundaries is established based on an analysis of the results published in poster form [Plant95a] (listed in Appendix E). The second part of Chapter 3 discusses the tools required to locate features within MRI images that are useful for registration. The tools are created as part of this project to facilitate integration into the image processing system and to ensure control over the data structures. A simple drawtool is designed for the user to define region of interest (ROI) boundaries on the images. The calculation of statistics from the ROIs is also explained and the chapter goes on to discuss the requirements for defining a path structure for storing the ROI boundaries.

Applying various image processing techniques to MRI finger images to determine features useful for registration is the focus of Chapter 4. Standard techniques including contrast stretching, standardization and thresholding are applied and also composite methods are proposed as part of this research. The Fourier Transform is also introduced in Chapter 4 and various frequency domain filters are applied to MRI finger images. The use of Fourier Descriptors is also discussed. Chapters 4 and 5 outline two new processes, established for this work. The first process is an automated sequence of image processing techniques which consistently derive tissue boundaries which are assumed to be characteristic of the two bones in the MRI finger image. The bone boundaries provide reliable features to be used in the registration process. The second new process designed for this work is the combination of the bone boundaries from many slices. A sequence of algorithms create images that contain boundaries that are assumed to define the largest possible bone shape across many slices. Such boundaries have potential to remove many of the registration problems and improve the registration results.

Chapter 5 describes the different methods that have been considered for the registration step. Simple techniques such as similarity detection and superimposition are described. Also, more complex Hough Transform methods are examined to fit an ellipse to the boundaries derived in Chapter 4 and also to describe its irregular shape. The use of moments to aid registration is also discussed in Chapter 5.

Finally, the proposed registration system, analysis and conclusions are given in Chapter 6. Suggested future work is also described.

At the end of the thesis are some appendices. A set of graphs showing inter observer variability in the development of a set of criteria for drawing region of interest boundaries can be found in Appendix A. As a step towards determining interior points of a polygonal ROI boundary, a detailed description of polygon complexities as summarised in Chapter 3 is given in Appendix B. A pseudocode listing of the algorithm used to find the interior points of a polygon is given in Appendix C. Appendix D gives a detailed explanation of the Generalised Hough Transform results that are summarised in Chapter 5. The abstract to the published poster [Plant95a] can be found in Appendix E and, finally, a published paper outlining preliminary findings of this research [Williams2000] can be found in Appendix F.

Chapter 2

Literature Review

The investigated literature is presented in this chapter. Firstly, general registration is discussed and secondly, medical registration is discussed in more detail.

2.1 Applications of Registration

Registration has received much interest in imaging processing literature. Applications of registration can be divided into medical and non-medical applications. Non-medical applications of registration include:

- aerial photographs [Borgefors88, Kuglin75];
- microcellular systems [Kim96];
- printed circuit boards [Bose90];
- radar images [Chellappa97, Fornaro95];
- range images [Bergevin96, Chen95].

Medical applications of registration include:

- computed tomography (CT) [Bajcsy83, Bajcsy89, Bartoo89, Dann88, Dann89, Engelstad88, Grimson96, Hemler94, Hemler95, Hemler96, Holton95, Kaplan89, Kovacic89, Lavallee95, Maguire91, Maintz96, Maurer97, Moshfeghi91, Petti94, Taneja94, vanHerk95, Wang96, West96, West99, Westermann96, Wong96, Zuiderveld96];
- computed radiography (CR) [Althof97];
- digital subtraction angiography (DSA) [Mandava89, Venot84b, Zuiderveld89];
- gamma ray imaging [Kenny90, Mandava89, Venot84a, Venot84b];
- magnetic resonance imaging (MRI) [Amit97, Apicella88, Apicella89, Bartoo89, Bookstein91, Bydder95, Chen94, Collins92, Dann89, Davis97,

DeMunck96, Engelstad88, Grimson96, Hemler94, Hemler95, Hemler96, Holton95, Kruggel95, Lavallee95, LeGoualher99, Lelieveldt99, Maguire91, Maintz96, Mandava89, Maurer97, Moshfeghi91, Petti94, Schwartz96, Studholme97, Taneja94, Turkington93, vanHerk95, Wang96, West96, West99, Wong96, Yang96, Zuiderveld96];

- Magneto-Encephalo-Graphy (MEG) / Electro-Encephalo-Graphy (EEG) [Schwartz96, Singh79];

- positron emission tomography (PET) [Apicella88, Apicella89, Bajcsy83, Dann89, Kovacic89, Maguire91, Studholme97, Turkington93, West96, West99, Wong96, Yang96, Zuiderveld96];

- radiation therapy images [Cai96];

- single-photon emission computed tomography (SPECT) [Bartoo89, DeMunck96, Engelstad88, Holton95, Kaplan89, Kruggel95, Maguire91, Turkington93, vanHerk95, Zuiderveld96];

- video images [DeCastro87a, Herbin89, Venot88];

- x-ray images [Amit96, Lavallee95, Mandava89, Venot84a, Venot84b].

The work of this thesis is only concerned with registering medical images.

2.2 Medical Image Registration Methods

Some comprehensive reviews of medical image registration are given in [Elsen93, Maintz98, Maurer93]. Van den Elsen *et al.* [Elsen93] state that “a wide variety of image matching methods have been proposed for medical applications, but assumptions made in these methods differ considerably”.

This section presents a review of current medical image registration methods. The registration methods are analysed in terms of their applicability to this research in order to determine appropriate methods for registering MRI finger images.

The review of registration work presented here is organised around a classification scheme designed by Maintz and Viergever [Maintz98]. The criteria they give is appropriate to the work of this thesis, highlighting the main considerations made in arriving at a registration method for MRI finger images.

The criteria classes are:

1. Dimensionality;
2. Nature of registration basis;
3. Nature of transformation;
4. Domain of transformation;
5. Interaction;
6. Optimization procedure;
7. Modalities involved;
8. Subject.
9. Object.

Maintz and Viergever [*ibid.*] also state that a registration procedure can always be decomposed into three major parts:

1. the problem statement;
2. the registration paradigm;
3. the optimization procedure.

Each of the criteria classes are now discussed in more detail.

2.2.1 Dimensionality

Image matching can be performed on data organised into different numbers of dimensions. 2D registration methods are concerned with aligning images (or slices) taken in the same plane relative to the patient. Examples of 2D applications include x-ray images, video images, MRI slices.

Some researchers are interested in single 2D images, for example, Amit and Kong [Amit96] register x-rays of a hand. Venot *et al.* [Venot88] register video images of hands.

Some medical imaging techniques produce a set of 2D slices. Some researchers treat this scenario as a 2D problem and register individual slices, for example, Bajcsy *et al.* [Bajcsy83]. In contrast, other researchers stack the 2D slices to give a 3D representation of the object being imaged. Bajcsy *et al.* [Bajcsy83] register an entire CT scan using a total of 20 stacked atlas slices. They later create a 3D model from a stack of CT slices [Bajcsy89]. Hemler *et al.* [Hemler94, Hemler95] construct a 3D CT surface from a stacked set of 2D boundaries. Dann *et al.* [Dann89] create a 3D atlas from a stack of 2D contours. Wang *et al.* [Wang96] treat a stack of image slices as a volume to search for implanted markers.

3D methods consider an image, not as a set of individual slices, but as a volumetric data set that can be registered with another (2D or 3D) image. Examples of 3D image registration are [Ashton97, Bergevin96, Collins92, Dann88, Davis97, Grimson96, Holton95, Kovacic89, Kruggel95, Maguire86, Schwartz96, Studholme97, Taneja94, Turkington93, West96, West99, Westermann96].

Some researchers have multi-dimensional registration requirements. Lavallée and Szeliski [Lavallee95] register 3D (MRI or CT) images to 2D x-ray projections in computer and robot assisted surgery.

In some methods, time may be included as an extra dimension; matching a time series of 2D images then becomes a 3D method and matching a time series of 3D images becomes a 4D method [Elsen93].

When 2D methods are used to register data obtained from 3D objects, it is assumed that the images to be matched are made in exactly the same plane relative to the patient. Special patient positioning is required to meet this assumption, which complicates the imaging protocol [*ibid.*]. This is especially true for MRI, where small variations in patient position may result in large changes in the content of a particular slice (as noted in Section 1.2.1). Van den Elsen *et al.* [*ibid.*] express the view that “even with careful provisions, the accuracy is rarely sufficient to warrant the adequacy of a 2D matching approach”. However, they are still used by some researchers reporting success with registering x-ray images and video images. The MRI finger images of this application are a set of 2D slices. These slices must be registered so that comparisons of synovium can be made in the monitoring of rheumatic disease. Therefore, a goal of this research is to assess the applicability of 2D methods for the registration of MRI finger images.

For many papers there appears to be a lack of discussion on the dimension of the images being registered. Authors of 3D methods are usually explicit about their dimension as are authors who stack the 2D slices into a 3D model. The majority of papers concern multimodal registration. Omitting a discussion of slice comparison is strange as movement between or during scanning can affect which cross-sections are imaged and also the parallelism of the slices. Chen *et al.* [Chen94] do look for the best matching slice in one image set to another reference slice before registration. They also assume the slices are parallel. With MRI finger images, it is possible that slices from subsequent occasions, or due to movement, are not parallel.

2.2.2 Nature of registration basis

Some registration methods use points on the images to perform registration; these are known as point methods. Point methods involve determining the co-ordinates of corresponding points in different images and estimating the geometric transformation required to register the images using these corresponding points [Maurer93].

Registration algorithms may use either intrinsic or extrinsic points, or a combination of both. Intrinsic points are patient related properties, for example, anatomical landmark points (known as fiducial points [Maurer93]), geometric features or surfaces of skin. Extrinsic image properties are induced by artificial objects that are “added” to the patient, for example, skin markers. Contrast agents, such as Gadolinium (explained in Section 1.1.3), are considered to be intrinsic [Elsen93].

Intrinsic Methods

Intrinsic methods rely on patient-generated image content only [Maintz98]. Choosing appropriate points on an image is a key factor in the success of a registration method that uses intrinsic points. Selecting appropriate anatomical landmarks is a labour-intensive, interactive process, which must be conducted by a knowledgeable user. Intrinsic point methods cause no discomfort or hindrances to the patient. Naturally, it must be possible to extract similar structures from both images being registered [Elsen93].

Intrinsic registration methods can be based on a set of landmarks [Amit96, Maguire86, Maguire91], segmented structures [Bajcsy83, Hemler94, Hemler95, Hemler96, Lavallee95, Petti94, Taneja94, Turkington93] or directly from the image grey values.

Hemler *et al.* [Hemler95, Hemler96] use thresholding to segment the skin surface of brain images to create a boundary. Skin surfaces alone are unsuitable as landmarks in our specific finger application, due to the danger of slippage (explained in Section

1.2.1). Also, as discussed in Section 4.1.3, MRI finger image grey levels cannot be used for segmenting structures by thresholding or for direct registration.

Extrinsic Methods

Extrinsic methods add markers to the patient prior to scanning. For MRI, appropriate non-metal markers with imaging capabilities must be made. Successful extrinsic markers can be viewed easily, can be extracted from images and have potential for automatic detection. Van den Elsen *et al.* state that “an obvious disadvantage of extrinsic methods is that they cannot be used in retrospect” [Elsen93].

A commonly used extrinsic object is a stereotactic frame [Hemler95] screwed rigidly to the patient’s skull. Such frames are used for localization and guidance purposes in neurosurgery, which is one of the main applications of registration [Maintz98]. Maintz and Viergever [*ibid.*] also state that “the invasive nature of the frame during neurosurgery is not an additional strain on the patient. However, mounting a frame for the sole purpose of registration is not permissible.” This is assumed to be due to legal or ethical reasons. The authors also claim that until recently, the stereotactic frame method provided the “gold standard” for registration accuracy. Other implantable markers are used by [Maurer97, West96, West99]. The markers are made from hollow plastic cylinders, which will contain solutions that appear bright on the image being acquired. These markers are also invasive as they have a plastic base or post that is screwed into the patient’s skull.

Externally attached markers [Holton95, Maguire91, Wang96] are non-invasive, but tend to be less accurate [Maintz98]. Optical digitizing systems [Grimson96, Westermann96] are also used as a non-invasive method.

Experiments performed at UHW have found external markers to be of no use for MRI finger images. Small cylindrical tubes of copper sulphate were attached to the finger prior to scanning. Correct repositioning of the tubes on a later scanning date

is almost impossible. Also, internal slippage (explained in Section 1.2.1) would make the external markers of no benefit in registering the internals of the finger joint. A long-lasting dye could be used on the patient's finger, but this is not ideal for the patient.

As extrinsic markers have already proved unsuitable for this research, future work only investigates intrinsic methods. Locating useful features in MRI finger images to be used in registration is a key issue in this research.

2.2.3 Nature of transformation

A registration transformation is called *rigid* when only translations and rotations are used. When the transformation maps parallel lines onto parallel lines, it is called *affine*. When lines are mapped onto lines, without necessarily preserving parallelism, the transformation is called *projective*. Finally, when lines are mapped onto curves, the transformation is called *curved* or *elastic* [Maintz98].

It is essential that the transformation used for registration is adequate to describe the deformation of the body part under study [Elsen93]. For Rheumatology, where analysis of synovium is the primary issue, great care has to be taken that registration does not lose information vital to the application.

Some researchers use elastic mappings for intra-patient, inter-patient or patient to atlas matching [Bajcsy83, Bajcsy89, Dann88, Dann89, Moshfeghi91]. One image (or the atlas) is deformed to fit the other image. Such deformations would change the synovium detail within MRI finger images and are therefore considered detrimental to the purpose of this thesis.

The global rigid transformation is used most frequently in registration applications [Maintz98]. (The term *global* is explained in the next section). It is popular because, in many cases, the rigid body constraint is at least approximately satisfied [*ibid.*]. The most common application is the human head [*ibid.*]. For MRI finger joints, movement

during or between scanning (explained in Section 1.2.1) could affect the rigid body constraint.

2.2.4 Domain of transformation

A transformation is called *global* if it is applied to the entire image and *local* if sections of the image have their own transformations applied [Maintz98]. Local transformations are seldom used directly as they may affect the local continuity of an image [*ibid.*]. In this work, global transformations are applied to particular features in the images to derive registration parameters which are applied to the entire image.

Applying rigid transformations globally is sufficient if the object being imaged is relatively stable. The other transformations could introduce distortions that were not present in the images beforehand [Elsen93]. Van den Elsen et al. [*ibid.*] argue that local rigid transformations seem, at first glance, to be useless, as the transformed image contains gaps (tears) that were not in the original images to be registered. However, they also state that such transformations are useful for a multimodal or time study in which the local region corresponds to a bone.

2.2.5 Interaction

There are three categories of interaction for registration algorithms: interactive, semi-automatic and automatic. Interactive methods require user input to determine the transformation [Elsen93]. Semi-automatic methods require user interaction to select image properties to be used in a computer determined transformation. The user may also provide information for starting, guiding, or stopping the matching procedure [*ibid.*]. Automated methods do not require user interaction [*ibid.*].

The amount of interaction required is an important indicator of the clinical applicability of a method [*ibid.*]. Maintz and Viergever [Maintz98] argue that “in many methods there is a trade-off between minimal interaction and speed, accuracy or ro-

bustness”. In interactive or semi-automatic methods, a trained operator is necessary but the results may be subjectively influenced [Elsen93].

2.2.6 Optimization procedure

Registration algorithms may be direct or search-oriented. A direct method simply carries out a specific transformation. A search-oriented method starts from at least one initial guess and, guided by a goodness-of-match measure, tries to find the best transformation. An exhaustive search is classified as direct [Elsen93].

When point-to-point matching is used in both direct and search-based methods, accuracy generally increases with the number of points used. However, interactive landmark selection may introduce errors which will lessen the accuracy [*ibid.*].

Direct methods assume registration is simple enough to be performed as a straightforward calculation. Generally, this is not true and complexities have to be broken down into manageable parts [*ibid.*].

In search-based methods, a goodness-of-match function can be used to rate the transformations. The rating function has to be calculated often, which may compromise the accuracy of rating with computational speed and storage. A search-based method will assume that an optimal solution exists. Suitable rating functions are necessary to avoid an exhaustive search, which is usually not practical as it is too costly in time [*ibid.*].

2.2.7 Modalities involved

Some registration applications are concerned with multimodal images, *i.e.* registering images acquired from different formation techniques. Some examples of multimodal image registration are given here.

- Registering MRI images with CT images

Hemler *et al.* [Hemler94, Hemler95, Hemler96] identify similar objects or structures in images to be registered. Their technique is designed for brain images and is also augmented to include images of the spine. Holton *et al.* [Holton95] use markers to register images of the head. Petti *et al.* [Petti94] register brain images by minimising the volume lying outside the intersection between one structure and its transformed counterpart. Maguire *et al.* [Maguire91] select landmarks to register brain images. Maintz *et al.* [Maintz96] extract ridge-like structures from brain images for registration. Implantable markers are often used to register images of the head [Maurer97, West96, West99]. Moshfeghi [Moshfeghi91] elastically deforms one image to match another. Taneja *et al.* [Taneja94] use a surface matching algorithm to register head images.

- registering PET images with MRI images

Apicella *et al.* [Apicella88, Apicella89] use correlation to register images of the same scale. Kruggel and Bartenstein [Kruggel95] register brain volume surfaces by an initial 3D rigid transformation and then an elastic match that minimises the overall squared differences between the surfaces. Maguire *et al.* [Maguire91] select landmarks to register brain images. Turkington *et al.* [Turkington93] use a surface-fitting algorithm for three-dimensional image registration. West *et al.* use implantable markers to register images of the head [West96, West99]. Wong *et al.* [Wong96] use landmarks to register head and neck images. Yang *et al.* [Yang96] segment the brain into four different tissue types to perform registration.

- registering PET images with CT images

Wong *et al.* [Wong96] use landmarks to register head and neck images.

- registering SPECT images with MRI images

Bartoo and Hanson [Bartoo89] use the image grey levels to classify brain tissues. Holton *et al.* [Holton95] use markers to register images of the head. Kruggel and Bartenstein [Kruggel95] register brain volume surfaces by an initial 3D rigid transformation and then an elastic match that minimises the overall squared differences between the surfaces. Maguire *et al.* [Maguire91] select landmarks to register brain images. Turkington *et al.* [Turkington93] use a surface-fitting algorithm for three-dimensional image registration.

- registering SPECT images with CT images

Bartoo and Hanson [Bartoo89] use the image grey levels to classify brain tissues. Kaplan and Swayne [Kaplan89] use anatomic or externally placed landmarks to register chest and abdominal images.

- registering x-ray images with CT/MRI images

Lavallée and Szeliski [Lavallee95] register 3D medical images (MRI or CT) with 2D x-ray projections during computer and robot assisted surgery.

Other registration applications are concerned with monomodal images *i.e.* images originating from a single image formation technique. Examples of monomodal image registration are given here.

- registering pairs of CT images

Holton *et al.* [Holton95] use markers to register images of the head.

- registering pairs of MRI images

Holton *et al.* [Holton95] use markers to register images of the head. Kruggel and Bartenstein [Kruggel95] register a time series of brain images by an initial 3D rigid transformation and then an elastic match that minimises the overall squared differences between the surfaces.

- registering pairs of PET images

Junck *et al.* [Junck90] use correlation to rotate functional brain images to a standard vertical orientation, identify the antero-posterior centerline and align multiple images from the same brain level.

- registering pairs of SPECT images

Holton *et al.* [Holton95] use markers to register images of the head. Junck *et al.* [Junck90] use correlation to rotate functional brain images to a standard vertical orientation, identify the antero-posterior centerline and align multiple images from the same brain level.

- registering pairs of DSA images

Venot *et al.* [Venot84a] and Venot and Leclerc [Venot84b] developed new similarity measures for the registration of DSA images. They suggest their new method is better than traditional similarity measures such as the correlation coefficient, the correlation function and the sum of absolute values of differences. However, they specify that their method is applied to non-noisy, dissimilar data. MRI finger images are noisy, therefore, this method is not pursued for this application.

Other types of registration modalities are:

- images to a model

Amit and Kong [Amit96] create a model from a graph of landmarks to register x-rays of hands. Bajcsy *et al.* [Bajcsy83] create a deformable atlas to register brain images.

- patients to external landmarks or images

Grimson *et al.* [Grimson96] use an optical digitizing system to aid a surgeon marking internal landmarks to guide the progression of the surgery. Lavallée and Szeliski [Lavallee95] register 3D medical images (MRI or CT) with 2D x-ray projections during computer and robot assisted surgery.

The work of this thesis is concerned primarily with registering monomodal images, *i.e.* images originating from a single image formation technique. In this case, the technique is MRI. The purpose of registering monomodal images is for quantitative comparison, which increases the precision of treatment monitoring with serial images [Maurer93].

2.2.8 Subject

Intrasubject registration is when the images involved are from a single patient. *Intersubject* registration is when the images involved are from more than one patient. Another category of registration subject is when one image is constructed from an information database obtained using many subjects. This type of registration is known as *atlas* registration [Maintz98]. Intrasubject registration is by far the most common subject registration [*ibid.*]. Intersubject and atlas registration are used to gather statistics on the size and shape of specific tissue structures [*ibid.*]. This thesis is concerned primarily with intrasubject registration.

2.2.9 Object

Medical registration applications have been applied to a variety of objects in the literature, including:

- abdomen/pelvic images [Venot84a, Venot84b];
- breast images [Davis97].
- chest/lung/abdomen images [Althof97, Kaplan89, Kenny90, Moshfeghi91];
- ear images [Herbin89];
- eye images [DeCastro87a, Peli87];
- hands [Amit96, Venot88];
- head and brain images [Amit97, Apicella89, Bajcsy83, Bajcsy89, Bartoo89, Bookstein91, Bydder95, Chen94, Collins92, Dann89, Davis97, DeMunck96, Engelstad88, Grimson96, Hemler94, Hemler95, Hemler96, Holton95, Kovacic89, Kruggel95, LeGoualher99, Maintz96, Maurer97, Petti94, Schwartz96, Studholme97, vanHerk95, Venot88, West96, West99, Westermann96, Wang96, Wong96, Yang96, Zuiderveld96];
- heart [Maguire86];
- humerus [Mandava89];
- knees [Herbin89, Venot88, Zuiderveld89];
- spinal images [Hemler94, Lavallee95];
- thorax [Lelieveldt99];

2.3 Conclusions

The majority of published work in the area of medical image registration is concerned with multimodal registration of head or brain images. The particular application of this work is monomodal registration of MRI finger images. No work on registering MRI finger images has yet been found in the literature by the author.

There are many differences between the brain and finger image registration problem. A popular extrinsic technique for the registration of head and brain images is the application of a stereotactic frame. Extrinsic methods have been shown to be unsuitable for this research, therefore, future work only investigates intrinsic methods. Locating useful features in MRI finger images to be used in registration is a key issue in this research. Finger movement during scanning has already been shown to be a serious problem in this application (explained in Section 1.2.1). Maurer *et al.* [Maurer97] claim that, for brain images, “the effect of patient movement without rigid head fixation during scanning is negligible”. Thresholding has been used to segment the skin surface of brain images to create a boundary [Hemler95, Hemler96]. Skin surfaces alone are unsuitable for MRI finger images, due to the danger of slippage (explained in Section 1.2.1). In Section 4.2.3, structural boundaries that approximate the bones within the finger image are located. Lastly, grey level clustering has been used to segment brain tissue types [Bartoo89]. Section 4.1.3 shows that MRI finger image grey levels cannot be used for segmenting structures by thresholding or for direct registration.

Correlation methods are very useful for monomodal image registration, particularly when comparing serial images of the same patient, for example, when looking for small changes caused by disease [Maurer93]. Correlation methods try to find the optimum registration method by maximising the similarity between images of the same patient; these images differ mainly because of different image acquisition conditions and also possibly because of small object changes. An intensity scaling might first be necessary to correct for the differences in acquisition times, injected activities, such as Gadolinium

(explained in Section 1.1.3), and backgrounds [*ibid.*].

Many similarity criteria have been experimented with in the literature, including the correlation function, the correlation coefficient, the sum of squares and the sum of absolute values of differences [*ibid.*]. Suitable correlation methods to apply to MRI finger images are investigated in Chapters 4 and 5. In Section 4.2.3 intensity scaling is applied to correct the differences in the three weighted scans (explained in Section 1.1.1), and the Gadolinium-enhanced images (explained in Section 1.1.3).

Chapter 3

Defining and Storing Region of Interest Boundaries

Scanning patients with rheumatoid arthritis allows monitoring the progress of the disease with the prospect of improving drug therapy and also of early secure diagnosis. Early secure diagnosis may in turn warrant aggressive therapies. To this end, the MRI finger images must be analysed.

The commercially available SMIS software was used to outline regions of interest (ROIs) on the finger images. Statistics calculated from the ROI results were published as a poster [Plant95a]. The first part of this chapter analyses the method used to generate the poster data. A set of criteria for drawing ROI boundaries is developed to ensure that the boundaries are reproducible. Particular deficiencies with the SMIS software are also noted.

At the University Hospital of Wales, an image viewer [OConnor98a, OConnor98b] has been designed and created for the display of MRI finger images. The viewer incorporates various image processing functions that can be applied to the finger images. One of the main advantages of the viewer is that it is an extensible system and has potential for the addition of numerous image processing techniques as required by those involved in specific projects. The conclusions of the analysis on creating ROI boundaries, provided in this chapter, generate enough reasons for the production of a drawtool to add to the functions of the viewer.

The second part of this chapter describes the development of the so-called *drawtool*, completed as part of the work of this thesis, for defining ROI boundaries. Once an ROI boundary is created, statistics are calculated from pixel intensities within the ROI. The formulae used to calculate the statistics are explained in Section 3.2.5. Section 3.2.6 explains why storing information about the ROI boundary is advantageous in many applications. Further, a path structure for storing ROI boundaries is developed and RIFF files are examined as a means of storing the path structure in a file.

3.1 A Set of Criteria for Drawing Region of Interest Boundaries

The anatomy represented in MRI finger images varies in shape and size from patient to patient. The observed effect of rheumatoid arthritis on the joint depends on the degree of disease activity at the time of scanning. A comparison of statistics generated from selected regions of interest (ROIs) will aid clinicians' analysis and understanding of rheumatoid arthritis. Therefore, it is absolutely vital that the definition of ROI boundaries is consistent and reproducible on subsequent scanning occasions and by different observers.

As a first step towards this, a set of criteria is established for the physical drawing of the ROI boundaries, firstly using an existing drawing package and then using a newly developed package. The criteria will aid the calculation of statistics which have clear medical meaning. This section outlines these criteria and explains the work conducted in establishing them.

Theoretically there are two aspects to reproducibility:

1. **variability** - whether the same results are obtained on successive attempts.
The degree of spread shows the variability;
2. **bias** - a measure of the extent to which one observer's results are consistently higher or consistently lower than those of another observer.

Variability in quantification of images may arise from:

- Patient variability (change with time).
- Equipment variability - drift in the machine and registration of the images.
- Observer variability, of which there are two types:
 1. Intra observer variability, *i.e.* variability within the results of one observer.
How accurately can one observer reproduce his/her own results?
 2. Inter observer variability, *i.e.* between observers. Can two observers produce the same results independently?

3.1.1 Assessment of Previous Image Analysis

This section explains the determination of the results for the published poster [Plant95a] and analyses these results.

Ten rheumatoid arthritis (RA) patients were scanned at the University Hospital of Wales (UHW) with the Gadolinium-protocol (explained in Section 1.1.3). All patients had erosive RA, with varying levels of disease activity. The middle finger (usually on the right hand) proximal interphalangeal (PIP) joint of each patient was scanned. Initial observations of the images obtained for the ten patients were seen to coincide with clinical diagnoses.

In order to measure the effect of the contrast agent (Gadolinium) on the images, Surrey Medical Instruments (SMIS) software was used to draw ROI boundaries on the images, from which statistics were calculated. For each of the ten patients, a middle slice (*e.g.* slice 4 or slice 5) was chosen for analysis. The analysis was carried out on the chosen slice for all scans taken per patient. The specified regions chosen to draw ROI boundaries on were the proximal phalanx, middle phalanx, synovium dorsal, synovium palmar and cartilage (illustrated in Fig. 1.3).

At this stage the size of an ROI, given by the number of pixels, was not being considered. Only the mean pixel intensity for a physical region was required. Therefore, the ROI boundaries were drawn well within each of the specified regions, rather than around it, to provide an accurate measure of mean pixel intensity for each tissue region. The mean pixel intensities of each ROI were plotted on a graph to show percentage increases in intensities.

The results showed that Gadolinium does enhance active synovium in RA patients. In fact, Gadolinium enhances all regions of the entire image to varying degrees. The enhancement was minimal in non-synovium regions, but active synovium was enhanced greatly. Inactive synovium was only minimally enhanced, as with the other regions. In some active cases, over 100% increase in synovium pixel intensity was obtained,

resulting in much improved clarity.

Results of the analysis were presented as a poster at the American Conference of Rheumatology [Plant95a].

The method used to determine the results for the poster and the reproducibility of the ROI boundaries was analysed by collaboration with staff at UHW [Plant95b]. Observer and Rheumatology knowledge were combined to further analyse the patient images and assess the feasibility of producing criteria for drawing the ROIs. Dr. M. J. Plant, Senior Registrar, Rheumatology, UHW, provided the Rheumatology knowledge.

As part of the analysis, the ROI boundaries were re-drawn on the same specified regions as previously (*i.e.* the proximal phalanx, middle phalanx, synovium dorsal, synovium palmar and cartilage) and in addition the tendon (illustrated in Fig. 1.1). The boundaries were drawn using the SMIS software by two observers, the author and Dr. Plant. The mean pixel intensities from both observers' ROI boundaries were compared and the following inconsistencies noted.

1. By the end of a series of scans (*i.e.* the Gadolinium-protocol), the patient's finger had often moved and the shape and size of the synovium region appearing on that scan had changed. This problem of registration generally worsens if the patient is re-scanned at a later time.

2. Hardware problem - when trying to draw a freehand shape, the mouse cursor often jumps. An improvement could be the use of a light pen, although this raises the problem of parallax due to the screen not being flat. Another possible improvement would be to use a digitizer.

As stated earlier, the size of the ROIs has not been considered. However, the size of the synovium (*i.e.* its area in a given slice, quantified by the number of pixels) could be a useful statistic in assessing improvement in disease. This necessitates drawing an ROI boundary to specify the region, rather than within a vaguely specified region, as was done previously. Drawing around a region is sometimes a very difficult task.

On some images, the boundary around the synovium is not easily seen. Some areas of synovium are observed to be heterogeneous, that is, they contain a mixture of grey levels. Thus, clarification is required of whether only the bright areas in the synovium (which are much easier to outline) or the whole region should be enclosed.

In attempting to outline whole regions, some drawbacks with the SMIS software are highlighted (noted below).

Drawbacks with the SMIS Software

As the synovium has no set shape or size, and varies completely from patient to patient, a rectangle or ellipse is of no use in drawing around the synovium. The only other options available from SMIS are a polygon or a freehand shape.

Drawing a freehand shape with SMIS involves moving the mouse cursor around the region with the left mouse button depressed. This is very difficult and inaccurate as the mouse cursor often “jumps”.

With SMIS, depressing the left mouse button allows the user to select vertices for a polygon. Completion of the polygon is achieved by selecting the first vertex again. This procedure is much simpler than the one for freehand shape definition but also has problems associated with it. The final mouse click is frequently not accurately placed and goes unrecognised by the SMIS software; an extra click at the starting point is necessary. Sometimes the SMIS software completes the polygon prematurely.

It would be advantageous to draw around regions on one image and then copy the ROI boundaries to the other images, saving a great deal of time and effort. However, SMIS has no capabilities for saving the ROI boundaries that have been drawn.

These drawing problems form part of the need for an extensible system. The software developed to address these kinds of problems and limitations is discussed in Sections 3.2 and 3.2.6.

3.1.2 Criteria for Drawing ROIs

Having analysed the way ROI boundaries were previously drawn, this section concentrates on developing a suitable set of criteria for drawing these boundaries. There can be no general criterion for drawing ROI boundaries on finger images, due to the differing natures of the specified tissue regions. An initial set of criteria for drawing ROI boundaries, based on the assessment made in Section 3.1.1, is summarised as:

1. For the proximal phalanx use a rectangle in its head (the elliptical part) only;
2. For the middle phalanx use a rectangle in the middle only;
3. For cartilage use a freehand boundary;
4. For the tendon use a rectangle;
5. For the synovium dorsal use a freehand boundary or a polygon;
6. For the synovium palmar use a freehand boundary or a polygon;
7. For synovium dorsal and palmar, draw the boundary just outside the region.

The criteria are assessed by both observers independently to see how reproducible the results are. ROI boundaries are drawn on slice 4, a central slice on which each tissue region is clearly seen. Boundaries are drawn on the pre-injection scan and the first two post-injection scans only, for all 10 Gadolinium-protocol patients. The first 3 scans show the initial peak and decay of the contrast agent, Gadolinium.

Problems Encountered using the Criteria Independently

A number of problems were encountered by both observers and these are explained here.

1. It is sometimes difficult to establish the position of the middle of the middle phalanx.
2. Distinguishing between bone and synovium is often difficult.
3. Outlining boundaries for synovium is often difficult due to the overlap of grey levels in the soft tissue surrounding the synovium.
4. The tendon is often very small.
5. Images are often very dark.
6. The cartilage cannot always be seen.
7. The synovium is not always enhanced.
8. There is considerable heterogeneity (*i.e.* a mixture of grey levels) present in the bones.

Comparison of Independent Exercises

Several discoveries were made during the independent analysis and it also became clear that several issues required clarification. In particular:

1. Synovium dorsal is easier to outline than synovium palmar.
2. In a synovium region, should only the bright areas be drawn around, or should the whole region be drawn around?
3. It is much easier to draw an ROI boundary well within a region, than to measure the exact size of a region by drawing around it.

Again there is some uncertainty over whether highlighted areas of synovium only or the whole region should be drawn around. Different assumptions, made by both observers, meant that one observer's ROIs were generally larger than the other's. However, there was not much discrepancy in the mean pixel intensities. A more rigorous analysis of the differences in observations is offered below.

Observations from the Images

Synovial tissue has variable blood supply. The contrast agent, Gadolinium, highlights synovium which has a rich blood supply. Therefore, there could be more synovium present in the proximal interphalangeal (PIP) joint than is observed by eye. Some areas of synovium may become ischaemic (lacking blood supply) and autoamputate. With less blood, it is expected that the synovium will become less active (or entirely inactive). This raises an important problem in how to measure the amount of synovium in the PIP joint where there is also some inactive synovium present.

One patient's images show more synovium dorsal than has been seen on images from the other patients, due to the finger being positioned further forward in the scanner than usual. This indicates that the synovium dorsal may extend further back than previously realised and raises questions about whether the patients' fingers are positioned correctly for scanning.

Subsequent scanning of a patient, following treatment, could show a change of shape and size in the synovium, but it is difficult to be sure that this indicates improvement in the disease. The change in shape and size could be due to incorrect positioning for scanning (discussed in Section 1.2.1). A measure for the assessment of improvement needs to be determined. Current interests for UHW lie in the area of the synovium, its mean pixel intensity, and possibly the speed of increase of Gadolinium enhancement, that is, how quickly it reaches its peak intensity.

Registration presents a further problem when re-scanning, in that the slices are unlikely to be of exactly the same cross-sections of the finger as previously. One possible solution would be to combine information from four central slices (examined in Section 5.4, for comparison with another scan. However, this will lose vital spatial resolution important to the clinicians.

Due to the varying complexity of the images, it is inadvisable to have just one observer. Rather, averaged results should be obtained from two independent observers,

or an automated method should be sought.

3.1.3 Analysis of Data

In this section, the statistics calculated from the ROI boundaries drawn in Section 3.1.2 are analysed to show the effect of inter observer variability in the analysis of MRI finger images.

A spreadsheet was set up, with one sheet for each of the six specified tissue regions (*i.e.* proximal phalanx, middle phalanx, synovium dorsal, synovium palmar, cartilage and tendon). On each sheet the mean pixel intensities for the six ROIs obtained by both observers are columnised. The differences and averages of the two columns are calculated. The differences are then plotted against the averages on an XY scatter graph. For synovium, the process was repeated for the area of the ROI as well. Fig. 3.1 gives an example of the created graphs.

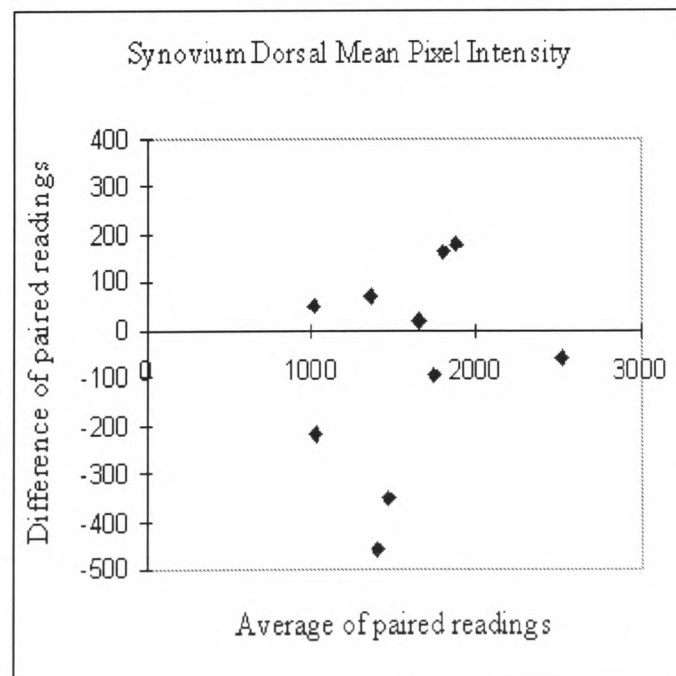


Figure 3.1: Inter Observer Variability.

The scatter graphs show any inter observer variability and bias in drawing the ROIs. In particular:

1. If the points are near the x -axis then there is little inter observer variability. Conversely, if the points are further away from the x -axis, then there is inter observer variability.
2. If the plotted values are scattered evenly either side of the x -axis, this shows no bias. If all points are above or below the x -axis, there is bias in the results. This indicates that one observer has, through positioning of an ROI, produced statistics which are consistently higher or consistently lower than those of the other observer.

In Fig. 3.1 there is no bias, but there is some variability.

Analysis of Graphs

Presented below is a summary of the inter observer variability and bias as shown by the graphs, which can be found in Appendix A.

1. The synovium dorsal has a lot of inter observer variability, but no bias (illustrated in Figs. A.1 and A.2).
2. The synovium palmar has a lot of inter observer variability and bias (illustrated in Figs. A.3 and A.4).
3. The proximal phalanx shows very little inter observer variability and no bias (illustrated in Fig. A.5).
4. The middle phalanx shows some inter observer variability and a little bias (illustrated in Fig. A.6).
5. The cartilage shows considerable inter observer variability, and bias (illustrated in Fig. A.7).

6. Generally, there is not much inter observer variability in the tendon and no bias (illustrated in Fig. A.8).

The synovium results show considerable variation, especially palmar which also is very biased. Most of the error is due to the observers making different assumptions, as noted in Section 3.1.2. This clearly shows the need for a clearer and better defined set of criteria for drawing the ROI boundaries.

3.1.4 Further Image Analysis to Enhance the Criteria

The synovium areas are quite difficult to measure. The different assumptions made by both observers (noted in Section 3.1.2) are developed into two methods to investigate:

Method 1

measure enhanced areas only within synovium regions (excluding enhancement in tissues outside the joint).

Method 2

measure the whole synovium region (including any synovium which has not been enhanced).

Before an independent assessment of the revised criteria was carried out, the pre-injection scan and the second post-injection scan were compared, for all 10 patients, to observe, by eye, where the synovium was enhanced. Observations from this comparison are tabulated in Table 3.1. Where synovium was observed to be enhanced, ROI boundaries were drawn to assess the feasibility and effectiveness of the two methods above.

<i>Patient</i>	<i>Synovium Dorsal</i>	<i>Synovium Palmar</i>
1	diffusely enhanced; dorsal bulge;	no obvious enhancement; demarcation seen between capsule and connective tissue;
2	diffusely enhanced;	flexor tendon not seen in whole length (a different slice may improve this);
3	thin strip of non- enhancing tissue;	demarcation seen between capsule and connective tissue;
4	very little dorsal enhancement;	very prominent palmar enhancement, which is partly heterogeneous; some synovium in the palmar joint space;
5	diffusely enhanced;	difficult; 2 relatively bright areas, rest slightly bright, difficult to define; tail has possibly enhanced more than the proximal phalanx; may need to measure the whole synovium palmar region, which would be easier to do;
6 (poor image)	enhanced, but not so bright;	tissue, not enhanced, possibly difficult to outline; low signal area through the middle; demarcation between capsule and connective tissue;
7	enhanced, except for one low signal area;	no enhancement in synovium palmar but enhancement in palmar joint space;
8 (Not very good image)	tiny area of enhanced synovium;	can see demarcation line, enhanced above and below the line; large synovium palmar region difficult to see; palmar joint space enhanced a little;
9 (finger well positioned)	diffusely enhanced;	mass of tissue but no enhancement;
10	diffusely enhanced, but with some low signal areas;	no enhancement, but demarcation line very clear;

Table 3.1: Comparison of the second post-injection scan with the pre-injection scan.

The observations listed in Table 3.1 are summarised here. From a sample of ten sets of images, from different patients:

- 9 patients were observed to have synovium dorsal enhancement;
- 3 patients were observed to have synovium palmar enhancement;
- 3 patients were observed to have enhancement in the joint space;
- 3 patients were observed to have enhancement in both synovium dorsal & synovium palmar;
- 1 patient was observed to have no enhancement in either synovial tissue areas.

Nine out of ten patients were observed to have Gadolinium-enhanced synovium.

During the analysis, some further observations were made from the images. In particular:

1. In patient 1, the synovium palmar region may include the capsule of the joint.
2. In patient 1, the finger has noticeably moved within approximately 5 minutes of scanning. The bones and joint have moved, but not the skin. This could be due to slippage (explained in Section 1.2.1).

With the added information obtained in the above examinations, the two methods for drawing ROI boundaries are refined as:

Method 1

For synovium dorsal, synovium palmar and palmar joint space, outline enhanced areas only, relative to the pre-Gadolinium scan. If in doubt compare with the bone enhancement. Exclude any enhancement outside the joint capsule.

Method 2

For synovium dorsal, outline as much as can be seen. For synovium palmar, outline the tissue, excluding the joint capsule where visible and any enhancement below the demarcation line. Measure as far back (towards the wrist) as can be seen, and as far forwards as the shoulder of the proximal phalanx.

Comparing the methods indicates that it is easier to measure just the bright areas than the whole of a synovium region.

3.1.5 Establishing a Coefficient of Variation

The exercise carried out in Section 3.1.2 was repeated using the revised criteria for drawing ROI boundaries, developed in Section 3.1.4. Spreadsheets were set up and similar scatter graphs are created (as in Section 3.1.3) to assess any improvement in the inter observer variability and bias.

To test the reproducibility of the results, a coefficient of variation (γ) was defined and added to the previous results. The coefficient of variation is defined as:

$$\gamma = \frac{100\sigma_d}{\mu} \quad (3.1)$$

where σ_d is the standard deviation of the differences between observers and μ is the mean of the averages of the observer's results. Equation 3.1 is a commonly used measure in the medical field, and in particular is well-known to rheumatologists. The coefficient of variation gives a measure of any intra- or inter-observer variability. Naturally, a near zero coefficient shows minimal variation. The coefficient also shows if either of the two methods are preferable.

At this stage intra observer variability was also assessed. The exercise from Section 3.1.2 is again repeated independently by both observers. Spreadsheets were again set up and each observers results are plotted on a graph to show any intra observer

variability or bias. The graphs for this exercise can be found in Appendix A, Figs. A.9 to A.18.

A summary of the observer variability and bias studies can be found in Table 3.2. The table lists the coefficients of variation calculated for both inter and intra observer variability. The calculations are applied to the mean pixel intensities and number of pixels for both synovium regions, with ROI boundaries drawn using both methods.

A number of observations are made from the summary in Table 3.2. In particular:

1. Estimation of pixel intensity is more precise than estimation of area.
2. Method 2 gives consistently better results than Method 1 for synovium dorsal but consistently worse results for synovium palmar.
3. Comparison of the intra observer variability results show that each observer has a preference for different methods.

<i>Method</i>	<i>Tissue</i>	<i>Parameter</i>	γ (%) (Inter - Observer)	γ (%) (Intra - Obs. 1)	γ (%) (Intra - Obs. 2)
1	Synovium Dorsal	mean pixel intensity	11.6	7.1	12.4
1	Synovium Dorsal	number of pixels	30.7	17.4	26.4
1	Synovium Palmar	mean pixel intensity	9.4	8	11.6
1	Synovium Palmar	number of pixels	35.7	19.2	160.5
2	Synovium Dorsal	mean pixel intensity	6.7	9.8	5.1
2	Synovium Dorsal	number of pixels	13.4	14	10.3
2	Synovium Palmar	mean pixel intensity	14.4	12	7.5
2	Synovium Palmar	number of pixels	61.2	32.2	30.3

Table 3.2: Summary of the observer variability and bias studies.

3.1.6 Conclusions

Revised criteria for drawing reproducible region of interest boundaries have been established. A number of observations are made in analysing inter- and intra-observer variability and bias. In particular:

1. Measurement of the area of synovium is less precise than measuring the pixel intensity.
2. Inter observer variability - method 2 is more reliable for synovium dorsal and less reliable for synovium palmar. This partly relates to the fact that the palmar aspect of the joint is more complicated anatomically.
3. There is generally less intra observer variability than inter observer variability (as expected). Method 1 appears superior. The coefficient of variation produced by observer 1 for the area of synovium, using Method 1, was 17% - 19%, which is moderately good.
4. Some of the poor variability is due to outliers which could possibly be improved by tighter definitions.

3.2 The Region of Interest Drawtool

Analysing the method used to generate the poster data in the previous section has created sufficient reasons for the production of a drawtool to add to the functions of the viewer. This section describes the development of the drawtool.

Once an ROI boundary is defined, statistics are calculated. The statistics describe the nature of the ROI in terms of its size and average pixel intensity. For Gadolinium-enhanced images (explained in Section 1.1.3), a comparison of the average pixel intensity before and after the Gadolinium injection describes the synovium activity in the joint [Plant95a].

As the images are set to a grey scale, the boundaries of the ROIs are drawn in different colours, *e.g.* red, green, blue, so that they are easily seen. A colour key is associated with the statistics so that it is clear to which ROI each set of statistics relates.

The boundaries of tissue regions within cross-sectional MRI image slices do not easily conform to a basic shape, such as a rectangle. However, these irregular shapes can be approximated with a polygon.

A polygon is drawn around a region of interest (ROI) by the user selecting the vertices for each segment. The vertices are stored in a list called the vertex list. The Visual Basic LINE function is used to draw the polygon edges between each vertex.

3.2.1 Interior Points of a Polygon

To calculate the statistics of an ROI, it is necessary to know which pixels lie on and within the ROI boundary. As the LINE function is used to draw each edge, the co-ordinates of the pixels along the edges are not automatically known. Once the edge co-ordinates are known it becomes easier to determine the interior points. There are a number of techniques that can be used to find the interior points of a polygon. These techniques are explained in this section and the optimum method chosen.

The simplest method is to examine every pixel in the image to see whether it lies inside the polygon. This is time consuming and wasteful and can be improved by the use of a bounding box [Rogers85]. Fig. 3.2(a) shows that using a bounding box can significantly reduce the number of pixels examined. However, for the polygon in Fig. 3.2(b) the reduction is much smaller.

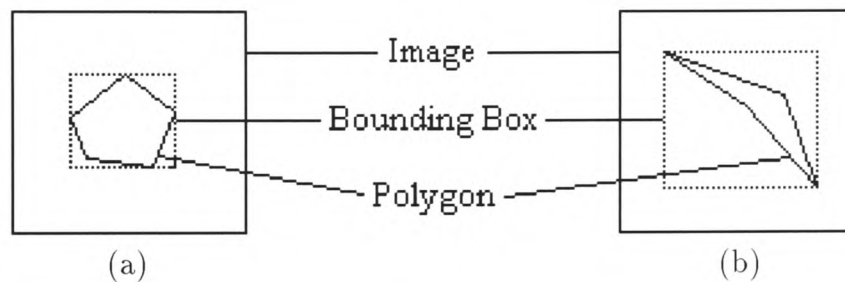


Figure 3.2: Bounding box examples.

A better method is to obtain the co-ordinates of all pixels that lie on each edge of the polygon (Bresenham's Algorithm [Rogers85], explained in Section 3.2.2, is suitable for this). Provided these edge co-ordinates are sorted into scan-line order, it is possible to extract pairs of co-ordinates to scan between to find all the interior points. This is known as an ordered edge list algorithm. This algorithm is incorporated into the draw-tool. The algorithm is very powerful as only pixels lying on or within the boundary are processed and these pixels are processed only once. The algorithm's main disadvantage is the expense associated with maintaining and sorting the list of edge co-ordinates [Rogers85].

There are other techniques which provide an alternative to the ordered edge list algorithm. These techniques are explained now and their limitations for this application are highlighted. The techniques are the edge fill algorithm [Ackland80], the fence fill algorithm [Dunlavey83] and the edge flag algorithm [Ackland81]. These algorithms are used for filling polygons. To fill the polygon, pixels are activated. A repeated activation of a pixel has a negation effect.

The Edge Fill Algorithm

The edge fill algorithm [Ackland80] is very simple.

For each scan-line intersecting a polygon edge at (x_i, y_j) , complement all pixels lying to the right of (x_i, y_j) , *i.e.* (x_{i+k}, y_j) , for $k = 1, 2, \dots, n - 1$.

The algorithm is very poor in that it is applied to the whole image, whereas the ordered edge list algorithm is only applied to those pixels which lie on or within the polygon boundary. Also, each pixel may be processed more than once.

The Fence Fill Algorithm

The number of pixels addressed in the edge fill algorithm can be reduced by introducing a fence. This is the fence fill algorithm [Dunlavey83]. The fence is a vertical line and is conveniently placed at one of the polygon vertices.

For each scan-line intersecting a polygon edge at (x_i, y_j) :

If the intersection is to the left of the fence, complement all pixels lying to the right of (x_i, y_j) but left of the fence.

If the intersection is to the right of the fence, complement all pixels lying to the left of (x_i, y_j) but right of the fence.

Despite improving the edge fill algorithm, the fence fill algorithm still processes pixels outside of the polygon and pixels are processed more than once.

The Edge Flag Algorithm

The disadvantages of the edge fill and fence fill algorithms can be eliminated by a modification called the edge flag algorithm [Ackland81]. The edge flag algorithm is made up of two steps. The first step outlines the boundary to establish pairs of span bounding pixels on each scan-line. The second step fills the polygon between these bounding pixels.

Boundary outline:

For each edge intersecting the polygon, complement the leftmost pixel that lies to the right of the intersection.

Fill:

For each scan line intersecting the polygon at (x_i, y_j) :

Set Inside to FALSE

for $x = x_i$ to x_{n-1}

if the pixel at x is set to the boundary value then

negate Inside

end if

if Inside = TRUE then

set the pixel at x to the polygon value

else

reset the pixel at x to the background value

end if

next x

The edge flag algorithm processes each pixel only once, but still processes pixels that lie outside the polygon. Software implementations show that the ordered edge list and the edge flag algorithm execute at about the same speed [Whitted81].

The Edge Flag Algorithm does not require building, maintaining and sorting edge lists as it relies on being able to complement pixels. When applied to this application of drawing polygons on medical images, the algorithm has limited use. To implement the edge flag algorithm would require using a list for the contour, as complementing pixels on the images is counterproductive. This then removes the main advantage of the algorithm and converts it into an ordered edge list algorithm. Alternatively, an extra copy of the image could be stored in memory, which is equally inefficient.

This thesis now resumes with the ordered edge list algorithm and shows a number of other problems that arise, which are not explicit in the literature. The algorithm uses Bresenham's Algorithm (explained in Section 3.2.2) to calculate the edge co-ordinates of each polygon edge. The edge co-ordinates are stored in a list and sorted into scan-line order (y first, then x). Extracting pairs of edge co-ordinates will define the interior points of a polygon [Rogers85].

3.2.2 Bresenham's Algorithm

Bresenham's Algorithm [Bresenham65] seeks to select the optimum pixel locations to represent a straight line. These locations are represented by the variables x and y . Depending on the slope of the line, the algorithm increments by one unit in either x or y . The other variable is incremented by either zero or one, by examining the distance between the actual line location and the nearest grid locations. This distance is called the error. The algorithm is cleverly constructed so that only the sign of the error term needs to be examined.

The speed of the algorithm is increased by using integer arithmetic to eliminate the use of division [Rogers85]. The General Bresenham Algorithm is applicable to all four quadrants of an image, which enables the calculation of edge co-ordinates for lines in any direction.

The General Bresenham Algorithm is implemented in this work to calculate the edge co-ordinates for each non-horizontal polygon edge. The co-ordinates are sorted into scan-line order (y first, then x) using a simple sort routine. Extracting pairs of edge co-ordinates to scan between should define all the interior points [Rogers85].

3.2.3 Implementation of Bresenham's Algorithm

An image can be thought of as a matrix of discrete cells, each of which can be made bright. Each cell is called a picture element, or pixel. It is not possible, except in special circumstances, to directly draw a straight line from one addressable point, or pixel, to another addressable point, or pixel. The line can only be approximated by a series of dots (pixels) close to the path of the line. Only in the special cases of completely horizontal, vertical, or $\pm 45^\circ$ lines will a straight line of dots or pixels appear. All other lines will appear as a series of stair steps. This is called aliasing (illustrated in Fig. 3.3) [Rogers85].

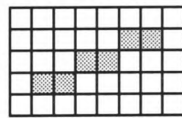


Figure 3.3: Aliasing example.

This staircase effect means that for some lines it is extremely likely that the polygon boundary on certain scan-lines will be made up of more than one consecutive pixel. (In Fig. 3.3, the boundary contains two consecutive pixels on each scan-line.)

Consider the polygon in Fig. 3.4. The General Bresenham Algorithm calculates all co-ordinates that lie on each polygon edge. The edge co-ordinates are stored in an edge list and sorted into scan-line order, (y first, then x). Extracting pairs of edge co-ordinates from this list will immediately create errors. For instance, on scan-line j , edge co-ordinates A and B will be extracted to scan between, followed by C and D , whereas A and D should be the two points to scan between.

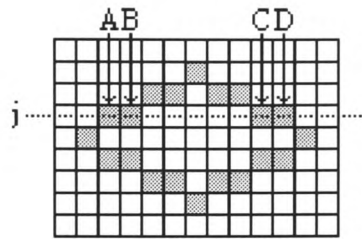


Figure 3.4: Consecutive pixels from shallow lines.

The direction of the edge can be used to determine which of the consecutive pixels should be stored in the edge list (illustrated in Fig. 3.5). For an anticlockwise cycle of vertices, a scan-line proceeding from left to right and intersecting a polygon edge will enter the polygon if the direction of the edge is down and will exit the polygon if the direction of the edge is up. Therefore, for downward pointing edges, the leftmost pixel only should be put in the edge list and for upward pointing edges, the rightmost pixel only should be put in the edge list. (The necessity of specifying the direction of the polygon is developed in Section 3.2.4.)

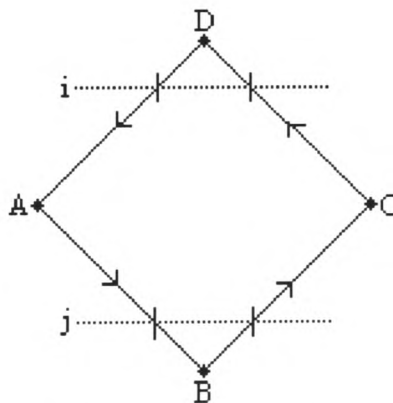


Figure 3.5: Anticlockwise cycle of vertices.

This simple amendment to Bresenham's Algorithm ensures that only the outermost of the consecutive edge pixels on any scan-line are stored in the edge list.

3.2.4 Polygon Complexities

For every scan-line, intersections with a polygon are distinguished as edges and vertices. As has been shown, edge intersections represent polygon edges. Pairs of edge pixels can be scanned between to find the interior points of the polygon on that scan-line. A simple initial check that the edge co-ordinate at the intersection is not in the vertex list is sufficient to show that it is an edge intersection.

However, if the edge co-ordinate at the intersection is a vertex, a new set of problems is raised. In this section a brief overview of these problems is given. A more detailed description of the problems and how they are solved is given in Appendix B.

Solving these problems requires the direction of the polygon to be specified. In this work, the direction of the polygon is taken to be anticlockwise and the vertices are (re-)ordered accordingly. A set of rules are established, based on the anticlockwise cycle. Alternatively, a clockwise cycle may be used, but this would necessitate changes to the established rules.

The polygon vertices can be grouped as those which:

- are edge equivalent - *i.e.* they can be treated as ordinary edge co-ordinates;
- are a peak or a trough - *i.e.* they have to be treated differently;
- lie on a horizontal edge - these require a third approach.

Each of these types of vertices are now explained.

Edge Equivalent Vertices

Some vertices can be treated as edge co-ordinates as the scan-line intersecting with these vertices either enters or exits the polygon (illustrated in Fig. 3.6). In Fig. 3.6(a) vertices A and C are treated as non-vertex edge co-ordinates and are scanned between to find the interior points of the polygon along scan-line j . In Fig. 3.6(b), vertex A is treated as a non-vertex edge co-ordinate and is paired with the edge co-ordinate at point p to scan between.

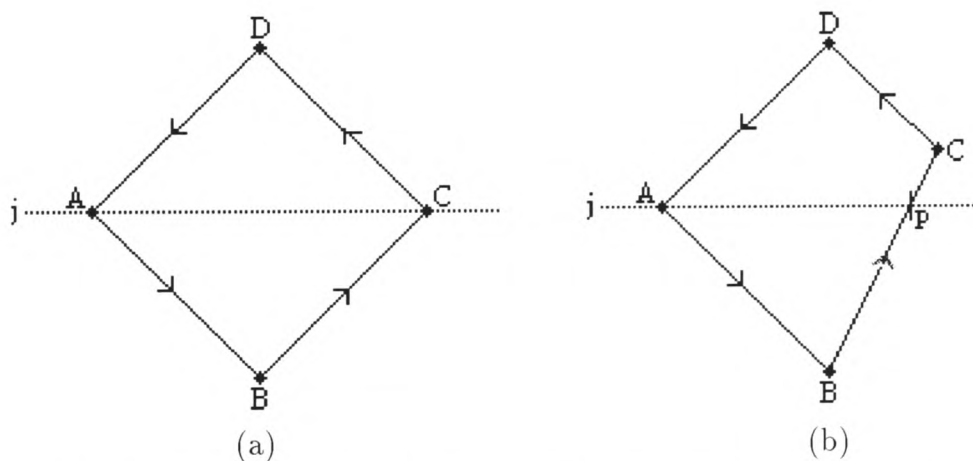


Figure 3.6: Edge equivalent vertices (a) vertices A & C treated as non-vertex edge co-ordinates (b) vertex A treated as a non-vertex edge co-ordinate.

Peaks / Troughs

Some of the vertices extracted from the edge list could be peaks or troughs (illustrated in Fig. 3.7). In Fig. 3.7, vertices C , F and H are considered peaks and vertices B , D and G , troughs. Some peaks and troughs are considered *external* to the polygon, for example, vertices B , D , F and H . The other peaks/troughs are considered *internal* to the polygon. An external peak/trough represents a single pixel on the boundary and, therefore, must be treated differently. An internal peak/trough lies within the polygon along a scan-line and is, therefore, ignored.

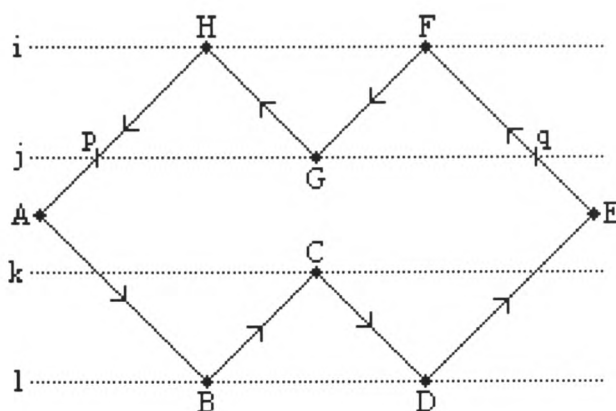


Figure 3.7: Vertices as peaks/troughs.

Horizontal Edges

Horizontal edges may occur at different locations in a polygon. Figs. 3.8 to 3.11 show some examples of how horizontal edges may be situated in polygons. A horizontal edge may be the only part of a polygon on a particular scan-line, for example, scan-line j in Fig. 3.8, or be independent of the polygon on the rest of the scan-line, for example, scan-line i in Fig. 3.8. Other cases of horizontal edges are when they are combined with other parts of the polygon, such as starting (Fig. 3.9a), ending (Fig. 3.9b) or occurring in the middle (Figs. 3.10 and 3.11) of a scan-line.

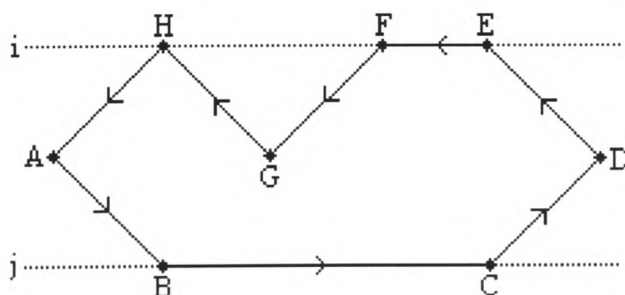


Figure 3.8: Independent horizontal edges.

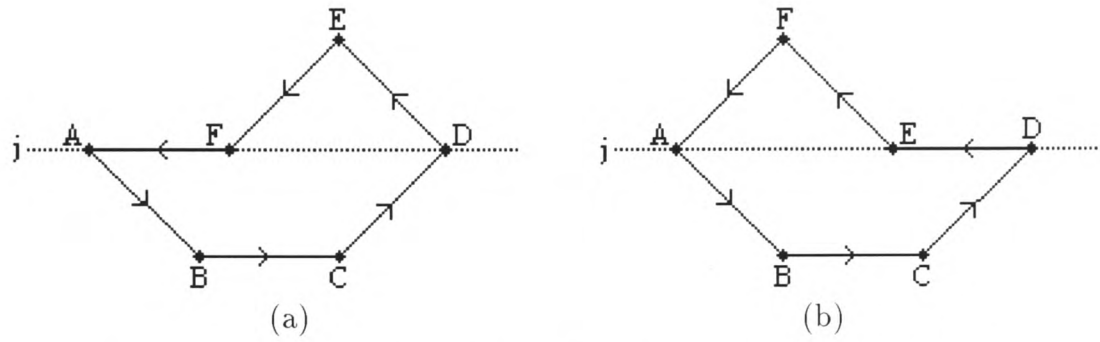


Figure 3.9: Horizontal edges, (a) example 1 (b) example 2.

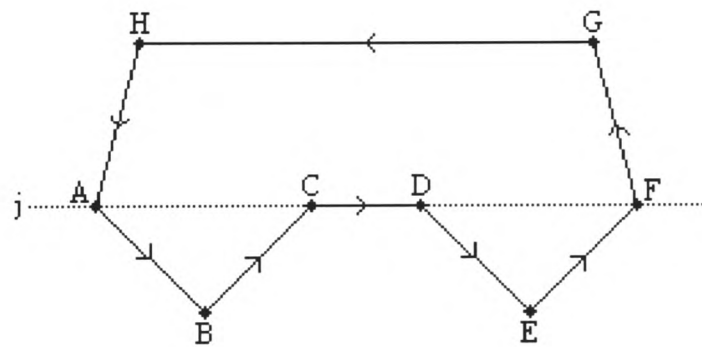


Figure 3.10: Horizontal edges, example 3.

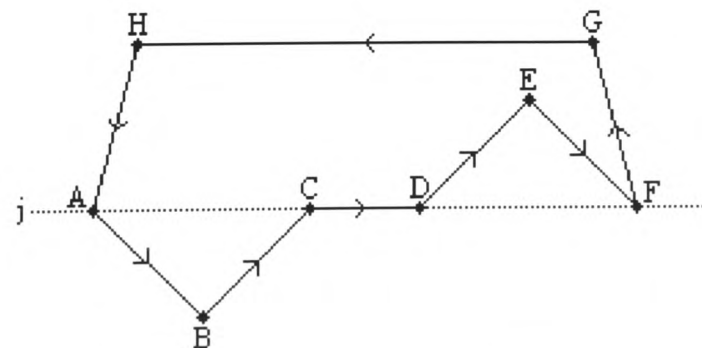


Figure 3.11: Horizontal edges, example 4.

Each of these cases must be treated differently. To determine the rules for each case, consider what occurs immediately prior to and after each horizontal edge along the scan-line on which it falls. A summary of the derived rules are presented here. A more detailed description of the rules is given in Appendix B.

The end vertices of an independent horizontal edge, such as BC and EF in Fig. 3.8, are treated as edge equivalent vertices (explained in Section 3.2.4).

Now consider the horizontal edges, AF and DE , in Fig. 3.9(a) and (b) respectively. AF and DE fall at the beginning and end, respectively, of scan-line j . Vertex A in Fig. 3.9(a) and vertex D in Fig. 3.9(b) can be treated as edge equivalent vertices (explained in Section 3.2.4). Vertex F in Fig. 3.9(a) and vertex E in Fig. 3.9(b) must be ignored as, in both examples, vertices A and D are the correct pair to be scanned between.

Now consider the polygons in Figs. 3.10 and 3.11. In both examples, the horizontal line CD falls in the middle of the polygon along scan-line j . In both cases, vertex A will already have been determined as the starting point for scanning. Therefore, vertex C is ignored. In Fig. 3.10, vertex D is ignored as there is more of the polygon to come along scan-line j , after D . (Vertex F is the true end point for scanning in this example.) However, in Fig. 3.11, vertex D is the end point for scanning from A . (Vertex F is an external trough (explained in Section 3.2.4).))

In Appendix B, a fuller explanation of each case of horizontal edges is given and how the rules to treat them are derived. It is shown that the direction of the line is crucial in determining which vertex is the true end point for scanning. Thus, the need to define the direction of the polygon is again made explicit.

The Interior Points of a Polygon Algorithm

Having considered all possible polygons, an algorithm is constructed to determine all those pixels which lie on and within the ROI boundary, from which statistics are calculated.

Once the polygon has been defined using the drawtool, initial preparatory steps are:

1. Ensure the polygon vertices have an anticlockwise cycle (the developed rules are based on an anticlockwise cycle of vertices);
2. Remove any vertices that lie on the middle of a horizontal edge (as the vertices are user defined, it is possible for this to occur);
3. Use the above amendment to the General Bresenham Algorithm to determine all edge co-ordinates for each polygon edge;
4. Sort the edge co-ordinate list into scan-line order (y first, then x).

The edge co-ordinates can now be extracted from the edge list and the established rules will determine which co-ordinates are the correct ones for scanning between on each scan-line. A pseudocode listing of the algorithm can be found in Appendix C.

3.2.5 Region of Interest Statistics

Once an ROI boundary is created, statistics are calculated. The interior points of the ROI are determined using the algorithm in Section 3.2.4. This section gives the formulae used to calculate the statistics.

The size of the ROI is determined by calculating the number of pixels within the region, including the boundary. The average pixel intensity, \bar{x} , for an $m \times n$ region is calculated with Equation 3.2

$$\bar{x} = \frac{\sum_{i=0}^{m-1} \sum_{j=0}^{n-1} x_{ij}}{m \times n} \quad (3.2)$$

where x_{ij} is the pixel intensity at (i, j) . The average pixel intensity has potential to describe how active the synovium is in a Gadolinium-enhanced image of a patient with rheumatoid arthritis [Plant95a].

The standard deviation gives a measure of spread of the pixel intensities within an ROI. Equation 3.3 gives the formula used for calculating the standard deviation, σ , for an $m \times n$ region.

$$\sigma = \sqrt{\frac{\sum_{i=0}^{m-1} \sum_{j=0}^{n-1} (x_{ij} - \bar{x})^2}{m \times n}} \quad (3.3)$$

The statistics are displayed in a table with a colour key associating to which ROI each set of statistics relates. The statistics can also be stored in a text file.

A histogram showing the spread of grey levels within an ROI is also created. As the grey level range is 0 to 4095, the histogram is grouped into 16 blocks of 256 grey levels each. The number of pixels falling within each block is also displayed.

3.2.6 The Region of Interest Path Structure

The drawtool of Section 3.2 allows the user to draw around regions of interest (ROIs) on the images. Some forms of image analysis require the use of the same ROI boundaries on different images. Examples are comparing finger slices from scans taken on different occasions in a clinical trial or in assessing the stability of the MRI scanner in imaging fluids (as is required in other UHW projects). Storing the ROI boundaries would be beneficial in such tasks.

This section explains the necessary data structure for defining an ROI boundary. The requirements for the data structure are explained in terms of the expected use of the drawtool.

Initial Considerations

An ROI boundary is a path around the ROI. The vertices that make up the boundary form a very efficient path definition. A path structure facilitates storage of the path and its characteristics or properties. A general path structure facilitates all types of ROIs, for all images and all UHW projects. Thus, the extensibility of the system as a whole is continued.

Firstly, consider the different ROI boundary shapes. Rectangles and polygons are implemented in the drawtool of this project. Other UHW projects require different drawtool shapes, for example, freehand [OConnor98b], which, once drawn, is the same as a polygon. Therefore, it is necessary to define a general path structure which facilitates all possible shapes for all UHW projects. A general path structure ensures consistent data storage across all UHW projects. This approach allows for the incorporation of an editor based on paths if required by other UHW projects.

Secondly, consider the different properties of an ROI boundary:

1. Does the ROI boundary form an open or a closed region?
2. How many vertices/segments are in the ROI boundary?
3. What is the colour of the boundary (colour is used to distinguish between ROIs)?
4. What type of line is used (for example, solid, dotted, dashed)?

A general ROI path structure contains information for all properties of ROI boundaries.

Codes, referred to as *action codes*, are used to store the boundary information. Each property has its own action code. The code is a number that defines which action to take when the system is faced with a choice about how to render a line.

Each segment is most easily described by the co-ordinates of its end vertices, with an accompanying action code defining the shape of the segment between those vertices. Storing these end vertices and accompanying action codes only is an efficient use of computer storage space. Another action code stores the number of vertices on the ROI boundary.

The general path structure allows for the inclusion of circles and ellipses. Circles and ellipses are usually defined by their centre points and radii. To conform to the general storage of pairs of vertices that mark the ends of a segment, circles and ellipses can be stored similarly. For a circle, centre (C_x, C_y) and radius r , two points from the circle circumference are stored, such as $(C_x - r, C_y)$ and $(C_x + r, C_y)$. For an ellipse, centre (C_x, C_y) and major and minor radii a and b respectively, four boundary points are stored, such as $(C_x - a, C_y)$, $(C_x + a, C_y)$, $(C_x, C_y - b)$ and $(C_x, C_y + b)$.

The ROI boundary is stored in a data structure composed of a header, containing the action codes and data, containing the end vertices of each segment of the boundary (illustrated in Fig. 3.3 for an ROI boundary with n vertices).

Header				Data						
action code 1	action code 2	...	action code n	x_1	y_1	x_2	y_2	...	x_n	y_n

Table 3.3: Region of interest path structure.

To allow encoding of all possible ROI boundaries, action codes are defined for the following boundary properties:

- The number of vertices that make up the boundary.
- The shape of the boundary (rectangle, polygon, circle, ellipse, freehand, hybrid).
- Whether the ROI boundary is a closed or open region (for a closed region the two end vertices are joined together).
- What colour the ROI boundary is.
- What line type has been used for the ROI boundary.
- Reserved action codes (allows room for later additions to the data structure).

Numbers are used to signify which action to take. For example, the action code for boundary shape is defined as:

1 = rectangle.

2 = circle/ellipse.

3 = polygon.

4 = freehand.

5 = hybrid.

The action code for closed/open boundary is a binary code, where “0” is closed and “1” is open.

Tables. 3.4 and 3.5 give two examples of ROI boundaries that have been stored in the path structure. Table. 3.4 gives an example of a red rectangle. The path structure is listed as:

4 vertices in a rectangle (2) that is a closed (0) region and is red (10) the line is solid (00) and the reserved codes are 00. The vertex co-ordinates then follow ((100, 110), (100, 125), (120, 110), (120, 125)).

4	2	0	1	0	0	0	0	0	0	100	110	100	125	120	110	120	125
---	---	---	---	---	---	---	---	---	---	-----	-----	-----	-----	-----	-----	-----	-----

Table 3.4: Path structure example of a red rectangle.

Table. 3.5 gives an example of a blue polygon. The path structure is listed as:

5 vertices in a polygon (3) that is a closed (0) region and is blue (30) the line is solid (00) and the reserved codes are 00. The vertex co-ordinates then follow ((30, 90), (100, 50), (200, 100), (190, 200), (70, 210)).

5	3	0	3	0	0	0	0	0	0	30	90	100	50	200	100	190	200	70	210
---	---	---	---	---	---	---	---	---	---	----	----	-----	----	-----	-----	-----	-----	----	-----

Table 3.5: Path structure example of a blue polygon.

Resource Interchange File Format (RIFF) Files

The ROI boundary information contained in the general path structure must be stored in a file. The standard MS-DOS file access functions, such as `_lopen()`, can be used to store data in a file. However, multimedia functions provide several advanced features, such as memory-buffered access and functions for creating and reading the data from Resource Interchange File Format (RIFF) files [Conger93]. The RIFF standard is ideal for storing blocks of data in a single file. In this section, RIFF files are presented and

applied to storing ROI boundary information via the general path structure explained in the previous section.

The RIFF format provides a generalized method for storing different types of data in an organized format in a single disk file. The RIFF format is easy to use and supports any type of data. The basic idea behind the RIFF file format is that each disk file consists of a series of “chunks” of data. Each chunk has a header which begins with a four-letter code that identifies the chunk. Following the chunk identifier is a value that gives the chunk’s length in bytes. The chunk length is very important as it makes it possible to easily locate the next chunk in the file. RIFF files are not just a big block of data, but an organized series of independent units, which makes RIFF files easy to navigate.

Fig. 3.12 illustrates the RIFF structure for a simple file containing two blocks of data. All RIFF files start with an outermost RIFF chunk that encompasses the entire file. The first four bytes of any RIFF file will be the ASCII character codes for the letters R, I, F, F, which make RIFF files easy to identify. Next is a value that stores the length of the file, followed by another four-character code that specifies the “form-type” for the file. The form-type allows certain predefined RIFF files to be recognised. After the form type come all of the chunks that make up the file’s data. Each chunk starts with a four-character ID value and then the length of that chunk. Note that the chunks themselves do not have a “form-type” like the RIFF chunk.

A RIFF file can be designed as a hierarchical system of “parent” and “child” chunks to any desired level of nesting. In navigating a RIFF file, moving to a subchunk level from a parent chunk is referred to as “descending” into the subchunk, while moving back up to the parent level is referred to as “ascending”. Multimedia functions exist which make creating, reading and modifying RIFF files very easy [Conger93].

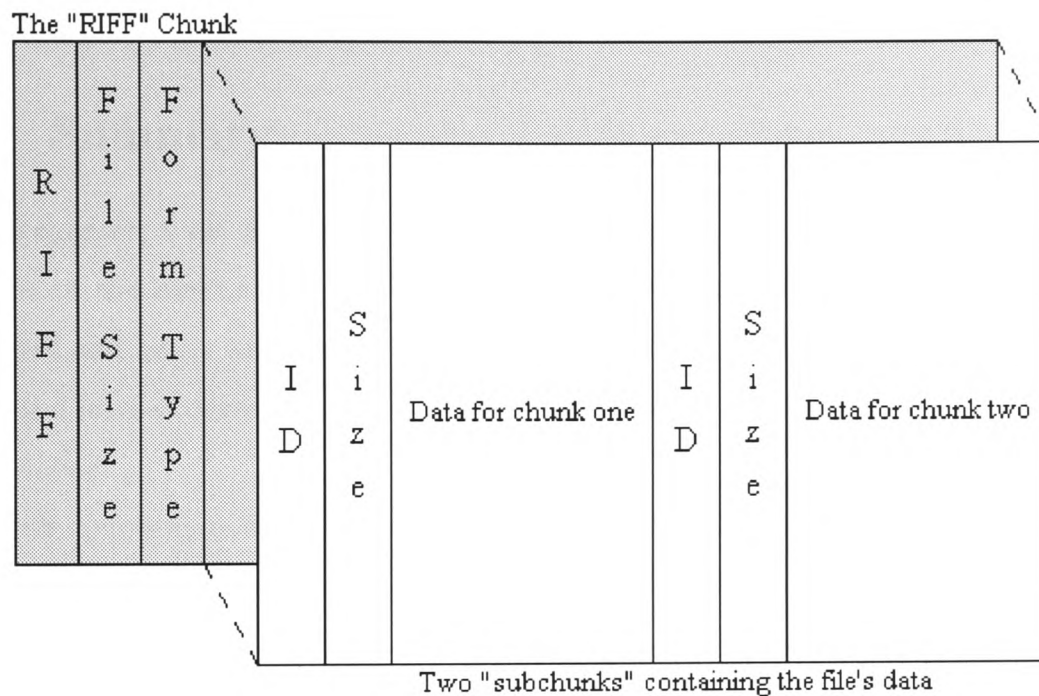


Figure 3.12: RIFF file hierarchy of chunks.

RIFF files are used to store the ROI boundary information in the path structure. An ROI is made up of segments. Each segment can be stored separately in a chunk, but this means that only one ROI could be stored in a RIFF file and the path structure header information would unnecessarily be repeated for every segment.

Instead, at the top level of chunks, each ROI is stored in a chunk. Therefore, a set of ROIs can be stored in a single RIFF file. The path structure, consisting of header and data, is stored in the *data* section of each chunk.

Other UHW projects may require ROI boundaries that have segments taken from different shapes. These “hybrid” boundaries can easily be accommodated in this RIFF structure. A parent chunk will define the general information of the boundary and child chunks will store the information from each segment.

Other UHW projects use editing tools to amend the ROI boundary [OConnor98b]. The path structure is very easily changeable for amendments to the boundary and the

multimedia functions make rewriting the path structure to RIFF files very easy.

3.3 Summary

In this chapter, a set of criteria for drawing ROI boundaries is established. A critical analysis of the method used to produce data for the published poster [Plant95a] is presented and better methods for drawing reproducible ROI boundaries are developed. Inter- and intra-observer variability and bias are examined and a coefficient of variation is developed.

The requirements for creating region of interest (ROI) boundaries are explained. A robust algorithm for determining the interior points of a polygon is also presented. A brief overview of the derived rules for finding these interior points is given in this chapter. A detailed explanation of the rules is given in Appendix B. A pseudocode listing of the algorithm can be found in Appendix C.

Once an ROI boundary is drawn, statistics are calculated. The statistics calculated for each ROI are explained and the formulae used, given. Histograms are also created.

Storing the ROI boundaries is advantageous in many applications. A general path structure for storing boundary information is developed and RIFF files are shown to be useful for storing the path structure in a file.

In the next chapter, the MRI images are processed to find features which can be used for the registration process in Chapter 5.

Chapter 4

Processing of Raw Image Data

In Chapter 2 an overview of registration methods is presented. Before applying relevant methods to this application, it is necessary to derive features within MRI images that can be used for registration. Determining such features is the focus of this chapter.

Recall from Chapter 2 that extrinsic point methods are unsuitable for this application. Therefore, only intrinsic point methods are investigated. Intrinsic points are patient-related properties, for example, pixel intensities, anatomical landmark points (known as fiducial points [Maurer93]), geometrical features or surfaces of skin. Skin surfaces alone are unsuitable as landmarks in this application, due to the danger of slippage (explained in Section 1.2.1).

Firstly, the use of pixel intensities is examined via a number of well known and some newly developed image processing techniques. Secondly, the identification of useful anatomical features is investigated via well known image processing techniques and new methods are derived in the context of this research. A new combined method is presented which derives structural boundaries that represent the bones in an MRI finger image. These boundaries can be used for the registration process (to be explained in Section 5.3). Thirdly, frequency domain techniques are examined and applied to MRI finger images. The Discrete Fourier Transform, the Convolution Theorem and various frequency domain filters are discussed. The method of Fourier Descriptors is examined as a means of determining the parameters required to register a pair of images.

4.1 Locating Features By Pixel Intensities

The purpose of this section is to examine whether MRI finger image pixel intensities can produce enough information to make possible the registration of the images. The well known image processing techniques examined here are contrast stretching, standardizing and thresholding. A new standardizing method is presented that combines information from more than one image to produce sequences of images with the same mean and standard deviation.

4.1.1 Contrast Stretching

The MRI finger images (explained in Section 1.1.2) have a grey level range of 0 (black) to 4095 (white). However, different weighted images (explained in Section 1.1.1) have differing contrast. Fig. 4.1 shows three different weighted images. The T1-weighted image is considerably darker and has lower contrast than both the PD- and T2-weighted images.

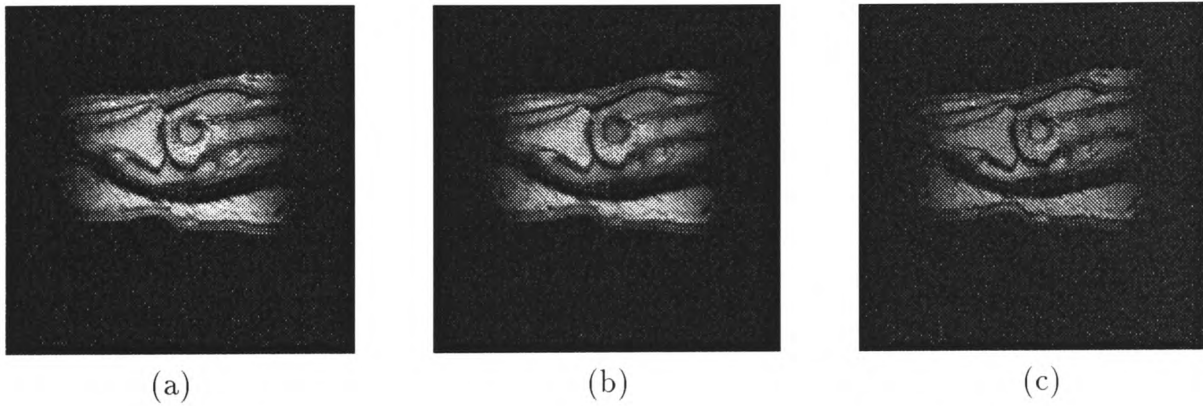


Figure 4.1: (a) PD-weighted image (b) T2-weighted image (c) T1-weighted image.

Locating a particular feature within two or more images having different weightings can be hampered by very large cross-image pixel intensity differences in tissue regions. Contrast stretching [Gonzalez92, Sonka96] increases the active range of grey levels in an image. Stretching the *used* grey levels out to the maximum possible range of grey levels, will increase the contrast such that the weighted images have a more similar appearance of grey levels. Equation 4.1 gives a formula for contrast stretching.

$$B_{i,j} = \frac{B_{max} - B_{min}}{A_{max} - A_{min}}(A_{i,j} - A_{min}) + B_{min} \quad (4.1)$$

for $i, j = 0, 1, 2, \dots, 255$, where B_{min} and B_{max} are the selected minimum and maximum grey level, respectively, for the new contrast-stretched image B , and A_{min} and A_{max}

are the minimum and maximum grey levels, respectively, from the current image A .

Fig. 4.2 shows the effect of contrast stretching the images in Fig. 4.1.

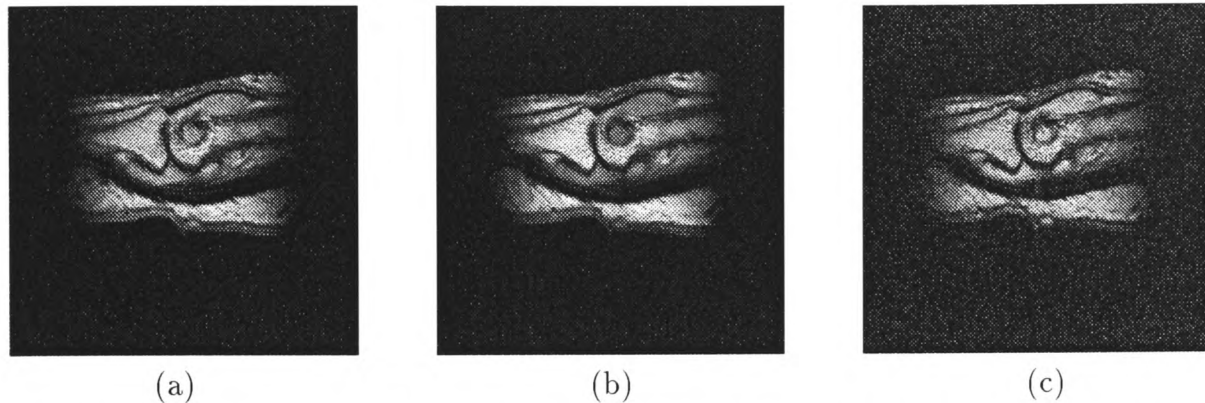


Figure 4.2: (a) PD-weighted image contrast stretched (b) T2-weighted image contrast stretched (c) T1-weighted image contrast stretched.

The three weighted images now look more alike, compared to each other, in terms of contrast and have more similar, though not equal, means and standard deviations, as can be seen in Table 4.1. Contrast stretching alone does not provide any new information that can be used for registration. However, when other image processing techniques, such as standardization (explained in Section 4.1.2), produce very dark images, contrast stretching will brighten the image so that further processing decisions can be made.

<i>Fig. (weight)</i>	<i>4.1a (PD)</i>	<i>4.1b (T2)</i>	<i>4.1c (T1)</i>
Mean	383	290	253
Standard deviation	622.2952	496.1749	331.5253
<i>Contrast stretched</i>			
<i>Fig. (weight)</i>	<i>4.2a (PD)</i>	<i>4.2b (T2)</i>	<i>4.2c (T1)</i>
Mean	389	388	441
Standard deviation	631.8603	664.2108	578.9117

Table 4.1: Means and standard deviations for Figs. 4.1 & 4.2.

4.1.2 Standardization

Section 4.1.1 introduces the problem of locating features within different-weighted images. Contrast stretched images do not reveal features useful for registration, but do produce images with more similar, but not equal, means and standard deviations. *Standardizing* is a technique which will produce images with approximately the same mean and standard deviation. In this section, consideration is given to well known standardizing techniques and a new method, derived for this work, which combine information from more than one image, to produce images with approximately the same means and standard deviations. Standardizing images in this way is particularly useful for locating structural features (to be explained in Section 4.2).

One very simple standardizing technique is to subtract the average grey level intensity of an image from every pixel in the image. However, this method does not take into account the variance of the grey levels. A better method of standardizing is to subtract the mean from each pixel and then divide by the standard deviation. That is:

$$B_{i,j} = \frac{A_{i,j} - \bar{x}_A}{\sigma_A} \quad (4.2)$$

for $i, j = 0, 1, 2, \dots, n - 1$, where \bar{x}_A is the average pixel intensity of image A and σ_A is the standard deviation of image A .

The above process is performed for all $n \times n$ pixels in the image. The resulting image has zero mean and the standard deviation is 1. Contrast stretching (explained in Section 4.1.1) the standardized image will re-spread the pixel intensities across the grey-level range available. Fig. 4.3 shows the result of standardizing (by Equation 4.2) and contrast stretching (by Equation 4.1) the images in Fig. 4.1.

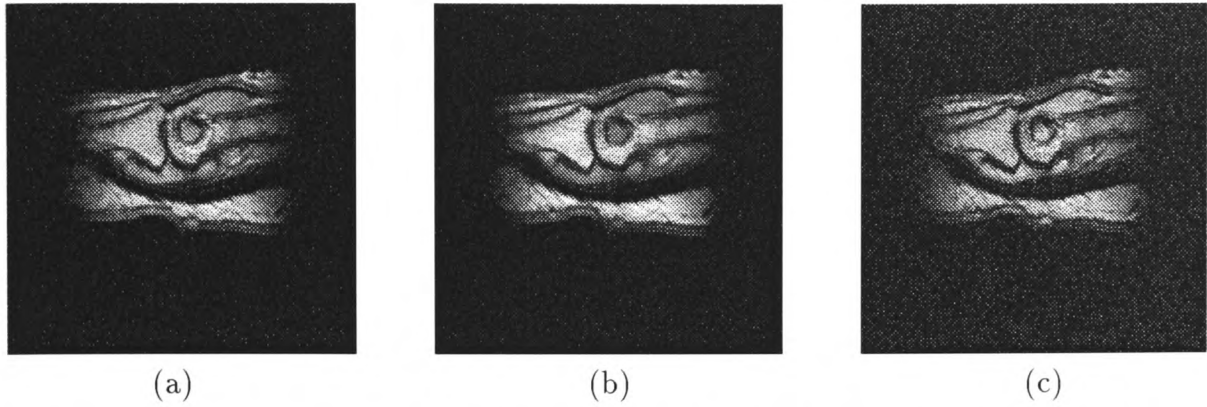


Figure 4.3: (a) PD-weighted image standardized and contrast stretched (b) T2-weighted image standardized and contrast stretched (c) T1-weighted image standardized and contrast stretched.

The standardizing process is performed on each image independently. The resulting images appear more alike and have more similar measures of spread, as in the contrast stretching case in Section 4.1.1. However, making the images have *identical* measures of spread, will help towards locating the same structures (explained in Section 4.2) within these images. To achieve this, a new approach was developed for these images. The method combines information from two images so that the standardized images have the same mean and standard deviation.

Let A and B be two images with different contrast. A simple technique is to divide each pixel in image B by the average pixel intensity of B and then multiply by the average pixel intensity of image A . Both images now have the same mean, but different variances. Instead a method was developed which includes both the mean and the standard deviation and is based on equation 4.2, thus combining information from both images.

Let C be the required standardized version of an image A with respect to image B . Equation 4.3 gives the new formula for standardization. The standardized image C , is defined in terms of images A and B , for $i, j = 0, 1, 2, \dots, 255$, where \bar{x}_A and \bar{x}_B are the average grey levels of image A and B respectively and σ_A and σ_B are

the standard deviations of image A and B respectively. Fig. 4.4 shows the result of applying Equation 4.3 to the images in Fig. 4.1

$$C_{i,j} = \left(\frac{A_{i,j} - \bar{x}_A}{\sigma_A} \right) \sigma_B + \bar{x}_B \quad (4.3)$$

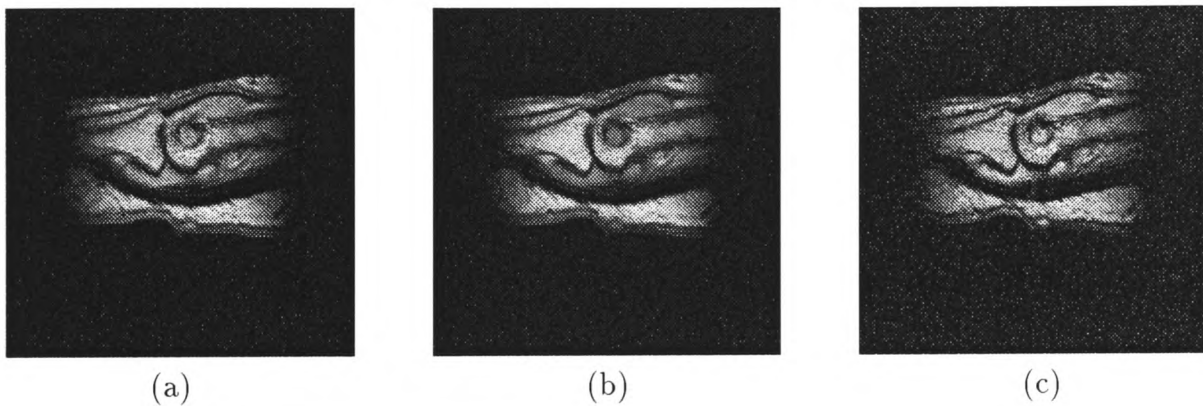


Figure 4.4: (a) PD-weighted image (b) T2-weighted image, new standardizing method (c) T1-weighted image, new standardizing method.

Table 4.2 gives a comparison of the mean and standard deviation for the images in Figs. 4.1 and 4.4. As can be seen, the new method produces means and standard deviations that are almost equal.

<i>Fig. (weight)</i>	<i>4.1a (PD)</i>	<i>4.1b (T2)</i>	<i>4.1c (T1)</i>
Mean	383	290	253
Standard deviation	622.2952	496.1749	331.5253
<i>New standardizing method</i>			
<i>Fig. (weight)</i>	<i>4.4a (PD)</i>	<i>4.4b (T2)</i>	<i>4.4c (T1)</i>
Mean	383	383	384
Standard deviation	622.2952	622.2724	622.2108

Table 4.2: Means and standard deviations for Figs. 4.1 and 4.4.

The new standardizing technique is a very useful tool as a pre-processing step for weighted images and Gadolinium-enhanced images in deriving bone boundaries (explained later in Section 4.2.3).

4.1.3 Grey Level Thresholding

If tissues or landmarks could be classified or segmented by grey level values only, then clearly registration would be greatly simplified.

Consider the rectangles drawn on the finger image in Fig. 4.5. The rectangles lie within the proximal phalanx (PP), the middle phalanx (MP), the synovium dorsal (SD), the synovium palmar (SP), the joint space (JS), the tendon (T) and the eroded hole (H). A plot of average grey level plus or minus one standard deviation, for each rectangle, is given in the graph in Fig. 4.6.

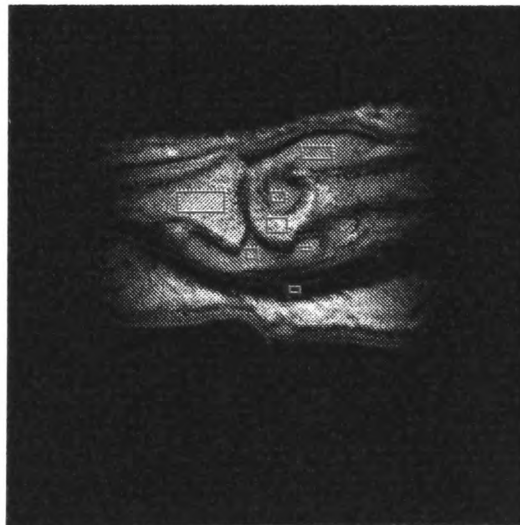


Figure 4.5: MRI finger scan with rectangles drawn in the proximal phalanx, middle phalanx, tendon, hole, joint space, synovium dorsal and synovium palmar.

The graph illustrates the fact that for different regions of interest (ROIs), the average grey levels are very similar. Within plus or minus one standard deviation of the mean, many grey levels fall within different tissue regions. The range for each tissue region overlaps substantially with those of other regions. Thus, defining boundaries

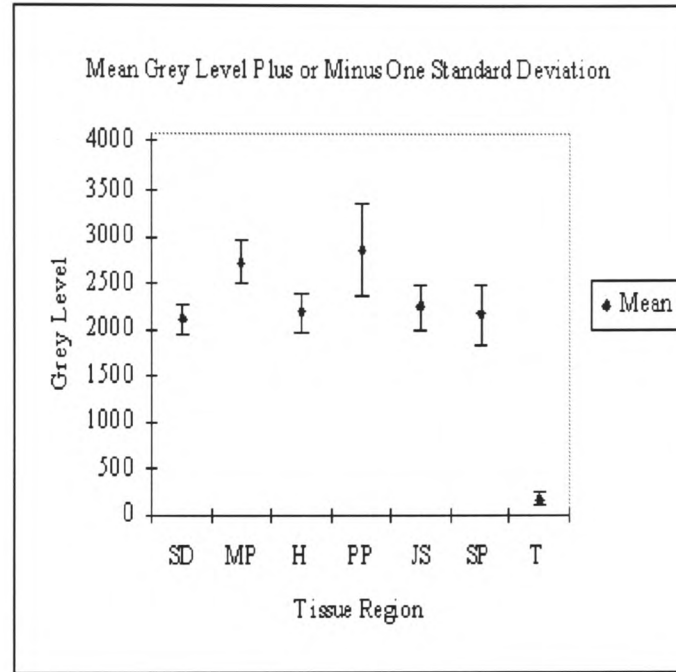


Figure 4.6: Average grey level plus or minus one standard deviation for each rectangle in Fig. 4.5.

for ROIs or landmarks by grey level alone is almost impossible for these sorts of images. Therefore, registration based on image grey levels alone is insufficient for this application and the identification of structural features will be required.

4.1.4 Reducing the number of grey levels

The MRI finger images have a grey level range of 0 (black) to 4095 (white). Reducing the number of grey levels [Rycroft98] may help to define tissue regions more clearly. A banded thresholding algorithm can be used to combine a set of grey levels into a single value. Fig. 4.7(a), (b), (c), (d), (e), (f) shows the result of reducing the number of grey levels in Fig. 4.5 to 64, 32, 16, 8, 4 and 2 respectively.

The resulting images do not have clear, smooth boundaries. This approach did not lead to an improvement for this application.

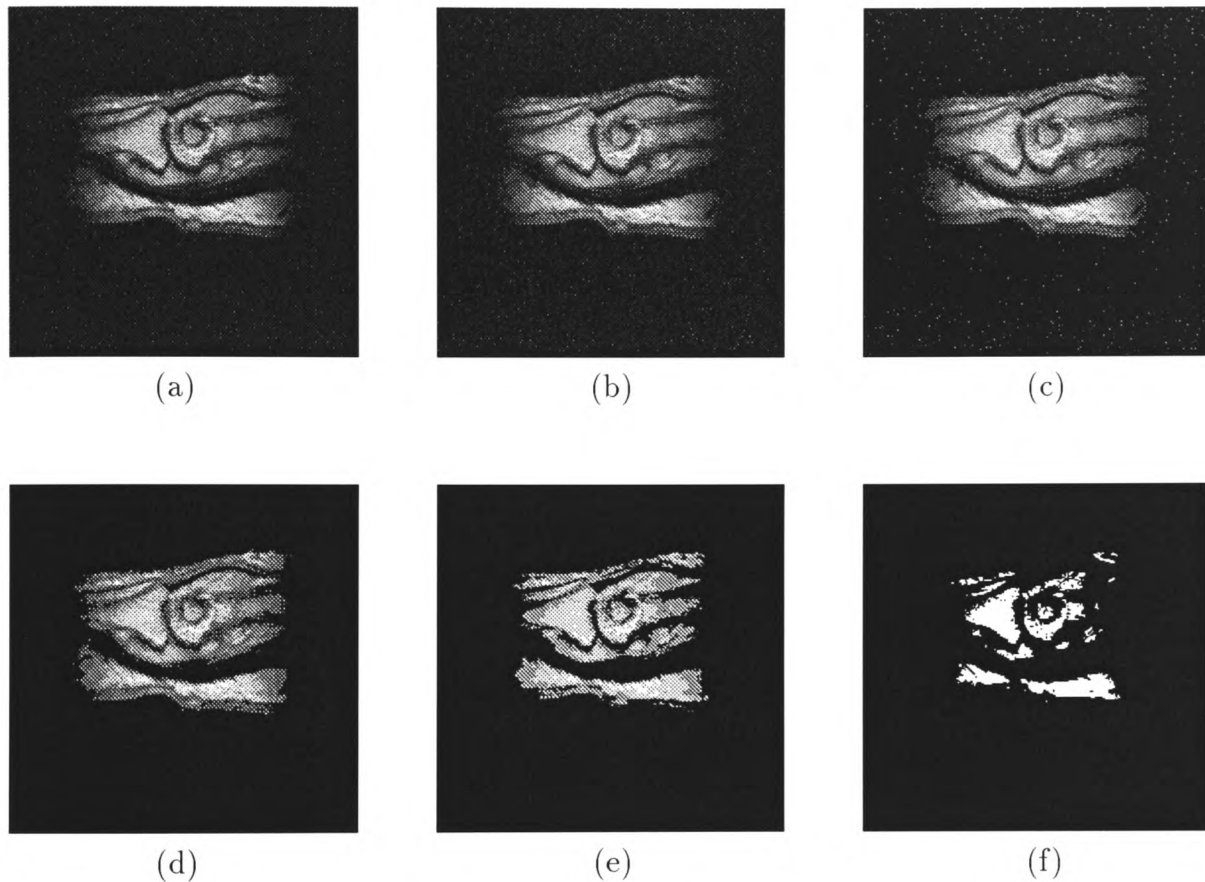


Figure 4.7: Number of grey levels of Fig. 4.5 reduced to (a) 64 (b) 32 (c) 16 (d) 8 (e) 4 (f) 2.

4.2 Locating Structural Features

In Section 4.1 it is shown that pixel intensities alone do not provide useful features for registration. Therefore, it is necessary to find some structural features within the images that can be used for registration. Some processing of the images is necessary to assist in locating such features. In this section, some well known image processing techniques, such as edge detection, are investigated. A new algorithm is presented which derives structural boundaries that can be used in the registration process (explained in Chapter 5).

4.2.1 Edge Detection and Gradient Operators

An edge can be defined as the boundary between two regions with distinct grey-level properties [Gonzalez92]. Section 4.1.3 shows that MRI finger images cannot be segmented in terms of grey level values alone. However, edge detectors can be used to locate useful structural features of an image. In this section, first derivative edge detectors are described and applied to MRI finger images.

The most common edge detectors are gradient operators. The gradient [Gonzalez92] of an image $f(x, y)$ at location (x, y) is the vector:

$$\nabla \mathbf{f} = \begin{bmatrix} G_x \\ G_y \end{bmatrix} = \begin{bmatrix} \frac{\partial f}{\partial x} \\ \frac{\partial f}{\partial y} \end{bmatrix}$$

Gradient vectors point in the direction of the maximum rate of change of f at (x, y) . In edge detection, the magnitude, ∇f , is of primary interest, where

$$\nabla f = \text{mag}(\nabla \mathbf{f}) = [G_x^2 + G_y^2]^{\frac{1}{2}}$$

This quantity equals the maximum rate of increase of $f(x, y)$ per unit distance in the direction of $\nabla \mathbf{f}$. Much simpler to implement is the commonly practised approximation to the gradient by using absolute values:

$$\nabla f \approx |G_x| + |G_y|$$

The simplest way to implement gradient operators is to pass a mask, of size 3×3 for example, over an image. As the mask passes over each 3×3 array of image pixels, calculations are performed for the centre pixel from its nearest neighbours.

Examples of gradient operators are Sobel [Gonzalez92, Sonka96, Schalkoff89, Low91]:

-1	0	1
-2	0	2
-1	0	1

$$G_x$$

-1	-2	-1
0	0	0
1	2	1

$$G_y$$

$$G_x = (z_3 + 2z_6 + z_9) - (z_1 + 2z_4 + z_7)$$

$$G_y = (z_7 + 2z_8 + z_9) - (z_1 + 2z_2 + z_3)$$

and Prewitt [Gonzalez92, Sonka96, Schalkoff89]:

-1	0	1
-1	0	1
-1	0	1

$$G_x$$

-1	-1	-1
0	0	0
1	1	1

$$G_y$$

$$G_x = (z_3 + z_6 + z_9) - (z_1 + z_4 + z_7)$$

$$G_y = (z_7 + z_8 + z_9) - (z_1 + z_2 + z_3)$$

where z_1, \dots, z_9 correspond to the grey levels of a subset of 3×3 pixels (with z_1 in the top left position and z_9 in the bottom right position).

Note that all the mask coefficients sum to zero, indicating a response of 0 in regions of uniform intensity, as expected of a derivative operator.

Sobel and Prewitt edge detectors were applied to MRI finger images to determine some boundary, or shape within an image that can be used for registration. Fig. 4.8(b) and (c) show the effect of applying the Sobel and Prewitt Edge Detectors to the image in Fig. 4.8(a).

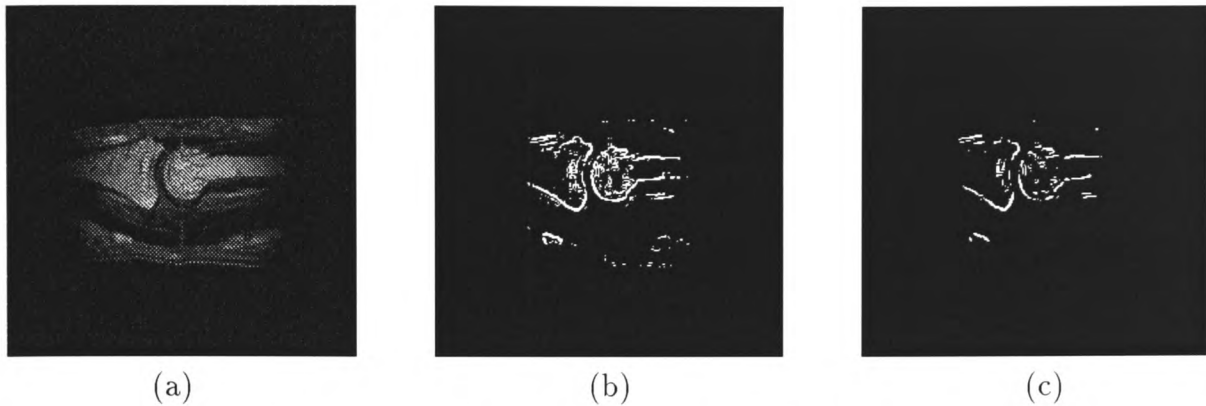


Figure 4.8: (a) MRI finger scan (b) Sobel Edge Detector (c) Prewitt Edge Detector.

The resulting images yield a great deal of information that is difficult to register without further processing. Thus, on their own, they are of little help.

A simplification algorithm has been developed which is designed to reduce the amount of information in the edge detected images to a more useful level. By selecting a minimum number of pixels, all horizontal, vertical, and $\pm 45^\circ$ diagonal straight lines of image pixels of length less than a desired minimum are removed from the image. Finding an appropriate minimum length requires some trial and error. Fig. 4.9 shows the straight line reduction effect for the image in Fig. 4.8(b), with the minimum pixel length set to 8.



Figure 4.9: Sobel Edge Detector, with binary threshold and minimum pixel length straight line reduction.

Fig. 4.9 displays some features to be found in MRI finger images. In particular, the vertical lines that lie either side of the cartilage and the horizontal lines from the proximal phalanx are potential characteristics of a finger image. The diagonal lines which approximate the corners of the bones do not always appear in the segmented images. Finding common, simple features in images of the same patient taken over time will aid the registration process.

4.2.2 Laplacian and Zero Crossings

The Laplacian [Gonzalez92, Sonka96, Schalkoff89, Low91] of an image is a second-order derivative defined as:

$$\nabla^2 f = \frac{\partial^2 f}{\partial x^2} + \frac{\partial^2 f}{\partial y^2}$$

The Laplacian may also be implemented in digital form for a 3×3 region by:

$$\nabla^2 f = 4z_5 - (z_2 + z_4 + z_6 + z_8)$$

The Laplacian is seldom used in edge detection due to its unacceptable sensitivity to noise and the double edges it produces [Gonzalez92]. The Laplacian is normally used to determine whether a pixel is on the dark or light side of an edge [Gonzalez92].

As a second derivative operator, the Laplacian has a zero crossing at the location of each edge. This property gives the Laplacian a more general use in locating edges [Gonzalez92]. This concept is based on convolving an image with the Laplacian of a 2D Gaussian function of the form:

$$h(x, y) = \exp\left(-\frac{x^2 + y^2}{2\sigma^2}\right)$$

Let $r^2 = x^2 + y^2$, then the Laplacian of h is:

$$\nabla^2 h = \left(\frac{r^2 - \sigma^2}{\sigma^4}\right) \exp\left(-\frac{r^2}{2\sigma^2}\right) \quad (4.4)$$

and the zero crossings are at $r = \pm\sigma$.

Haralick [Haralick84] defines the zero crossings as:

$$A \left(1 - k \left(\frac{x^2 + y^2}{\sigma^2} \right) \exp \left(-\frac{x^2 + y^2}{2\sigma^2} \right) \right) \quad (4.5)$$

where k is set so that the resulting weights sum to zero and A scales the values so that integer arithmetic can be used.

Figs. 4.10(b) and 4.11(b) show zero crossings applied to the finger images in Figs. 4.10(a) and 4.11(a) respectively, using a 5×5 mask derived from Equation 4.5, with

$$k = \frac{25}{\sum_{x=-2}^2 \sum_{y=-2}^2 \left(\frac{x^2 + y^2}{\sigma^2} \right) \exp \left(-\frac{x^2 + y^2}{2\sigma^2} \right)}$$

and $A = 1$.

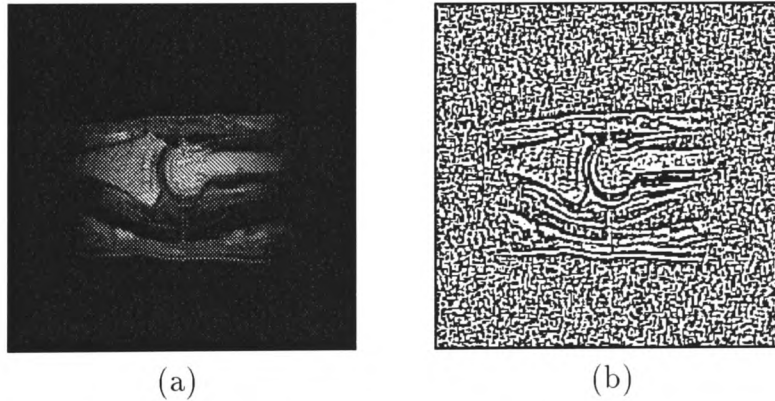


Figure 4.10: (a) MRI finger scan (b) zero crossings of image showing clear boundaries.

In Fig. 4.10(b) there are some well defined boundaries, however, Fig. 4.11(b) shows an example where the boundaries are not so clearly defined. Despite Figs. 4.10(a) and 4.11(a) having seemingly black backgrounds, the corresponding regions in Figs. 4.10(b) and 4.11(b) demonstrate that considerable information has been detected by the zero crossings. These ‘noisy’ regions indicate that the apparently uniformly black regions in the original images exhibit noise. These results contradict the statement made by Gonzalez and Woods [Gonzalez92]:

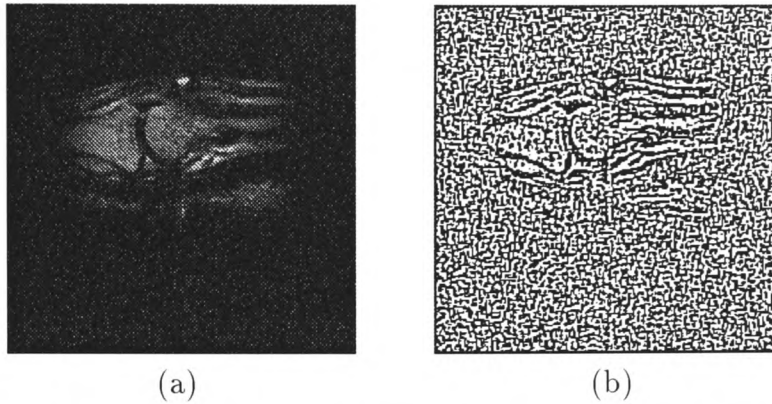


Figure 4.11: (a) MRI finger scan (b) zero crossings of image showing relatively unclear boundaries.

...edge detection by gradient operations tends to work well in cases involving images with sharp intensity transitions and relatively low noise. Zero crossings offer an alternative in cases when edges are blurry or when a high noise content is present. The zero crossings offer reliable edge location, and the smoothing properties of $\nabla^2 h$ reduce the effects of noise. The price paid for these advantages is increased computational complexity and time.

Figs. 4.10(a) and 4.11(a) yield different results partly due to the fact that Fig. 4.11(a) contains a lower contrast than Fig. 4.10(a). The MRI finger images in this application will vary in contrast, making the use of zero crossings alone unreliable. In Section 5.2 some results of post-processing of the zero crossings images are given.

4.2.3 Bone Boundaries

In this section, a new method for determining structural boundaries is derived. These boundaries are characteristic of the shapes of the bones and will subsequently be referred to as bone boundaries. The method is composed of a sequence of processes that starts with an MRI finger image and results in a black and white image with clear bone boundaries displayed. The sequence will be referred to as the boundary sequence from here on.

Consider the MRI finger image in Fig. 4.12(a). The first step in determining bone boundaries is to apply a 3×3 scaling mask [Gonzalez92] to the image. The purpose of the scale is to merge the highly heterogeneous regions of pixels within the image into blocked regions (illustrated in Fig. 4.12(b)). This stage is interactive as the user assesses whether or not the scaling is sufficient. The mask weights are initially set to 1.0, but can be manually adjusted by the user if the resulting image is over- or under-scaled. Once a suitable scaling is determined the remaining stages are automatically completed.

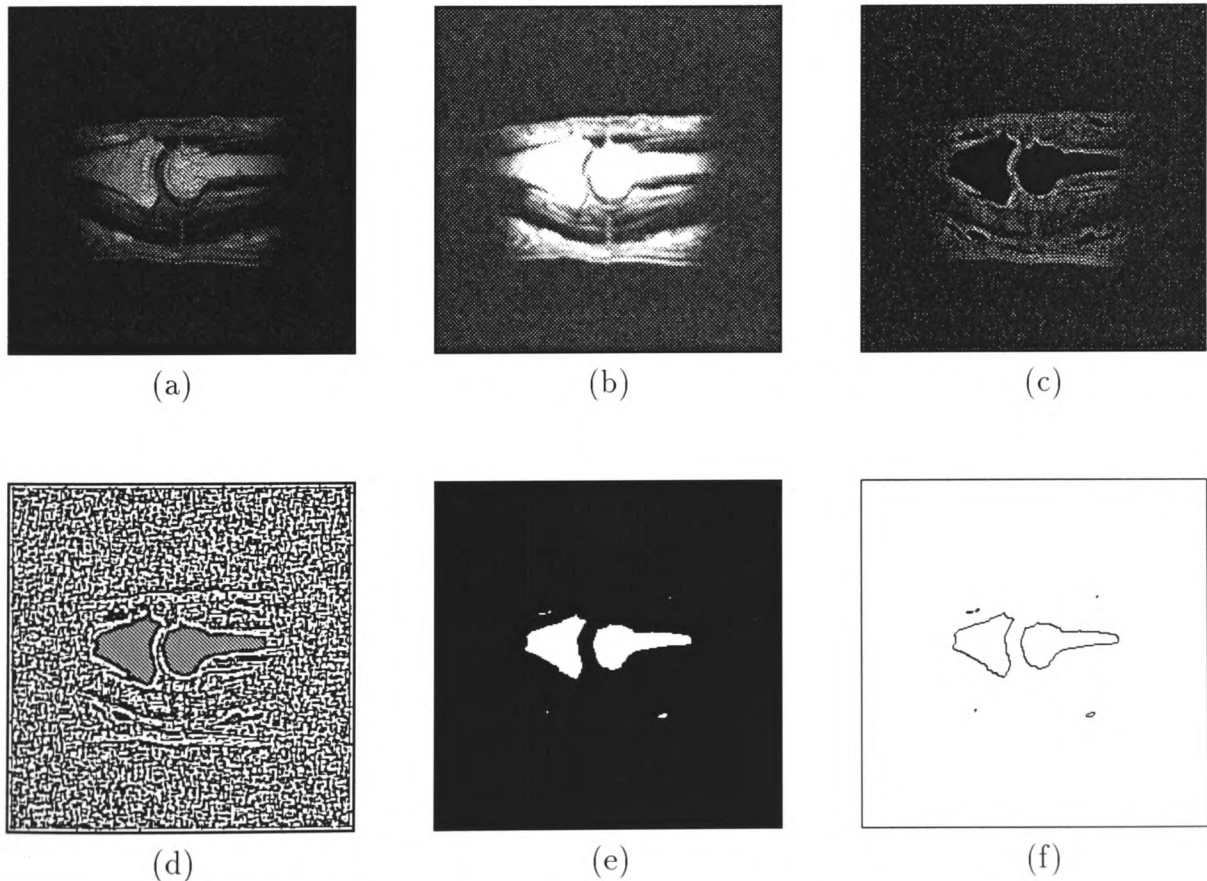


Figure 4.12: The boundary sequence.

The second stage of the sequence is the application of the Laplacian derivative operator. The Laplacian gives a response of zero in regions of unchanging intensity. Therefore, the brightly merged regions from stage one are now seen as black regions (illustrated in Fig. 4.12(c)). This is important for the third stage.

When an image is convolved with $\nabla^2 h$ (Equation 4.4), negative values are represented by black, positive values are represented by white and zeros are represented by mid-grey [Gonzalez92]. Therefore, the black regions in Fig. 4.12(c) become mid-grey in Fig. 4.12(d) while the rest of the image is a mixture of black and white.

The bone areas can now be clearly seen and are easily extracted with the use of a banded thresholding algorithm to make the mid-grey become the foreground and the rest become background (illustrated in Fig. 4.12(e)). Identifying the zero crossings from this image as the boundaries between black and white is a simple matter [Gonzalez92].

The resulting image is a black and white image with clearly defined bone boundaries. Fig. 4.12(f) shows the boundaries derived from the finger image in Fig. 4.12(a).

The boundary sequence works well for images of the same weight (Section 1.1.1) as the images have similar contrast initially. However, choosing the right scaling weights at stage one can be time consuming. This problem is worsened when considering images taken from different weighted scans (explained in Section 1.1.1) or Gadolinium enhanced images (explained in Section 1.1.3) as these images have different contrast initially. Determining correct scale factors to produce images with the same brightness after stage one is very time consuming and subjective and will have a great deal of inter-observer variability.

In Section 4.1.2 it was shown that standardizing differently weighted images results in images with the same mean and standard deviation. The standardized weighted images have more similar contrast than the original images. Applying the *same* scale at stage one of the boundary sequence to standardized images will have better results,

similar to those from images of the same weight initially. The boundary sequence can then be applied as above.

Fig. 4.13 show the result of applying the boundary sequence to the standardized images in Fig. 4.4. The two structural regions of interest are very similar, with subtle differences. Notice the gap in the region representing the proximal phalanx in Fig. 4.13(c).

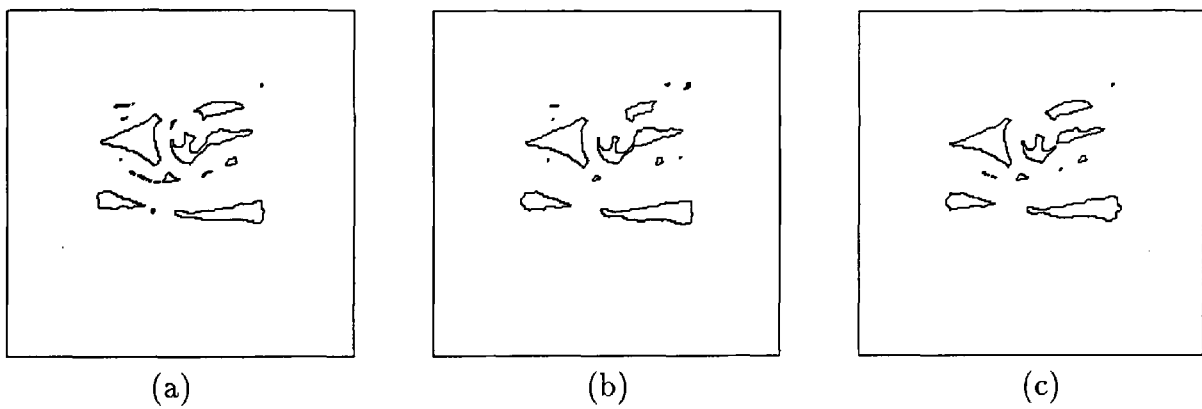


Figure 4.13: Boundary sequence on different weighted images.

The boundary sequence produces images that can be used for registration (explained in Section 5.3).

4.3 Frequency Domain Techniques

Joseph Fourier (1768 - 1830) derived a technique which transforms real data, such as a set of pixel intensity values, into the frequency domain. This technique, the Fourier transform [Rinck93, Gonzalez92, Sonka96, Schalkoff89, Low91, Bracewell86], is now widely used in various applications.

There are many frequency domain image processing techniques which can be applied to an image. Standard image processing techniques, such as edge detection (explained in Section 4.2.1), may be more efficiently performed in the frequency domain. This efficiency comes from the Convolution Theorem (explained in Section 4.3.2) which

reduces the spatial convolution to multiplication in the frequency domain. However, this improvement must be balanced against the extra processing time required to first calculate the Fourier Transform of the image data and then calculate the inverse Fourier Transform after processing to obtain the corresponding real data.

This section briefly explains the Fourier Transform and the Convolution Theorem. Then, frequency domain filters are explained and their specific application to MRI finger images given. Also, Fourier Descriptors are examined as a means of identifying the parameters required to register a pair of images.

4.3.1 The Fourier Transform

In this section, the Fourier Transform is explained briefly. For a more detailed explanation the reader is referred to [Gonzalez92, Sonka96, Schalkoff89, Low91, Bracewell86].

If $f(x)$ is a continuous function of a real variable x , then the *Fourier Transform* of $f(x)$ is [Gonzalez92]:

$$F(u) = \int_{-\infty}^{\infty} f(x)e^{-2\pi iux} dx$$

and its inverse is:

$$f(x) = \int_{-\infty}^{\infty} F(u)e^{2\pi iux} du$$

The Fourier transform of a real function is generally complex, that is:

$$F(u) = R(u) + iI(u) \tag{4.6}$$

where $R(u)$ and $I(u)$ are the real and imaginary components of $F(u)$, respectively. Equation 4.6 can be expressed in exponential form [Gonzalez92], that is:

$$F(u) = |F(u)|e^{i\phi(u)}$$

where

$$|F(u)| = (R^2(u) + I^2(u))^{\frac{1}{2}}$$

and:

$$\phi(u) = \tan^{-1} \left[\frac{I(u)}{R(u)} \right]$$

The magnitude function $|F(u)|$ is called the *Fourier spectrum* of $f(x)$ and $\phi(u)$ is called the *phase angle*.

The Fourier transform can easily be extended to data in two dimensions, which is more applicable to image processing. If $f(x, y)$ is a continuous function of two real variables, x and y , then the two-dimensional Fourier transform and its inverse are defined by:

$$F(u, v) = \int \int_{-\infty}^{\infty} f(x, y) e^{-2\pi i(ux+vy)} dx dy$$

$$f(x, y) = \int \int_{-\infty}^{\infty} F(u, v) e^{2\pi i(ux+vy)} du dv$$

and the Fourier spectrum and phase are defined by:

$$|F(u, v)| = (R^2(u, v) + I^2(u, v))^{\frac{1}{2}}$$

$$\phi(u, v) = \tan^{-1} \left[\frac{I(u, v)}{R(u, v)} \right]$$

In practice, an image is discretized into a square ($n \times n$) array and therefore the two-dimensional discrete Fourier transform (DFT) is applied to the image data. The two-dimensional DFT for an $n \times n$ image and its inverse are defined as [Gonzalez92]:

$$F(u, v) = \frac{1}{n} \sum_{x=0}^{n-1} \sum_{y=0}^{n-1} f(x, y) e^{-2\pi i(ux+vy)/n}$$

for $u, v = 0, 1, 2, \dots, n-1$ and

$$f(x, y) = \frac{1}{n} \sum_{u=0}^{n-1} \sum_{v=0}^{n-1} F(u, v) e^{2\pi i(ux+vy)/n}$$

for $x, y = 0, 1, 2, \dots, n-1$.

Implementing the DFT requires a large number of complex multiplications and additions. Gonzalez and Woods [Gonzalez92] show that the development of the *Fast Fourier Transform* (FFT) [Cooley65] reduces the computational time required from $O(n^2)$ to $O(n \log_2 n)$, when n is a power of 2. This time reduction is a great saving when applying the Fourier Transform to a large 256×256 image.

4.3.2 The Convolution Theorem

The convolution [Gonzalez92, Sonka96, Schalkoff89, Low91, Bracewell86] of two functions can be thought of as a weighted average, where one function gives the values to be averaged and the other function holds the weights. In image processing in the spatial domain, convolution is most easily understood as an $m \times m$ mask of weights that passes over all possible $m \times m$ arrays of pixels within an image. The two-dimensional, discrete convolution $(*)$ of an image $f(x, y)$ with a linear operator $h(x, y)$ for an $n \times n$ image is:

$$f(x, y) * h(x, y) = \sum_{j=0}^{n-1} \sum_{k=0}^{n-1} f(j, k) h(x - j, y - k)$$

for $j, k = 0, 1, 2, \dots, n - 1$.

The convolution theorem is the foundation of frequency domain techniques [Gonzalez92]. The convolution theorem states that convolution in the spatial domain equates to multiplication in the frequency domain. That is:

$$f(x, y) * h(x, y) \Leftrightarrow F(u, v) \times H(u, v)$$

where F and H are the Fourier transforms of f and h respectively.

In some cases it is more efficient to take the Fourier transform of an image, multiply by a chosen transfer function (H) and then take the inverse Fourier transform to obtain the new image.

4.3.3 Filters

Two categories of frequency domain filters are *Lowpass Filters* and *Highpass Filters* [Gonzalez92, Sonka96]. Edges and other sharp transitions (such as noise) in an image make up a large proportion of the high-frequency components in the Fourier transform of the image. Reducing the high-frequency content of an image is the basis of lowpass filtering; a consequence of such filtering is a blurring effect on the image. Increasing the high-frequency components relative to the low-frequency components is the basis of highpass filtering and results in a sharpening effect on the image.

As registration requires some detail from the image, for example, edges or a boundary, lowpass filtering (blurring) is of little use to this application. Highpass filtering (sharpening), however, has the potential to enhance the image detail which may then aid the registration process. In the following, some examples of highpass filters are given with their application to MRI finger images.

To apply a frequency domain filter to an image, the image must first be transformed into the frequency domain. The Fast Fourier Transform (FFT) is the quickest way to achieve this. Then the filter may be applied to the image. Finally, the filtered image is transformed back to the spatial domain by applying the inverse FFT.

Ideal Highpass Filter

The Ideal highpass filter is defined as:

$$H(u, v) = \begin{cases} 0 & \text{if } D(u, v) \leq D_0 \\ 1 & \text{if } D(u, v) > D_0 \end{cases}$$

where D_0 represents the radius of this radially symmetric function and $D(u, v)$ is the distance from a point (u, v) to the origin of the frequency plane, that is:

$$D(u, v) = (u^2 + v^2)^{\frac{1}{2}}$$

In practice, when the filter is applied to an image, $D(u, v)$ is actually the distance from a point (u, v) to the centre of the frequency plane. Therefore, $D(u, v)$ must be defined as:

$$D(u, v) = [(u - cu)^2 + (v - cv)^2]^{\frac{1}{2}} \quad (4.7)$$

where (cu, cv) is the centre of the frequency plane.

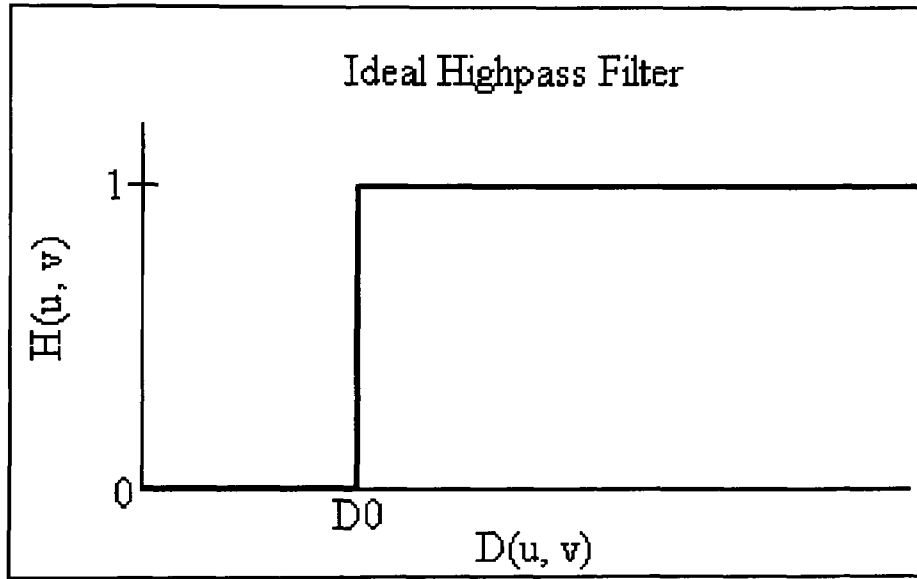


Figure 4.14: Radial cross-section of the Ideal highpass filter.

The filter is called *ideal* as all frequencies inside a circle of radius D_0 are eliminated while all frequencies outside the circle are unaffected (illustrated in Fig. 4.14).

Butterworth Highpass Filter

The Butterworth highpass filter, of order n , is defined as:

$$H(u, v) = \frac{1}{1 + [D_0/D(u, v)]^{2n}}$$

where D_0 is the radius and $D(u, v)$ is given by Equation 4.7.

Unlike the Ideal highpass filter, the low frequency components within the circle are not eliminated, but are greatly attenuated (illustrated in Fig. 4.15). Changing the value of D_0 allows control over how many frequencies are attenuated. Changing the value of n controls how quickly the filter rises to 1. As n increases the Butterworth filter becomes more like the Ideal filter. In this application, n is set to 1.

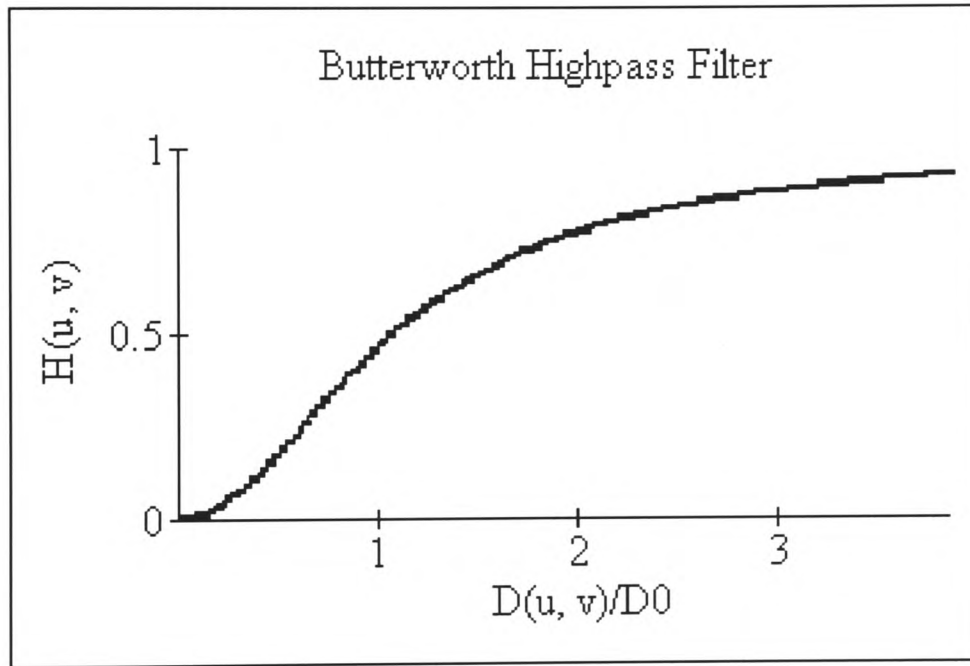


Figure 4.15: Radial cross-section of the Butterworth highpass filter for $n = 1$.

Exponential Highpass Filter

The Exponential highpass filter is defined as:

$$H(u, v) = e^{-D_0/D(u,v)}$$

where D_0 is the radius and $D(u, v)$ is given by Equation 4.7.

The Exponential highpass filter is similar to the Butterworth highpass filter in that the low frequency components within the circle are not eliminated, but are greatly attenuated (illustrated in Fig. 4.16).

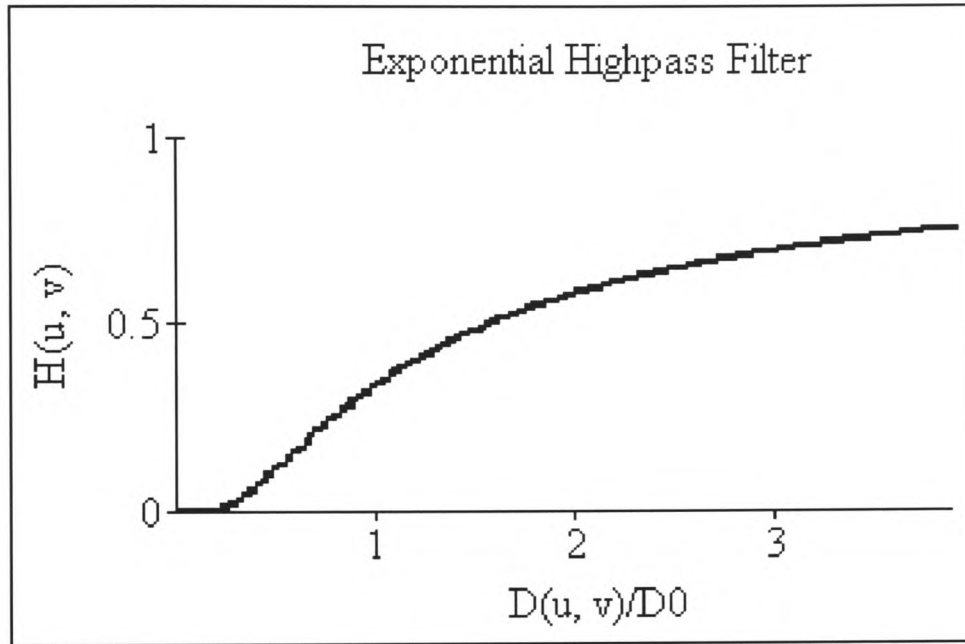


Figure 4.16: Radial cross-section of the Exponential highpass filter.

Application of Filters to MRI Finger Images

The effect of highpass filtering is to sharpen image edges. The amount of sharpening is dependent on the choice of D_0 . As D_0 increases, more low frequency components are attenuated. Edges and abrupt changes in grey level are associated with high frequency components. Therefore, it is expected that the sharpening of edges will improve the boundaries of particular regions of interest, which will then greatly improve the registration process. However, with MRI finger images, this expectation is not realised as described below.

In order to determine the next stage in the registration process, it is necessary to be able to see the resulting effect of each filter. However, the resulting highpass filtered images are very dark and need to be contrast stretched (explained in Section 4.1.1).

Experimentation with the Ideal highpass filter shows that, as D_0 increases, boundary detail is lost and speckled detail becomes more prominent. This means that the sharpest edges in MRI finger images are not boundaries between specific tissue types

but come from the heterogeneity within specific tissue structures.

Experimentation with both the Butterworth and the Exponential highpass filters show that these filters do not enhance boundary edges in MRI finger images sufficiently to aid the registration process.

Fig. 4.17(a) to (c) show the results of applying the ideal, Butterworth and exponential filters, respectively, to the finger image in Fig. 4.8(a), with $D_0 = 50$.

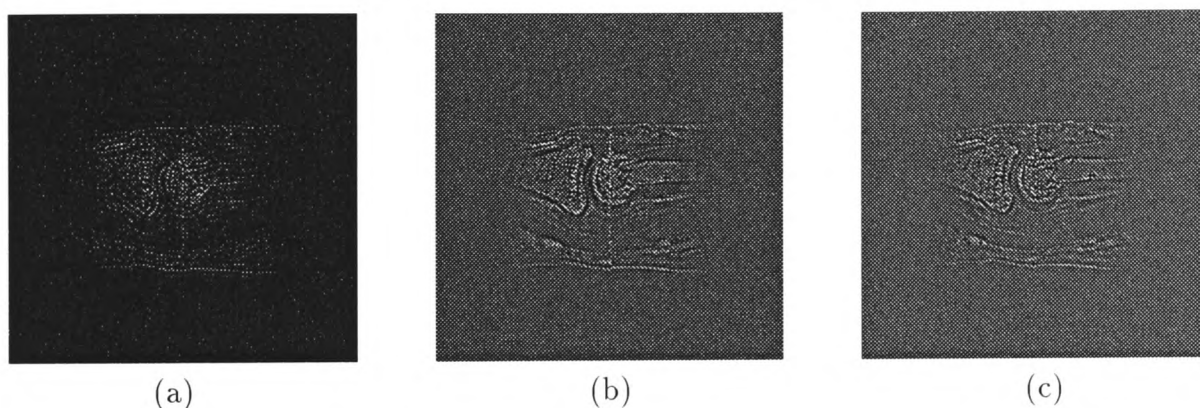


Figure 4.17: Effect of highpass filters with $D_0 = 50$ (a) ideal (b) Butterworth (c) exponential.

4.3.4 Fourier Descriptors

The identification and registration of objects in images can be aided by the use of measures of ‘shape’. A digital boundary can be described by a sequence of so-called Fourier descriptors [Gonzalez92, Sonka96]. These descriptors convey shape information. The general shape of a boundary is conveyed by just a few of the descriptors in the sequence while the majority of the descriptors contain the fine detail of the boundary. In this section, the derivation of Fourier descriptors is given, followed by their application to MRI finger images.

Suppose an image contains a closed boundary. The boundary may be expressed as an anti-clockwise sequence of pixels. Further, each pixel may be described as a complex number by using its co-ordinates, (x, y) , as the real and imaginary components, *i.e.*

$(x + iy)$. If there are n points on the boundary, the two-dimensional boundary may be described as a one-dimensional sequence [Gonzalez92]:

$$s(k) = x(k) + iy(k)$$

for $k = 0, 1, 2, \dots, n - 1$. The Discrete Fourier Transform (DFT), $a(u)$, of this sequence can be calculated giving:

$$a(u) = \frac{1}{n} \sum_{k=0}^{n-1} s(k) e^{-i2\pi uk/n}$$

for $u = 0, 1, 2, \dots, n - 1$.

The complex coefficients, $a(u)$, are called the *Fourier Descriptors* of the boundary. The inverse DFT restores $s(k)$, that is:

$$s(k) = \sum_{u=0}^{n-1} a(u) e^{i2\pi uk/n}$$

for $k = 0, 1, 2, \dots, n - 1$.

If only M Fourier coefficients are retained, *i.e.* by setting $a(u) = 0$ for $u > M - 1$, the boundary is approximated to:

$$\hat{s}(k) = \sum_{u=0}^{M-1} a(u) e^{i2\pi uk/n}$$

for $k = 0, 1, 2, \dots, n - 1$. Although only M terms are used to construct each point, the same number of points exist in the approximate boundary.

The low-frequency and high-frequency components of the Fourier Transform correspond to global shape and fine detail characteristics respectively in the image. As M decreases, more detail is lost on the boundary and the boundary will be approximated by its most general shape characteristics. M is normally selected to be an integer power of 2 so that the FFT (explained in Section 4.3.1) can be used to perform the calculations.

The application of Fourier Descriptors to registering MRI finger images has a great advantage in that images of the same patient will differ in fine detail (high-frequencies), but should have the same overall basic shape (low-frequencies).

Application of Fourier Descriptors to MRI Finger Images

In this section, Fourier Descriptors are examined as a means of providing the parameters required for registration. The Fourier Descriptors are applied to the images containing bone boundaries (explained in Section 4.2.3).

Some simple transformations can be applied to the Fourier Descriptors to create descriptors that are invariant to rotation, translation and scale. Such descriptors are often applied to pattern recognition applications, for example, character recognition. In this application, it is necessary to determine a translational and rotational offset between a pair of images in order to register them. Therefore, invariant Fourier Descriptors are of little use in this application.

The centre of gravity of an image is represented by the complex vector a_0 [Granlund72]. The displacement between centres of gravity from two images of the same object could indicate the translational offset required for registration. Determining the rotational offset is not as easy. To rotate an image about the origin, the descriptors can be multiplied by $e^{j\theta}$, where θ is the angle of rotation. Consider a set of descriptors, b_n , derived from rotating the original descriptors, a_n , that is:

$$b_i = a_i e^{j\theta}$$

where $a_i = x_{ai} + jy_{ai}$ and $b_i = x_{bi} + jy_{bi}$, for $i = 0, 1, 2, \dots, n - 1$.

It is possible to derive the angle of rotation, θ , via some simple algebraic manipulations, that is:

$$x_{bi} + jy_{bi} = (x_{ai} + jy_{ai}) e^{j\theta} = (x_{ai} + jy_{ai}) (\cos\theta + j\sin\theta)$$

$$x_{bi} + jy_{bi} = x_{ai}\cos\theta - y_{ai}\sin\theta + j(x_{ai}\sin\theta + y_{ai}\cos\theta)$$

Therefore,

$$x_{bi} = x_{ai}\cos\theta - y_{ai}\sin\theta \quad (4.8)$$

$$y_{bi} = x_{ai}\sin\theta + y_{ai}\cos\theta \quad (4.9)$$

From Equation 4.8

$$\cos\theta = \frac{x_{bi}}{x_{ai}} + \frac{y_{ai}\sin\theta}{x_{ai}} \quad (4.10)$$

Substituting Equation 4.10 into Equation 4.9 gives:

$$y_{bi} = x_{ai}\sin\theta + y_{ai}\left(\frac{x_{bi}}{x_{ai}} + \frac{y_{ai}\sin\theta}{x_{ai}}\right)$$

$$y_{bi} = x_{ai}\sin\theta + \frac{y_{ai}x_{bi}}{x_{ai}} + \frac{y_{ai}^2\sin\theta}{x_{ai}}$$

$$y_{bi} - \frac{y_{ai}x_{bi}}{x_{ai}} = \sin\theta\left(x_{ai} + \frac{y_{ai}^2}{x_{ai}}\right)$$

$$\frac{y_{bi}x_{ai} - y_{ai}x_{bi}}{x_{ai}} = \sin\theta\left(\frac{x_{ai}^2 + y_{ai}^2}{x_{ai}}\right)$$

$$\frac{y_{bi}x_{ai} - y_{ai}x_{bi}}{x_{ai}^2 + y_{ai}^2} = \sin\theta$$

$$\theta = \sin^{-1}\left(\frac{y_{bi}x_{ai} - y_{ai}x_{bi}}{x_{ai}^2 + y_{ai}^2}\right)$$

For all descriptors, the angle of rotation derived is the same. However, this test case does not work so easily in practice. When an image is rotated, the resulting pixel co-ordinates must be rounded to the nearest grid location, thus introducing some error. When determining θ from the Fourier Descriptors of two images, where one image is a rotation of the other, the angle of rotation for each pair of descriptors is not the same. This complicates the process of finding a rotational offset between a pair of images.

Another problem is that the bone boundaries derived from two images of the same finger over time may differ considerably due to movement or incorrect positioning for scanning (explained in Section 1.2). Therefore, the Fourier Descriptors may be derived from boundaries with large differences in shape. This cannot be a good basis for any registration method. Therefore, it is necessary to apply Fourier Descriptors to selected open curves that are very similar. This is possible, but requires that the user selects the open curve. Applying Fourier Descriptors to open curves is a possibility; however, the translational offset, represented by the difference in the centres of gravity, has great potential for error if the open curves defined on two images are not the same. Translational registration based on centre of gravity could lead to mis-registrations. It is considered that this causes great enough potential error, without even considering the rotational offset, to warrant a better approach. These issues are further discussed in Section 5.5, where moments are applied to combined slice boundaries.

4.4 Conclusions

In this chapter, various standard and new image processing techniques are applied to MRI finger images in both the spatial domain and the frequency domain. The aim of these techniques is to locate features within the images that can be used for registration.

Current contrast stretching and standardizing techniques alone do not produce any new information for registration and give no correlation between images of different contrast. The new standardizing technique (explained in Section 4.1.2) is particularly useful for images that are differently weighted or are Gadolinium enhanced. The new approach uses the mean and standard deviation from more than one image to produce images with the same spread. This process is a fundamental pre-processing step for the boundary sequence (explained in Section 4.2.3).

Registration cannot be based on image grey levels alone as the grey levels within different tissue regions overlap. Also, within particular regions of interest, the grey levels are heterogeneous. Re-mapping the grey levels to reduce the number of grey levels in an image does not produce clear, smooth, bounded regions in the images.

The classic edge detectors on their own produce images with too much information. However, a new straight line reduction algorithm is applied to reduce the amount of information to the most significant parts. The resulting images show some characteristics of MRI finger images that can be used in the registration process (explained in Chapter 5).

The application of zero-crossings is very sensitive to image noise and the resulting images are not always easily visualised. The straight line reduction algorithm can simplify the images in terms of the number of straight lines seen, but the shape detail in the image is too easily lost.

The derivation of bone boundaries using the newly developed boundary sequence (explained in Section 4.2.3) is by far the most useful. These boundaries are used in Chapter 5 for the registration process.

The application of frequency domain filters reveals that the sharpest edges in MRI finger images are not boundaries between different tissue structures, but come from the heterogeneity within tissues.

The method of Fourier Descriptors can give translational registration from the difference in the centroid of two images of the same finger. Determining an angle of rotation between two images is not as easy. Also, positional differences in the finger on two occasions forces the application of Fourier Descriptors to user-selected open curves on the images. If the defined open curves are not the same, which is highly likely, then registration based on the centroid could lead to gross mis-registrations.

Much of the work of this chapter was presented at the 2nd IMA conference on Image Processing and published in the conference proceedings [Williams2000]. A copy of the paper can be found in Appendix F.

Chapter 5

Registration Methods

In Chapter 4 attention was given to locating structural features in MRI images that can be used for registration. In this chapter, the identified structural features are used in some existing and new registration techniques.

Firstly, a search for registration is made with the sum of absolute values of differences method [Barnea72]. Secondly, a new, simple superimposing method is used to directly assess (mis-)registration or search for a best-fit. The results for both of these methods are presented in [Williams2000]. Thirdly, Hough Transform methods [Gonzalez92, Cideciyan90, Sonka96, Schalkoff89, Low91] are applied to the bone boundaries derived in Section 4.2.3. Results from the fitting of ellipses to the derived boundaries leads to a novel approach of combining the slices. The combined slice effect creates images that appear more similar over time. Applying the Hough Transform to such images produces better registration results. Further, the combined slice images reveal information about the MRI finger images that was not realised previously. Finally, moments are applied to the combined slice images to assess their feasibility for improving the registration results.

5.1 Similarity Detection

Barnea and Silverman [Barnea72] present a class of sequential similarity detection algorithms (SSDAs) which they use for translational registration.

Let an image, S , and window, W , be defined as in Fig. 5.1. S is an $L \times L$ search area and W an $M \times M$ window containing a subimage from a second, reference image. Within image S , each $M \times M$ subimage (which is uniquely referenced by its top left coordinates) is compared with window W to determine the best match. The parameters L and M are set, with M smaller than L , so that, at registration, a complete subimage is contained within the search area.

By searching a subset of the allowed range of reference points, translational registration is determined by finding a point, (i^*, j^*) , which references the most similar

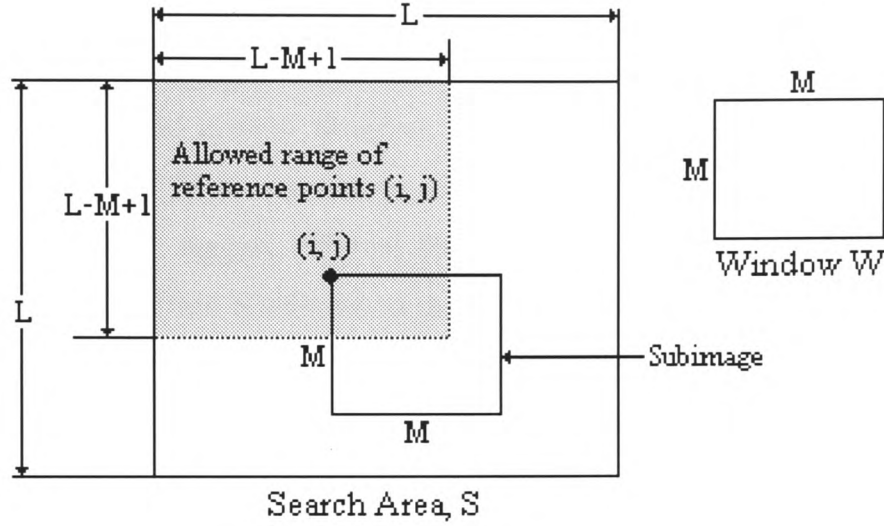


Figure 5.1: SSDA.

subimage to the window W . The choice of M will be crucial in determining the speed of the algorithm as M^2 pixels are processed for every reference point (i, j) .

One measure used to determine similarity is the sum of absolute values of differences (SAVD) [Barnea72, Yu89] of the corresponding pixels from the subimage and the window. That is:

$$\|E(i, j)\| \equiv \sum_{i=1}^M \sum_{j=1}^M |S(i, j) - W(i, j)|$$

An extension to the SAVD is the normalised method, which subtracts the mean of each subimage and the window from their respective pixel grey levels, *i.e.*

$$\|E(i, j)\| \equiv \sum_{i=1}^M \sum_{j=1}^M |S(i, j) - \hat{S}(i, j) - W(i, j) + \hat{W}|$$

where $\hat{S}(i, j)$ is the mean grey level of subimage S at reference point (i, j) and \hat{W} is the mean grey level of window W (taken from a second, reference image). The normalised SAVD gives the added advantage of ignoring different mean intensities in two regions of similar distributions of intensity, *i.e.* due to being of the same type of tissue. This advantage is particularly useful for registering Gadolinium enhanced images (Section 1.1.3) and different weighted images (Section 1.1.1).

The normalised SAVD method has been applied to sections of the MRI finger images of this project. For some local regions the resulting translation to achieve registration, by eye, look like a good match. However, even on pairs of images believed to exhibit relatively little actual finger movement, the best-fit result for different local regions from the same images suggest different translations to achieve registration. Further, when the SAVD algorithm is applied to the whole finger, the resulting transformation does not always match the local transformations. Combining transformations from different local regions could mean distorting one image to match the other. Distorting an MRI finger image could change the shape or size of the synovium. The aim of this research is to aid clinicians' understanding of the effect of rheumatic disease on synovium. To this end, a post-registration analysis of the shape and size of synovium could be crucial.

5.2 Superimposition

In this section a new, simple method for a registration search is derived from the basic concept of search within SSDA (explained in Section 5.1).

Suppose an image, A , called the *active* image, is to be registered with a *reference* image, R . The relative translation required to achieve registration is determined by considering the similarity of the contents of two equal sized subimages from each of the two images. A new image, N , is created by superimposing the active subimage onto the reference subimage.

The size of the subimage is set by the user drawing a rectangle around the whole finger or a particular region of interest in the active image. The rectangle is then automatically copied onto the reference image.

Each pixel in N which is outside the rectangle takes its value from the pixel in the corresponding position in the active image. Within the subimage rectangle, pixel values are assigned from the following test and the number of (mis-)matching pixels

are calculated:

$$N_{i,j} = \begin{cases} A_{i,j} & : A_{i,j} = R_{i,j} \\ Red & : A_{i,j} < R_{i,j} \\ Blue & : A_{i,j} > R_{i,j} \end{cases}$$

for all i, j in the subimage.

The rectangle can be automatically or manually moved within a search space to locate the position at which the greatest number of matching pixels occurs.

It was expected, where a good match of contents should occur, that corresponding pixels in two images of the same weight would differ in intensity by a small amount. However, closer examination of MRI finger images reveals that within some tissue regions pixel intensities differ by 500 or more grey levels. To accommodate this difference, a tolerance, Tol , was introduced to the above test. That is:

$$N_{i,j} = \begin{cases} A_{i,j} & : R_{i,j} - Tol \leq A_{i,j} \leq R_{i,j} + Tol \\ Red & : A_{i,j} < R_{i,j} - Tol \\ Blue & : A_{i,j} > R_{i,j} + Tol \end{cases}$$

for all i, j in the subimage. Pixel $A_{i,j}$ is said to match pixel $R_{i,j}$ if pixel $A_{i,j}$ lies within plus or minus the tolerance of $R_{i,j}$. The number of these matching pixels is calculated.

This algorithm raises some very important issues, such as, what is an acceptable tolerance level for registration and what total of “matching” pixels would warrant the term “registered”. On examination, where tolerance levels are increased to 300 or 400, “registration” is possible. This level of tolerance is deemed to be too high and therefore a modified approach is necessary, as described below.

Combined Methods

The newly developed superimposition method can be used directly on MRI finger images, or as a post-processing registration step on images containing features, located by methods explained in Chapter 4. In this section a combination of edge detectors or zero crossings followed by superimposition is shown to improve registration.

In Section 4.2.1 features of MRI finger images are located by applying the Sobel edge detector with a binary threshold and the straight line reduction algorithm. Two similarly derived images of the same finger can be superimposed as above and a best match searched for. As the images contain only black or white pixels there is no need for a tolerance level.

In many cases the maximum number of matching pixels gives a position which looks, by eye, to resemble registration. Within the user-selected subimage rectangle, the percentage of matching pixels at registration exceeds 90%. However, this measure is not altogether helpful, due to the vast quantity of background pixels in this type of image. A more correct measure is to calculate the number of matching foreground pixels alone, as these represent the actual structural features of the finger images. The positions at which maximum matching pixels are located are the same as previously, although the percentage of matching pixels falls to between 24% and 69%.

The combined approach is also applied to pairs of images produced by applying zero crossings (explained in Section 4.2.2) to MRI finger images. The speckled nature of the zero crossings images makes it almost impossible to see the detail in the superimposed image well enough for analysis. As an intermediate step, the straight line reduction (SLR) algorithm (explained in Section 4.2.1) was introduced to simplify the images to make superimposition more meaningful. By selecting a minimum number of pixels, the SLR algorithm removes from the image all horizontal, vertical, and $\pm 45^\circ$ diagonal straight lines of image pixels of length less than a desired minimum. If the chosen minimum is too small, too much detail is retained in the image. If the chosen minimum

is too large then the curved detail around the finger joint is quickly lost while still retaining some unnecessary background information. No optimum value, which would be generally applicable to a range of MRI finger images, could be found to solve both of these.

5.3 Hough Transform Approaches to Registration

The boundary images derived in Section 4.2.3 can be used to register a pair of images through consideration of the shapes of the boundaries. The entire boundaries do not conform well to any geometric entity; however, particular open curves on the boundaries are characteristically elliptic.

The Hough Transform [Gonzalez92, Cideciyan90, Sonka96, Schalkoff89, Low91] is a well-known and useful tool for determining boundary shapes. The Hough Transform can be used to detect lines, circles, ellipses or even a non-standard shape.

Two Hough Transform based matching methods are presented in this chapter. The first method uses the Hough Transform to determine a best-fit ellipse to open boundaries. These elliptic shapes in the images may not be aligned with the cartesian image axes, therefore the fitting of ellipses at different orientations must be considered. The second method uses the Generalised Hough Transform to describe the irregular shape of the closed boundary. In both methods, the differences in the ellipse parameters, or the arbitrary shape parameters, detected in the two images determine the relative translation and rotation required to register the images.

5.3.1 The Hough Transform

Consider a point (x_i, y_i) lying on a particular straight line of equation $y = mx + c$, illustrated in Fig. 5.2(a). An infinite number of lines pass through the point (x_i, y_i) , all being represented by the equation $y_i = mx_i + c$. Rearranging that equation as $c = -x_i m + y_i$ describes the equation of a single line in the mc plane (also called the

parameter space). The lines potentially passing through a second point on the line, (x_j, y_j) , also have a corresponding single line in mc space ($c = -mx_j + y_j$). By denoting the intersection of the two lines (illustrated in Fig. 5.2(b)) in mc space by the point (m', c') we have that $y = m'x + c'$ is the line passing through both (x_i, y_i) and (x_j, y_j) in xy space.

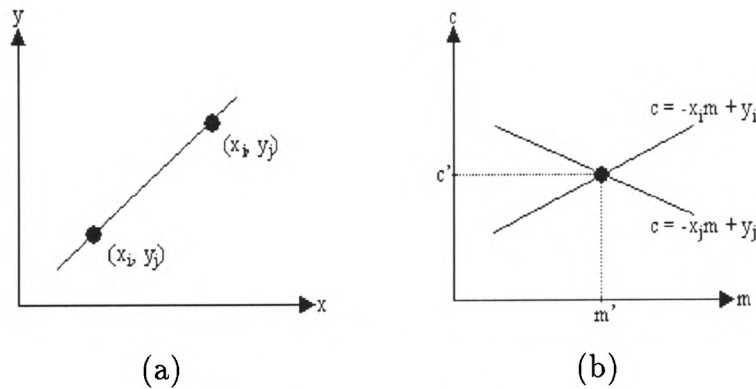


Figure 5.2: Lines in xy and mc space.

In the continuous parameter space, mc , there are an infinite number of m and c combinations. To implement the Hough Transform it is necessary to subdivide the parameter space into discrete *accumulator cells*, for given ranges of m $[m_{min}, m_{max}]$ and c $[c_{min}, c_{max}]$, at specific intervals. All cells in the accumulator array are initialised to zero. Then, for every point (x_i, y_i) in the image, the parameter m is set to each possible value m_k in $[m_{min}, m_{max}]$ and $c = -x_i m_k + y_i$ is solved for c . The resulting c is rounded to the nearest discrete value in $[c_{min}, c_{max}]$, say c_l , and $A(m_k, c_l)$ is incremented by 1. At the end of the procedure, the maximum in the accumulator array, M , at position $A(m_k, c_l)$, corresponds to the position of the highest number of intersections. However, M will not exactly correspond to the number of points in the xy plane lying on the line $y = m_i x + c_j$, due to rounding of calculations (explained in Section 5.3.2).

There is a problem, however, with using cartesian co-ordinates for a straight line, in that the magnitude of m approaches infinity as the line approaches the vertical. To avoid this difficulty, the polar co-ordinates of a straight line, $x\cos\theta + y\sin\theta = r$, can be used instead. The procedure for the Hough Transform, however, remains the same. The points on a line in xy space are now represented as sinusoidal curves in $r\theta$ space, with intersections again indicating the straight line that passes through both (x_i, y_i) and (x_j, y_j) .

The Hough Transform can be applied to geometric entities other than straight lines and even to open sections of boundaries. The basic difference in implementation is the number of parameters in the accumulator array. A circle, for instance, has 3 parameters, whereas an ellipse has 5 parameters. In the next section, the formulae for detecting ellipses at any orientation in the Hough Transform procedure are explained.

Ellipses at any Orientation

An ellipse can be thought of as a set of n points, (x_i, y_i) , defined by:

$$\begin{aligned} x_i &= c_x + a\cos\theta \\ y_i &= c_y + b\sin\theta \end{aligned} \tag{5.1}$$

for $i = 0, 1, 2, \dots, n-1$, where (c_x, c_y) is the centre of the ellipse, a and b are the major and minor radii respectively and $0^\circ \leq \theta < 360^\circ$. Fig. 5.3(a) illustrates an ellipse centred at the origin and having radii parallel to the cartesian axes. However, in this application we need to consider ellipses at any orientation as the best-fit ellipse to a bone contour may not be aligned with the cartesian axes. Fig. 5.3(b) shows the ellipse of Fig. 5.3(a) having been rotated anti-clockwise through angle Ω .

An ellipse can be rotated about its centre, (c_x, c_y) , by using standard geometry techniques. First, the ellipse is translated to the origin by subtracting (c_x, c_y) from every point (x_i, y_i) . Then the ellipse is rotated by Ω degrees. Finally, the ellipse is translated so that its centre is, again, (c_x, c_y) . This process is represented by the

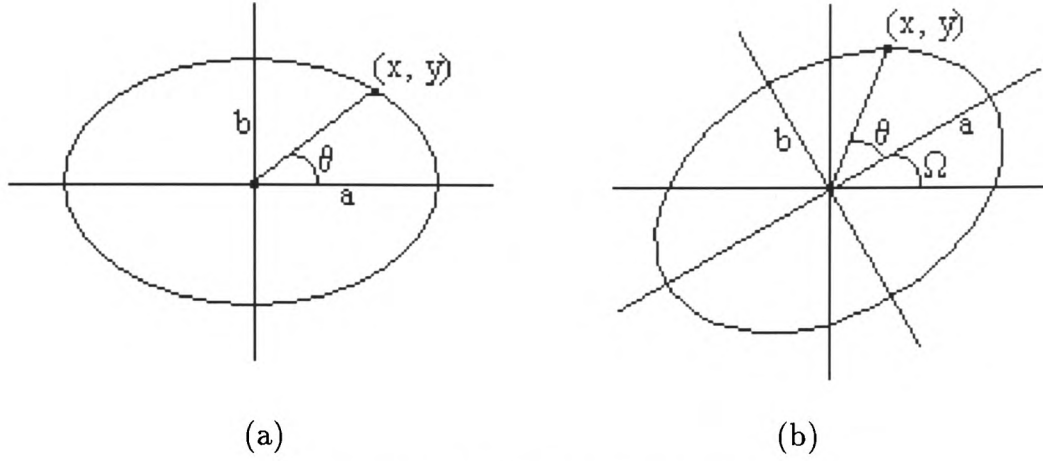


Figure 5.3: Ellipse parameters.

transformation indicated by the following matrices. A point (x, y) is transformed to a new location (x', y') by:

$$\begin{pmatrix} x' & y' & 1 \end{pmatrix} = \begin{pmatrix} x & y & 1 \end{pmatrix} \begin{pmatrix} 1 & 0 & 0 \\ 0 & 1 & 0 \\ -c_x & -c_y & 1 \end{pmatrix} \begin{pmatrix} \cos\Omega & \sin\Omega & 0 \\ -\sin\Omega & \cos\Omega & 0 \\ 0 & 0 & 1 \end{pmatrix} \begin{pmatrix} 1 & 0 & 0 \\ 0 & 1 & 0 \\ c_x & c_y & 1 \end{pmatrix}$$

i.e.

$$x' = (x - c_x) \cos\Omega - (y - c_y) \sin\Omega + c_x \quad (5.2)$$

$$y' = (x - c_x) \sin\Omega + (y - c_y) \cos\Omega + c_y$$

Substituting Equation 5.1 into Equation 5.2 yields:

$$x'_i = (c_x + a \cos\theta - c_x) \cos\Omega - (c_y + b \sin\theta - c_y) \sin\Omega + c_x$$

$$y'_i = (c_x + a \cos\theta - c_x) \sin\Omega + (c_y + b \sin\theta - c_y) \cos\Omega + c_y$$

for $i = 0, 1, 2, \dots, n - 1$, hence

$$x'_i = a \cos\theta \cos\Omega - b \sin\theta \sin\Omega + c_x \quad (5.3)$$

$$y'_i = a \cos\theta \sin\Omega + b \sin\theta \cos\Omega + c_y$$

for $i = 0, 1, 2, \dots, n - 1$.

Equation 5.3 defines an ellipse centred at (c_x, c_y) and lying at an orientation of Ω . Rearranging Equation 5.3 in terms of the centre point gives:

$$\begin{aligned} c_x &= x'_i - a \cos \theta \cos \Omega + b \sin \theta \sin \Omega \\ c_y &= y'_i - a \cos \theta \sin \Omega - b \sin \theta \cos \Omega \end{aligned} \quad (5.4)$$

for $i = 0, 1, 2, \dots, n - 1$.

The Hough Transform takes all points, (x_i, y_i) , on the boundary and solves Equation 5.4 for $0^\circ \leq \theta < 360^\circ$, a suitable range of Ω and appropriate values of a and b , each at specified intervals. The accumulator array is five-dimensional with ranges for c_x, c_y, a, b and Ω . Each element $A(c_x^k, c_y^l, a_p, b_q, \Omega_r)$ is initialised to zero. For every (c_x^k, c_y^l) solution of Equation 5.4 obtained, $A(c_x^k, c_y^l, a_p, b_q, \Omega_r)$ is incremented by 1. At the end of the process a value of M at position $A(c_x^k, c_y^l, a_p, b_q, \Omega_r)$ in the accumulator array should indicate that the corresponding ellipse is common to M points on the boundary. Clearly, the largest value of M indicates the parameter values for the best-fit ellipse to the boundary.

Computational Efficiency

The Hough Transform algorithm involves many calculations. Firstly, for every boundary pixel there is a search through all considered orientations, *i.e.* $0^\circ \leq \Omega < 360^\circ$ in steps of, say, 1° . For each Ω there is a search through all possible points on an ellipse, *i.e.* $0^\circ \leq \theta < 360^\circ$, in steps of, say, 1° . For each θ there is a search through all possible values of major-radius, a , in steps of, say, 1, of the ellipse considered and then for each a there is a search through all possible values of minor-radius, b , in steps of, say, 1, of that ellipse. For all boundary pixels and for all considered values of Ω, θ, a and b , the corresponding values of c_x and c_y are calculated.

An example to give an idea of the potential size of the calculations involved is given here. For a 256×256 image, a and b cannot exceed 128 if the ellipse is to be contained within the image. (In theory, it is possible that an image may contain part of a larger ellipse.) For n boundary pixels and the Ω and θ ranges being 360 in steps of 1° , there would be $360 \times 360 \times 128 \times 128 \times 2 \times n$ calculations. That is, $4,246,732,800 \times n$ calculations.

Finding the best fit ellipse of a set of co-ordinates, at any orientation, can be computationally very expensive. To minimise computer time and effort the following restrictions are imposed.

Firstly, ellipses are symmetrical. Therefore, orientations, Ω , of 0° to 360° lead to the same ellipses as are produced for Ω in 0° to 180° or -90° to 90° . Thus, the range of Ω considered may be halved without loss of solutions.

Secondly, consider the ellipse $f(c_x, c_y, a_1, b_1, \Omega)$ in Fig. 5.4(a) and the ellipse $f(c_x, c_y, a_2, b_2, \Omega)$ in Fig. 5.4(d), where $a_2 = b_1$ and $b_2 = a_1$. Rotating ellipse (a) by Ω (Fig. 5.4(b)) is the same as rotating ellipse (d) by $-(90 - \Omega)$. Similarly, rotating ellipse (a) by $-\Omega$ (Fig. 5.4(c)) is the same as rotating ellipse (d) by $(90 - \Omega)$. Therefore, if there are no restrictions on whether $a > b$ or vice versa, then the number of computations can be reduced by only considering positive (or only negative) angles of rotation, *i.e.* either $0^\circ \leq \Omega < 90^\circ$ or $-90^\circ \leq \Omega < 0^\circ$.

5.3.2 Hough Transform Results on Test Images

Fig. 5.5 is a test image which contains ellipses with differing values of c_x, c_y, a, b and Ω as listed in Table 5.1. The ellipses are shown as black boundaries on a white background.

The Hough Transform is applied to the image in Fig. 5.5. For all foreground pixels, the centre co-ordinates, (c_x, c_y) , of ellipses which might pass through the pixels are calculated using Equation 5.4 for a range of a and b , $0^\circ \leq \theta < 360^\circ$ and $0^\circ \leq \Omega \leq 90^\circ$,

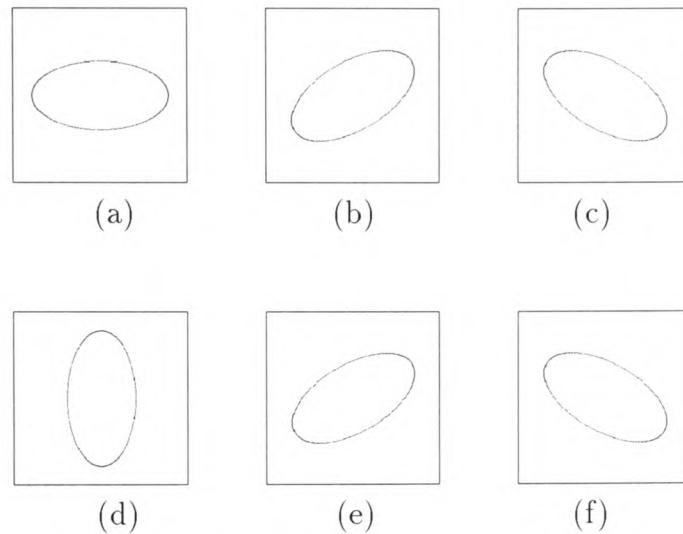


Figure 5.4: Orientations of ellipses.

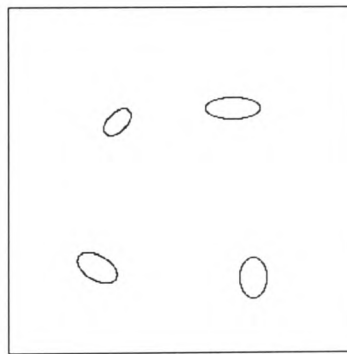


Figure 5.5: Test Ellipses.

each at specified intervals. Each c_x and c_y have been given to the nearest discrete value to give pixel location (c'_x, c'_y) and each corresponding $A(c'_x, c'_y, a, b, \Omega)$ in the accumulator array (which has been initialised to zero) is incremented by one. At the end of the process, the best-fit ellipse is found by searching for a maximum in the accumulator array. The maxima found for the four test ellipses in Fig. 5.5 are listed in Table 5.2. In each case, the best-fit ellipse indicated by $(c'_x, c'_y, a, b, \Omega)$ is a perfect match with the corresponding test ellipse in Table 5.1.

<i>Ellipse</i>	c_x	c_y	a	b	Ω	<i>No. pixels</i>
Ellipse 1	80	85	7	12	45°	76
Ellipse 2	65	192	16	9	30°	98
Ellipse 3	165	75	20	8	0°	100
Ellipse 4	180	200	10	15	0°	92

Table 5.1: Test Ellipses.

<i>Ellipse</i>	Ω search (step)	Maximum in accumulator	c'_x	c'_y	a	b	Ω
Ellipse 1	0° to 90° (1°)	356	80	85	7	12	45°
Ellipse 2	0° to 90° (1°)	360	65	192	16	9	30°
Ellipse 3	0° to 90° (1°)	360	165	75	20	8	0°
Ellipse 4	0° to 90° (1°)	360	180	200	10	15	0°

Table 5.2: Best fit ellipses indicated by a maximum in the accumulator array.

The results in Table 5.2, although completely accurate in yielding a perfect best-fit ellipse in terms of $(c'_x, c'_y, a, b, \Omega)$, highlight a feature of the Hough Transform in that the maxima found do not exactly match the number of boundary pixels. In theory, if a boundary contained, say, 100 pixels, the maximum in the accumulator array would be expected to be close to, and no more than, 100. In practice, the number of pixels supposedly lying on the best-fit ellipse is frequently much larger than the actual known number of points. This apparently misleading value is due to several calculations being rounded to map to the same pixel. Therefore, each pixel on an ellipse may contribute to an array cell more than once. An example of this effect is given in Table 5.3.

<i>Ellipse</i>	x	y	a	b	θ	Ω	c'_x	c'_y
Ellipse 3	169	83	20	8	77	0°	165	75
Ellipse 3	169	83	20	8	78	0°	165	75
Ellipse 3	169	83	20	8	79	0°	165	75

Table 5.3: Consequence of rounding in calculations for Equation 5.4.

For a given point (169, 83) on the boundary, the Hough Transform uses Equation 5.4 to calculate (c_x, c_y) , for a range of a , b and Ω spaced at specific intervals. For $\theta = 77^\circ$, 78° and 79° , (c_x, c_y) have been rounded to pixel location (165, 75). In this case, $A(165, 75, 20, 8, 0)$ has been incremented 3 times for a single boundary pixel, due to necessary rounding of (c_x, c_y) values.

5.3.3 Hough Transform Results on Finger Images

In Section 5.3.2 the Hough Transform for ellipses was applied to a test image. In this section, the same method is applied to MRI finger images.

The boundaries derived in Section 4.2.3 are, as a whole, not very elliptical. However, there are areas which may be approximated by ellipses. The head of the proximal phalanx is characteristically elliptical as is the joint side of the middle phalanx. Fig. 5.6 shows user-defined open curves derived from boundaries from slice 2 of two consecutive images of the same finger. (The open curves are taken from the closed curve boundaries in Fig. 5.8.) The number of pixels on the open curves are displayed in Table 5.4. The Hough Transform is applied to these open boundaries and the best-fit ellipses are shown in Table 5.5.

<i>Fig.</i>	<i>Bone</i>	<i>No. open curve pixels</i>
5.6(a)	Middle Phalanx (MP)	52
5.6(b)	Proximal Phalanx (PP)	102
5.6(c)	Middle Phalanx (MP)	50
5.6(d)	Proximal Phalanx (PP)	103

Table 5.4: Numbers of boundary pixels on an open boundary of finger bone.

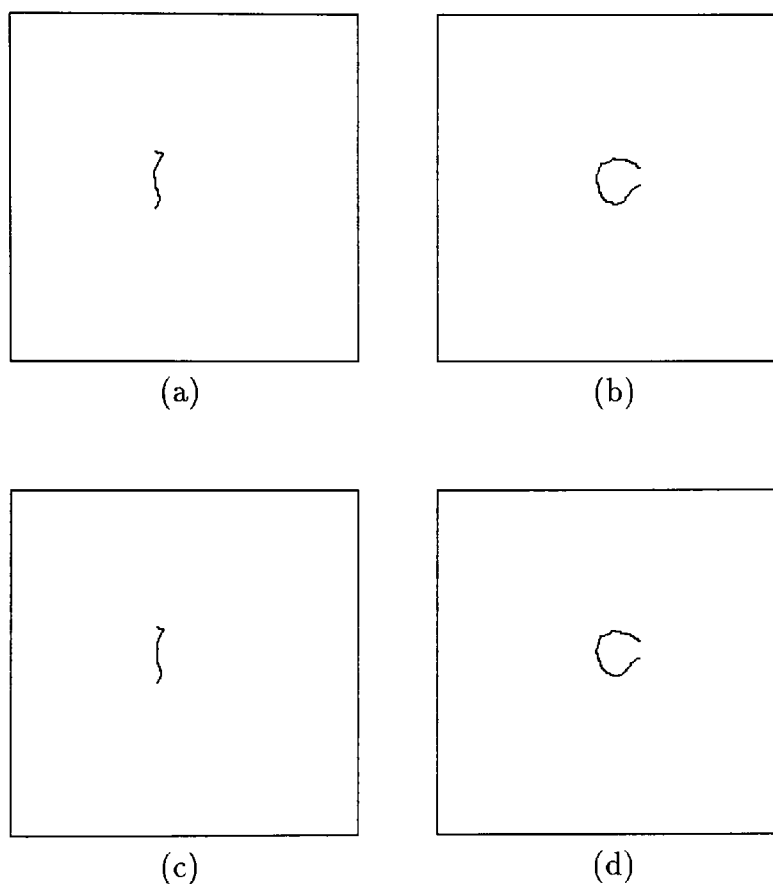


Figure 5.6: Open curves (a) first occasion middle phalanx (b) first occasion proximal phalanx (c) second occasion middle phalanx (d) second occasion proximal phalanx.

<i>Fig.</i>	<i>Bone</i>	<i>Ω range (step)</i>	<i>Maximum in accumulator</i>	c'_x	c'_y	a	b	Ω
5.6(a)	MP	0° to 90° (1)	100	114	118	8	17	8°
5.6(b)	PP	0° to 90° (1)	172	133	119	13	16	80°
			172	133	119	13	16	81°
5.6(c)	MP	0° to 90° (1)	114	115	117	8	18	7°
5.6(d)	PP	0° to 90° (1)	169	131	121	13	17	0°

Table 5.5: Best fit ellipses indicated by a maximum in the accumulator array.

For the proximal phalanx, the centres of the best-fit ellipses found in both images (Figs. 5.6(b) and 5.6(d)) are displaced from each other by 2 pixels in both the x - and y -direction. One ellipse lies on the vertical, while the other has been rotated so that

it almost lies on the horizontal. (For Fig. 5.6(b) there were two equally best-fitting ellipses.) In both images a is equal, but b differs by 1 pixel.

For the middle phalanx, the best-fit ellipses are displaced by 1 pixel in both the x - and y -direction with a being equal and b and Ω differing by 1 pixel and 1 degree respectively.

The original MRI images from which Fig. 5.6 were derived were taken such that there was a deliberate attempt at moving the finger by an intended 1 pixel, between the two scans. The results in Table 5.5 closely match our expectation of a 1 pixel mis-registration between the images. The difference in orientation of the proximal phalanx between the two images could be a result of bending at the articulated joint when the deliberate movement was introduced.

5.3.4 The Generalised Hough Transform

The nature of the boundaries derived in Section 4.2.3 cannot typically be represented by an analytic equation. However, an extension to the Hough Transform, known as the Generalised Hough Transform [Gonzalez92, Sonka96, Low91, Roach94], can be used to detect non-standard shapes in images.

The first stage of the Generalised Hough Transform is to define an arbitrarily chosen reference point (x_{ref}, y_{ref}) inside a boundary. Now each point, (x_i, y_i) , on a boundary can be described in terms of the distance, r , from the reference point, the angle, β , from the positive horizontal direction through (x_i, y_i) to the line joining (x_i, y_i) and (x_{ref}, y_{ref}) and the gradient, Ω , of the tangent at (x_i, y_i) . The geometrical relationships between (x_i, y_i) , (x_{ref}, y_{ref}) , r , β and Ω are illustrated in Fig. 5.7. In the discrete case, Ω is approximated by taking the direction (called orientation) from (x_i, y_i) to the next anti-clockwise adjacent pixel. Each point (x_i, y_i) on the boundary is related to the reference point (x_{ref}, y_{ref}) by Equation 5.5.

$$\begin{aligned} x_{ref} &= x_i + r \cos \beta \\ y_{ref} &= y_i + r \sin \beta \end{aligned} \quad (5.5)$$

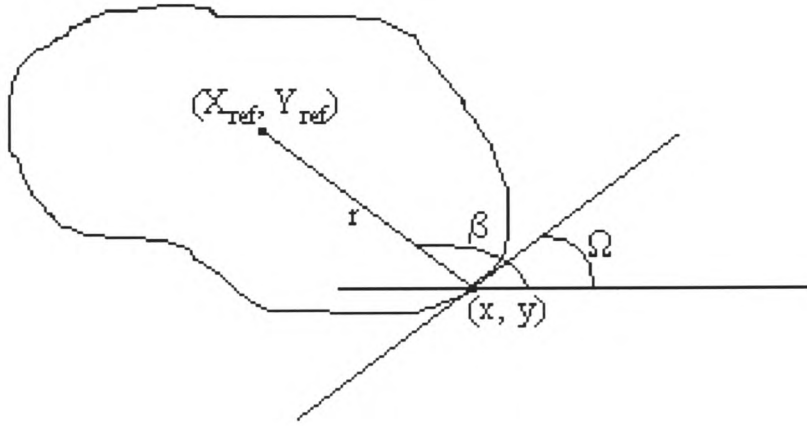


Figure 5.7: Geometry for R-Table entries.

Each r , β and Ω triplet found for each (x_i, y_i) are stored, grouped by Ω value, in a look-up table, called an *R-Table*. An example of an R-Table is given in Table 5.6.

Ω_1	$(r_{1,1}, \beta_{1,1}), (r_{1,2}, \beta_{1,2}), \dots, (r_{1,m}, \beta_{1,m_1})$
Ω_2	$(r_{2,1}, \beta_{2,1}), (r_{2,2}, \beta_{2,2}), \dots, (r_{2,m}, \beta_{2,m_2})$
Ω_3	$(r_{3,1}, \beta_{3,1}), (r_{3,2}, \beta_{3,2}), \dots, (r_{3,m}, \beta_{3,m_3})$
\vdots	\vdots
Ω_n	$(r_{n,1}, \beta_{n,1}), (r_{n,2}, \beta_{n,2}), \dots, (r_{n,m}, \beta_{n,m_n})$

Table 5.6: R-Table Example.

When the *R-Table* is formed it can be used to determine whether a shape in another image (called the *target*) matches (or partially matches) the *reference* image from which this *R-Table* has been derived. The basic steps of the Generalised Hough Transform are:

- Create an accumulator array in (x_{ref}, y_{ref}) .
- Find the orientation, Ω , at each point (x_i, y_i) on the boundary in the target image.
- For the value of Ω determined, find each corresponding pair of r and β values in the *R-Table*.
- For each Ω , r and β triplet obtained, solve Equation 5.5, and increment the accumulator array for every (x_{ref}, y_{ref}) obtained.

A large value in the accumulator array indicates that the shape, or part of it, has been found.

In the discussion so far it has been assumed that the orientation of the object is the same in both reference and target images. To allow for variations in orientation, a three-dimensional accumulator array must be created along with many sets of R-tables, one for each orientation, ϕ . Equation 5.5 is then modified to Equation 5.6.

$$\begin{aligned} x_{ref} &= x_i + r \cos(\beta + \phi) \\ y_{ref} &= y_i + r \sin(\beta + \phi) \end{aligned} \tag{5.6}$$

5.3.5 Generalised Hough Transform Results

More detailed descriptions of results can be found in Appendix D. The main findings are described here.

Consider the closed boundaries in Fig. 5.8. The boundaries are derived from the same slice of two consecutive images of the same finger. Further, between the two scans, a deliberate movement was introduced to try and mis-register the pair of images by a single pixel.

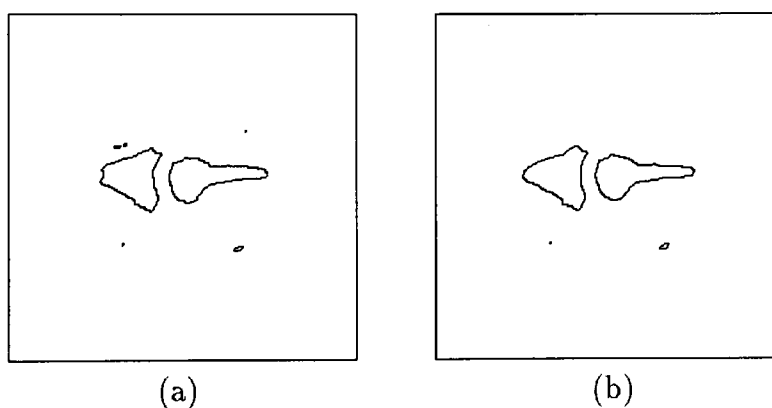


Figure 5.8: Closed boundaries of two MRI scans of a PIP joint.

To test the Generalised Hough Transform algorithm a single boundary, say, the proximal phalanx boundary in Fig. 5.8(a), is used as both the reference image and the target. As would be expected, in all such test cases the Generalised Hough Transform algorithm finds the same boundary with 100% matching pixels in exactly the same location.

The Generalised Hough Transform algorithm is now applied to the boundaries in both images in Fig. 5.8. One boundary is chosen to be the reference image from which the R-Table is created, and the same boundary in the other image is the target. The Generalised Hough Transform determines how many boundary pixels in the target image are the same as those in the reference image. Clearly, a high percentage of matching pixels implies that the boundaries are similar. Conversely, a small percentage

of matching pixels implies that the boundaries are not similar. In all cases, reference and target are reversed and the results compared. The displacement of the reference point (x_{ref}, y_{ref}) in the target image from the corresponding point in the reference image gives the relative translation and rotation required to register the images.

Table 5.7 shows the complete Generalised Hough Transform results for the boundaries in Fig. 5.8. (MP, here, stands for the middle phalanx and PP, for proximal phalanx.) The 100% matches in the test cases when a single boundary is used as both reference and target are included. Comparing the results when reference and target are reversed show complete accuracy in the number of pixels found to match between both images. The percentage of matching pixels differs minutely due to the slight difference in the total number of pixels on each boundary. More importantly, the relative translation between the two images is identical. This result shows that there is a possible mis-registration of a single pixel in the x -direction for the middle phalanx only.

Image used in R-Table			Fig. 5.8(a)			Fig. 5.8(b)		
Fig.	Bone	No. Coords	No.	%	Ref	No.	%	Ref
5.8(a)	MP	164	164	100	(x, y)	87	53.0	(x+1, y)
5.8(a)	PP	189	189	100	(x, y)	86	45.5	(x, y)
5.8(b)	MP	168	87	51.8	(x-1, y)	168	100	(x, y)
5.8(b)	PP	191	86	45.0	(x, y)	191	100	(x, y)

Table 5.7: Generalised Hough Transform results for Figs. 5.8(a) & 5.8(b).

The results in Table 5.7 are obtained for orientation, $\Omega = 0$. Comparing these results with small changes in orientation, two additional pixels were found to match on the proximal phalanx for $\Omega = 1^\circ$, *i.e.* a 1.1% increase, with a mis-registration of a single pixel in the y -direction.

Large changes in orientation of the boundaries in Fig. 5.8 will greatly reduce the number of matching pixels due to the approximate symmetry of the boundary about the axis of its greatest dimension. Applying the Generalised Hough Transform to open

curves should allow a wider range of orientations and a better number of matching pixels.

Table 5.8 shows the Generalised Hough Transform results for the open boundaries of Fig. 5.6. When a single open boundary is used as both reference and target the results give a perfect match of 100% matching pixels in exactly the same location, as was achieved in the closed curve case above. The results in this table indicate that the two bones are mis-registered in different directions. The middle phalanx is seen as being displaced by 1 pixel in the x -direction and the proximal phalanx by 1 pixel in the y -direction. Small changes in orientation do not improve these results.

Image used in R-Table			Fig. 5.6 top			Fig. 5.6 bottom		
Fig.	Bone	No. Coords	No.	%	Ref	No.	%	Ref
5.6(a)	MP	80	80	100	(x, y)	43	53.8	(x+1, y)
5.6(b)	PP	95	95	100	(x, y)	40	42.1	(x, y-1)
5.6(c)	MP	80	43	53.8	(x-1, y)	80	100	(x, y)
5.6(d)	PP	95	40	42.1	(x, y+1)	95	100	(x, y)

Table 5.8: Generalised Hough Transform results for Fig. 5.6.

The Generalised Hough Transform is applied to a variety of images and the results are detailed in Appendix D. In all experiments, the number of matching pixels for images of the same finger is, on average, 50%. A registration procedure would need to yield a very high percentage of matching pixels to give confidence in the results. The low percentages indicate a relatively poor accuracy of matching. This result reveals a fundamental characteristic nature of the boundaries being examined. The boundaries do appear, by eye, to be similar, *i.e.* they have the same characteristic shape, but there are actually many differences in locations of pixels along the boundary. Even the open curves do not result in the improvement expected.

5.4 Combining the Slices

A study of the bone boundaries derived in Section 4.2.3 shows that the derived boundaries from the equivalent slice of images taken over time are not always sufficiently similar for accurate registration. This is partly due to differences in the positioning of the finger on the different scanning occasions resulting in that slice corresponding to different cross-sections of the finger.

A new technique has been designed for this research to derive similar bone boundaries from images taken over time. Firstly, the less reliable soft tissue boundaries are removed from the images (explained in Section 6.2.3). Then, the bone boundaries from all four slices of an image are superimposed onto a new image (illustrated in Fig. 5.9(a)). The superimposed image is helpful in picturing the 2D slices derived from a volume. Filling the regions of the superimposed image (illustrated in Fig. 5.9(b)) creates a 2D image containing the maximum possible boundary shape for the bones across four slices. Finally, determining the boundary of this combined slice bone structure is quite simple using a scan-line algorithm (illustrated in Fig. 5.9(c)).

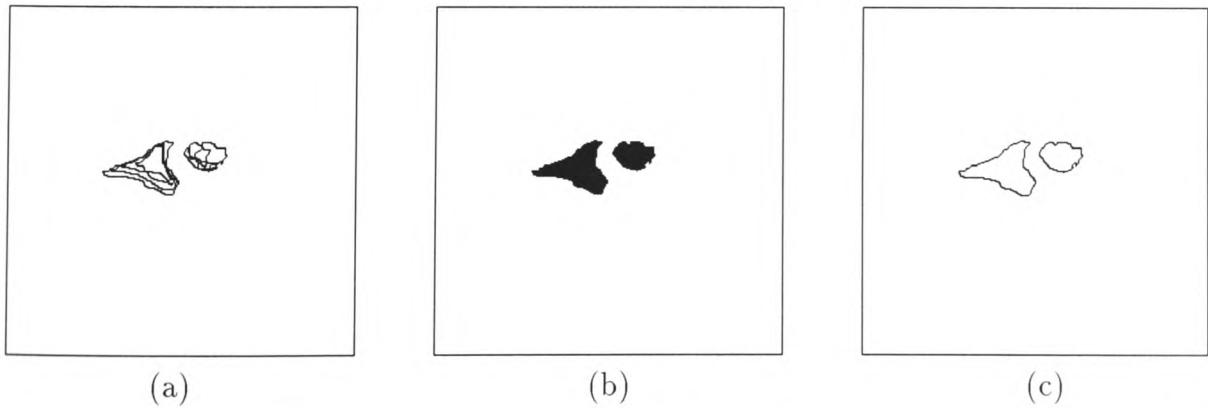


Figure 5.9: Combining the slices from Subject 1 (a) Merged image (b) Filled image (c) Detected boundary.

It is expected that the combined slice image boundaries derived from images of the same patient taken over time will be more similar and will produce better registration results than those obtained for the individual slices. This is because the combined slice boundaries are generated from a four-slice volume and will, therefore, contain less movement and/or positional error than individual slices.

The combined slice algorithm is applied to images from 5 subjects, taken on 2 occasions, illustrated in Figs. 5.10 to 5.14. The red pixels on these images illustrate the user-selected open curves used for the Hough Transform.

The search for registration is then made by applying the Hough Transform to a reference image from each subject (*i.e.* first occasion, T2-weighted image). Table 5.9 lists the derived best-fit ellipses for each of the five subjects.

The resulting best-fit ellipse(s) are then fitted to the open curves in the other images. The displacement of the ellipses between images of the same finger provide the rotation and translation necessary to register the images. Tables 5.10 to 5.14 show the best-fit ellipses for each of the five subjects respectively. The best-fit ellipses are listed in the top line of each section of each table. The results for fitting ellipses to the boundaries are listed in the tables and grouped by bone boundary. Fully worked examples are given in Chapter 6 and an analysis of the results is given in Section 6.3.

Particular problems with the results for the proximal phalanx boundary (explained in Section 6.3) warrant the selection of narrower open curves. The Hough Transform is re-applied to narrower proximal phalanx curves (illustrated by red pixels in Figs. 5.15 to 5.19) and the results are listed under “Narrower open curve results” in each table. In four out of five subjects, the narrower open curves produce a higher percentage of matching pixels. In some subjects, the percentage nearly doubles.

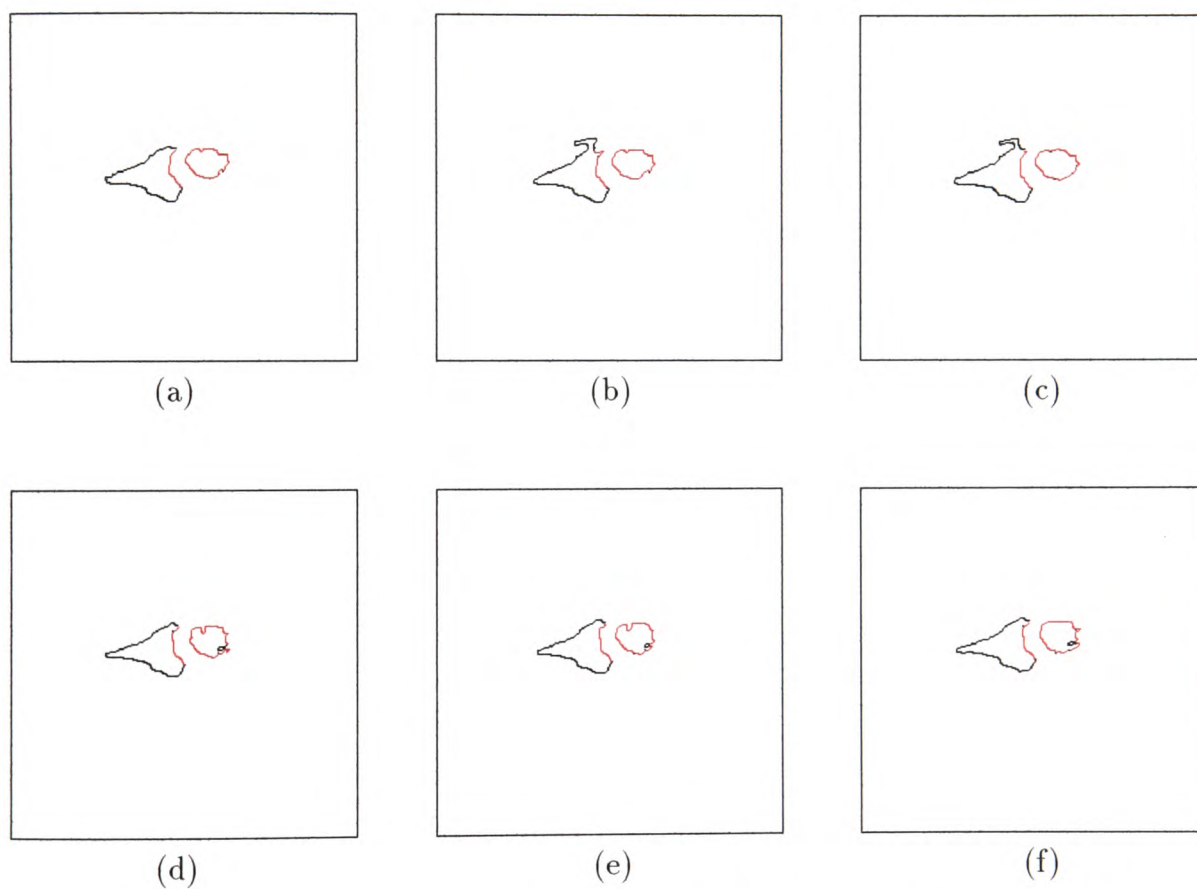


Figure 5.10: Open curves on combined slice boundaries for Subject 1 (a) first occasion T2-weighted (b) first occasion PD-weighted (c) first occasion T1-weighted (d) second occasion T2-weighted (e) second occasion PD-weighted (f) second occasion T1-weighted.

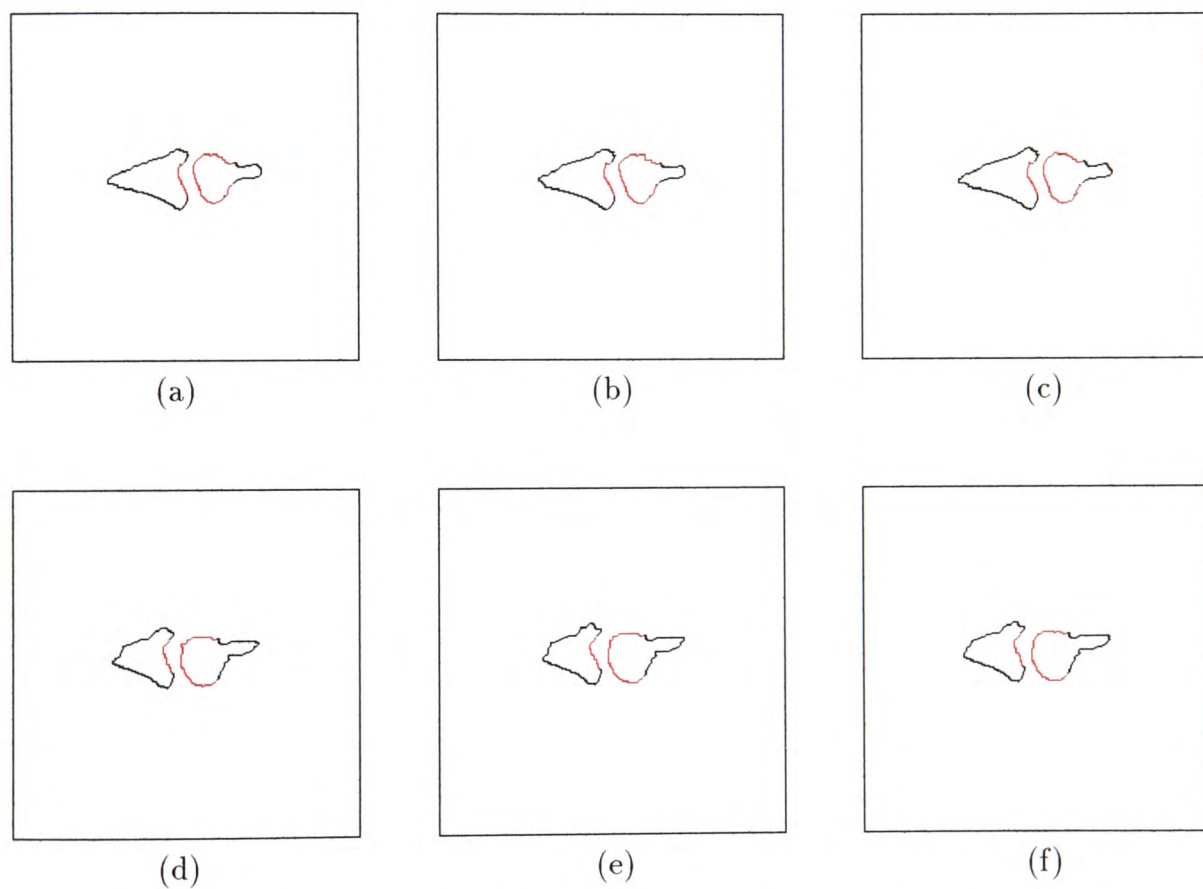


Figure 5.11: Open curves on combined slice boundaries for Subject 2 (a) first occasion T2-weighted (b) first occasion PD-weighted (c) first occasion T1-weighted (d) second occasion T2-weighted (e) second occasion PD-weighted (f) second occasion T1-weighted.

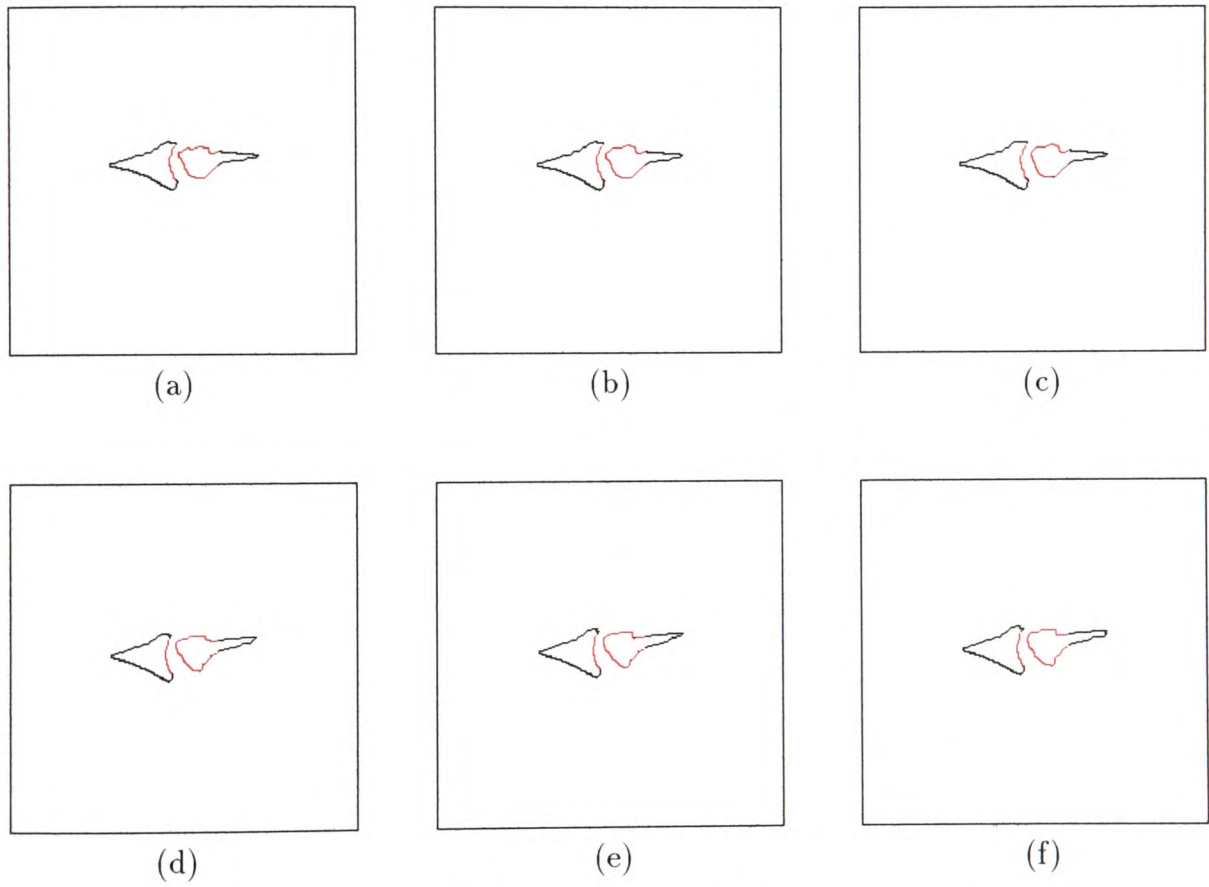


Figure 5.12: Open curves on combined slice boundaries for Subject 3 (a) first occasion T2-weighted (b) first occasion PD-weighted (c) first occasion T1-weighted (d) second occasion T2-weighted (e) second occasion PD-weighted (f) second occasion T1-weighted.

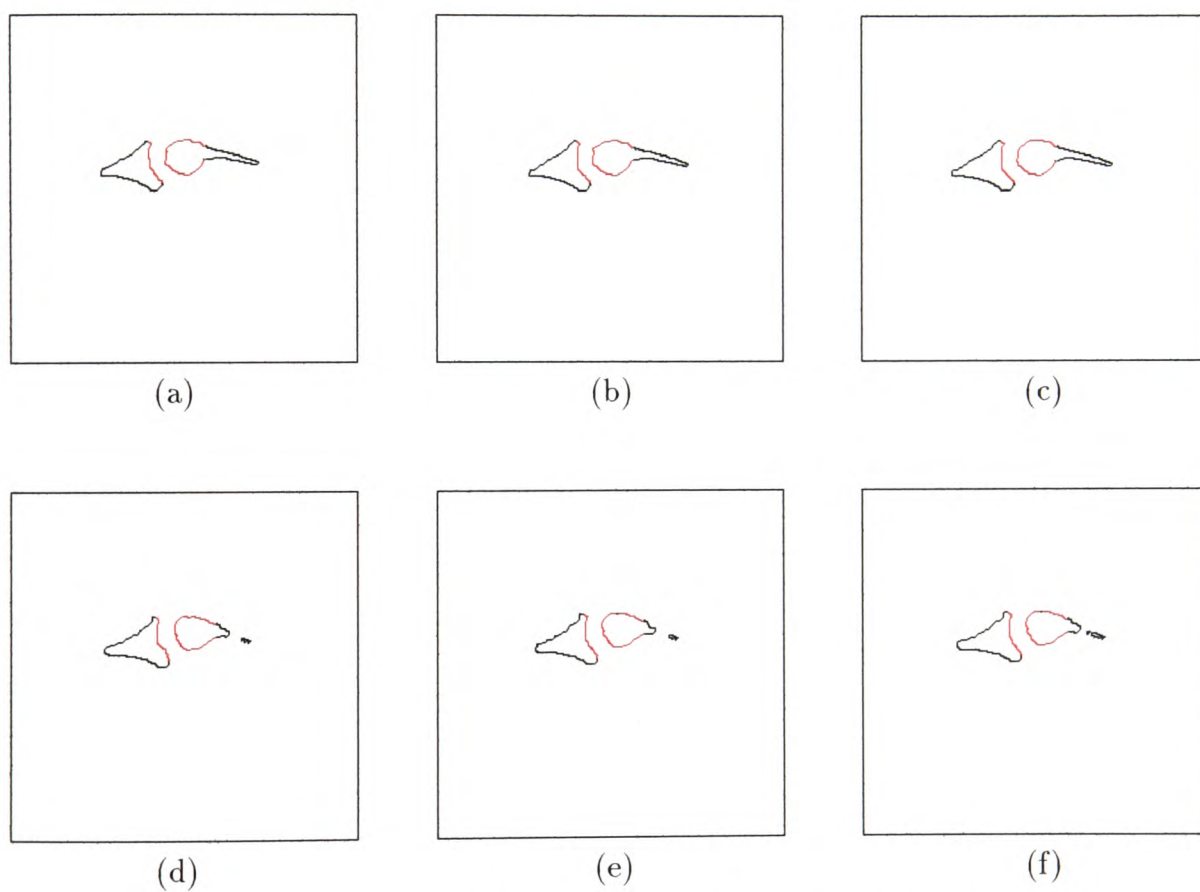


Figure 5.13: Open curves on combined slice boundaries for Subject 4 (a) first occasion T2-weighted (b) first occasion PD-weighted (c) first occasion T1-weighted (d) second occasion T2-weighted (e) second occasion PD-weighted (f) second occasion T1-weighted.

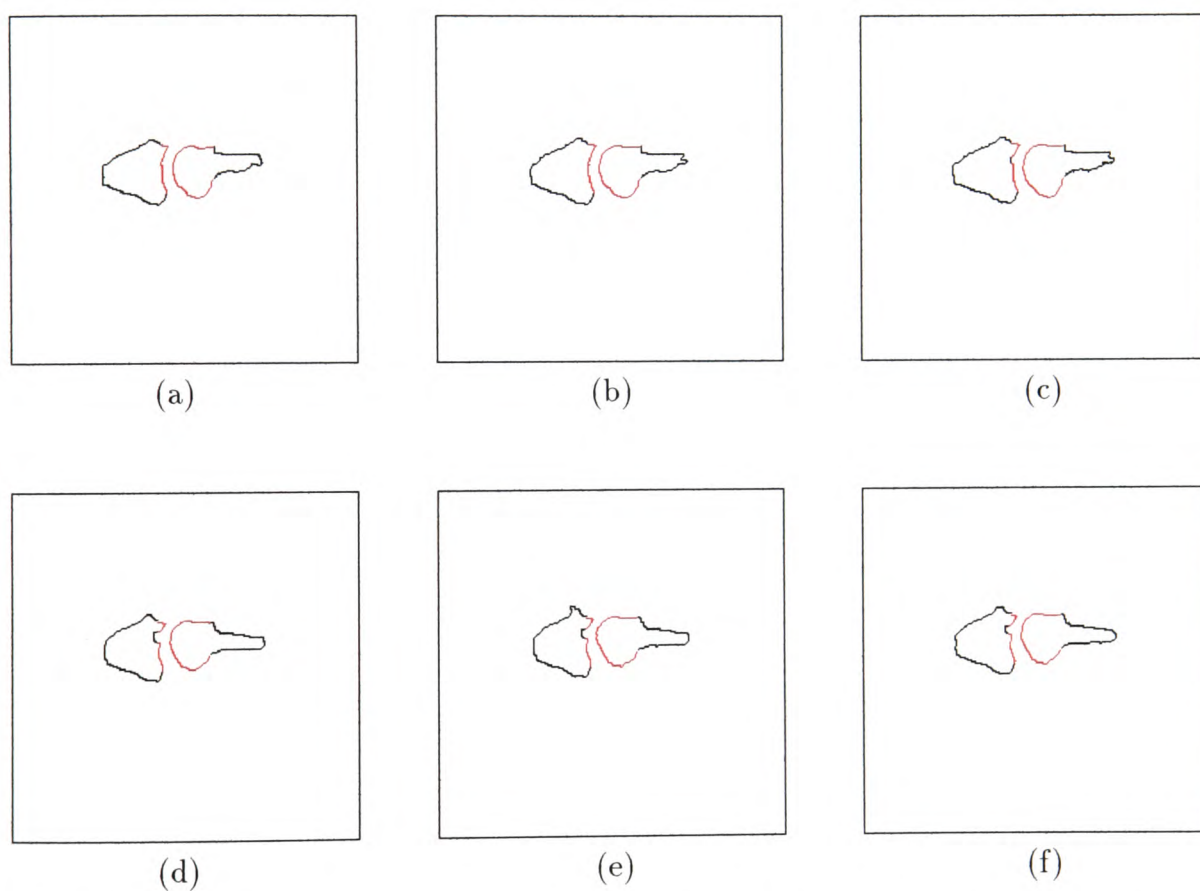


Figure 5.14: Open curves on combined slice boundaries for Subject 5 (a) first occasion T2-weighted (b) first occasion PD-weighted (c) first occasion T1-weighted (d) second occasion T2-weighted (e) second occasion PD-weighted (f) second occasion T1-weighted.

<i>Subject</i>	<i>Bone</i>	<i>cx</i>	<i>cy</i>	<i>a</i>	<i>b</i>	Ω	<i>% match</i>
1	MP	129	112	14	11	76	65
1	MP	129	111	14	11	89, 90	65
2	MP	135	124	16	8	57	87
3	MP	132	117	17	12	66	80
4	MP	115	107	17	11	66, 69	74
5	MP	124	109	11	22	9	72
1	PP	145	109	13	11	29	49
2	PP	150	121	12	18	0	54
3	PP	141	114	11	11	0 - 90	45
4	PP	130	104	13	14	79, 80	60
5	PP	136	114	19	15	71-72, 77	63
<i>Narrower open curve results</i>							
1	PP	140	115	9	3	33, 34	79
2	PP	149	121	11	18	0, 1	46
3	PP	136	114	12	7	58, 59	62
4	PP	127	104	12	11	61	72
5	PP	132	111	11	16	6	86

Table 5.9: Hough Transform best fit ellipses for 5 subjects.

<i>Bone</i>	<i>Weight</i>	<i>Occasion</i>	<i>cx</i>	<i>cy</i>	<i>a</i>	<i>b</i>	Ω	<i>% match</i>
MP	T2	1	129	112	14	11	76	65
MP	T2	1	129	111	14	11	89, 90	65
MP	PD	1	129	113	14	11	76	59
MP	PD	1	129	112	14	11	89, 90	59
MP	T1	1	130	113	14	11	71	74
MP	T2	2	131	112	14	11	75, 76	64
MP	PD	2	131	112	14	11	75, 76	60
MP	T1	2	131	112	14	11	72-74	64
PP	T2	1	145	109	13	11	29	49
PP	PD	1	146	109	13	11	2-4	39
PP	T1	1	145	109	13	11	9-10, 29	43
PP	T2	2	148	110	13	11	2	47
PP	PD	2	148	110	13	11	2	48
PP	T1	2	146	110	13	11	29	42
PP	T1	2	147	110	13	11	29	42
<i>Narrower open curve results</i>								
PP	T2	1	140	115	9	3	33, 34	79
PP	PD	1	140	115	9	3	33	78
PP	T1	1	144	117	9	3	13	79
PP	T2	2	145	117	9	3	18, 19	79
PP	PD	2	145	117	9	3	18, 19	78
PP	T1	2	145	118	9	3	13, 16 - 19	68
PP	T1	2	146	118	9	3	13	68

Table 5.10: Subject 1 Hough Transform results.

<i>Bone</i>	<i>Occasion</i>	<i>Weight</i>	<i>cx</i>	<i>cy</i>	<i>a</i>	<i>b</i>	Ω	<i>% match</i>
MP	1	T2	135	124	16	8	57	87
MP	1	PD	135	123	16	8	51	73
MP	1	T1	135	123	16	8	51	73
MP	2	T2	122	123	16	8	66	73
MP	2	PD	124	124	16	8	45	68
MP	2	PD	123	124	16	8	53	68
MP	2	PD	123	125	16	8	53	68
MP	2	T1	124	124	16	8	51	63
MP	2	T1	123	124	16	8	57-59	63
MP	2	T1	122	123	16	8	66	63
MP	2	T1	121	120	16	8	71	63
PP	1	T2	150	121	12	18	0	54
PP	1	PD	150	121	12	18	3	48
PP	1	T1	150	121	12	18	1	49
PP	2	T2	137	124	12	18	0	44
PP	2	PD	137	123	12	18	0	47
PP	2	T1	137	124	12	18	0	49
<i>Narrower open curve results</i>								
PP	1	T2	149	121	11	18	0, 1	46
PP	1	PD	149	121	11	18	1	44
PP	1	T1	149	121	11	18	3	51
PP	2	T2	136	123	11	18	1	45
PP	2	PD	136	123	11	18	1	55
PP	2	T1	136	123	11	18	1	54

Table 5.11: Subject 2 Hough Transform results.

<i>Bone</i>	<i>Occasion</i>	<i>Weight</i>	<i>cx</i>	<i>cy</i>	<i>a</i>	<i>b</i>	Ω	<i>% match</i>
MP	1	T2	132	117	17	12	66	80
MP	1	PD	132	116	17	12	69-71	83
MP	1	T1	132	116	17	12	70-71	76
MP	2	T2	128	128	17	12	66	87
MP	2	T2	128	129	17	12	66	87
MP	2	T2	127	125	17	12	88-90	87
MP	2	PD	128	128	17	12	66	87
MP	2	PD	127	125	17	12	82	87
MP	2	PD	127	124	17	12	88-90	87
MP	2	T1	128	128	17	12	66	83
PP	1	T2	141	114	11	11	0 - 90	45
PP	1	PD	141	114	11	11	0 - 90	41
PP	1	T1	141	114	11	11	0 - 90	40
PP	2	T2	137	122	11	11	0 - 90	35
PP	2	PD	137	122	11	11	0 - 90	33
PP	2	T1	137	122	11	11	0 - 90	27
<i>Narrower open curve results</i>								
PP	1	T2	136	114	12	7	58, 59	62
PP	1	PD	136	114	12	7	61	65
PP	1	T1	136	114	12	7	68	74
PP	2	T2	133	123	12	7	46	56
PP	2	PD	132	123	12	7	55	63
PP	2	T1	132	124	12	7	60	65

Table 5.12: Subject 3 Hough Transform results.

<i>Bone</i>	<i>Occasion</i>	<i>Weight</i>	<i>cx</i>	<i>cy</i>	<i>a</i>	<i>b</i>	Ω	<i>% match</i>
MP	1	T2	115	107	17	11	66, 69	74
MP	1	PD	116	108	17	11	63	64
MP	1	PD	115	106	17	11	75	64
MP	1	PD	115	105	17	11	79, 81	64
MP	1	T1	116	108	17	11	63	66
MP	1	T1	115	106	17	11	75	66
MP	1	T1	115	105	17	11	79, 81	66
MP	2	T2	121	106	17	11	63	58
MP	2	T2	120	103	17	11	81	58
MP	2	PD	120	105	17	11	77	73
MP	2	T1	121	108	17	11	63	74
MP	2	T1	120	105	17	11	77, 79	74
PP	1	T2	130	104	13	14	79, 80	60
PP	1	PD	129	104	13	14	69, 85	53
PP	1	PD	130	104	13	14	79, 80	53
PP	1	T1	130	103	13	14	69, 71-75, 79-80	58
PP	1	T1	130	104	13	14	74, 82-85	58
PP	1	T1	129	104	13	14	85	58
PP	2	T2	135	101	13	14	21	47
PP	2	PD	135	101	13	14	21-25	47
PP	2	T1	135	101	13	14	21, 35-39	46
<i>Narrower open curve results</i>								
PP	1	T2	127	104	12	11	61	72
PP	1	PD	127	104	12	11	61	62
PP	1	T1	127	104	12	11	52, 61	62
PP	2	T2	133	101	12	11	47 - 50	56
PP	2	PD	133	101	12	11	42, 43	55
PP	2	T1	133	101	12	11	42, 43	55

Table 5.13: Subject 4 Hough Transform results.

<i>Bone</i>	<i>Occasion</i>	<i>Weight</i>	<i>cx</i>	<i>cy</i>	<i>a</i>	<i>b</i>	Ω	<i>% match</i>
MP	1	T2	124	109	11	22	9	72
MP	1	PD	124	108	11	22	13	67
MP	1	T1	124	110	11	22	8	70
MP	2	T2	120	113	11	22	0	53
MP	2	T2	120	112	11	22	2	53
MP	2	PD	121	107	11	22	12, 13	55
MP	2	PD	121	106	11	22	14, 15	55
MP	2	T1	121	108	11	22	12	56
PP	1	T2	136	114	19	15	71, 72, 77	63
PP	1	PD	136	114	19	15	72	60
PP	1	T1	136	114	19	15	75	56
PP	2	T2	133	111	19	15	66	54
PP	2	PD	133	111	19	15	57, 67	45
PP	2	PD	133	110	19	15	85	45
PP	2	T1	133	111	19	15	69	56
<i>Narrower open curve results</i>								
PP	1	T2	132	111	11	16	6	86
PP	1	PD	131	111	11	16	3 - 5	67
PP	1	T1	132	111	11	16	6, 9	71
PP	2	T2	129	109	11	16	0	73
PP	2	PD	129	109	11	16	0	57
PP	2	T1	129	109	11	16	0	68

Table 5.14: Subject 5 Hough Transform results.

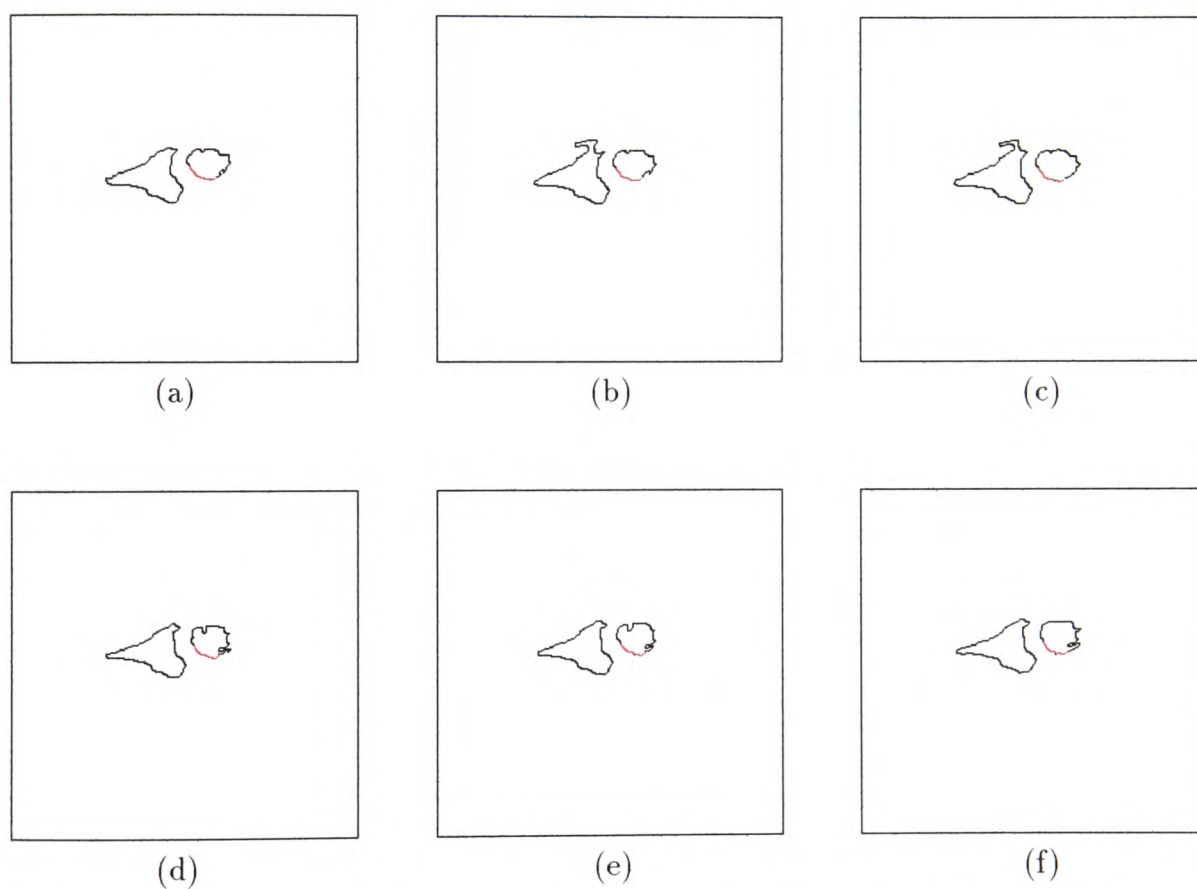


Figure 5.15: Narrower open curves on combined slice boundaries: Subject 1 (a) first occasion T2-weighted proximal phalanx (b) first occasion PD-weighted proximal phalanx (c) first occasion T1-weighted proximal phalanx (d) second occasion T2-weighted proximal phalanx (e) second occasion PD-weighted proximal phalanx (f) second occasion T1-weighted proximal phalanx.

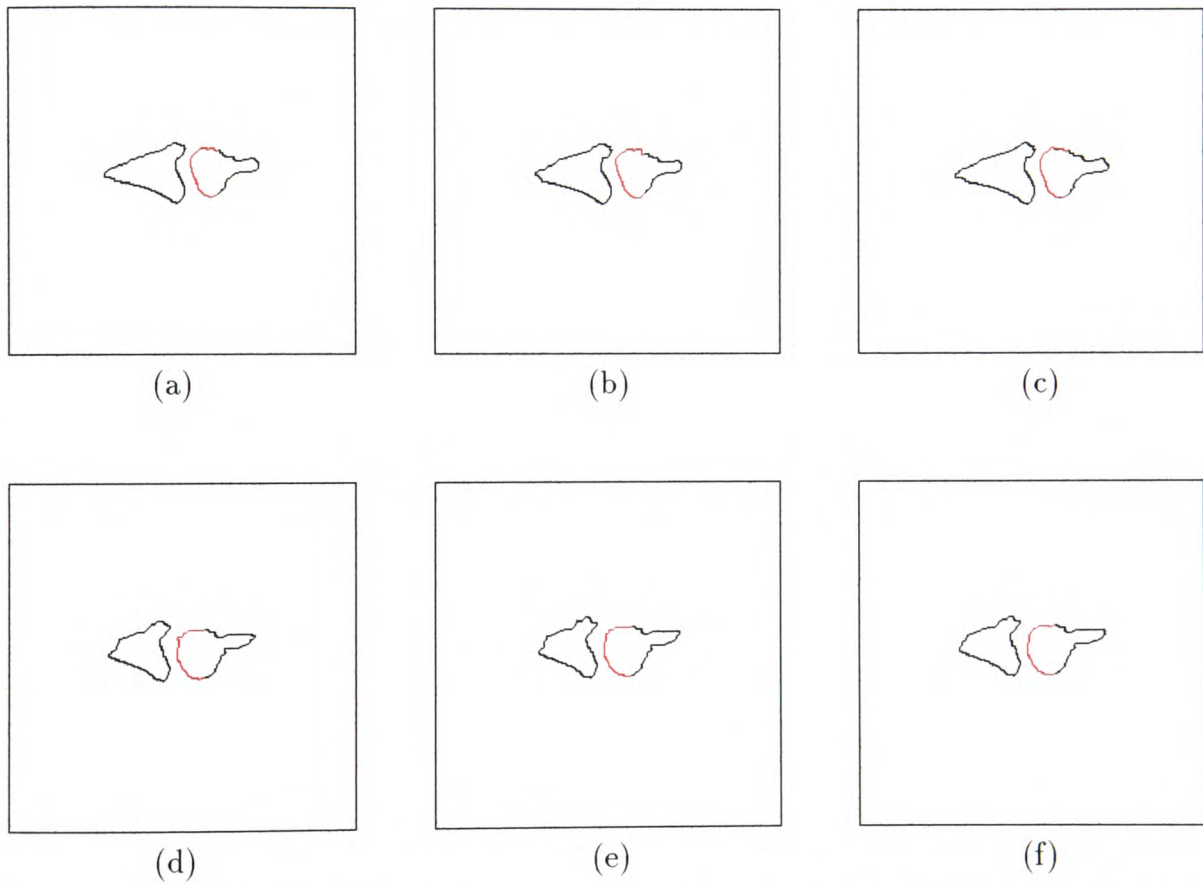


Figure 5.16: Narrower open curves on combined slice boundaries: Subject 2 (a) first occasion T2-weighted proximal phalanx (b) first occasion PD-weighted proximal phalanx (c) first occasion T1-weighted proximal phalanx (d) second occasion T2-weighted proximal phalanx (e) second occasion PD-weighted proximal phalanx (f) second occasion T1-weighted proximal phalanx.

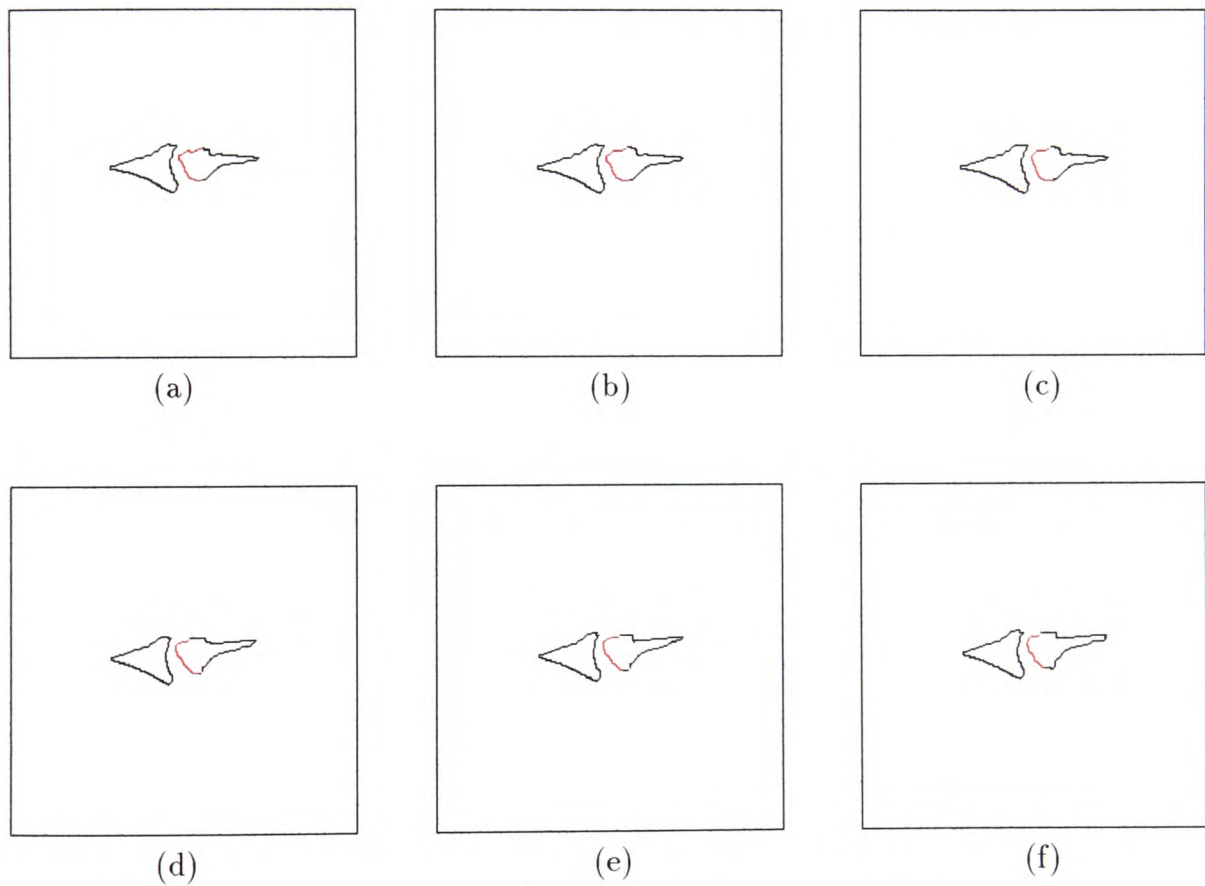


Figure 5.17: Narrower open curves on combined slice boundaries: Subject 3 (a) first occasion T2-weighted proximal phalanx (b) first occasion PD-weighted proximal phalanx (c) first occasion T1-weighted proximal phalanx (d) second occasion T2-weighted proximal phalanx (e) second occasion PD-weighted proximal phalanx (f) second occasion T1-weighted proximal phalanx.

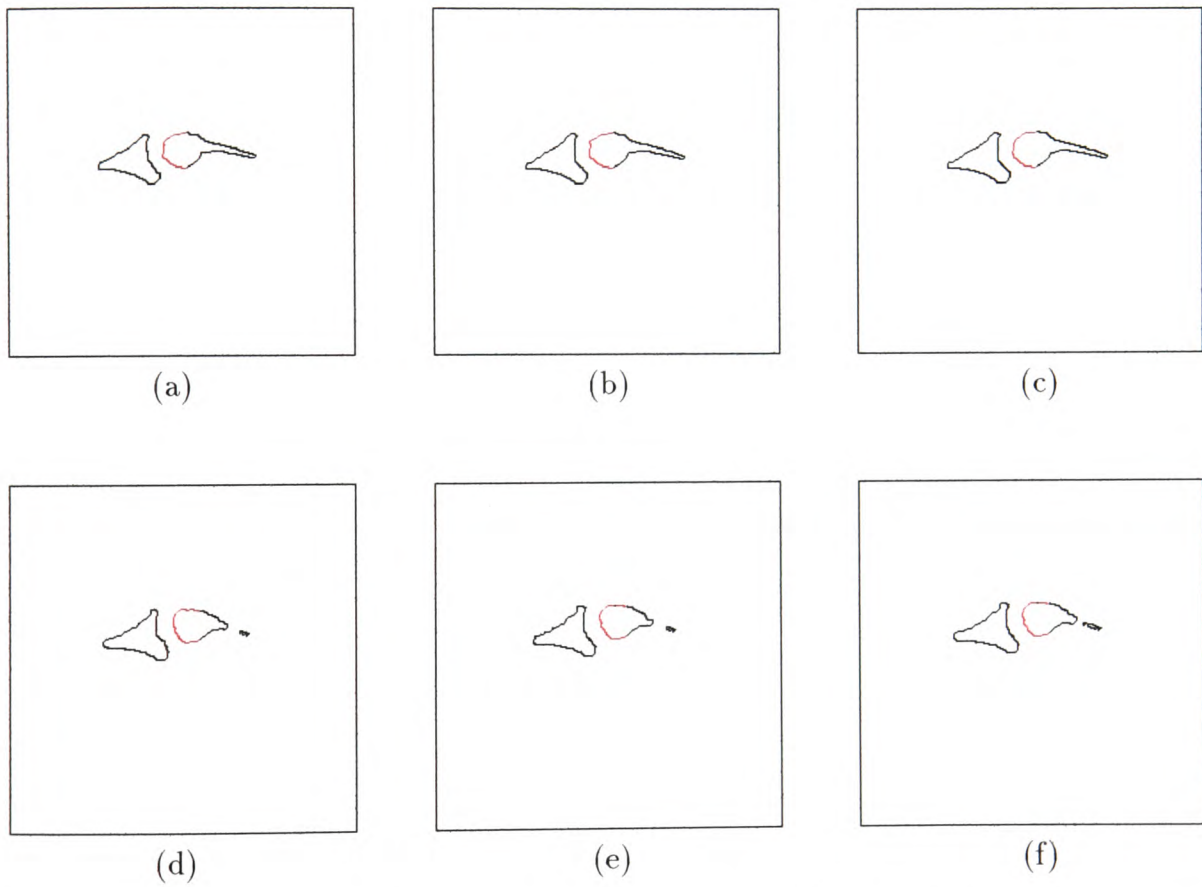


Figure 5.18: Narrower open curves on combined slice boundaries: Subject 4 (a) first occasion T2-weighted proximal phalanx (b) first occasion PD-weighted proximal phalanx (c) first occasion T1-weighted proximal phalanx (d) second occasion T2-weighted proximal phalanx (e) second occasion PD-weighted proximal phalanx (f) second occasion T1-weighted proximal phalanx.

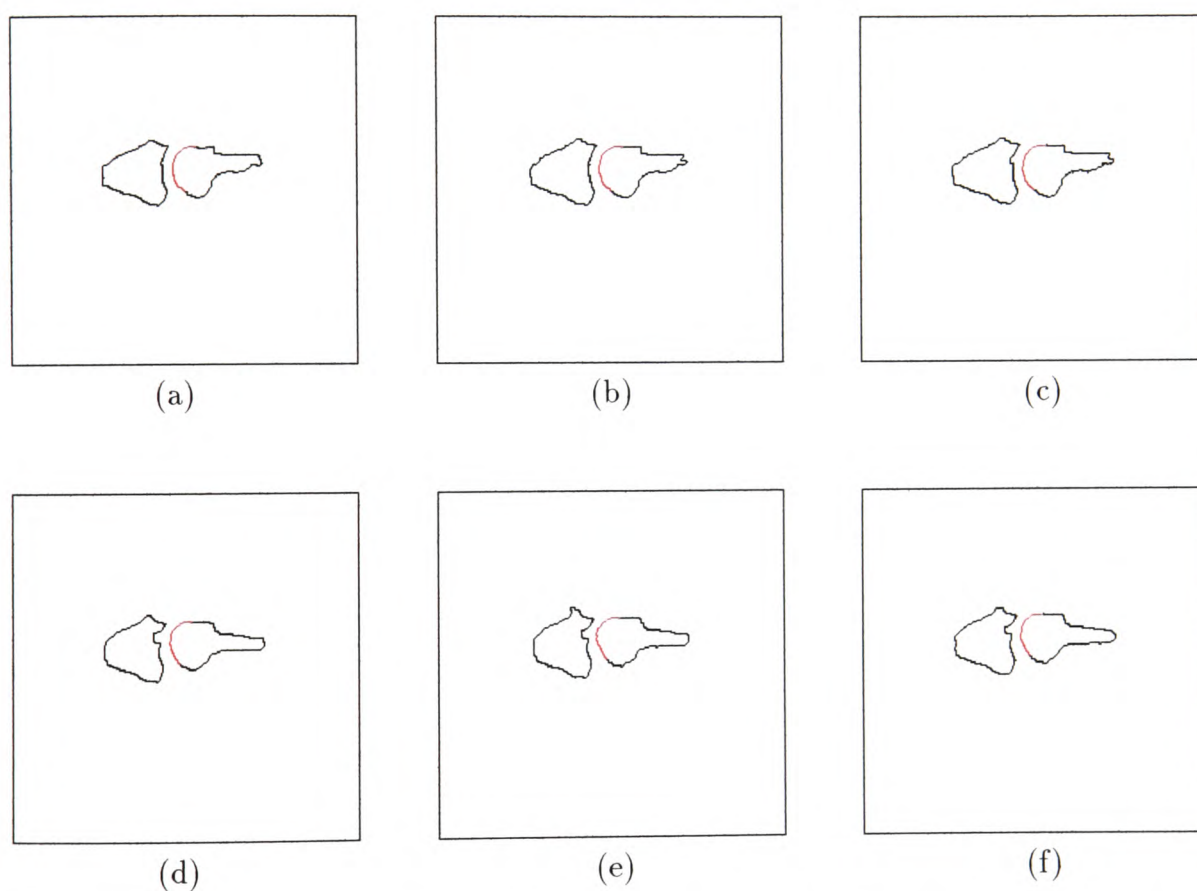


Figure 5.19: Narrower open curves on combined slice boundaries: Subject 5 (a) first occasion T2-weighted proximal phalanx (b) first occasion PD-weighted proximal phalanx (c) first occasion T1-weighted proximal phalanx (d) second occasion T2-weighted proximal phalanx (e) second occasion PD-weighted proximal phalanx (f) second occasion T1-weighted proximal phalanx.

5.5 Moments

The identification and registration of objects in images can be aided by the use of measures of ‘shape’. Moments are a descriptive technique and can be applied to grey level images or boundaries. Moments have been used in the available literature to register images by aligning their principal axes [Kovacic89, Bajcsy89], and for characterizing polygons in terms of the principal axes [Tough84, Tough88]. Moments are very useful in the application of pattern recognition [Bailey96, Mamistvalov98, Rothe96]. This section discusses the usefulness of moments in aiding the registration of MRI finger images.

For a 2D continuous function $f(x, y)$, the moment of order $(p + q)$ is defined as:

$$m_{pq} = \int_{-\infty}^{\infty} \int_{-\infty}^{\infty} x^p y^q f(x, y) dx dy$$

for $p, q = 0, 1, 2, \dots$

For a digitized image, the moments are:

$$\sum_{i=-\infty}^{\infty} \sum_{j=-\infty}^{\infty} i^p j^q f(i, j)$$

for $p, q = 0, 1, 2, \dots$

A set of seven invariant moments can be derived from these moments. These moments are invariant to translation, rotation, and scale change. The invariant moments are extremely useful in applications of pattern recognition. In this application, a rotational and translational offset is required for registration, therefore, invariant moments are not pursued in this project.

Moments can be applied to the original MRI finger images. However, as with the Superimposing method explained in Section 5.2, it is difficult to assess the accuracy of the results. Instead, moments are applied to filled boundary images as derived in Section 5.4. (An alternative method is to determine moments for the boundaries themselves.) An example of a combined slice filled image is given in Fig. 5.20.

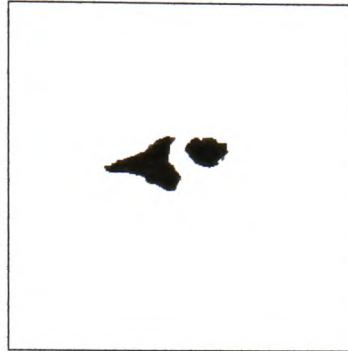


Figure 5.20: A combined slice filled image.

The centroid, (x_c, y_c) , can be used for translational registration, where

$$x_c = \frac{m_{10}}{m_{00}}, \quad y_c = \frac{m_{01}}{m_{00}}.$$

Results vary depending on how far forward the finger is positioned. Fig. 5.21 gives a typical example of the location of the centroid and subsequent translational registration for two images of the same finger taken over time.

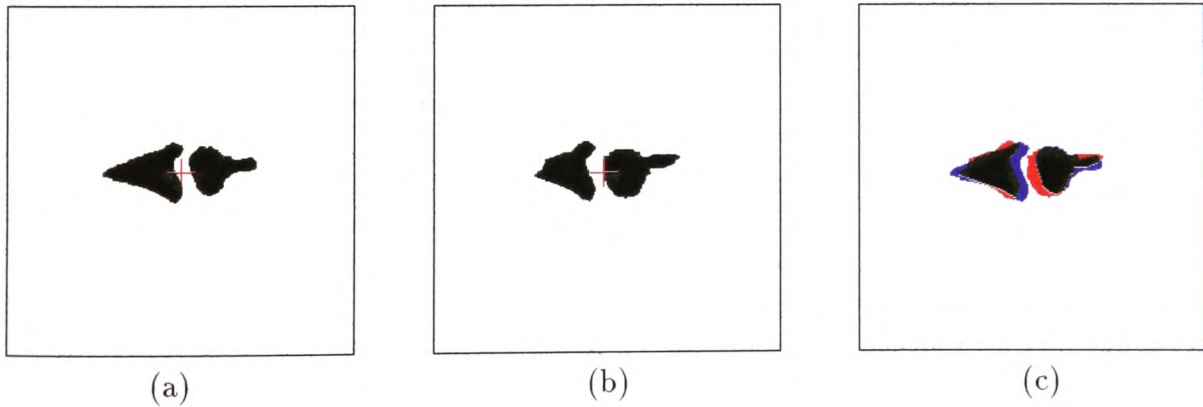


Figure 5.21: (a) & (b) Location of centroid on two images of the same finger (c) mis-registration of the two images.

The centroid appears to locate the centre of the field of view. Fig. 5.21(b) shows that incorrect positioning on a second occasion can lead to gross mis-registrations. A similar result will hold if the centroid is calculated for each bone separately, as the size of each bone differs considerably due to incorrect positioning for scanning.

It is possible to apply moments to user-selected open regions on the images. However, as discussed in relation to Fourier Descriptors in Section 4.3.4, if the open regions are not the same, matching based on the centroid could lead to gross mis-registrations.

The alternative method of determining moments for a boundary leads to similar results and the same conclusion as the registration is again based on the centroid of a user-defined open region. These findings confirm again the uniqueness of the MRI finger registration problem in comparison to the more common brain/head registration problem where the use of moments for registration has been successful.

The restrictions of moments and principal axes, as applied to MRI finger images, means that the results obtained by the Hough Transform fitting of ellipses to bone boundaries is by far the most useful method for registering MRI finger images.

5.6 Conclusions

In this chapter various registration methods are examined and applied to MRI finger images.

The sum of absolute values of differences approach to registration gives local results which are inconsistent with global results. To combine local results would mean distorting one image to fit another which will result in the loss of important synovium information.

Superimposing images is useful for registration but only when the tolerance level is raised to around 400. This problem is eliminated when derived black and white images are superimposed as there is no requirement for a tolerance level. Superimposing two similarly derived images results in reasonable registration accuracy. However, the

features in these images do not always correspond to the same part of tissue and are therefore not reliable enough on their own for registration.

The Hough Transform is extremely accurate in locating a test ellipse, in terms of its centre, (c_x, c_y) , major (a) and minor-radii (b) and its orientation (Ω). The number of pixels reported to lie on a test ellipse is typically much higher than in reality. This is due to the discretization of the parameter space which naturally incurs rounding error.

The boundaries derived in Section 4.2.3 are not particularly elliptical in general shape. However, certain open curves on the boundary are generally elliptic, *e.g.* the head of the proximal phalanx and the joint side of the middle phalanx. The Hough Transform can be used successfully to find a best-fitting ellipse, at any orientation, to selected open curves on the boundary. The discretization of the parameter space yields rounding error again. Despite these difficulties, the displacement of the ellipse parameters between two images can give the relative rotation and translation required to register the images.

The Generalised Hough Transform is completely accurate in its ability to match 100% pixels in exactly the same location when a single image boundary, or an open curve, is used as both reference and target image for a test case.

In the non-test case, the Generalised Hough Transform is completely accurate in finding the same number of matching pixels, with the same displacement between the two boundaries (or open curves) when reference and target are reversed.

However, in all experiments, the number of matching pixels between two images of the same finger is, on average, 50%. A very high number of matching pixels would give confidence in the registration procedure. This relatively poor accuracy of matching reveals a fundamental characteristic nature of these boundaries. Although, by eye, the two boundaries appear almost identical, *i.e.* there is a similar characteristic shape, there must be many differences in actual positions of pixels. This finding guides the author's approach to registration.

Results from the fitting of ellipses to the derived boundaries leads to a novel approach of combining the slices. The combined slice effect creates image boundaries that appear more similar over time than do corresponding single slices. Applying the Hough Transform to such images produces better registration results.

The application of moments to combined slice images is very sensitive to finger positioning prior to scanning. The centroid of an image could be useful for translational registration. However, incorrect positioning for scanning, over time, can lead to gross mis-registrations. Applying moments to user-selected open regions of the images is possible, but if the open regions are not the same, which is highly likely, then matching based on centroid could lead to a mis-registration.

The Hough Transform fitting of ellipses to open curves is by far the most reliable method for the registration of MRI finger images. Care must be taken over selecting the open region, but differences in the open regions are not as critical for the Hough Transform as for centroid matching. This is due to the ellipse being fitted to a fixed boundary in the Hough Transform as opposed to using moments where the centroid can move as the open region varies in size.

In Chapter 6, the proposed registration system for MRI finger images is described. In this system, the Hough Transform is used to determine the parameters required to register a pair of images.

Chapter 6

The Proposed Registration System, Analysis and Conclusions

This chapter details the proposed system for the registration of serially acquired medical images. As stated earlier, the particular application of this system is intra-patient analysis of MRI finger images. The purpose of the registration of MRI finger images is to aid clinicians' understanding of rheumatic disease.

6.1 The System

The final system for the registration of MRI finger images is composed of three stages. Firstly, the original images are processed to locate what the author considers to be the best features in MRI finger images to be used in the registration process. These features are located via a combination of standard techniques and also new techniques derived for this research. Secondly, a search for registration is made. The Hough Transform is used to find the best-fit ellipse to boundaries in the processed images. The displacement of the best-fit ellipse between images of the same patient provides the rotation and translation required to register those images. The final stage in the registration process is the actual registration of the original images.

At UHW the different weighted images are acquired simultaneously and are, therefore, subject to the same movement, if any, during scanning. Hence, it is assumed that such images are pre-registered. Images of the same subject acquired on more than one occasion require registration. For the purposes of this system, the T2-weighted image acquired on the first occasion is taken to be the reference image. The registration system proposed in this thesis is applied to the T2-weighted images acquired from subsequent occasions to register them to the reference image. It is possible to choose a different reference image and register the other images to it. The relative rotations and translations derived for the T2-weighted images are applied to the other weighted images as well.

The final system for the registration of MRI finger images is illustrated in Fig. 6.1 and is composed of the following steps:

1. Standardise all subsequent T2-weighted image slices based on the equivalent reference slice.
2. Derive feature boundaries for all standardised and reference image slices.
3. Remove all assumed soft tissue boundaries in all boundary image slices (explained in Section 6.2.3).
4. Combine the segmented bone boundary slices to create combined slice images.
5. Apply the Hough Transform to the combined slice T2 image from the first occasion to determine the best-fit ellipse to the boundary. Search to find the optimal location of this best-fit ellipse on the same image. This is necessary because particular rounding to the nearest pixel location, explained in Section 5.3.2, can cause error in the results of the Hough Transform. Search to find the optimal location of the best-fit ellipse to the boundaries on all the other combined slice images.
6. Register the original images using the relative rotation and translation obtained in step 5.

The next section provides a step-by-step account of the application of this system to MRI finger data.

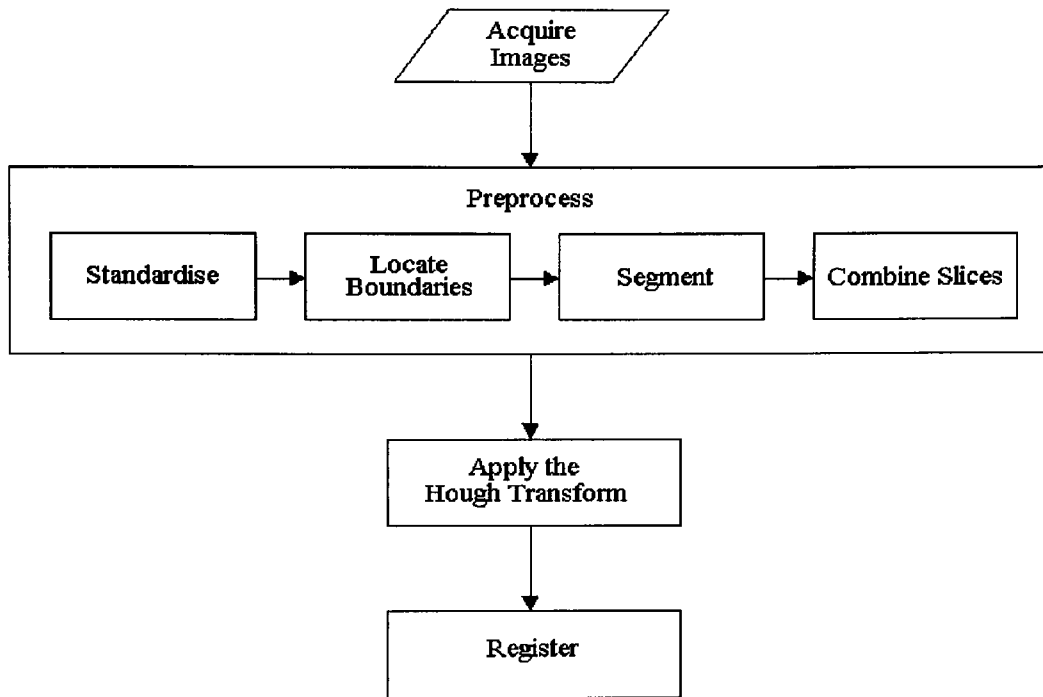


Figure 6.1: The final registration system.

6.2 Results of the Proposed System

The final registration system described above is applied to MRI finger images. The system is tested with images from five subjects. For each subject three sets of different weighted images (explained in Section 1.1.1), are acquired simultaneously. Each set of images is comprised of four sagittal cross-sections (explained in Section 1.1.2) - or slices - of the finger joint being imaged. As all three sets of images are acquired simultaneously, all slices are subject to the same movement, if any, during scanning. Therefore, such images are assumed to be pre-registered.

A second set of images of the same finger joint is acquired on a second occasion for all five subjects. Incorrect positioning for scanning, movement during scanning and changes within the finger necessitate registration. The registration system described above is applied to both sets of images to register them on a subject by subject basis.

For all subjects, the T2-weighted image acquired on the first occasion is taken to be the reference image. The registration system is applied to register the T2-weighted image acquired on the second occasion to the reference image.

In this section, a detailed description is given of the application of the registration system to one of the five subjects.

Consider the T2-weighted images acquired from subject 1, illustrated in Figs. 6.2 and 6.3. Fig. 6.2(a) to (d) are slices 1 to 4 respectively of the reference image and Fig. 6.3(a) to (d) are slices 1 to 4 respectively of the T2-weighted image acquired on the second occasion.

6.2.1 Step 1 - Standardise

The first step in the processing stage of the registration system is to standardise the images. Different weighted images have different means and standard deviations and different contrast, complicating the determination of similar features in both images. Even images of the same weight will have different means and standard deviations. Standardisation produces images with very similar, if not identical, means and standard deviations and very similar contrasts. Thus, the location of similar features is simplified. Details of the standardisation procedure are given in Section 4.1.2.

The T2-weighted image acquired on the second occasion is standardised according to the reference image, on an equivalent slice basis. For example, slice 1 of the T2-weighted image acquired on the second occasion is standardised based on slice 1 of the reference image. Slice 2 of the T2-weighted image acquired on the second occasion is standardised based on slice 2 of the reference image and so on. Fig. 6.4 shows the resulting standardised images for subject 1.

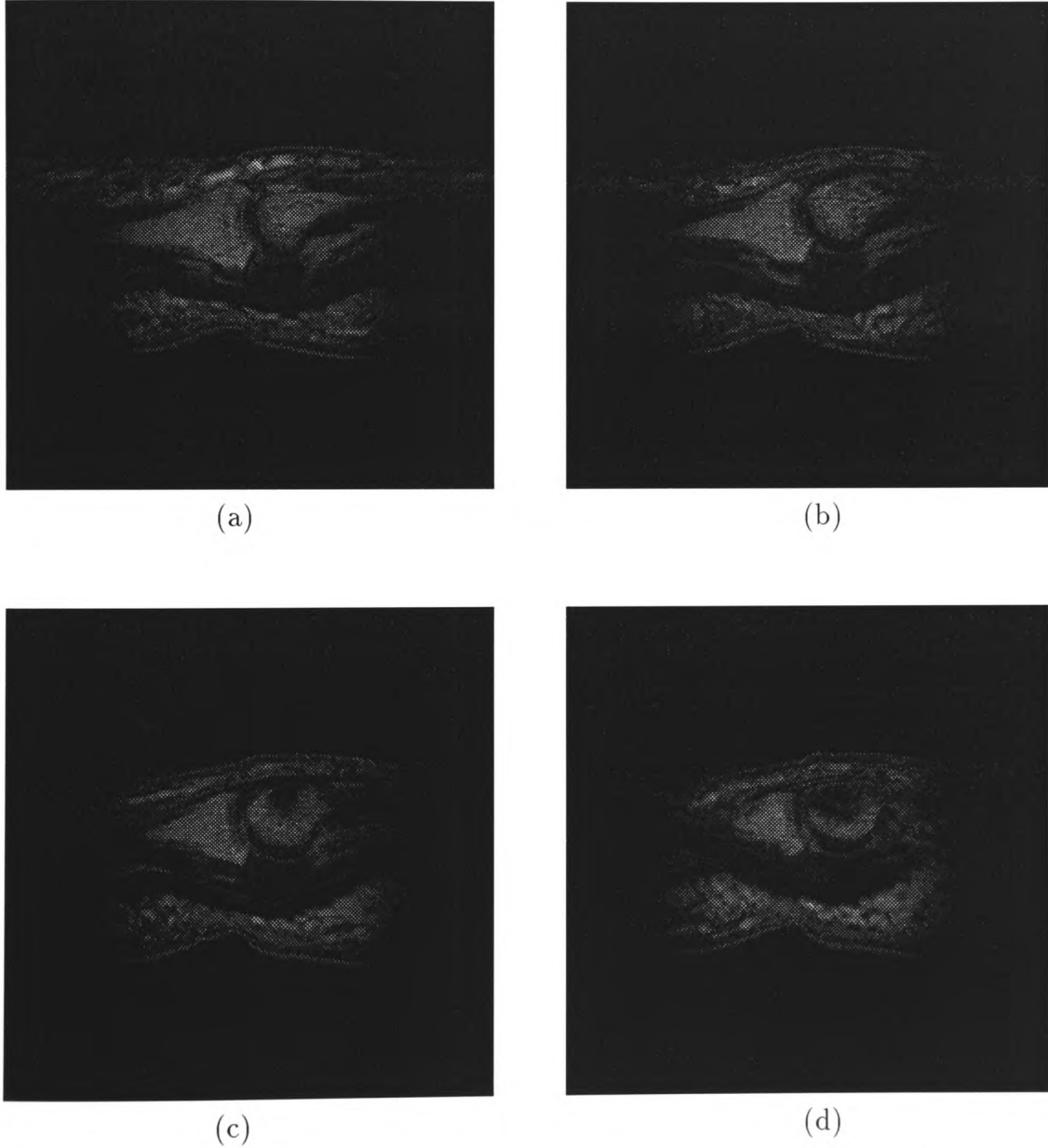


Figure 6.2: (a) to (d) Subject 1 reference (first occasion T2-weighted) image slices 1 to 4 respectively.

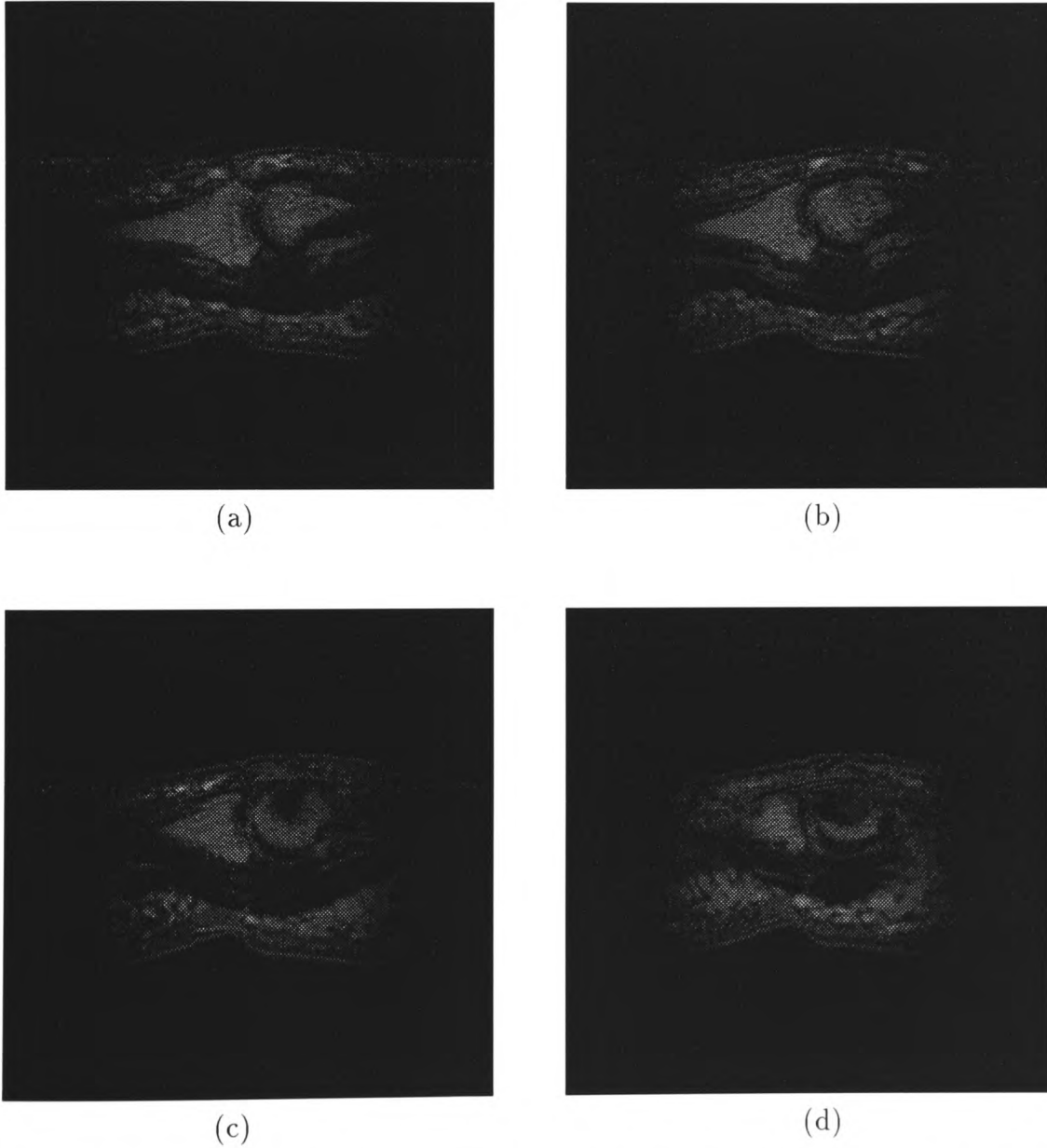


Figure 6.3: (a) to (d) Subject 1 second occasion T2-weighted image slices 1 to 4 respectively.

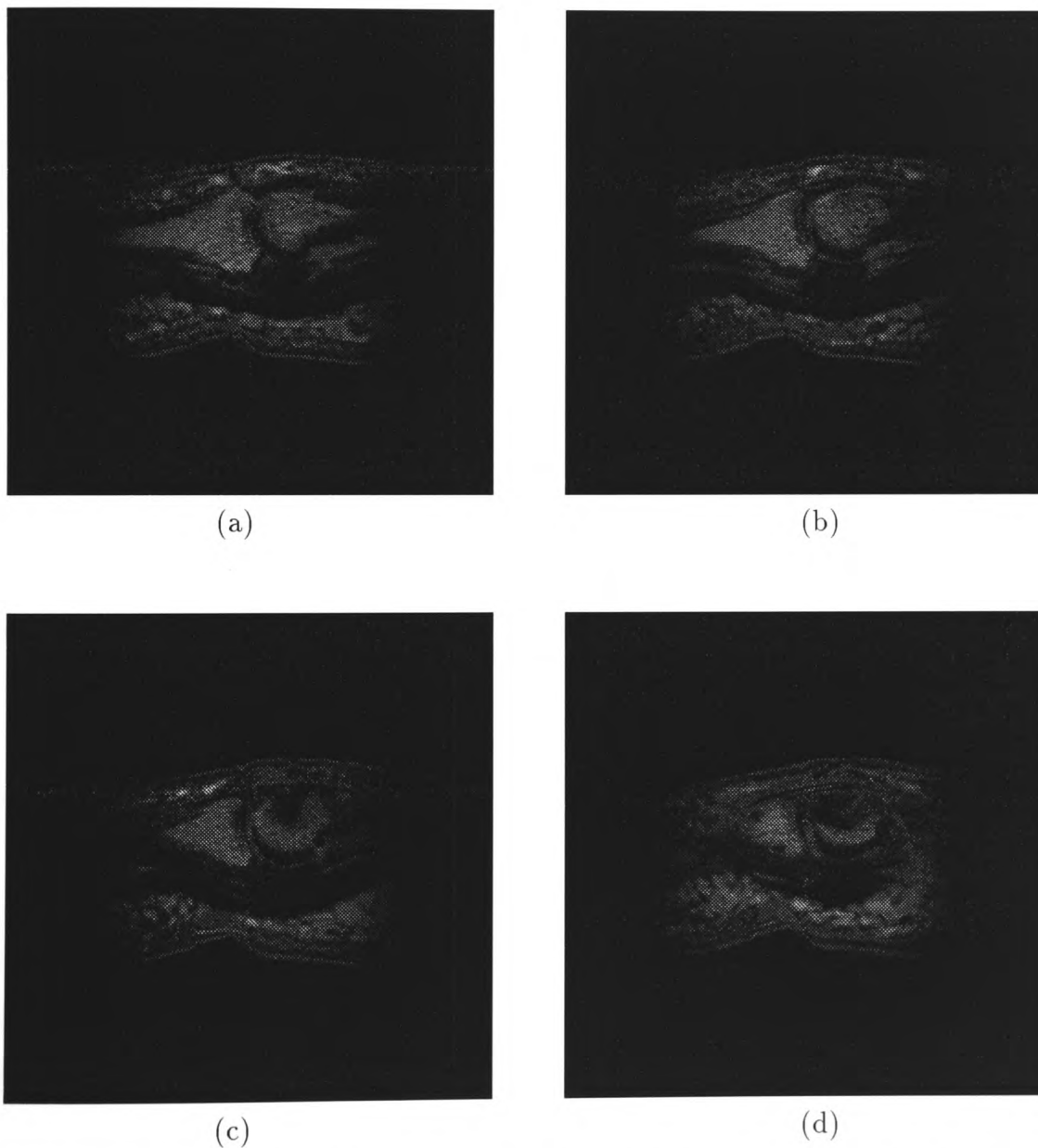


Figure 6.4: (a) to (d) Subject 1 standardised second occasion T2-weighted image slices 1 to 4 respectively.

6.2.2 Step 2 - Derive Bone Boundaries

Registration maps features or points in one image to features or points in another image. Therefore, it is necessary to derive similar features from both images. Step 2 of the processing stage is an automated sequence of image processing techniques that derive boundaries in the MRI finger images. It is assumed that some of the boundaries approximate the two bones in the joint. A detailed description of the boundary sequence is given in Section 4.2.3. The resulting boundaries derived for subject 1 are illustrated in Figs. 6.5 and 6.6.

6.2.3 Step 3 - Segment

The boundary sequence in step 2 produces images that contain many boundaries. It is assumed that some of these boundaries approximate segments of the two bones in the finger joint. The other boundaries are assumed to represent segments from various soft tissues. For all subjects, boundary regions approximating the bones were derived which were consistent with clinicians' interpretations of MRI finger images at the University Hospital of Wales. Boundaries approximating soft tissues are not derived consistently. Bone boundaries are considered by the author to be stable and reliable structures to be used in the registration process. Soft tissue boundaries are considered to be ambiguous. To avoid unnecessary complications and mis-registrations, all assumed soft tissue boundaries are removed from all the images derived in step 2. Segmenting such boundaries is easily done using a simple filling algorithm. Figs. 6.7 and 6.8 show the resulting segmented images for subject 1.

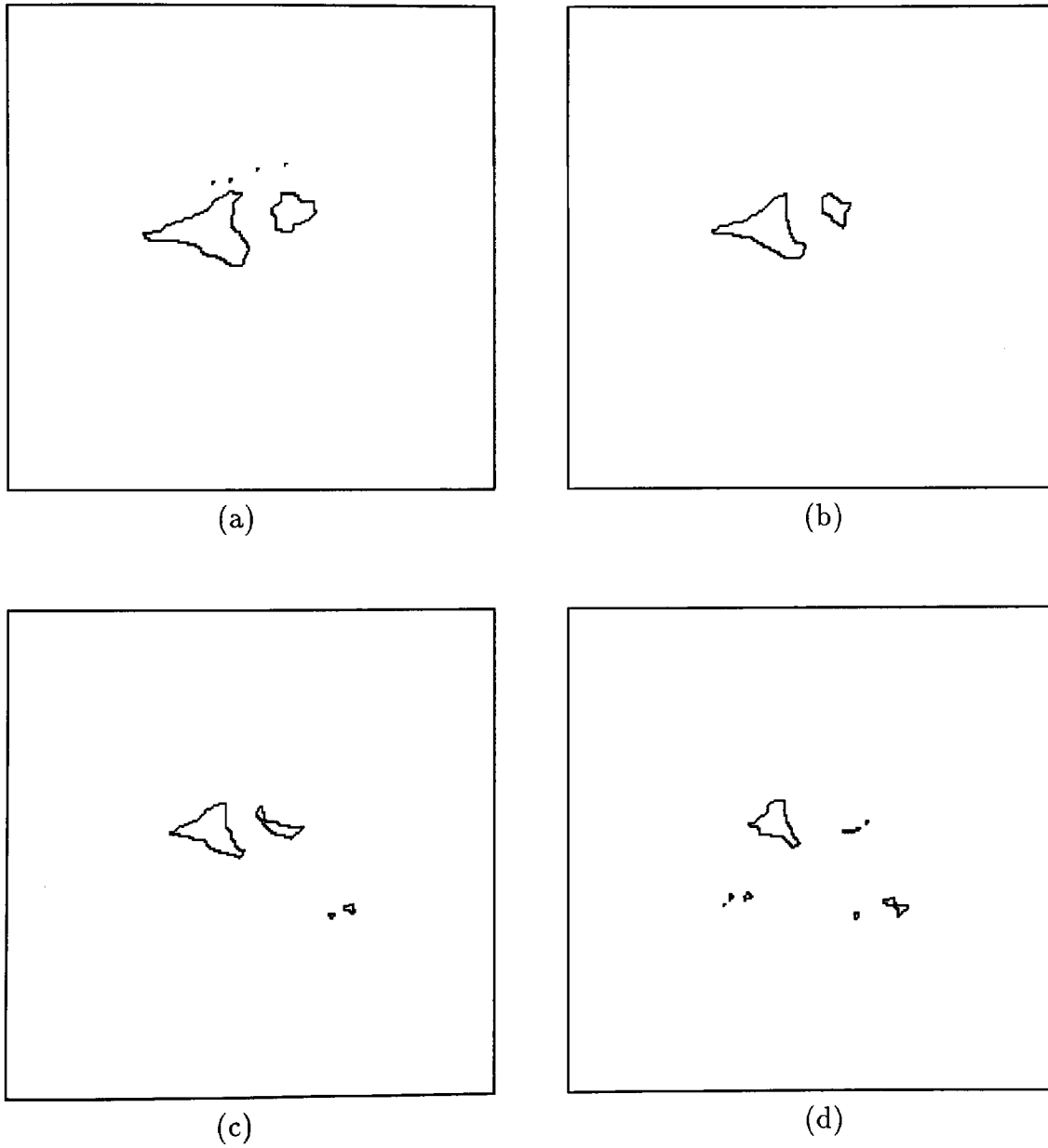


Figure 6.5: (a) to (d) Subject 1 boundaries derived from reference image slices 1 to 4 respectively.

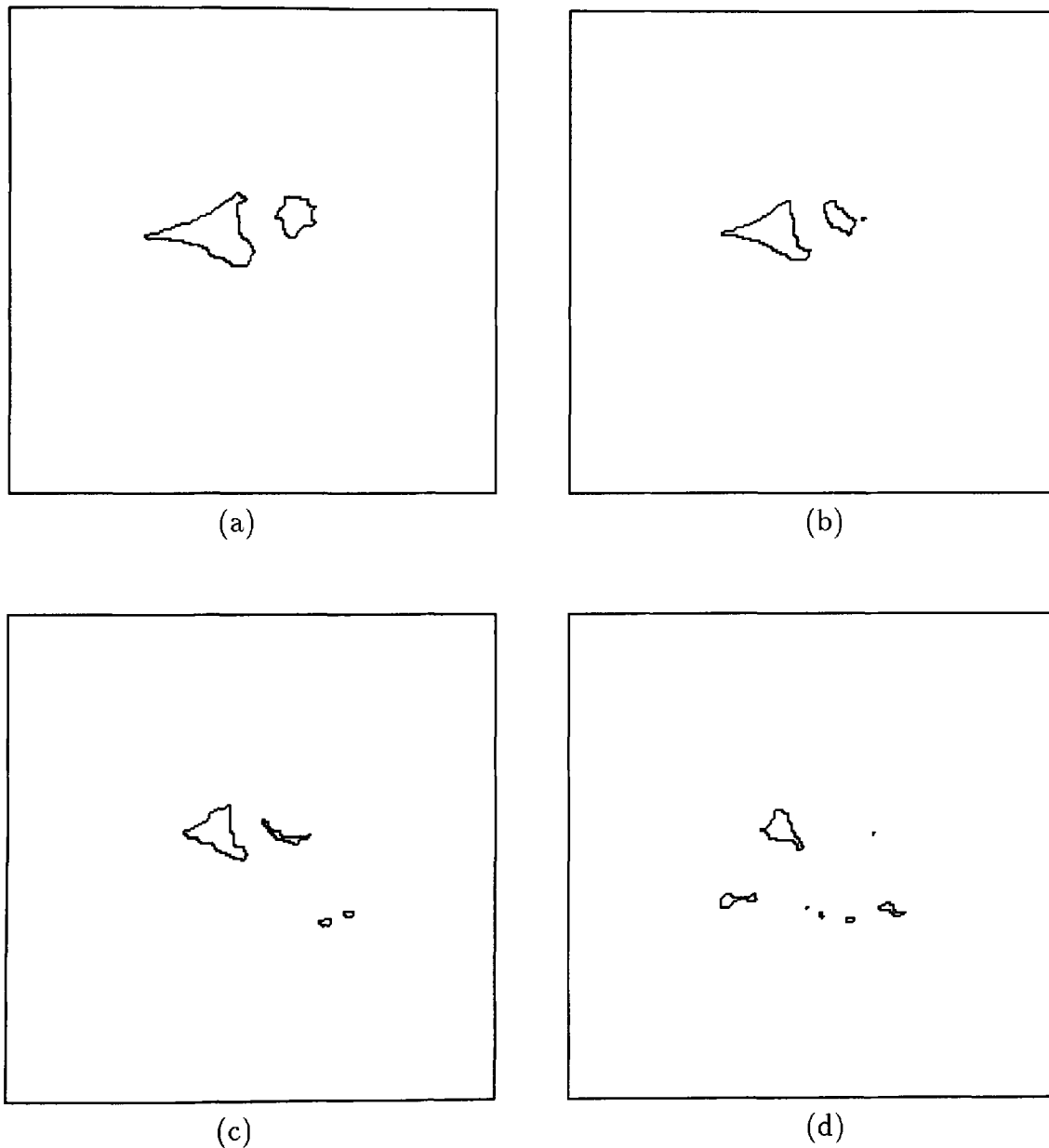


Figure 6.6: (a) to (d) Subject 1 boundaries derived from second occasion T2-weighted image slices 1 to 4 respectively.

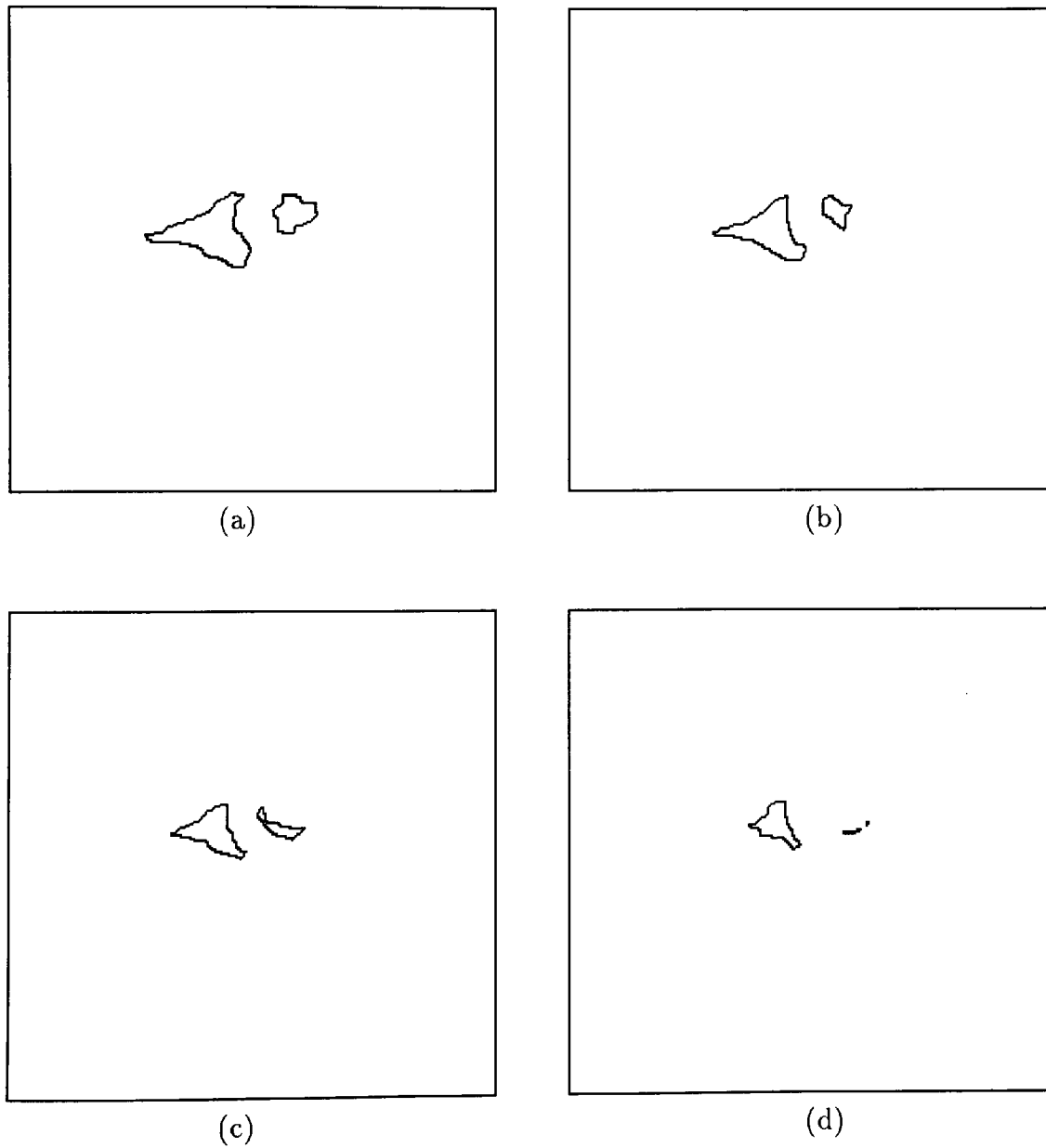


Figure 6.7: (a) to (d) Subject 1 segmented boundaries derived from reference image slices 1 to 4 respectively.

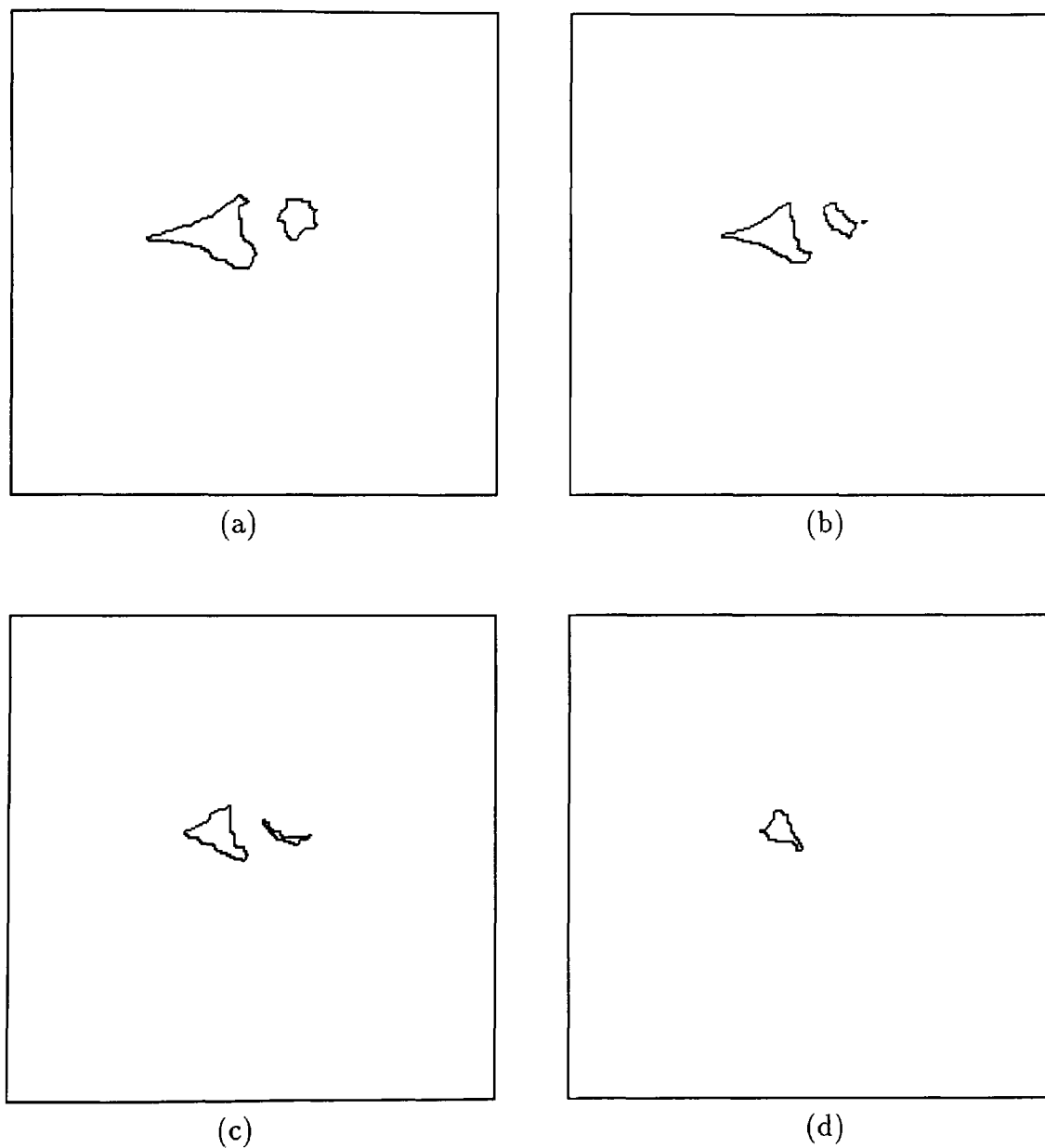


Figure 6.8: (a) to (d) Subject 1 segmented boundaries derived from second occasion T2-weighted image slices 1 to 4 respectively.

6.2.4 Step 4 - Combine the Slices

A study of the images derived in step 3 shows that the derived bone boundaries from images taken over time are not always sufficiently similar for accurate registration. This is partly due to differences in the positioning of the finger on the different scanning occasions.

A new technique has been designed for this research to derive similar boundaries from images taken over time. The boundaries from all four slices of an image are combined to give the maximum possible boundary shape for the bones across four slices. A detailed description of this technique is given in Section 5.4. Fig. 6.9 shows the resulting combined slice images for subject 1.

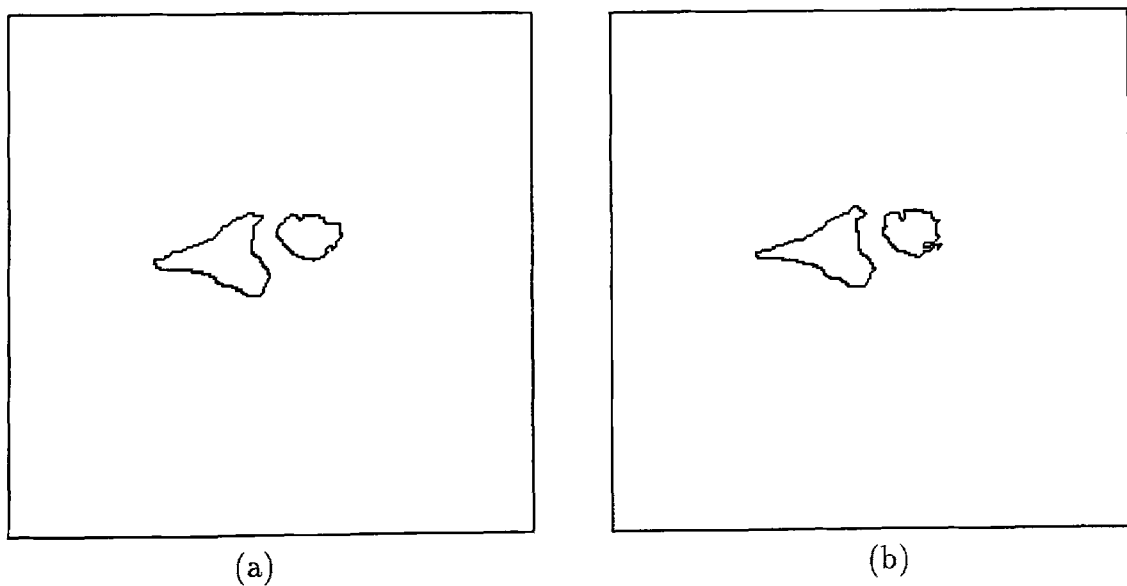


Figure 6.9: Subject 1 (a) combined slice reference image (b) second occasion combined slice image.

6.2.5 Step 5 - Determine the Registration Parameters

A registration algorithm will determine the relative rotation and translation required to register two images. In this application, the Hough Transform is used to determine the registration parameters. A detailed explanation of the Hough Transform is given in Section 5.3.

The Hough Transform is applied to user selected open segments from both boundaries in the combined slice reference image (illustrated by red pixels in Fig. 6.10(a)) separately and the resulting best-fit ellipses are recorded. The rounding to the nearest pixel problem explained in Section 5.3.2 causes the reported number of pixels lying on the best-fit ellipse to be much greater than in reality. Consequently, the *best-fit* ellipse is sometimes missed. To ensure the best locations of the best-fit ellipse have been determined, an extra search is made through all possible orientations of the best-fit ellipse, calculating the number of matching pixels at each orientation. The ellipse(s) yielding the maximum number of matching pixels are taken to be the best-fit ellipse(s). Each best-fit ellipse is then fitted to the equivalent boundary in the second occasion combined slice image (illustrated in Fig. 6.10(b)).

Table 6.1 shows the locations of the best-fit ellipses on each boundary. The two boundaries are labelled *MP* (the middle phalanx) and *PP* (the proximal phalanx). The best-fit ellipse is expressed in terms of its centre point (cx, cy) , its major- and minor-radii a and b respectively and the orientation of the ellipse, Ω . The number of boundary pixels that lie on the best-fit ellipse is also calculated as a percentage. For the middle phalanx (*MP*) three best-fit ellipses were found.

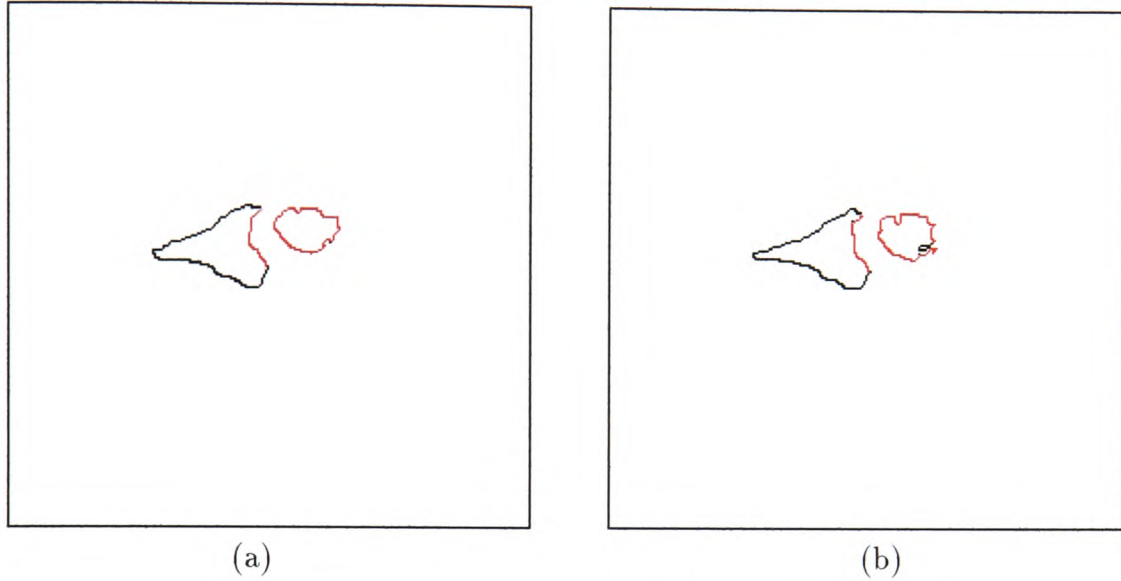


Figure 6.10: Subject 1 open curves on combined slice images (a) reference image (b) second occasion image.

<i>Bone</i>	<i>Occasion</i>	<i>Weight</i>	cx	cy	a	b	Ω	<i>% match</i>
MP	1	T2	129	112	14	11	76	65
MP	1	T2	129	111	14	11	89, 90	65
MP	2	T2	131	112	14	11	75, 76	64
PP	1	T2	145	109	13	11	29	49
PP	2	T2	148	110	13	11	2	47

Table 6.1: Subject 1 fitting the best fit ellipses.

6.2.6 Step 6 - Actual Registration

The final stage of the proposed system for the registration of MRI finger images is the actual registration of the original images. The relative rotation and translation derived in step 5 of the registration procedure are applied to *all* second occasion images to register them relative to the reference image. Fig. 6.11 shows the resulting images for subject 1 after applying the registration parameters derived in step 5. Little can be deduced regarding the accuracy of the registration merely by visual inspection, but a full analysis of the results follows in Section 6.3.

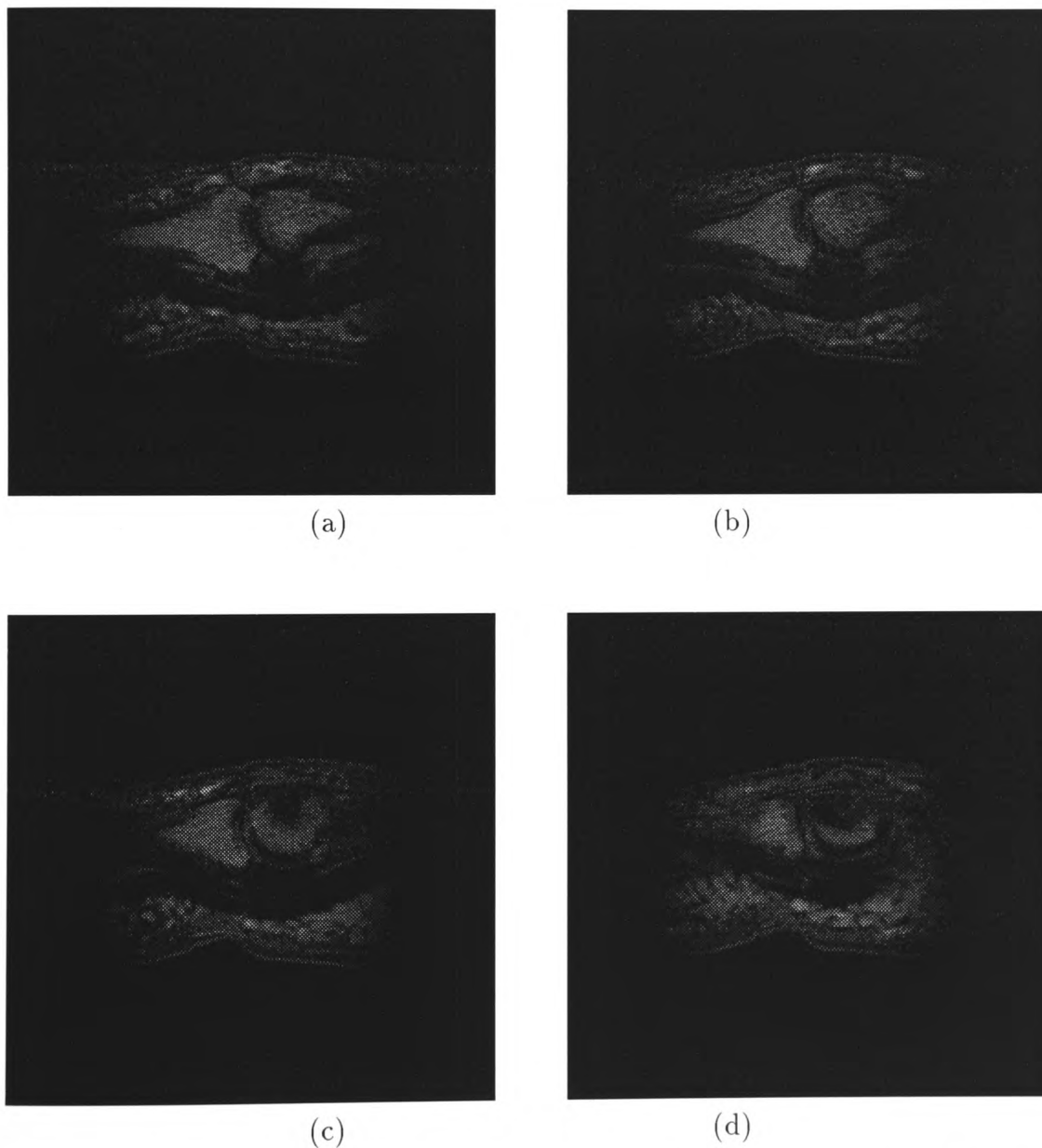


Figure 6.11: Applying the registration parameters to subject 1 second occasion images (a) to (d) slices 1 to 4 respectively.

6.3 Analysis of the Registration System and Results

In this section, an analysis of the registration system described above and results for five available subjects is given. Table 6.2 shows the registration results determined for the five subjects.

<i>Subject</i>	<i>Bone</i>	<i>Image (Occasion)</i>	<i>Reference Image (Occasion)</i>	<i>Translation (x, y)</i>	<i>Rotation</i>
1	MP	T2 (2)	T2 (1)	(2, 0)	0°
2	MP	T2 (2)	T2 (1)	(-13, -1)	9°
3	MP	T2 (2)	T2 (1)	(-4, 11)	0°
4	MP	T2 (2)	T2 (1)	(-6, -1)	-3°
5	MP	T2 (2)	T2 (1)	(-4, 3)	-7°
1	PP	T2 (2)	T2 (1)	(3, 1)	-27°
2	PP	T2 (2)	T2 (1)	(-13, 3)	0°
3	PP	T2 (2)	T2 (1)	(-4, 8)	0°
4	PP	T2 (2)	T2 (1)	(5, -3)	-58°
5	PP	T2 (2)	T2 (1)	(-3, -3)	-5°
<i>Narrower open curve results</i>					
1	PP	T2 (2)	T2 (1)	(5, 2)	-14°
2	PP	T2 (2)	T2 (1)	(-13, 2)	0°
3	PP	T2 (2)	T2 (1)	(-3, 9)	-12°
4	PP	T2 (2)	T2 (1)	(6, -3)	-11°
5	PP	T2 (2)	T2 (1)	(-3, -2)	-6°

Table 6.2: Registration parameters obtained from fitting the best fit ellipses for five subjects.

For each subject the registration system is applied to register the T2-weighted image acquired on the second occasion to the reference image (T2-weighted image acquired on the first occasion). Registration parameters are determined for both bone boundaries in the images, namely, the middle phalanx (*MP*) and the proximal phalanx (*PP*). The registration results determine the relative translations and rotations required to register the images. For example, for the *MP* from subject 1, a shift of 2 pixels in

the positive x -direction is all that is required to register the two sets of images taken over time. Where rotations are required, the rotation is performed first before the translation.

To analyse the results of the registration system, the derived best-fit ellipses are superimposed onto the combined slice boundary images (illustrated in Figs. 6.12 to 6.16). The open curves are illustrated in the top row of each figure.

The registration parameters are applied to the second occasion combined slice images to register them with the reference image. The registered images are then superimposed to illustrate the accuracy and problems of the registration system (illustrated in Figs. 6.17 to 6.21).

For all subjects, the achieved registrations appear sufficient for the entire MP boundary, with the exception of subject 2 (illustrated in Fig. 6.18).

In most subjects, the achieved registration appears adequate for the entire PP boundary. However, in two subjects, the resulting registrations are not correct, for example, subject 4 illustrated in Fig. 6.20. The reason for these poor results is the approximately circular curvature of the PP boundary segment on which the best-fit ellipses are located. Consequently, the best-fit ellipse can be located in many places on the boundary. This condition accounts for the large rotations to achieve registration listed in Table 6.2. The particular case of a circle is even worse. For the boundary being examined, all rotations are identical and no rotation result for registration is determined. This condition is seen in the registration results for subject 3, where the best-fit ellipse was, in fact, a circle. On this occasion using no rotation works quite well, but generally it will not be clear what rotation is best. Thus, a restriction must be incorporated into the system to prevent the best-fit ellipse being a circle, *i.e.* $a \neq b$, to ensure that the orientation of the entire boundary is determined.

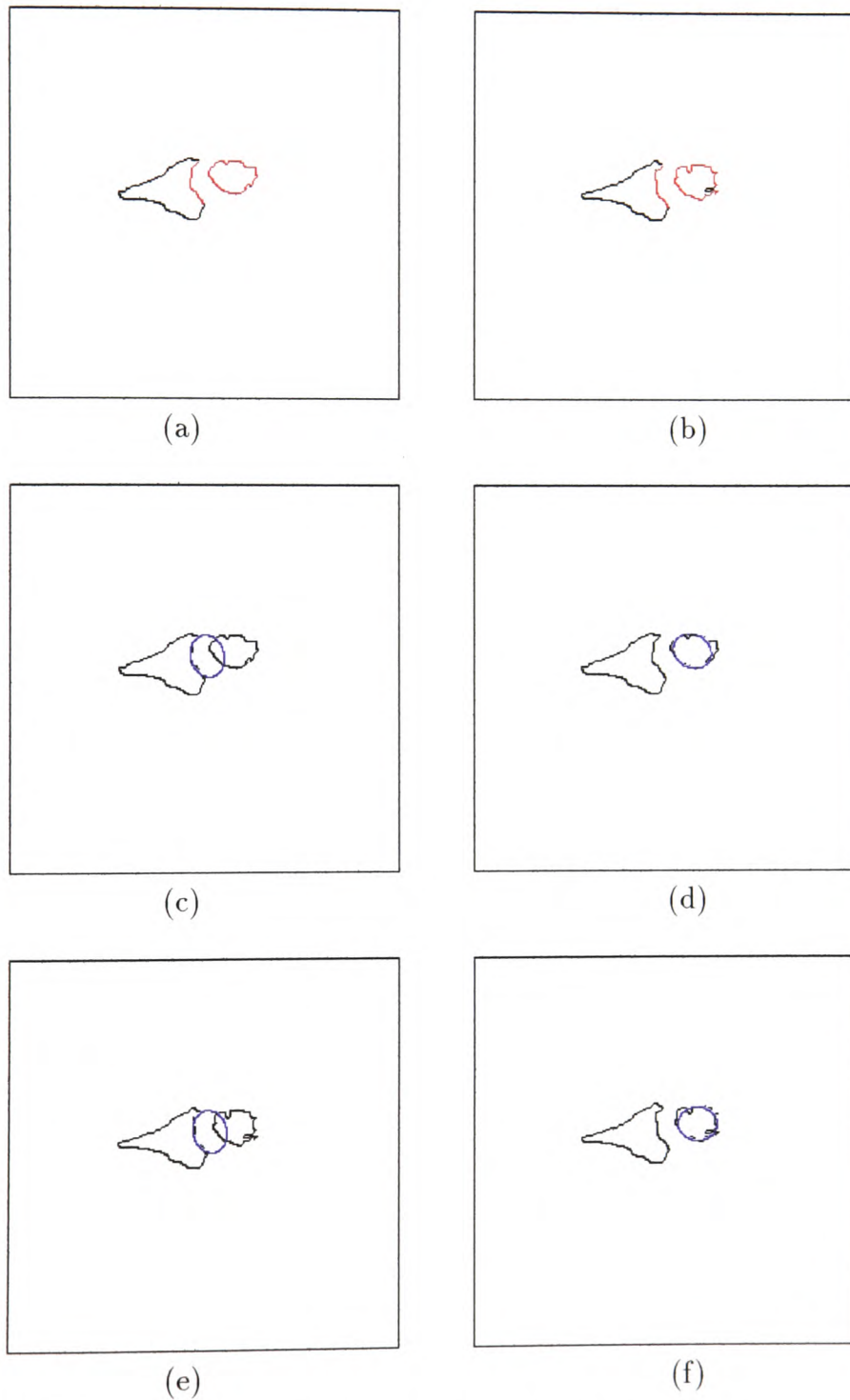


Figure 6.12: Subject 1 T2-weighted images (a) first occasion open curves (b) second occasion open curves (c) first occasion middle phalanx best-fit ellipse (d) first occasion proximal phalanx best-fit ellipse (e) second occasion middle phalanx best-fit ellipse (f) second occasion proximal phalanx best-fit ellipse.

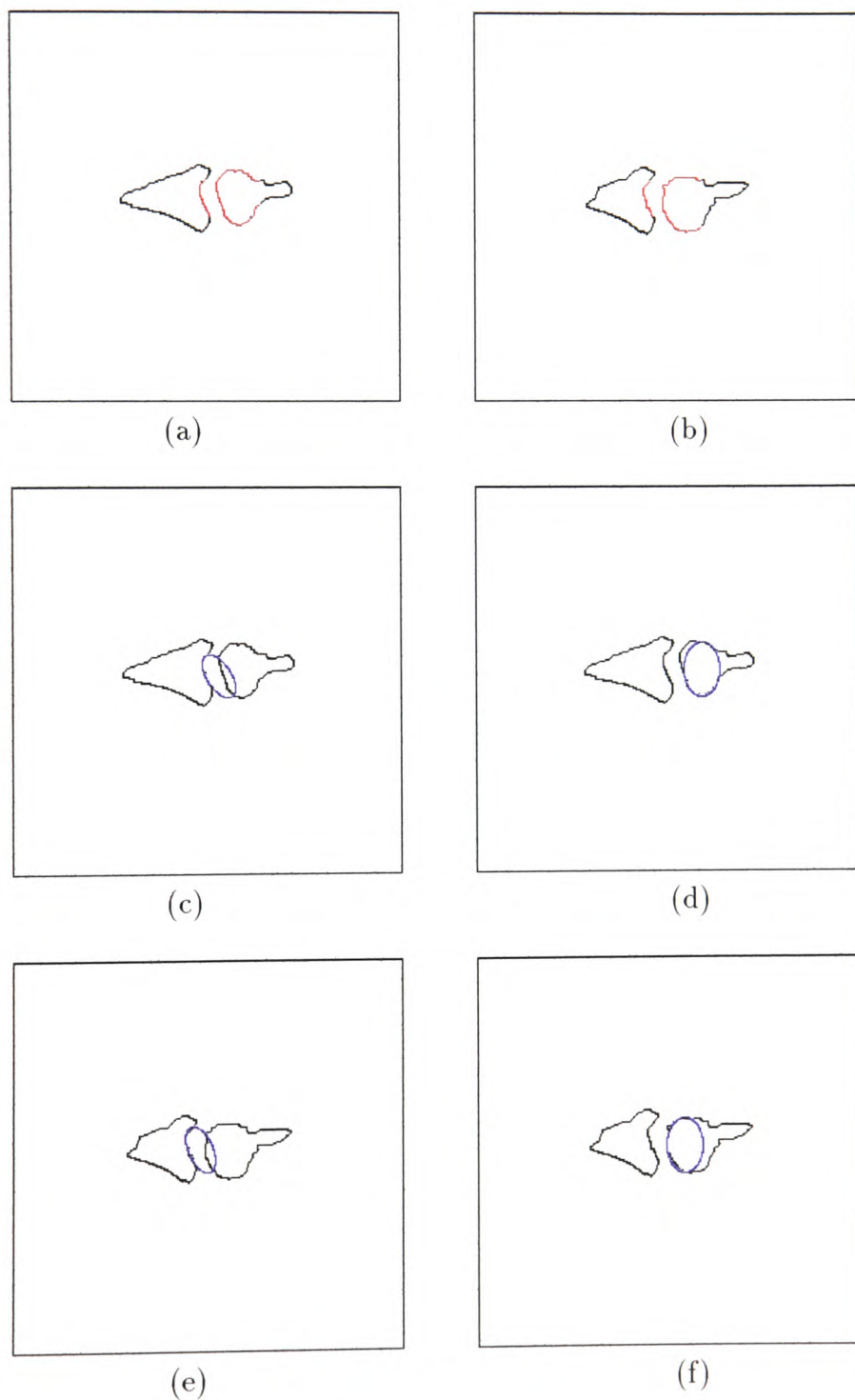


Figure 6.13: Subject 2 T2-weighted images (a) first occasion open curves (b) second occasion open curves (c) first occasion middle phalanx best-fit ellipse (d) first occasion proximal phalanx best-fit ellipse (e) second occasion middle phalanx best-fit ellipse (f) second occasion proximal phalanx best-fit ellipse.

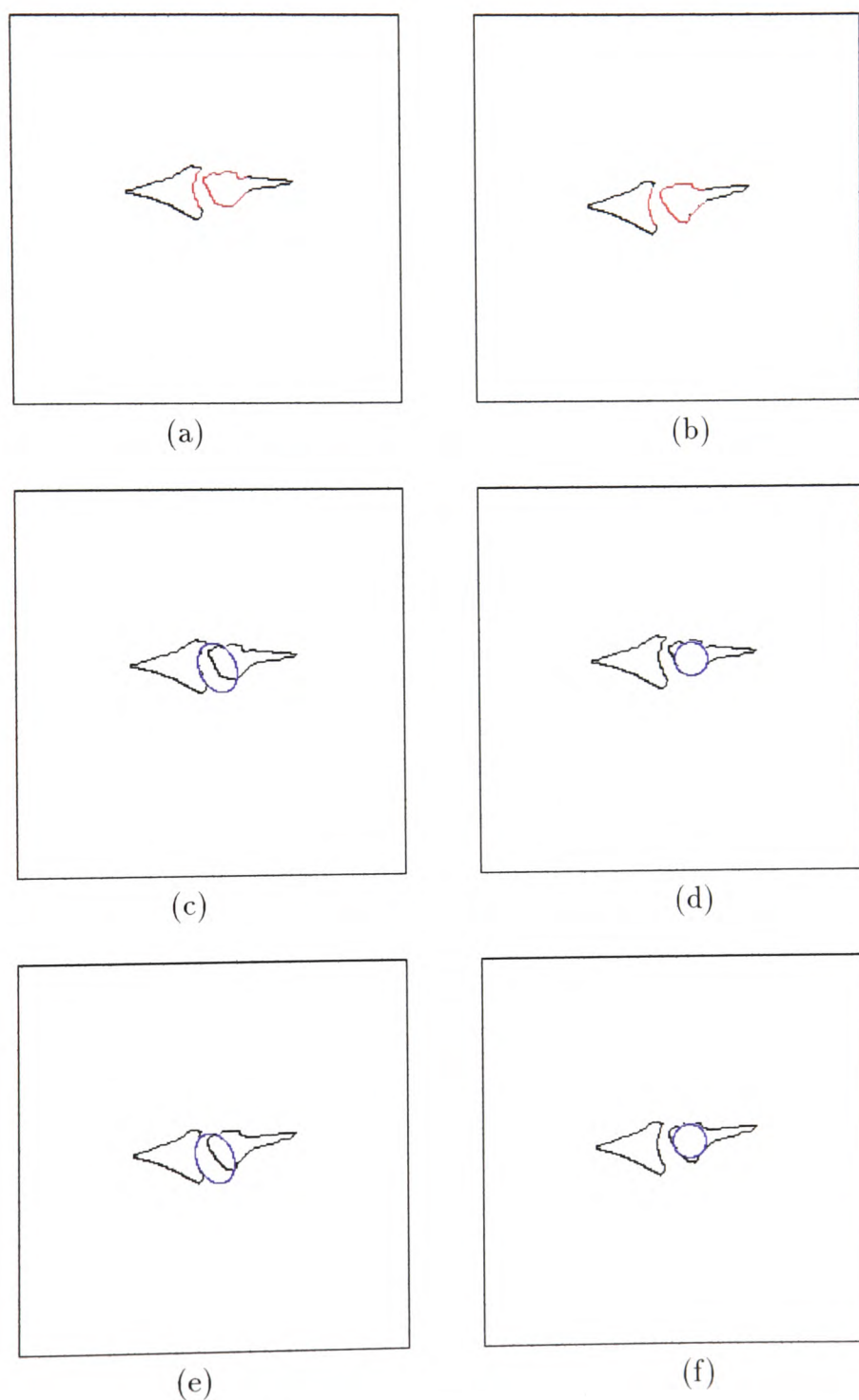


Figure 6.14: Subject 3 T2-weighted images (a) first occasion open curves (b) second occasion open curves (c) first occasion middle phalanx best-fit ellipse (d) first occasion proximal phalanx best-fit ellipse (e) second occasion middle phalanx best-fit ellipse (f) second occasion proximal phalanx best-fit ellipse.

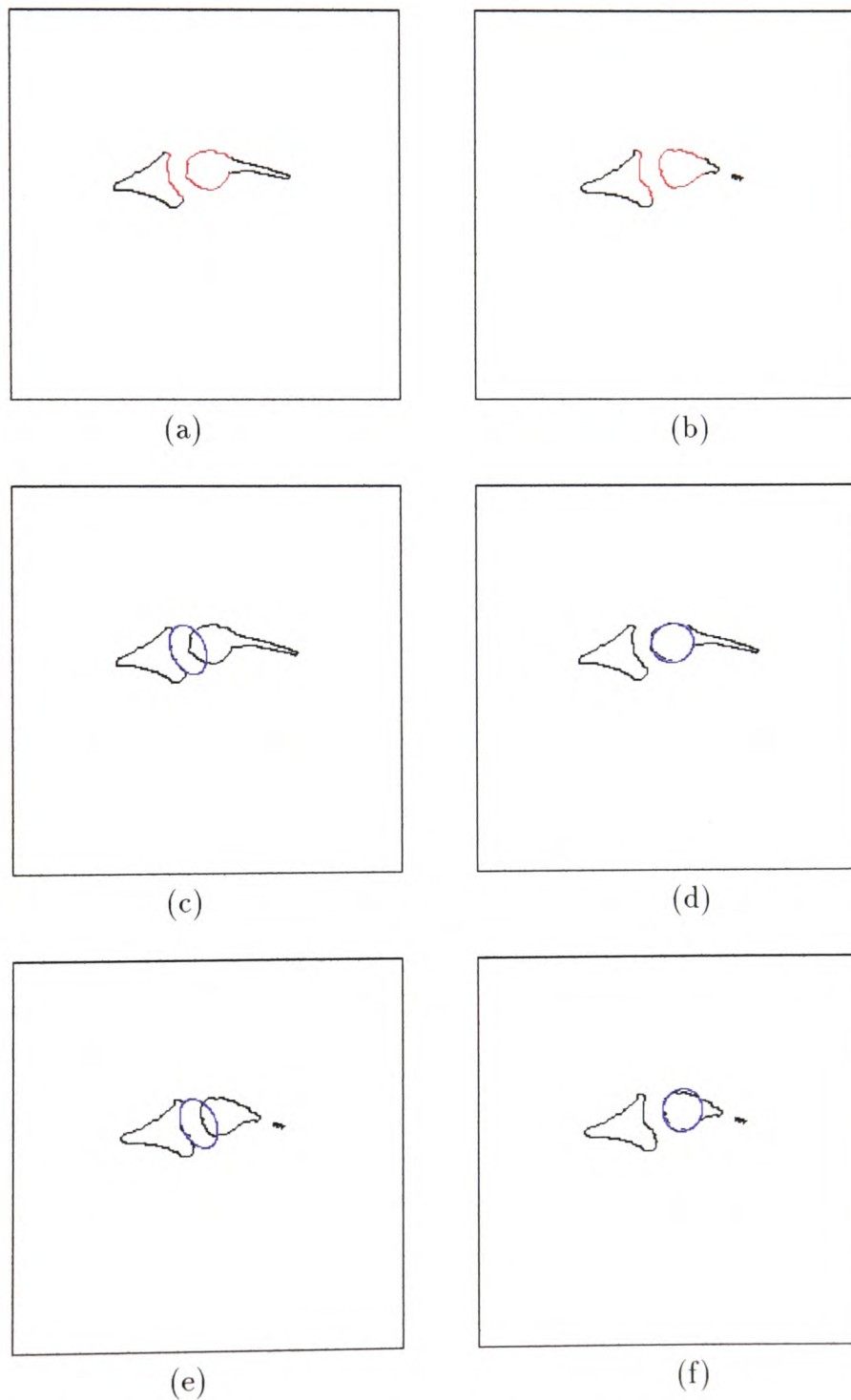


Figure 6.15: Subject 4 T2-weighted images (a) first occasion open curves (b) second occasion open curves (c) first occasion middle phalanx best-fit ellipse (d) first occasion proximal phalanx best-fit ellipse (e) second occasion middle phalanx best-fit ellipse (f) second occasion proximal phalanx best-fit ellipse.

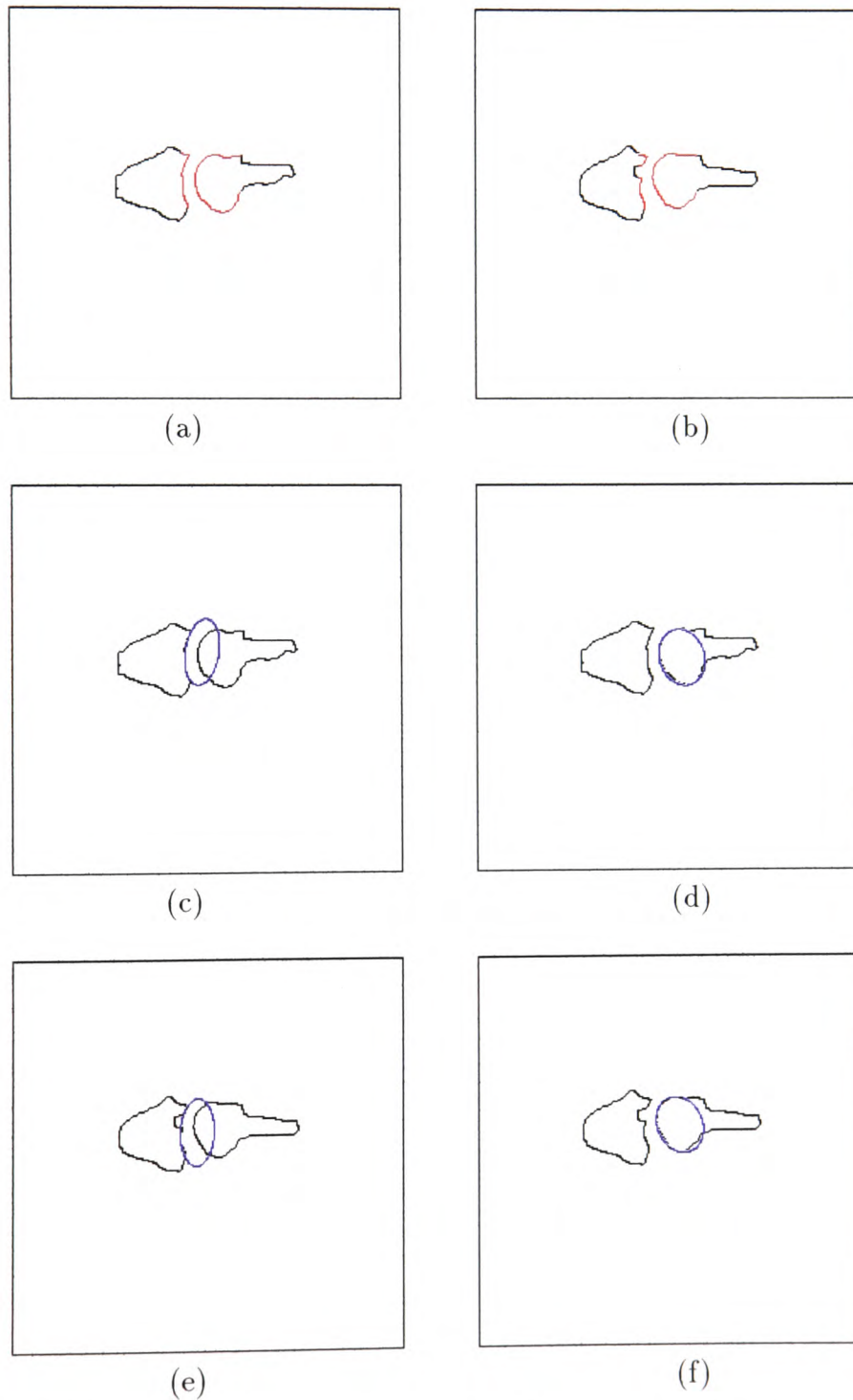


Figure 6.16: Subject 5 T2-weighted images (a) first occasion open curves (b) second occasion open curves (c) first occasion middle phalanx best-fit ellipse (d) first occasion proximal phalanx best-fit ellipse (e) second occasion middle phalanx best-fit ellipse (f) second occasion proximal phalanx best-fit ellipse.

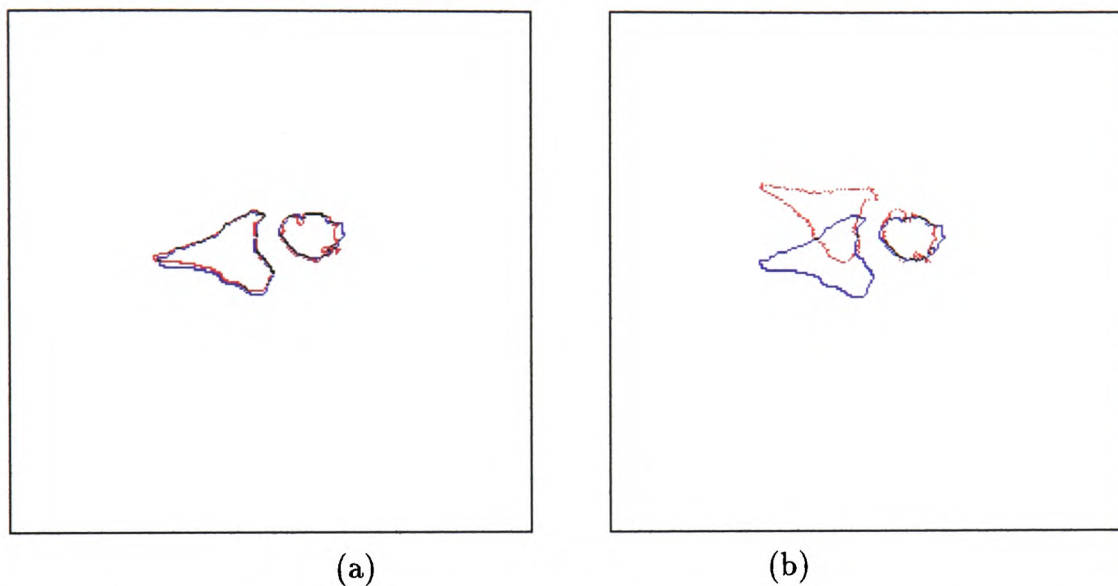


Figure 6.17: Superimposition of registration of combined slice boundaries, subject 1
(a) middle phalanx (b) proximal phalanx.

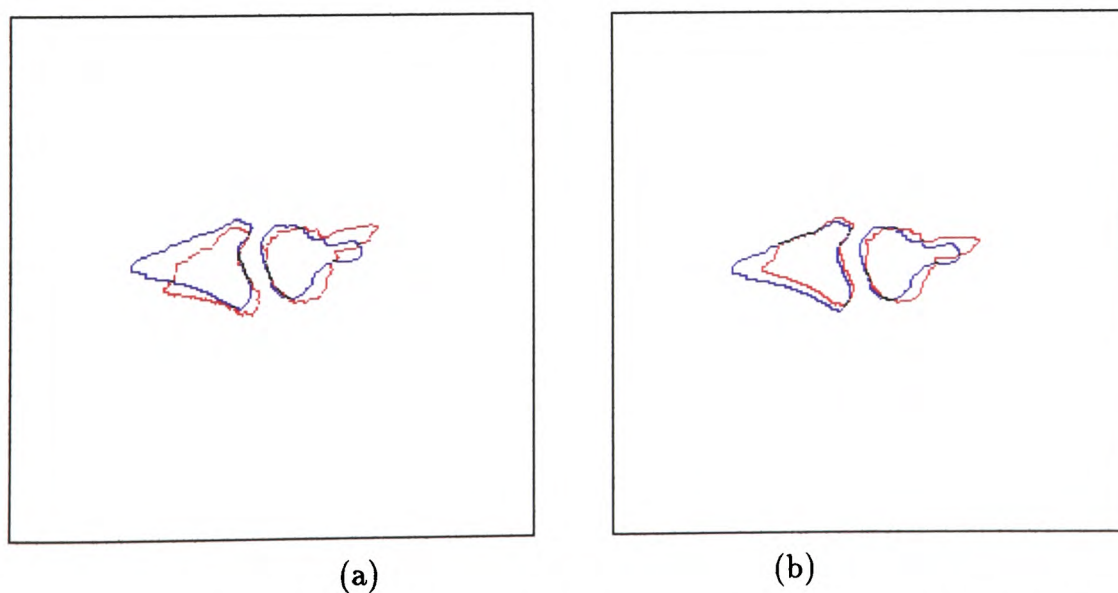


Figure 6.18: Superimposition of registration of combined slice boundaries, subject 2
(a) middle phalanx (b) proximal phalanx.

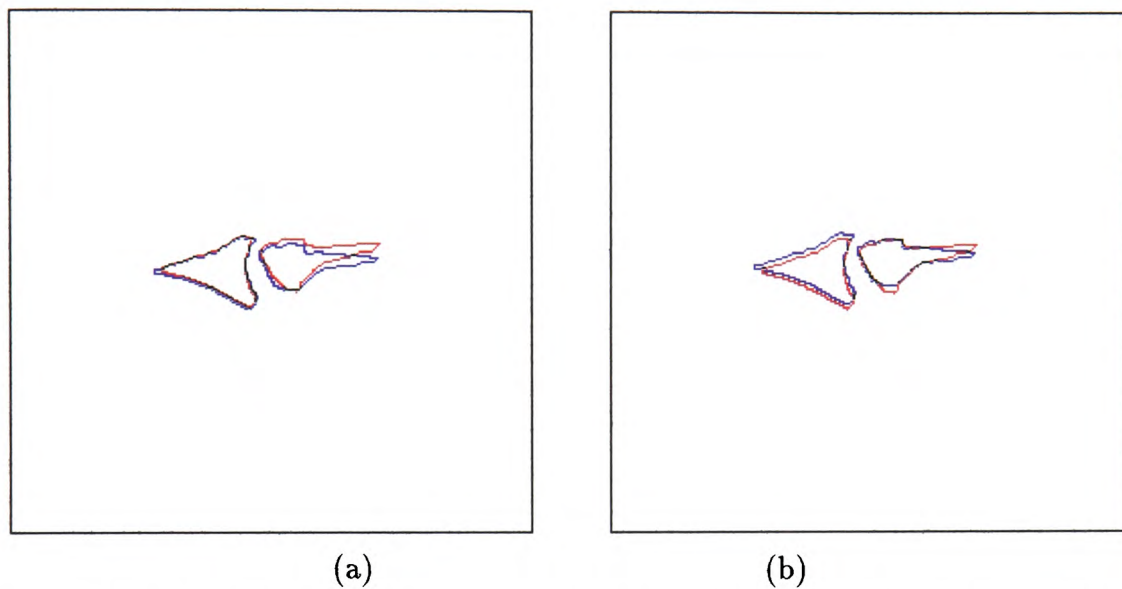


Figure 6.19: Superimposition of registration of combined slice boundaries, subject 3
(a) middle phalanx (b) proximal phalanx.

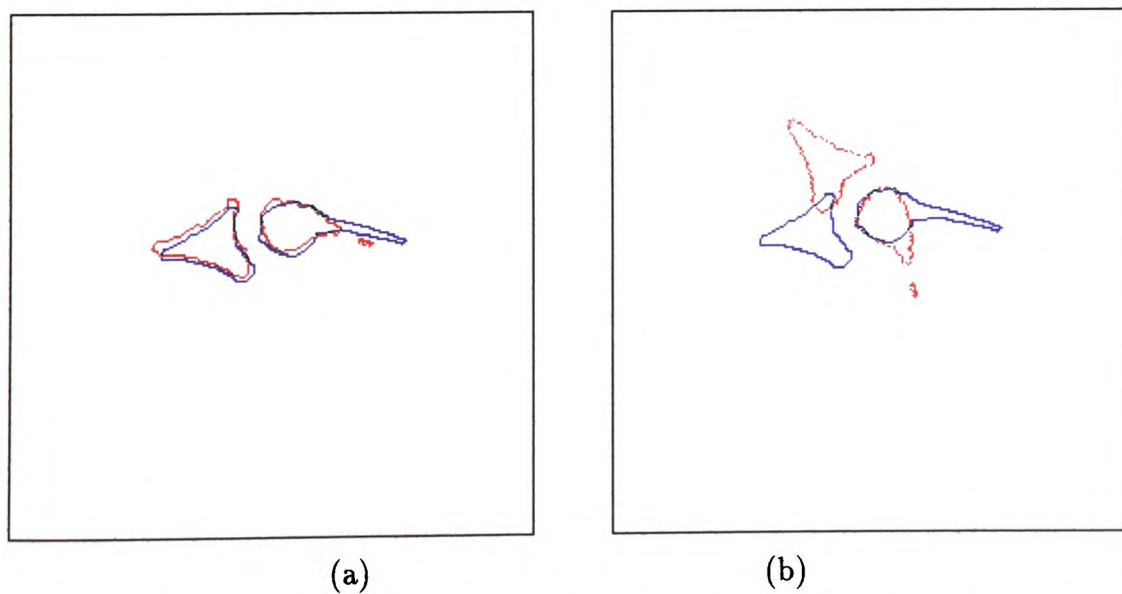


Figure 6.20: Superimposition of registration of combined slice boundaries, subject 4
(a) middle phalanx (b) proximal phalanx.

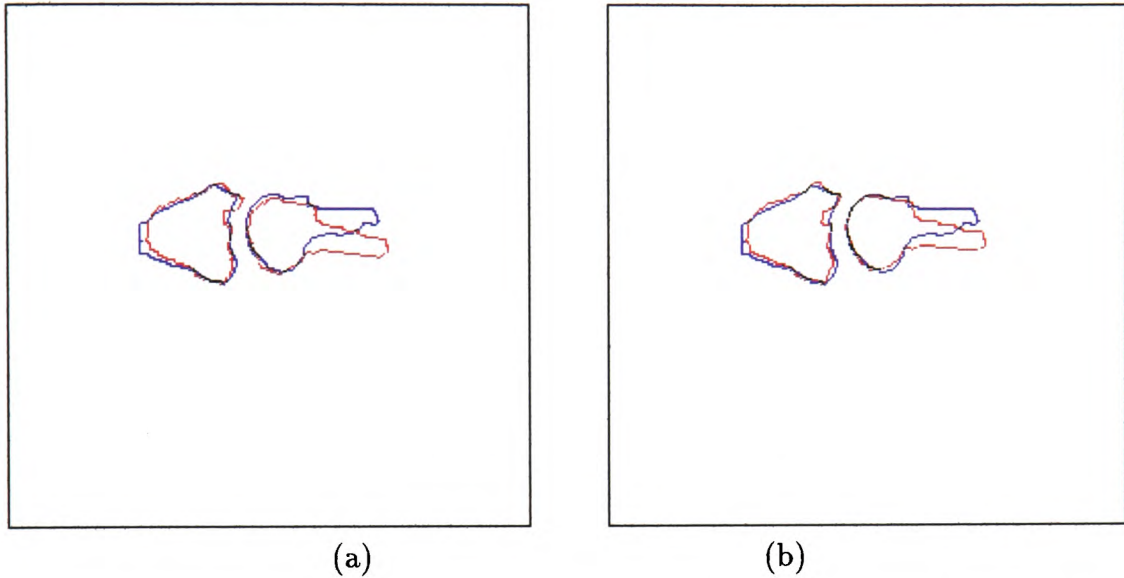


Figure 6.21: Superimposition of registration of combined slice boundaries, subject 5 (a) middle phalanx (b) proximal phalanx.

Selecting narrower open curves on the *PP* boundaries (illustrated in Figs. 6.22 to 6.26) will reduce the circularity problem described above. The best-fit ellipses obtained by re-applying the Hough Transform with these amendments are also given in Table 6.2, under the heading “Narrower open curve results”. The large rotations are improved in both subjects 1 and 4 and an ellipse with an orientation of 12° is obtained for subject 3, rather than a circle. In Section 6.3.1, it is shown that these amendments also improve the accuracy of the Hough Transform results.

Examining the way in which the best-fit ellipse actually fits the proximal phalanx highlights the fact that the combined slice boundaries of each subject over time are not the same size and shape. This is particularly evident in subject 2. The boundaries differ for a number of reasons. The *MP* and *PP* boundaries differ across the slices. The *MP* boundaries have the same characteristic shape, but the *PP* boundaries are sometimes completely different. Bone is made up of two structures. The dense (dark in MRI) cortical bone surrounds the less dense (lighter in MRI) trabecular bone [MedSci98, Plant95b]. The MRI finger images clearly show both densities for the

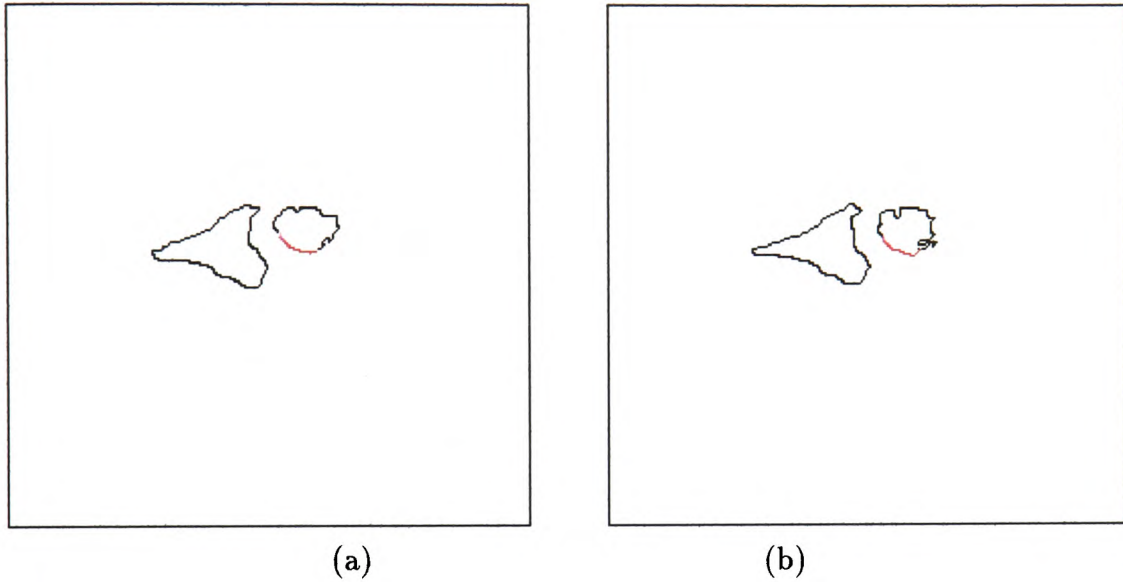


Figure 6.22: Narrower open curves on combined slice boundaries: Subject 1 T2-weighted images (a) first occasion proximal phalanx (b) second occasion proximal phalanx.

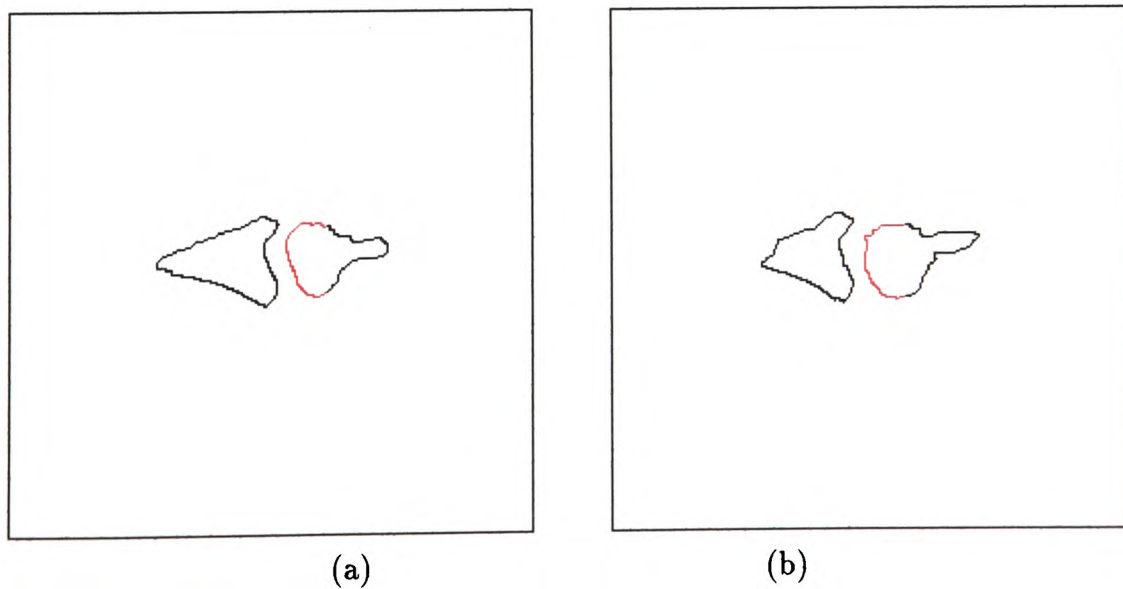


Figure 6.23: Narrower open curves on combined slice boundaries: Subject 2 T2-weighted images (a) first occasion proximal phalanx (b) second occasion proximal phalanx.

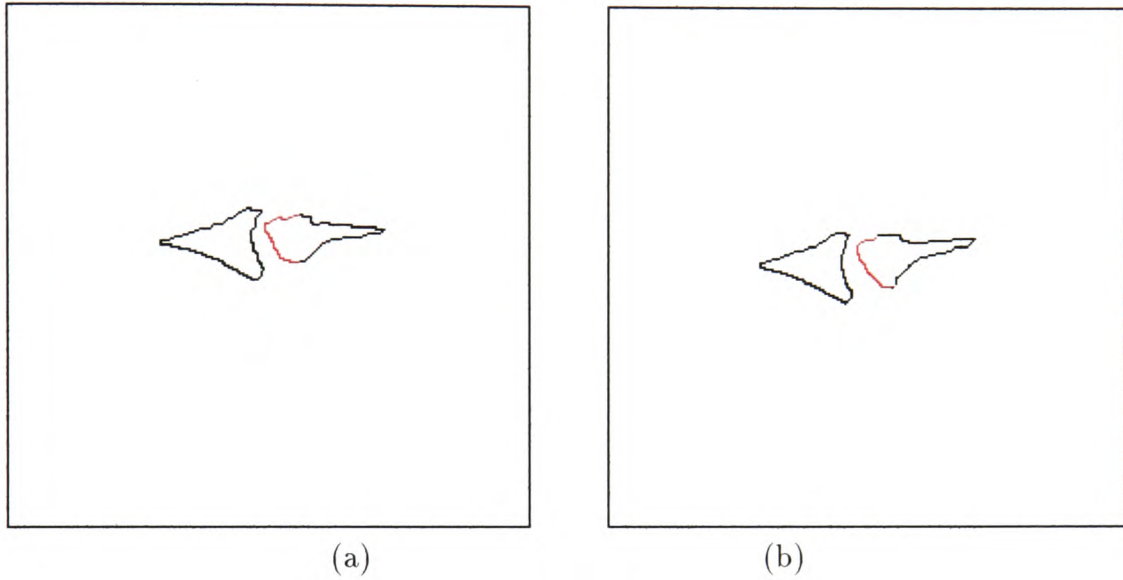


Figure 6.24: Narrower open curves on combined slice boundaries: Subject 3 T2-weighted images (a) first occasion proximal phalanx (b) second occasion proximal phalanx.

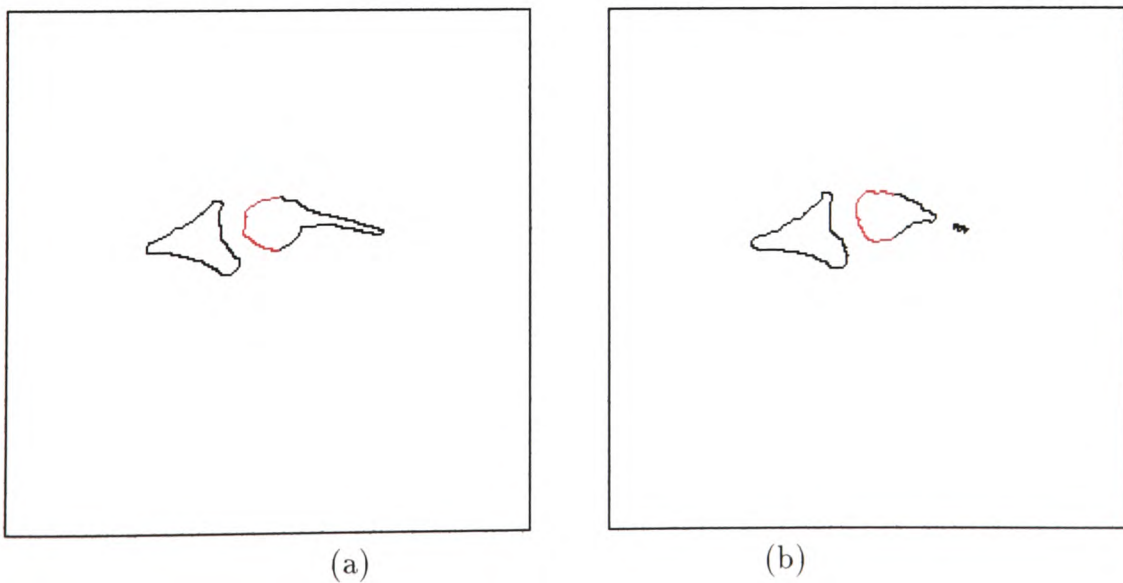


Figure 6.25: Narrower open curves on combined slice boundaries: Subject 4 T2-weighted images (a) first occasion proximal phalanx (b) second occasion proximal phalanx.

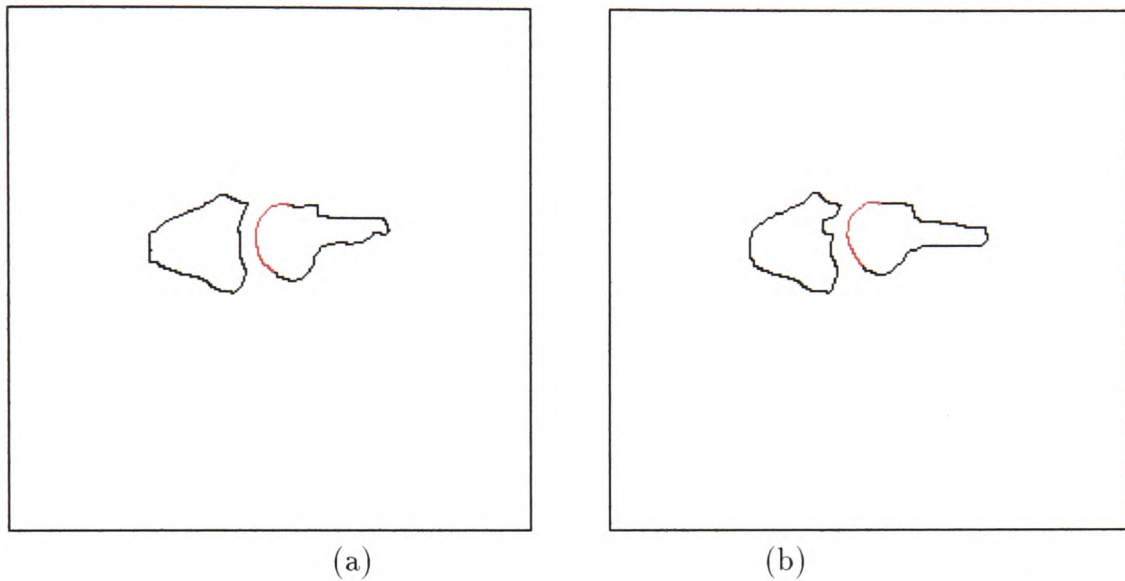


Figure 6.26: Narrower open curves on combined slice boundaries: Subject 5 T2-weighted images (a) first occasion proximal phalanx (b) second occasion proximal phalanx.

proximal phalanx and mostly trabecular bone for the middle phalanx. The automated sequence of algorithms that derive the bone boundaries starts with a scaling function that merges the heterogeneous trabecular bone regions. Consequently, the derived boundaries are representative of the lighter trabecular bone and omit the dense cortical bone. This condition does not really affect the middle phalanx boundaries, but does produce some very different boundaries for the proximal phalanx. Combining such boundaries could result in quite different combined slice boundaries

It is the aim at UHW to position the finger centrally in the MRI scanner. The acquired images will then represent the central volume of the finger. Thus, the four slices obtained will show symmetry about the centre. Consider the coloured version of a combined slice image illustrated in Fig. 6.27. The black, red, blue and green boundaries represent slices 1 to 4 respectively. The *MP* boundaries are nested and do not show symmetry about the central slices, suggesting that the four slices are not central to the finger. This could be as a result of different positioning of the finger

between scanning sessions or could indicate that the finger is not positioned centrally.

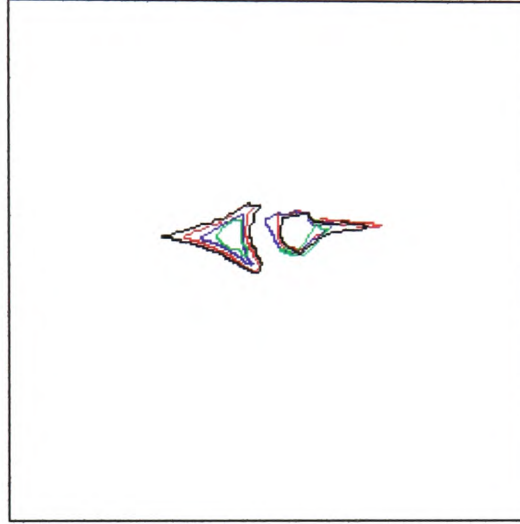


Figure 6.27: Merged boundaries from Subject 3, first occasion T2-weighted images.

There are also problems with the rotations determined for the middle phalanx. The position at which the best-fit ellipse is located is often on such a boundary that small rotations and translations of the best-fit ellipse can create more than one equivalent result. This condition is particularly seen in the superimposition of the best-fit ellipses for the middle phalanx onto the combined slice boundaries derived for subjects 2 and 5 (illustrated in Figs. 6.13 and 6.16 respectively).

6.3.1 Analysis of Assumptions

Each weighted image is acquired simultaneously and is, therefore, subject to the same movement, if any, during scanning. Therefore, it is assumed that the three weighted images are pre-registered. This assumption is backed up by some simple superimposition testing. Derived boundary image slices from different weighted scans are superimposed to show the pre-registration. For example, consider the superimposed images in Fig. 6.28. Fig. 6.28(a) shows, for subject 1 occasion 1, the superimposition of the PD-weighted combined slice boundary onto the T2-weighted combined slice

boundary. Fig. 6.28(b) shows, for subject 1 occasion 1, the superimposition of the T1-weighted combined slice boundary onto the T2-weighted combined slice boundary. A new image, N , is created by superimposing the active subimage onto the reference subimage. Pixel values are assigned from the following test:

$$N_{i,j} = \begin{cases} A_{i,j} & : A_{i,j} = R_{i,j} \\ Red & : A_{i,j} < R_{i,j} \\ Blue & : A_{i,j} > R_{i,j} \end{cases}$$

for all i, j in a specified subimage. (Note that no tolerance is needed here as the images are black and white.) The red and blue pixels indicate where pixels differ in the two images, however, the overall pre-registration is clearly seen.

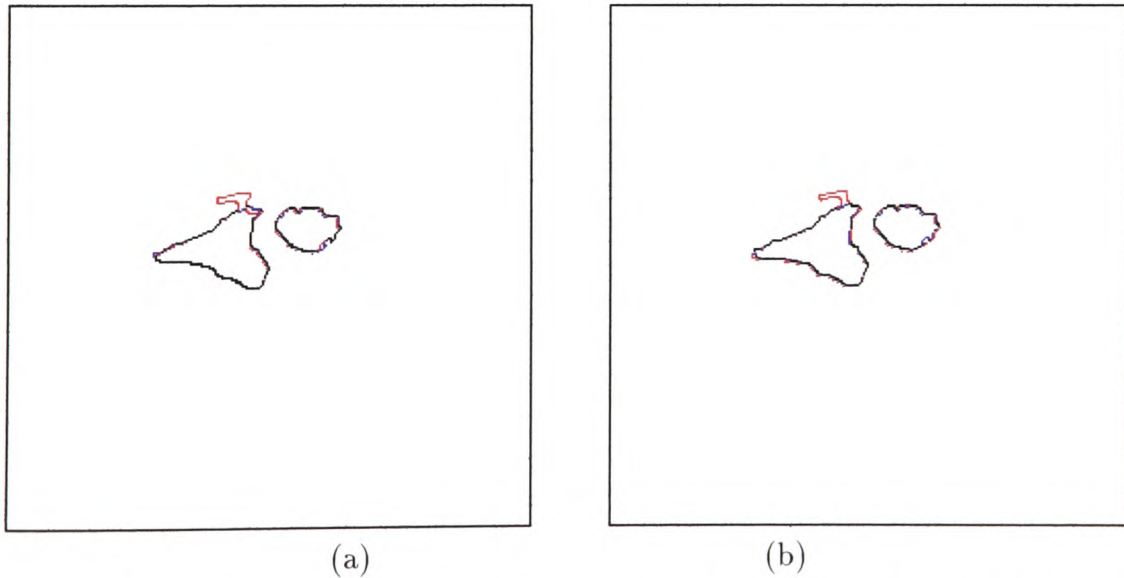


Figure 6.28: Superimposition of combined slice boundaries for subject 1 occasion 1 (a) PD-weighted combined slice boundaries superimposed onto T2-weighted combined slice boundaries (b) T1-weighted combined slice boundaries superimposed onto T2-weighted combined slice boundaries.

As the images are pre-registered, it is only necessary to take one image from both scanning sessions to calculate the registration parameters. The resulting parameters can be applied to all second occasion images to register them with the first occasion images.

To further test the registration system, the best-fit ellipse(s) determined for the reference image are also fitted to the combined slice boundaries for the other weighted images. As the images are assumed to be pre-registered, then the location of a best-fit ellipse should be the same for all the weighted images. Table 6.3 shows the best-fit ellipses determined for the first occasion images from subject 1.

<i>Bone</i>	<i>Occasion</i>	<i>Weight</i>	<i>cx</i>	<i>cy</i>	<i>a</i>	<i>b</i>	Ω	<i>% match</i>
MP	1	T2	129	112	14	11	76	65
MP	1	T2	129	111	14	11	89, 90	65
MP	1	PD	129	113	14	11	76	59
MP	1	PD	129	112	14	11	89, 90	59
MP	1	T1	130	113	14	11	71	74
PP	1	T2	145	109	13	11	29	49
PP	1	PD	146	109	13	11	2, 3, 4	39
PP	1	T1	145	109	13	11	9, 10, 29	43
<i>Narrower open curve results</i>								
PP	1	T2	140	115	9	3	33, 34	79
PP	1	PD	140	115	9	3	33	78
PP	1	T1	144	117	9	3	13	79

Table 6.3: Subject 1 fitting the best fit ellipses to different weighted image combined slice boundaries.

As can be seen from the table, three best-fit ellipses are determined by the Hough Transform for the reference (T2-weighted) image middle phalanx (*MP*) and a single best-fit ellipse for the proximal phalanx (*PP*). A search is made to find the best location of the best-fit ellipses on the other weighted image boundaries. For the *MP*, the same three orientations of ellipses are located at one pixel shifts in the *y*-direction

for the proton density-weighted (*PD*) image. For the T1-weighted image *MP*, the same one pixel shift is determined, but the orientation of the ellipse differs by at least 5 degrees. For the *PP* best-fit ellipse, the centre of the ellipse, (cx, cy) , is located on the T1-weighted image, but at a 1 pixel shift in the x -direction for the PD-weighted image. The orientation of the best-fit ellipse differs by at least 25 degrees for the PD-weighted image. The T1-weighted image locates the best-fit ellipse at the same orientation, but also at two other very different orientations.

Table 6.3 lists the results for subject 1 first occasion images only. Similar problems are found for the second occasion images and also for the other subjects. The reason for the discontinuity in the results is due to the nature of the boundaries being examined. The segment of *MP* boundary on which the best-fit ellipse is located is such that small changes in orientation and translations of the best-fit ellipse can result in more than one equivalent result. The segment of *PP* boundary on which the best-fit ellipse is located has approximately circular curvature resulting in many possible results. Thus, the Hough Transform fitting of a best-fit ellipse is very sensitive to slight changes in the boundaries being examined.

Selecting narrower open curves on the proximal phalanx (illustrated in Fig. 6.29) greatly improves the registration results. The narrower curve reduces the circular curvature of the boundary. The results from re-applying the Hough Transform to the narrower curves are also given in Table 6.3 under the heading “Narrower open curve results”). The percentage of boundary pixels lying on the best-fit ellipse is now nearly double what it was previously. In four out of the five subjects, narrowing the *PP* boundary greatly improves the percentage number of matching pixels.

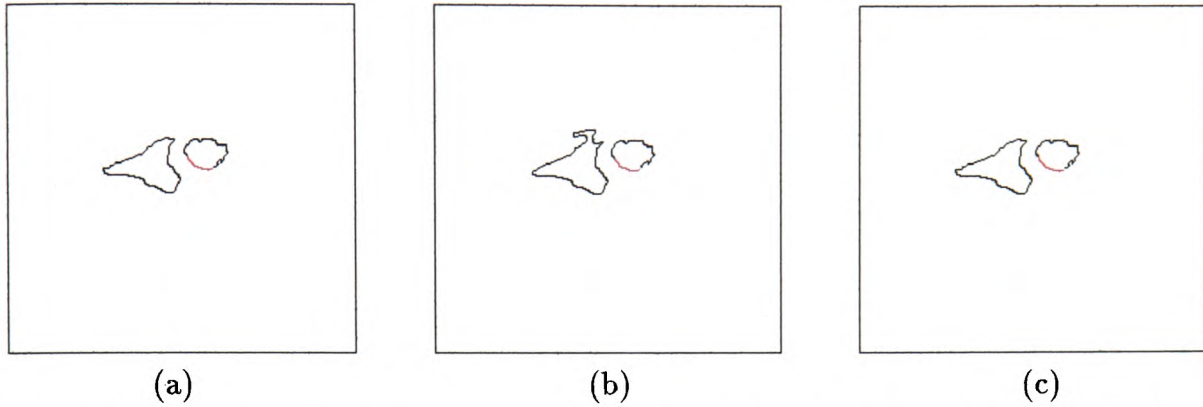


Figure 6.29: Narrower open curves on combined slice boundaries for Subject 1 (a) T2-weighted images (b) PD-weighted images (c) T1-weighted images.

6.4 Conclusions of Thesis

This thesis presents a novel system for the image processing and registration of MRI finger images. Such images are acquired at the University Hospital of Wales (UHW) from patients suffering from rheumatoid arthritis (RA). The purpose of this work is to aid clinicians' understanding of rheumatic disease and has already been of clinical benefit [Plant95a], listed in Appendix E.

Images of the same subject are taken over time and must be registered so that an accurate analysis of the effect of RA on the finger joint can be established. Movement during scanning, incorrect positioning for scanning and changes within the finger produce a need for registration.

Different weighted images (explained in Section 1.1.1) are acquired of the same finger. The weighted images are acquired simultaneously and are, therefore, subject to the same movement, if any, during scanning. It is assumed, therefore, that the weighted images taken on one occasion are pre-registered to each other.

The proximal interphalangeal finger joint poses a unique registration problem. No work on registering MRI finger images has been found in the literature by the author. The particular registration problems and complications are summarised here.

At UHW, the patient's finger is positioned in the MRI scanner with the aid of a plastic syringe. Any excess space in the syringe is packed to restrict movement during scanning. However, this restriction does not prevent all possible movement. Movement can occur in many directions. Forward and backward movements just require a simple translational shift to register the images. Rotational movements or bending at the articulated joint require a more complicated analysis. The nature of the positioning of the finger for scanning also means that on subsequent occasions it is impossible to reposition the finger in exactly the same location every time.

Many other researchers are interested in registering head or brain images. A very popular registration technique is the use of a stereotactic frame that is screwed rigidly to the patient's skull. This type of method is known as *extrinsic*. However, some authors even claim that, for brain images, "the effect of patient movement without rigid head fixation during scanning is negligible" [Maurer97]. In any case, extrinsic methods have been shown to be of no use to this application (explained in Section 2.2.2). Finger movement during or between scanning is one of the main reasons why registration is so vital.

MRI finger registration, therefore, requires an *intrinsic* method (explained in Section 2.2.2). Intrinsic methods are based on the image content only, for example, a set of landmarks, segmented structures or directly from the image grey values. Selecting appropriate anatomical landmarks is a labour-intensive, interactive process, which must be conducted by a knowledgeable user. Thresholding to segment the skin surface and thereby create a boundary is not a suitable method for MRI finger images due to the danger of slippage (explained in Section 1.2.1). Also, MRI finger image grey levels cannot be used to segment structures by thresholding or for direct registration (explained in Section 4.1.3).

Choosing appropriate features within MRI finger images is a key factor in the success of the registration method. For images taken over time, it must be possible to extract similar features from both images being registered. In Section 4.2.3, such structural boundaries within the finger image are located and these boundaries are used in the registration process.

Rheumatoid arthritis (RA) affects the synovial tissue, a normally thin lining of the joint, causing it to swell and destroy the joint. Registering MRI finger images of patients with RA will aid clinicians' understanding of the disease. To this end, an analysis of synovium, in terms of its size, shape and disease activity may be necessary. Therefore, any registration method which distorts an image is not employed in this thesis as vital information about synovium may be lost. Consequently, appropriate registration methods are taken to be rigid and global (explained in Sections 2.2.3 and 2.2.4 respectively). The boundaries used in the registration process represent segments of the two bones in the joint. However, registration parameters determined for both boundaries may not be the same making it impossible to produce a global registration without distorting the image.

A set of criteria for drawing region of interest boundaries is discussed in Section 3.1. Part of the work of this thesis is the creation of a drawtool (explained in Section 3.2) for the user-generation of region of interest (ROI) boundaries. Statistics are calculated from the ROIs (explained in Section 3.2.5) giving the size of the ROI, the average grey level and the standard deviation. A histogram of the spread of the grey levels is also made available by the drawtool. The design of a path structure for storing the ROI boundaries is detailed in Section 3.2.6 and RIFF files are shown to be suitable for storing the ROI path structure in a file.

Calculating statistics from MRI finger images shows that different weighted images have different means and standard deviations. Even images of the same weight do not have identical means and standard deviations. Therefore, standardising the images (explained in Section 4.1.2) is a necessary pre-processing technique before features are located in the images. Standardisation is performed on a comparative slice for slice basis. For example, slice 1 of a T2-weighted image acquired on a second occasion is standardised based on slice 1 of the reference image. However, if the chosen slices differ too much due to a large change in the positioning of the finger for scanning, then this could affect the derived features.

A number of standard image processing techniques have been experimented with to locate features in MRI finger images that can be used in the registration process. The Ideal Highpass Filter (explained in Section 4.3.3) shows that the sharpest edges in MRI finger images are not boundaries between specific tissue types but come from the heterogeneity within specific tissue structures. Therefore, a scaling algorithm is applied to the standardised images to merge the heterogeneous pixels into smooth regions. A sequence of algorithms is then applied to segment the smooth regions and locate their boundaries.

The boundaries derived by the processing stage are assumed to approximate segments of the two bones in the joint. These boundaries are consistently derived. Other boundaries, assumed to represent various soft tissues, are not consistently derived. The bone boundaries are considered to be reliable features for the registration process. The soft tissue boundaries are not considered reliable for the registration process and are, therefore, removed from the derived images.

A number of registration techniques have been experimented with. The sum of absolute values of differences approach to registration (explained in Section 5.1) gives local results which are inconsistent with global results. To combine local results would mean distorting one image to fit another which will result in the loss of important

synovium information.

A superimposition algorithm (explained in Section 5.2) has been applied to the original MRI finger images. The range of grey levels within the same tissue types varies so much that a tolerance level is required. However, the tolerance level has to be set to about 400 (out of a total of 4095 levels) to see a registration result. This level of tolerance is deemed to be too high. Superimposition can also be applied to derived boundary images. The derived images contain only black and white pixels and therefore do not require a tolerance level. Superimposing images taken over time produces some good registration results, but the registration only determines a translation shift. A rotational component is also necessary.

Two Hough Transform methods for registration were applied; these determined the required rotation and translation necessary to register two images. The Generalised Hough Transform (explained in Section 5.3.4) produces registrations where the number of matching pixels between two images of the same finger is, on average, 50%. A very high number of matching pixels would give confidence in the registration procedure. This relatively poor accuracy of matching reveals a fundamental characteristic nature of these boundaries. Although, by eye, two boundaries derived from images of the same patient taken on different occasions may appear almost identical, *i.e.* there is a similar characteristic shape, there are many small differences in actual positions of pixels along the characteristic shape.

The Hough Transform can also be used to fit an ellipse to a boundary. The boundaries derived in Section 4.2.3 are not particularly elliptical in general shape. However, certain open curves on the boundary are generally elliptic, for example, the head of the proximal phalanx and the joint side of the middle phalanx. The Hough Transform can be used successfully to find a best-fitting ellipse, at any orientation, to selected open curves on the boundary. The discretization of the parameter space yields a particular rounding feature of the Hough Transform. However, the displacement of the ellipse

parameters between two images can give the relative rotation and translation required to register the images.

Results of the Hough Transform fitting of ellipses shows that the derived boundaries can sometimes differ considerably across slices. A new technique has been developed to try and overcome this problem. The slice boundaries are combined to create the largest possible boundary shape across the four slices. The combined slice approach (explained in Section 5.4) produces images that contain boundaries that show greater similarity across different occasions of the same patient.

For the proximal phalanx (*PP*), the elliptical segments of boundary produce good registrations. The derived registration parameters appear adequate for the entire *PP* boundary. However, for certain subjects, the resulting registrations were misleading. The reason for this complication is the approximately circular curvature of the *PP* boundary segment on which the best-fit ellipses are located. Consequently, the best-fit ellipse can be located in many places on the boundary. The particular case of a circle is even worse as all rotations are identical and no rotation result for registration is determined. Thus, a restriction must be incorporated into the system to prevent the best-fit ellipse being a circle, *i.e.* $a \neq b$, to ensure that a useful ellipse is fitted. Narrowing the open curve on the proximal phalanx to reduce the circular curvature greatly improves the results.

Examining the way in which the best-fit ellipse actually fits the proximal phalanx (*PP*) highlights the fact that the combined slice boundaries of a subject over time are not the same size and shape. Further, the middle phalanx (*MP*) and proximal phalanx (*PP*) boundaries differ across the slices. The *MP* boundaries have the same characteristic shape, but the *PP* boundaries are sometimes completely different. The boundaries differ for a number of reasons. Bone is made up of two structures. The dense (dark in MRI) cortical bone surrounds the less dense (lighter in MRI) trabecular bone. The MRI finger images clearly show both densities for the *PP* and mostly

trabecular bone for the *MP*. The automated sequence of algorithms that derive the bone boundaries starts with a scaling function that merges the heterogeneous trabecular bone regions. Consequently, the derived boundaries are representative of the lighter trabecular bone and omit the dense cortical bone. This condition does not affect the characteristic shape and size of the *MP* boundaries obtained, but does produce some very different boundaries for the *PP*. Combining such boundaries could result in quite different combined slice boundaries.

The Hough Transform results for the combined slice boundaries show that, in general, the *MP* boundaries are more reliable than the *PP* boundaries. The Hough Transform fitting of a best-fit ellipse is very sensitive to slight changes in the boundaries being examined.

The variations in the boundaries obtained by combining the individual slice boundaries also suggest that the finger is not always positioned sufficiently centrally when MRI scans are taken.

The application of Fourier Descriptors and Moments to MRI finger images is very sensitive to finger positioning prior to scanning. The centroid of an image could be useful for translational registration. However, incorrect positioning for scanning, over time, can lead to gross mis-registrations. Applying Fourier Descriptors and Moments to user-selected open regions of the images is possible, but if the open regions are not the same, which is highly likely, then matching based on centroid could lead to a mis-registration.

The Hough Transform fitting of ellipses to open curves is by far the most reliable method for the registration of MRI finger images. Care must be taken over selecting the open region, but differences in the open regions are not as critical for the Hough Transform as for centroid matching. This is due to the ellipse being fitted to a fixed boundary when using the Hough Transform as opposed to using moments where the centroid may move as the open region varies in size.

The final registration system is composed of three stages. Firstly, the original images are processed to determine features to be used in the registration process. The derived features are boundaries that are assumed to approximate the two bones in the joint. The second stage of the registration system is the application of the Hough Transform to locate best-fit ellipses to the derived boundaries. Finally, the relative rotations and translations determined from the second stage are applied to the original images.

The developed system is semi-automatic and requires a knowledgeable user to consider the registration results for accuracy. The number of pixels lying on a best-fit ellipse is calculated and sometimes produces a very high percentage of fitting pixels. However, the above mentioned problems can produce results which are obviously not correct.

The combined slice approach to combining boundary images is an intermediate step between 2D methods and stacking the 2D slices.

The author believes that the work of this thesis has proposed a method of MRI finger image registration which successfully registers the middle phalanx in most cases and the proximal phalanx in some cases. In producing this registration system, many features of MRI finger images not previously reported have been discovered. These are listed here:

- images acquired simultaneously are pre-registered;
- necessity of using an intrinsic method;
- heterogeneity of grey levels within tissue regions;
- derivation of bone boundaries produces the most reliable structures for registration;
- combined slice boundaries represent a four slice volume and produce better registration results;
- many standard image processing techniques are very sensitive to small changes

along the bone boundaries.

- the Hough Transform fitting of ellipses to combined slice boundaries is the most reliable registration method for MRI finger images.

6.5 Future Work

The development of a combined slice image leads to improved registration results. The results also suggest that finger positioning needs to be improved. The combined slice image provides a mid-way analysis between 2D registration techniques and 3D methods based on a stack of 2D slices. Future work should investigate 3D techniques. Suggested techniques to investigate are stacking the 2D slices [Bajcsy83, Wang96] or possibly by creating a 3D image [Bajcsy89, Hemler94, Hemler95].

Further testing of the registration system can be done with the use of a phantom and/or a finger ex-vivo. Moving such objects by fixed amounts will enable a comparison between registration results and known quantities. Such experiments will also give an analysis of any geometric distortions in the MRI finger images.

The Hough Transform registration results are very sensitive to changes along the boundary. Other goodness-of-match measures can be experimented with to improve the results, *e.g.* least squares fitting of a curve to the finger boundary. It is expected that least squares fitting will accommodate the small changes along the characteristic boundary shape that cause many problems for the Hough Transform methods reported on in this thesis.

The effects of rheumatoid arthritis and osteo arthritis may change the bone surface over time, perhaps over durations as short as three to six months with severe disease. With the addition of further data it would be possible to re-analyse the performance of this system for patients with such severe disease.

Appendix A

Inter Observer Variability Graphs

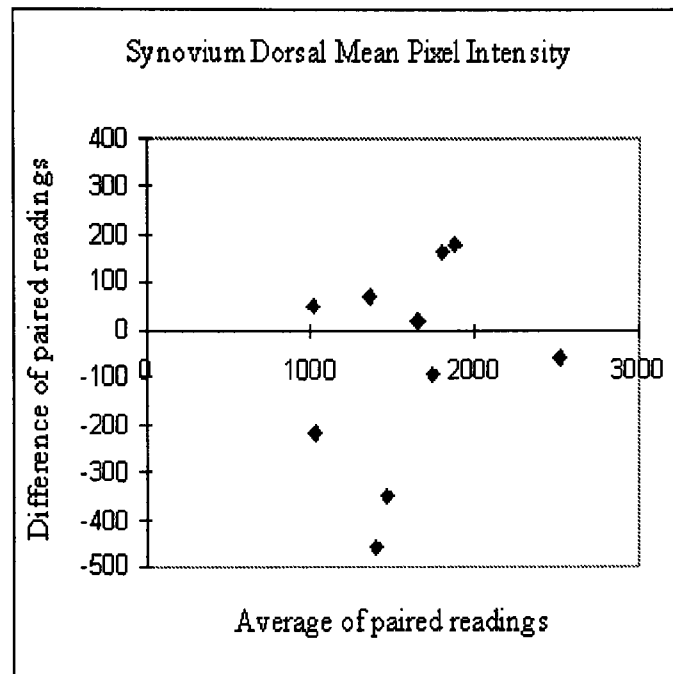


Figure A.1: Synovium Dorsal Mean Pixel Intensity.

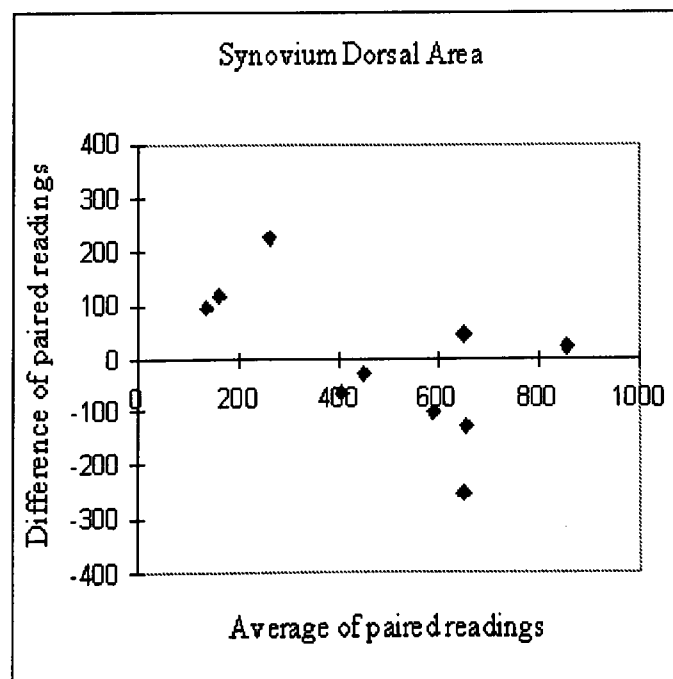


Figure A.2: Synovium Dorsal Area.

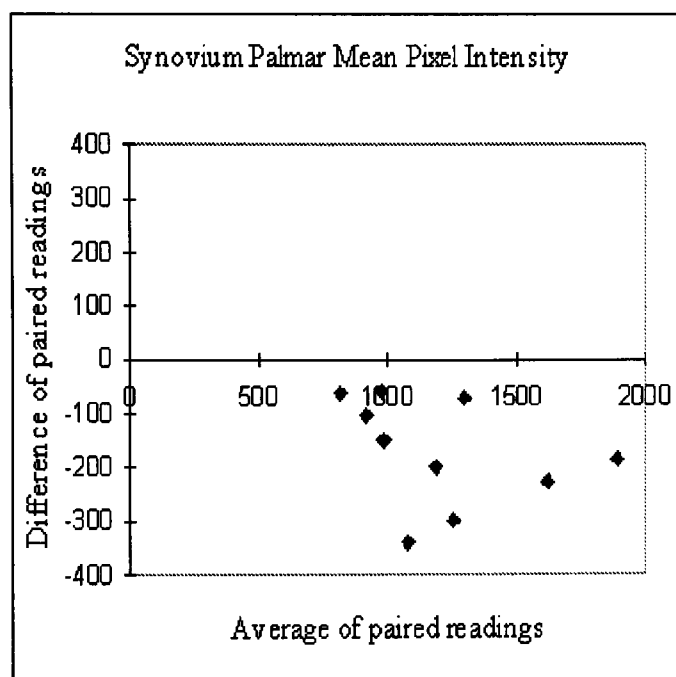


Figure A.3: Synovium Palmar Mean Pixel Intensity.

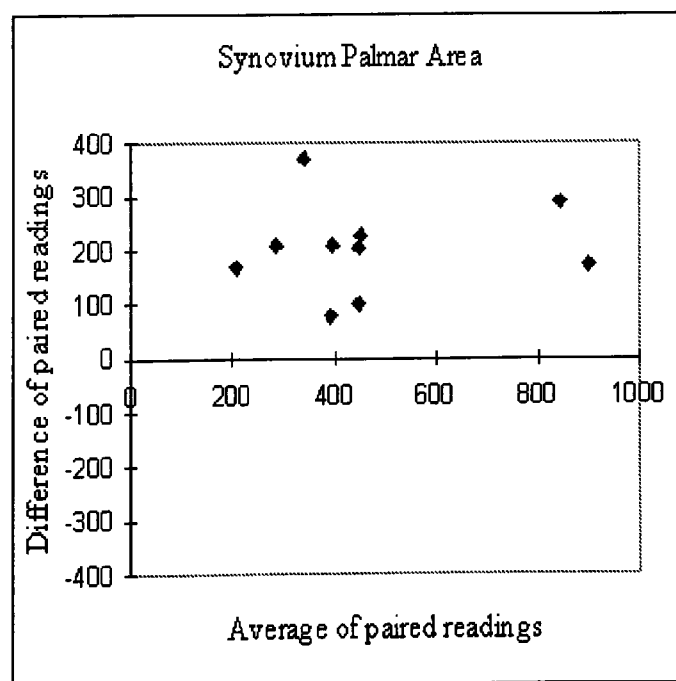


Figure A.4: Synovium Palmar Area.

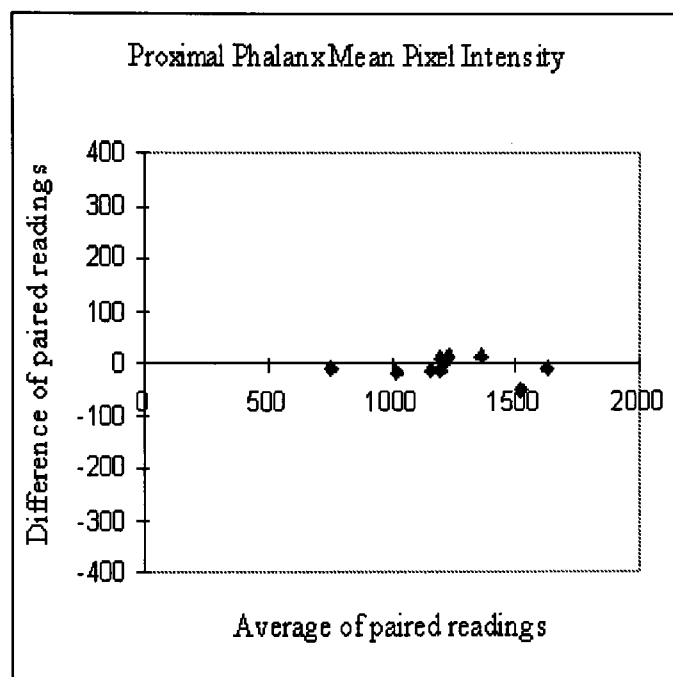


Figure A.5: Proximal Phalanx Mean Pixel Intensity.

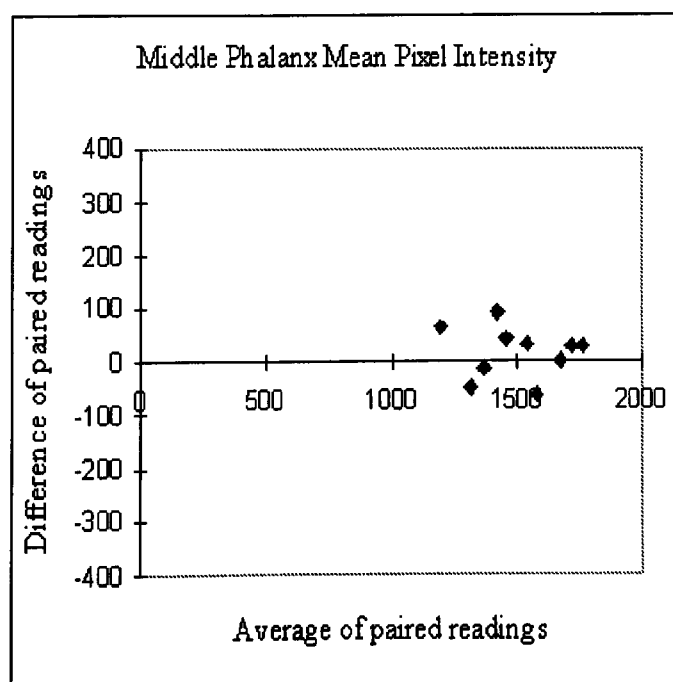


Figure A.6: Middle Phalanx Mean Pixel Intensity.

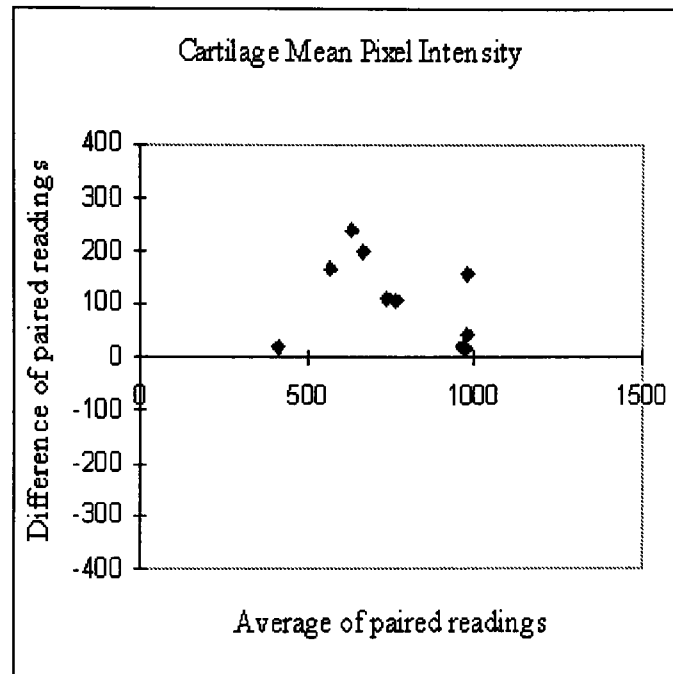


Figure A.7: Cartilage Mean Pixel Intensity.

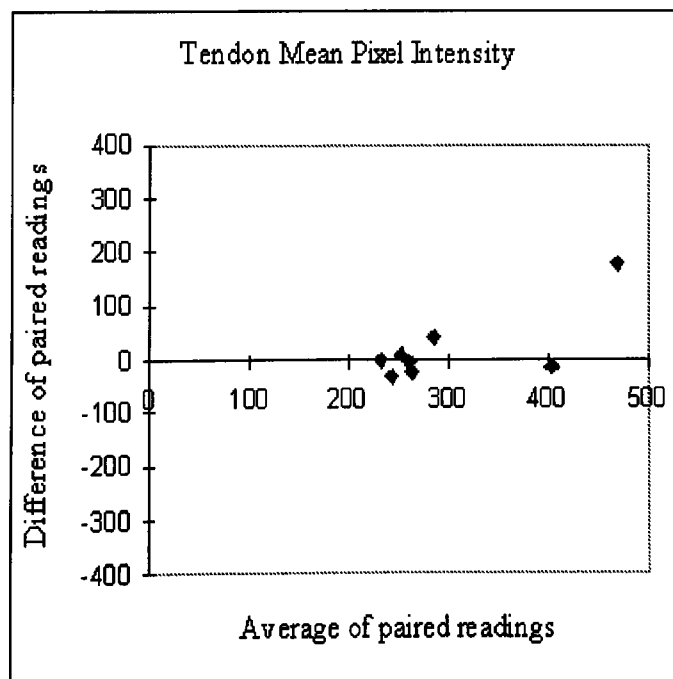


Figure A.8: Tendon Mean Pixel Intensity.

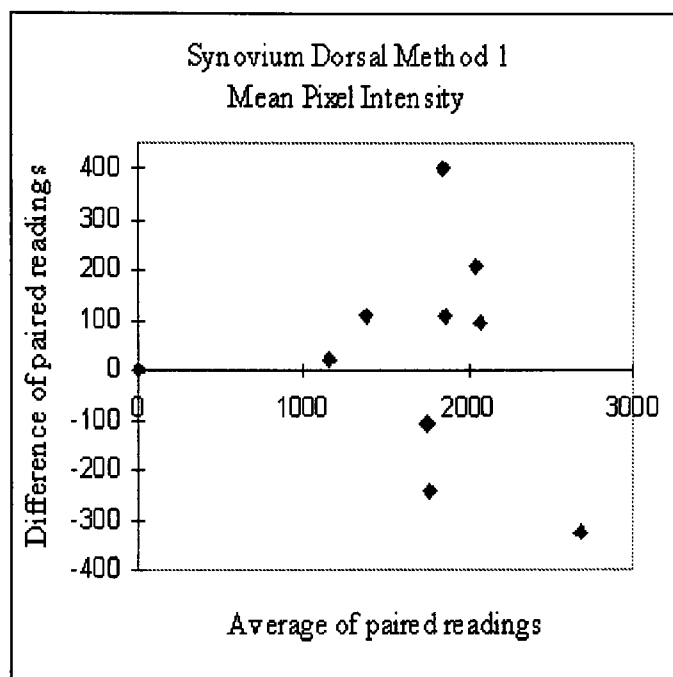


Figure A.9: Synovium Dorsal Method 1 Mean Pixel Intensity.

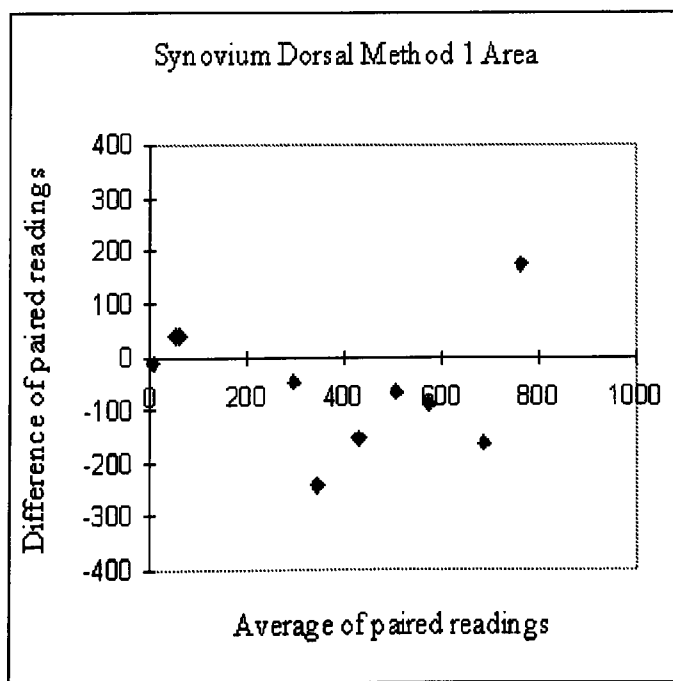


Figure A.10: Synovium Dorsal Method 1 Area.

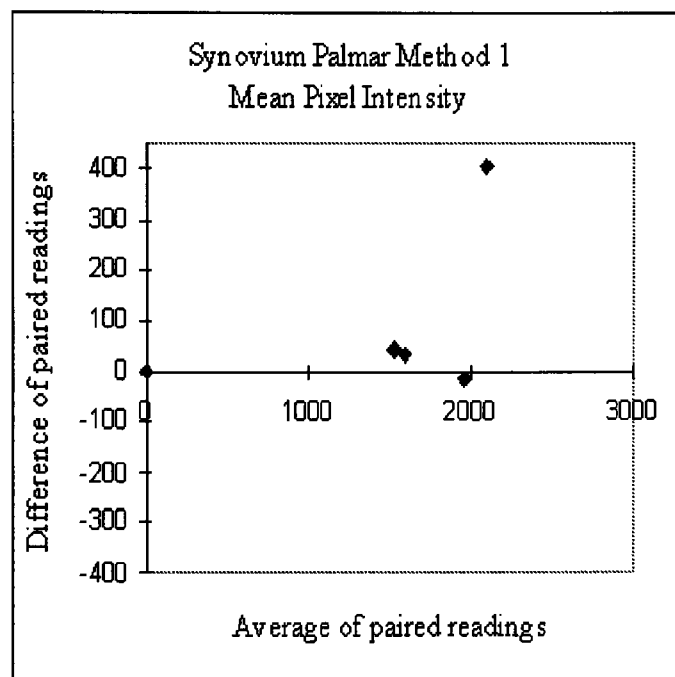


Figure A.11: Synovium Palmar Method 1 Mean Pixel Intensity.

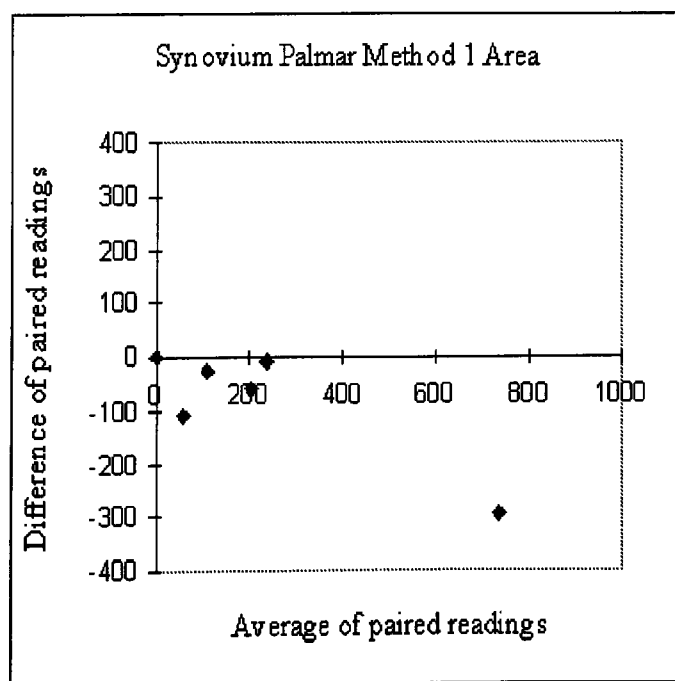


Figure A.12: Synovium Palmar Method 1 Area.

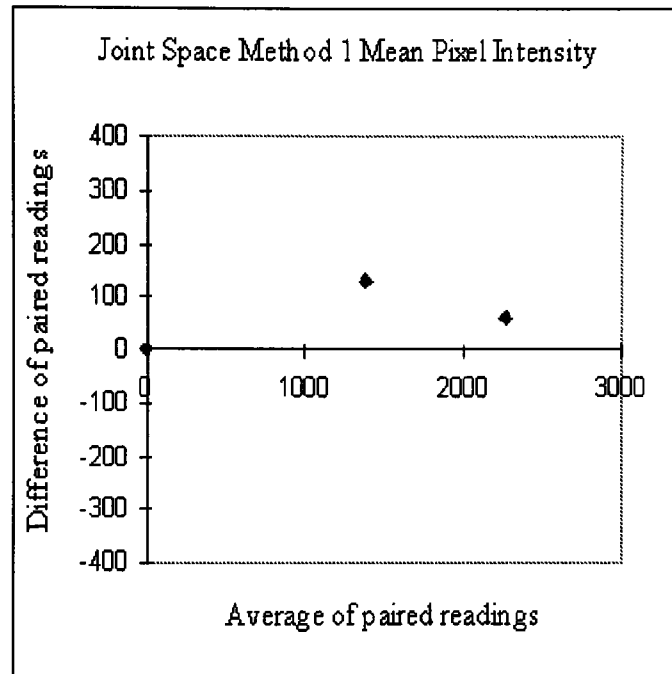


Figure A.13: Joint Space Method 1 Area.

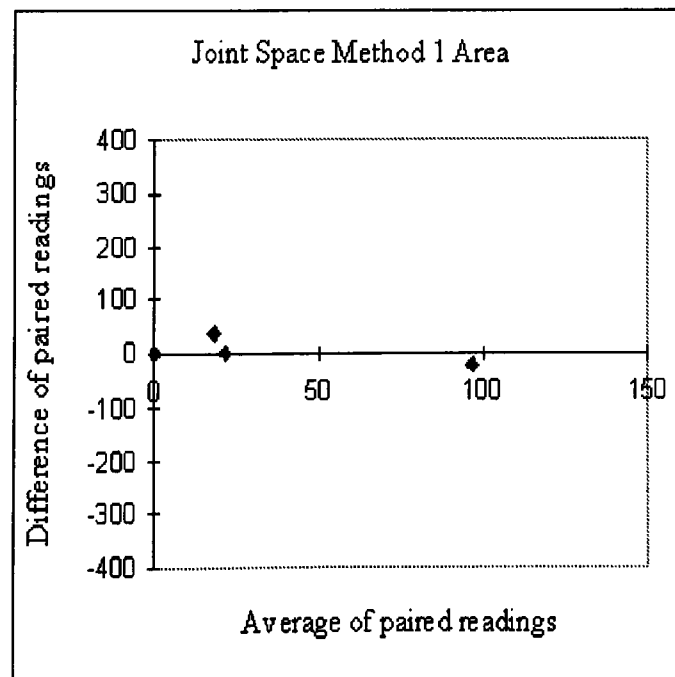


Figure A.14: Joint Space Method 1 Area.

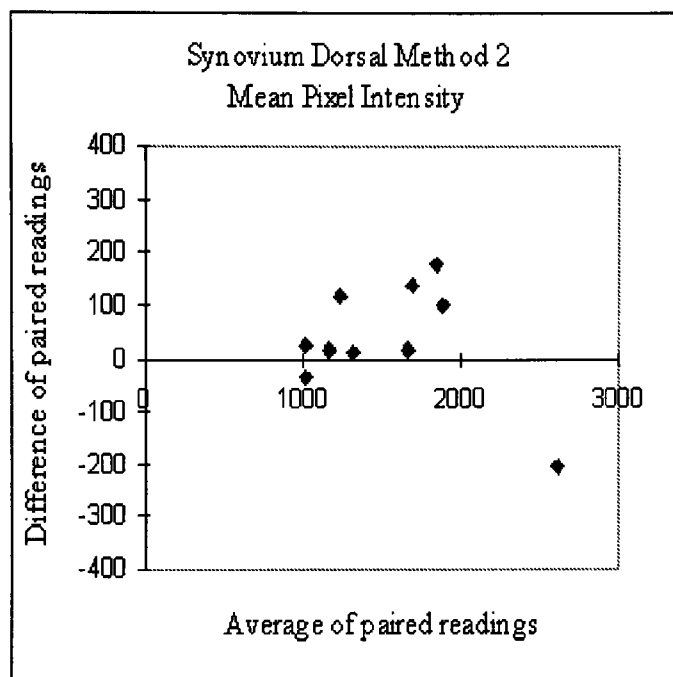


Figure A.15: Synovium Dorsal Method 2 Mean Pixel Intensity.

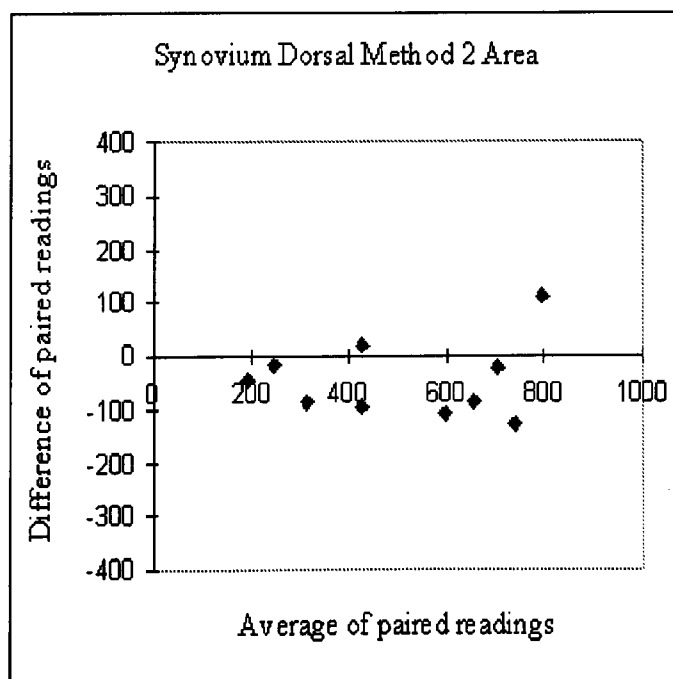


Figure A.16: Synovium Dorsal Method 2 Area.

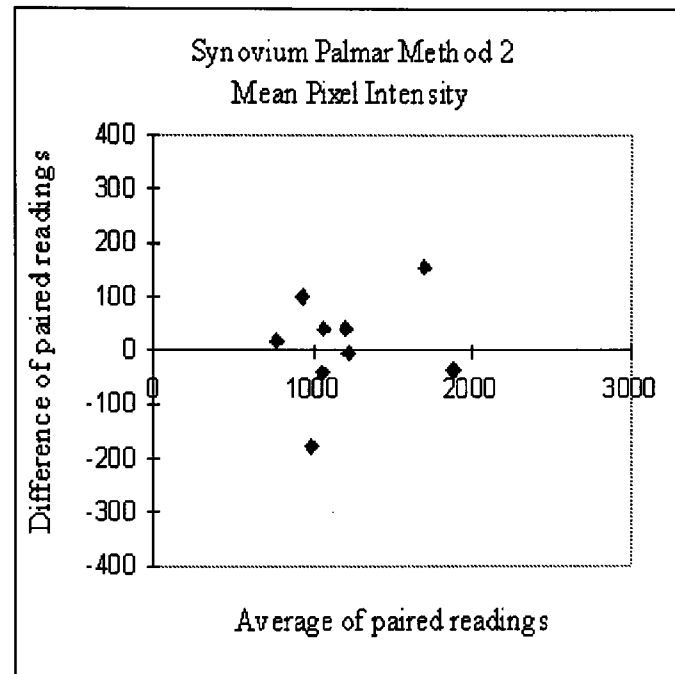


Figure A.17: Synovium Palmar Method 2 Mean Pixel Intensity.

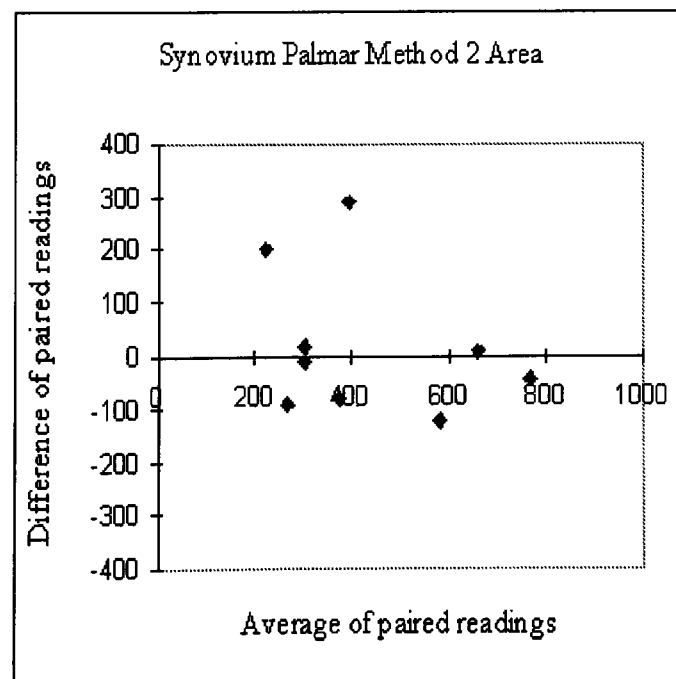


Figure A.18: Synovium Palmar Method 2 Area.

Appendix B

Polygon Complexities

In Chapter 3 a brief overview of the established rules for determining the interior points of a polygon is given. This appendix gives a detailed explanation of these rules.

Polygons are drawn around specific regions of interest (ROIs) in MRI finger images. The user selects the vertices that make up the polygon. The vertices are stored in a vertex list in an anticlockwise cycle. The Visual Basic Line function is used to draw the polygon edges. The General Bresenham Algorithm, as explained in Section 3.2.3, is used to find the edge co-ordinates for each polygon edge. The edge co-ordinates are stored in an edge list and sorted into scan-line order, *i.e.* y first, then x .

The co-ordinates in the edge list are distinguishable as those which are vertices and those which are edge co-ordinates. A simple check that a co-ordinate from the edge list is not in the vertex list is sufficient to show that it is an edge co-ordinate. Pairs of edge co-ordinates (*i.e.* not vertices) are extracted from the edge list as bounding pixels to scan between to find the interior points along a particular scan-line. Edge co-ordinates that are vertices must be treated differently.

The polygon vertices can be grouped as those which:

- are edge equivalent - *i.e.* they can be treated as non-vertex edge co-ordinates.
- are a peak or a trough - different rules are required depending on whether the peak/trough is *internal* or *external* to the polygon.
- lie on a horizontal edge - these require a third approach.

Each of these cases are now examined and rules are derived as to how they should be treated. Determining the rules for each case requires the direction of the cycle of vertices to be specified. In this work, the established rules are based on an anticlockwise cycle of vertices. If the obtained vertex list is clockwise, the order of the vertices is reversed. It is possible to use a clockwise cycle of vertices, but this would necessitate changes to the established rules.

B.1 Edge Equivalent Vertices

Some vertices can be treated as non-vertex edge co-ordinates (illustrated in Fig. B.1). Consider scan-line j intersecting with the polygon at vertices A and C in Fig. B.1(a) and vertex A and edge co-ordinate p in Fig. B.1(b). At A , scan-line j enters the polygon. At C and p respectively, scan-line j exits the polygon.

In Fig. B.1(a), vertices A and C are treated as a pair of non-vertex edge co-ordinates and are scanned between to find the interior points along scan-line j . In Fig. B.1(b), vertex A and edge co-ordinate p are paired to scan between.

A vertex is classified as edge equivalent, if the vertices either side of it in the vertex list also lie either side of it along the y -axis. In Fig. B.1(a) and (b), vertices B and D lie either side of vertex A in the anticlockwise cycle of vertices. Vertices B and D also lie either side of vertex A along the y axis. Therefore, vertex A is classified as edge equivalent. The same result is obtained for vertex C in Fig. B.1(a).

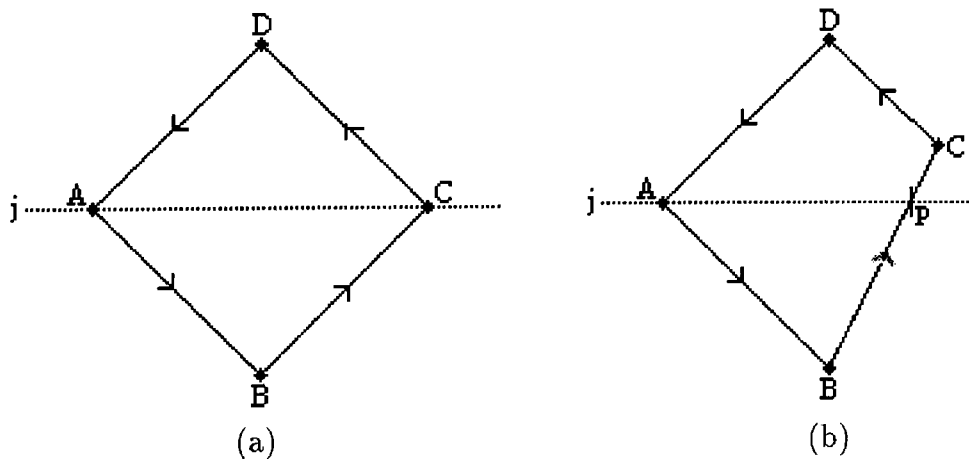


Figure B.1: Edge equivalent vertices (a) vertices A & C treated as non-vertex edge co-ordinates (b) vertex A treated as a non-vertex edge co-ordinate.

B.2 Peaks / Troughs

Some of the vertices extracted from the edge list could be peaks and some could be troughs. Consider the polygon in Fig. B.2. Vertices C , F and H are peaks and vertices B , D and G are troughs. Further, vertices B , D , F and H are considered to be *external* to the polygon and vertices C and G are considered to be *internal*.

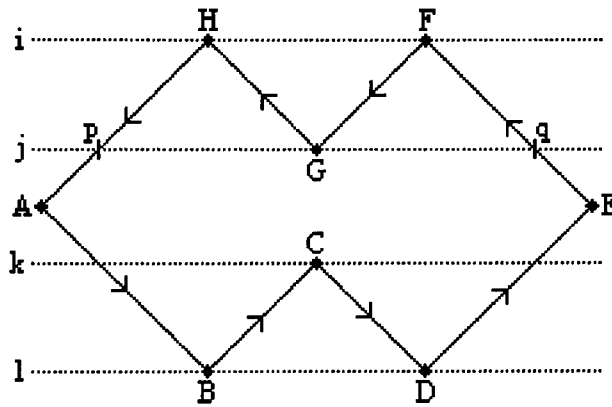


Figure B.2: Vertices as peaks/troughs.

To determine whether a vertex is an external or internal peak or trough requires two steps. The first step classifies the vertex as a peak/trough and the second step classifies the vertex as external or internal.

A vertex is classified as being a peak/trough if the vertices either side of it in the anticlockwise cycle of vertices both lie either above or below it along the y -axis. For example, consider vertex B in Fig. B.2. Vertices A and C lie either side of B in the anticlockwise cycle of vertices. Vertices A and C both lie above B along the y -axis. Therefore, B is classified as a peak/trough. The same result will follow for vertices C , D , F , G and H .

The second step determines whether the peak/trough vertices are external or internal to the polygon, by considering what has already happened along the scan-line. For example, vertex B in Fig. B.2, represents the first intersection with the polygon along scan-line l . Therefore, this “peak/trough” must be external. An external

peak/trough represents a single pixel on the polygon boundary and therefore a single pixel must be taken rather than scanning between two points. Continuing along scan-line l , another intersection with the polygon is found at vertex D . Again, D is classified as an external peak/trough and another single pixel is taken. Vertices F and H are also classified as external peaks/troughs by the same method.

Now consider the cases of vertices C and G in Fig. B.2. The intersection at point p means that scan-line j has entered the polygon at p . Therefore, p has already been determined as the start point for scanning. Vertex G , is the next co-ordinate in the edge list and must be tested to see if this vertex represents the end of the polygon along this scan-line. The fact that scan-line j has already entered the polygon at p and that G is a peak/trough, means that G must be internal to the polygon. As G is classified as an internal peak/trough, it cannot be the end of the polygon along scan-line j . Therefore, G is effectively ignored and the next co-ordinate from the edge list (q) is examined. As q is a non-vertex edge co-ordinate it is taken as the true end point for scanning between.

B.3 Horizontal edges

The final case of vertices are those which lie on a horizontal edge. As the scan-lines are horizontal lines proceeding from left to right, the co-ordinates from vertical edges are treated as non-vertex edge co-ordinates. A scan-line intersecting with these co-ordinates represents entering or exiting the polygon. Difficulties arise when a scan-line intersects with a horizontal edge. There are a number of cases of where a horizontal edge may occur in a polygon. The different cases are illustrated in Figs. B.3 to B.5.

A horizontal edge may be the only part of the polygon on a particular scan-line, for example, BC in Fig. B.3. Similarly, a horizontal edge may be independent to the rest of the polygon on a particular scan-line, for example, EF in Fig. B.3. Alternatively, a horizontal edge may start (AF in Fig. B.4(a)), end (DE in Fig. B.4(b)) or fall in the

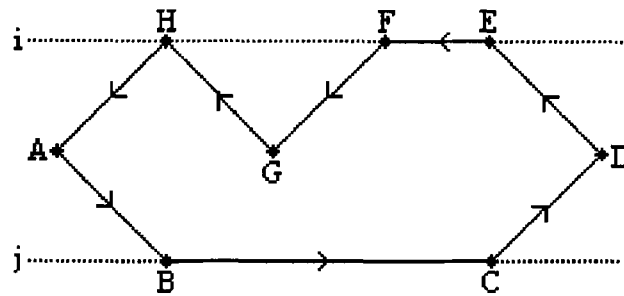


Figure B.3: Edge equivalent vertices on a horizontal edge.

middle of the polygon on a given scan-line (CD in Fig. B.6).

Each of these cases must be treated differently. The established rules are presented here and are based on an anticlockwise cycle of vertices for images with the origin at the top left corner.

Consider the horizontal edge BC in Fig. B.3. Scan-line j intersects with vertex B and is, therefore, entering the polygon. Similarly, at the intersection with vertex C scan-line j is exiting the polygon. Therefore, B and C are treated as non-vertex co-ordinates and are scanned between to find the interior points along scan-line j . The independent horizontal edge EF along scan-line i is treated in the same way.

The more difficult cases of horizontal edges are where the edges are not independent of the rest of the polygon along the scan-line on which they fall. For example, consider the polygon in Fig. B.4(a). The first intersection with the polygon along scan-line j is vertex A . Therefore, the scan-line is entering the polygon at A . Vertex F is the next co-ordinate in the edge list. As can be seen from the diagram, F is not the end point for scanning, along j . This is determined by considering the direction of the *previous* vertex to F in the vertex list, *i.e.* vertex E .

If the previous vertex has a lower y co-ordinate then

the intersection with the vertex is not exiting the polygon.

If the previous vertex has a higher y co-ordinate then

the intersection with the vertex is exiting the polygon.

(This latter case is illustrated in Fig. B.5 vertex F .)

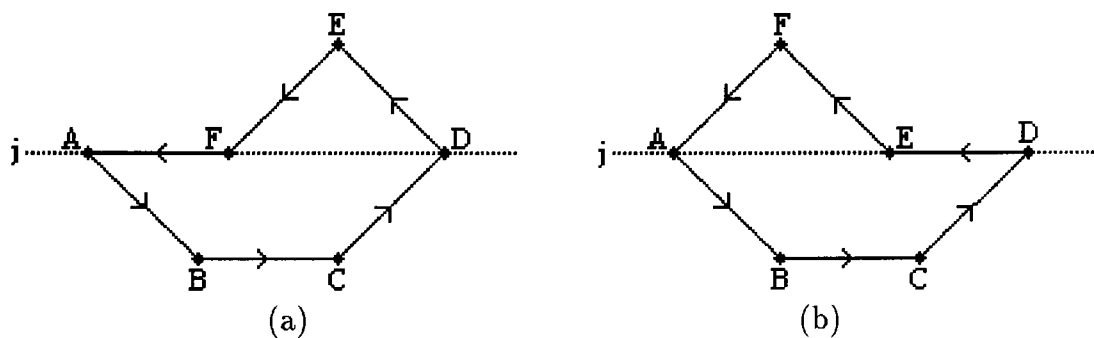


Figure B.4: Horizontal edges at the (a) start (b) end of a scan-line.

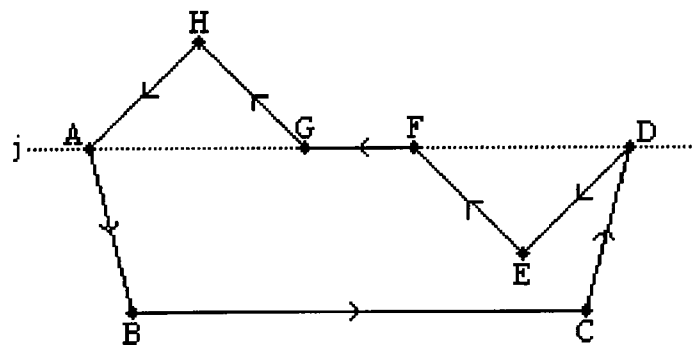


Figure B.5: Horizontal edge in the middle of a scan-line. Scan-line j intersecting at vertex F is exiting the polygon.

Now consider the polygon in Fig. B.4(b). Along scan-line j , the intersection with vertex A will already have been determined as the start point for scanning. The next co-ordinate in the edge list is vertex E , the start of the horizontal edge DE . As there must be another co-ordinate in the edge list for the end of this horizontal edge, E is

effectively ignored and D is tested to see if it is the end point for scanning. As D is the last co-ordinate on this scan-line, it is taken as the end point for scanning from A .

Finally, consider the polygons in Figs. B.6 and B.7. Using the above rules, vertex A is the start point for scanning along scan-line j and vertex C has been “ignored”. Vertex D , at the end of the horizontal edge, is tested to see if the scan-line intersecting at this point is exiting the polygon. In these examples, the *previous* vertex to D in the vertex list is the start of the horizontal edge (vertex C). Therefore, the *next* vertex in the vertex list is tested and the rules are inverted:

If the next vertex has a higher y co-ordinate, then

the intersection with the vertex is not exiting the polygon.

If the next vertex has a lower y co-ordinate, then

the intersection with the vertex is exiting the polygon.

Having considered all possible polygons, the above rules are combined into a single algorithm for determining the interior points of a polygon. A pseudocode listing of the algorithm is given in Appendix C.

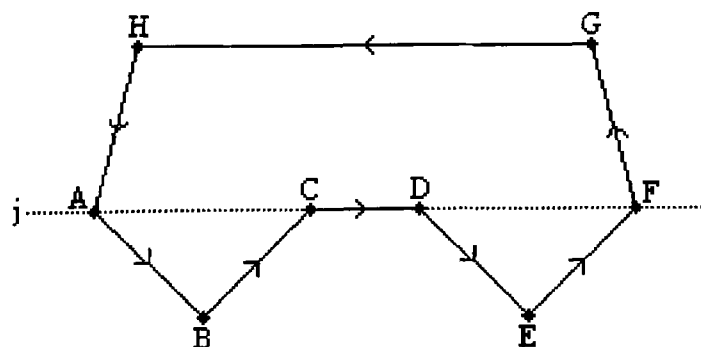


Figure B.6: Horizontal edge in the middle of a scan-line. Scan-line j intersecting at vertex D is not exiting the polygon.

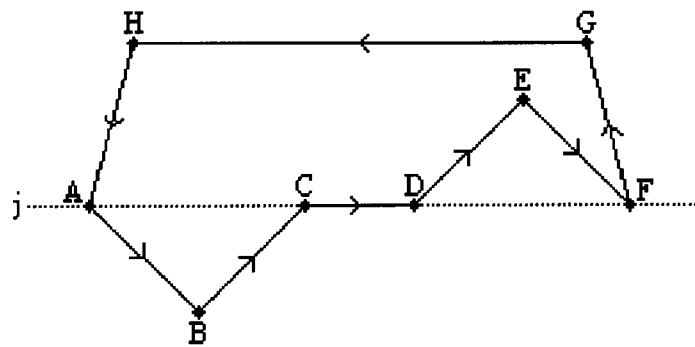


Figure B.7: Horizontal edge in the middle of a scan-line. Scan-line j intersecting at vertex D is exiting the polygon.

Appendix C

Pseudocode for Interior Points of a Polygon Algorithm

Chapter 3 presents an algorithm for determining the interior points of a polygon. A full description of the rules for determining these points is given in Appendix B. In this section a listing of the algorithm to find the interior points of a polygon is given in pseudocode. Firstly, here are some definitions:

- (sx, sy) and (ex, ey) are the start and end edge co-ordinates, respectively, between which to scan to find the interior points of the polygon along a particular scan-line.
- VERTEX_LIST_X and VERTEX_LIST_Y are two one-dimensional arrays which contain the x and y co-ordinates, respectively, for the vertices that make up the polygon.
- EDGE_LIST_X and EDGE_LIST_Y are two one-dimensional arrays which contain the x and y co-ordinates, respectively, for each edge co-ordinate, obtained using the General Bresenham Algorithm, as explained in Section 3.2.3.
- Function FIND_VERTEX(x, y) determines if point (x, y) is a vertex in the vertex list.
- Function TEST_EXEY(x, y) tests if (x, y) is the correct end point for scanning to from (sx, sy) .
- Function SCAN_LINE(sx, sy, ex, ey) retrieves the interior points from (sx, sy) to (ex, ey) for the statistics calculations explained in Section 3.2.5.
- i is an array counter.

The main algorithm is:

```

i = 0
loop through all edge coords
    sx = EDGE_LIST_X[i]
    sy = EDGE_LIST_Y[i]
    increment i
    FIND_VERTEX(sx, sy)    {test if (sx, sy) is in the vertex list}
    If (sx, sy) is a vertex and (sx, sy) is a peak/trough
        ex = sx    {(sx, sy) is an external peak/trough}
        ey = sy    {∴ only take 1 pixel}
    else
        loop until correct end point found
            ex = EDGE_LIST_X[i]
            ey = EDGE_LIST_Y[i]
            increment i
            {test if (ex, ey) is the true end point for scanning}
            TEST_EXEY(ex, ey)
        end loop
    end if
    {scan from (sx, sy) to (ex, ey) for the interior points}
    SCAN_LINE(sx, sy, ex, ey)
end loop

```

Function $\text{FIND_VERTEX}(x, y)$ determines whether (x, y) is a vertex by searching for (x, y) in the vertex list. If (x, y) is a vertex, the function also stores the previous and next vertices to (x, y) from the anticlockwise cycle of vertices. Firstly, some definitions:

- j is an array counter.
- (pre_x, pre_y) are the co-ordinates of the previous vertex to (x, y) , if (x, y) is a vertex.
- $(post_x, post_y)$ are the co-ordinates of the next vertex to (x, y) , if (x, y) is a vertex.

$\text{FIND_VERTEX}(x, y)$

$j = 0$

loop through all vertices

if $x = \text{VERTEX_LIST_X}[j]$ and $y = \text{VERTEX_LIST_Y}[j]$

$\{(x, y) \text{ is a vertex, } \therefore \text{ set } (pre_x, pre_y) \text{ and } (post_x, post_y)\}$

$pre_x = \text{VERTEX_LIST_X}[j-1]$

$pre_y = \text{VERTEX_LIST_Y}[j-1]$

$post_x = \text{VERTEX_LIST_X}[j+1]$

$post_y = \text{VERTEX_LIST_Y}[j+1]$

exit loop

end if

increment j

end loop

Function TEST_EXEY(x, y) tests if (x, y) is the correct end point to scan to from (sx, sy) for a particular scan-line.

TEST_EXEY(x, y)

 FIND_VERTEX(x, y) {test if (x, y) is in the vertex list}

 if (x, y) is not a vertex

(x, y) is an edge co-ordinate and is \therefore the true end point for scanning

 else {find correct end point}

 CASE (x, y) is an edge equivalent vertex

(x, y) is the true end point

 CASE (x, y) is a peak/trough {must be an internal peak/trough \therefore ignore}

(x, y) is not the true end point

 CASE (x, y) starts a horizontal edge

(x, y) is not the true end point {there is an end to the horizontal edge}

 CASE (x, y) ends a horizontal edge

 if (x, y) is the end of the polygon on this scan-line

(x, y) is the true end point

 else

 if (x, y) is exiting the polygon

(x, y) is the true end point

 else

(x, y) is not the true end point

 end if

 end if

 end CASE

 end if

Appendix D

Generalised Hough Transform Detailed Results

The Generalised Hough Transform is explained in Section 5.3.4 and the results summarised. In this section, the results of the Generalised Hough Transform are given in detail. The Generalised Hough Transform is applied to boundaries derived from MRI finger images as explained in Section 4.2.3. The initial stage of the boundary sequence requires a scaling factor. With differently-weighted images, the scaling factor required for each image will not be the same. The scaling factors used for each image are given in each section.

In each case the results (displayed in tables below) show the best number of matching pixels against registration position. As a test of the accuracy of the results, each image in a data set has the Generalised Hough Transform applied to itself. In each case, the results give a perfect match as would be expected.

For every pair of images used with the Generalised Hough Transform, both images are used as the reference image to create the R-Table (explained in Section 5.3.4) and the results compared.

The results are grouped in data sets. The first data set considers some PD-weighted images. The second data set considers Gadolinium-enhanced T1-weighted images. The third data set considers different weighted images. Finally, the last data set considers images from different patients.

In each data set, the Generalised Hough Transform has first been applied to the entire boundaries of both bones (the proximal phalanx (PP) and the middle phalanx (MP) (explained in Section 1.1.2)) in each image. Secondly, the Generalised Hough Transform has been applied to part of the boundaries of both bones in each image. Results are provided firstly with no orientation and then secondly with orientation.

D.1 PD-Weighted

D.1.1 Data set 1

In this section, the results derived from applying the Generalised Hough Transform to a pair of PD-weighted images (illustrated in Fig. D.1) are given.

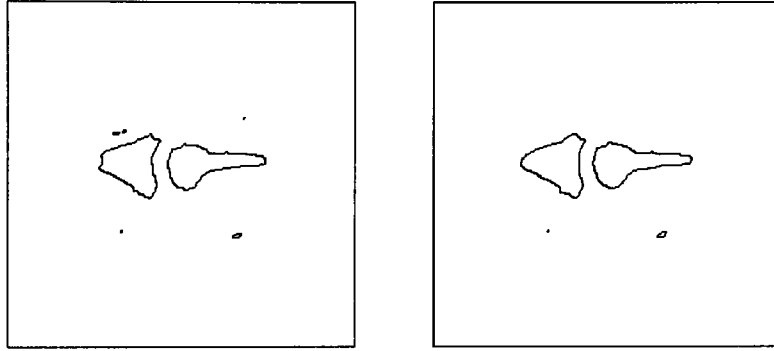


Figure D.1: Bone contours derived from two MRI scans of a PIP joint.

Table D.1 gives the Generalised Hough Transform results for the closed boundaries in Figs. D.1(a) and D.1(b). The scale weights used were $3/4$. The results in this table indicate that the two images are mis-registered by 1 pixel in the x-direction.

Image used in R-Table			Fig. D.1(a)			Fig. D.1(b)		
Fig.	Bone	No. Coords	No.	%	Ref	No.	%	Ref
D.1(a)	MP	164	164	100	(x, y)	87	53.0	(x+1, y)
D.1(a)	PP	189	189	100	(x, y)	86	45.5	(x, y)
D.1(b)	MP	168	87	51.8	(x-1, y)	168	100	(x, y)
D.1(b)	PP	191	86	45.0	(x, y)	191	100	(x, y)

Table D.1: Generalised Hough Transform results for Figs. D.1(a) & D.1(b).

Table D.2 gives the Generalised Hough Transform results for open boundaries in Fig. D.1. The scale weights used were $3/4$.

Image used in R-Table			Fig. D.1(a)			Fig. D.1(b)		
Fig.	Bone	No. Coords	No.	%	Ref	No.	%	Ref
D.1(a)	MP	80	80	100	(x, y)	43	53.8	(x+1, y)
D.1(a)	PP	95	95	100	(x, y)	40	42.1	(x, y-1)
D.1(b)	MP	80	43	53.8	(x-1, y)	80	100	(x, y)
D.1(b)	PP	95	40	42.1	(x, y+1)	95	100	(x, y)

Table D.2: Generalised Hough Transform results for Fig. D.1.

The results in this table indicate that the two bones are misregistered by different amounts. The MP is displaced by 1 pixel in the x-direction and the PP is displaced by 1 pixel in the y-direction.

Orientation Results for Closed Curves

Table D.3 gives the Generalised Hough Transform results for closed boundaries in Fig. D.1 (rotated by α degrees).

Image used in R-Table			Fig. D.1(a)			Fig. D.1(b) ($\alpha = 1^\circ$)		
Fig.	Bone	No. Coords	No.	%	Ref	No.	%	Ref
D.1(a)	MP	164	164	100	(x, y)	66	40.2	(x+1, y+1)
D.1(a)	PP	189	189	100	(x, y)	88	46.6	(x, y-1)
D.1(b)	MP	166	66	39.8	(x-1, y-1)	166	100	(x, y)
D.1(b)	PP	191	88	46.1	(x, y+1)	191	100	(x, y)
Image used in R-Table			Fig. D.1(a)			Fig. D.1(b) ($\alpha = -1^\circ$)		
Fig.	Bone	No. Coords	No.	%	Ref	No.	%	Ref
D.1(a)	MP	164	164	100	(x, y)	70	42.7	(x+1, y-1)
D.1(a)	PP	189	189	100	(x, y)	54	28.6	(x, y+1)
D.1(b)	MP	168	70	41.7	(x-1, y+1)	168	100	(x, y)
D.1(b)	PP	191	54	28.3	(x, y-1)	191	100	(x, y)
Image used in R-Table			Fig. D.1(a)			Fig. D.1(b) ($\alpha = \frac{1}{2}^\circ$)		
Fig.	Bone	No. Coords	No.	%	Ref	No.	%	Ref
D.1(a)	MP	164	164	100	(x, y)	47	28.7	(x+1, y)
D.1(a)	PP	189	189	100	(x, y)	80	42.3	(x, y)
D.1(b)	MP	94	47	50.0	(x-1, y)	94	100	(x, y)
D.1(b)	PP	191	80	41.9	(x, y)	191	100	(x, y)
Image used in R-Table			Fig. D.1(a)			Fig. D.1(b) ($\alpha = -\frac{1}{2}^\circ$)		
Fig.	Bone	No. Coords	No.	%	Ref	No.	%	Ref
D.1(a)	MP	164	164	100	(x, y)	82	50.0	(x+1, y)
D.1(a)	PP	189	189	100	(x, y)	83	43.9	(x, y)
D.1(b)	MP	168	82	48.8	(x-1, y)	168	100	(x, y)
D.1(b)	PP	191	83	43.5	(x, y)	191	100	(x, y)

Table D.3: Generalised Hough Transform closed curve orientation results for Fig. D.1.

Orientation Results for Open Curves

Table D.4 gives the Generalised Hough Transform results for closed boundaries in Fig. D.1 (rotated by α degrees).

Image used in R-Table			Fig. D.1(a)			Fig. D.1(b) ($\alpha = 1^\circ$)		
Fig.	Bone	No. Coords	No.	%	Ref	No.	%	Ref
D.1(a)	MP	80	80	100	(x, y)	36	45.0	(x+1, y)
D.1(a)	PP	95	95	100	(x, y)	40	42.1	(x, y-1)
D.1(b)	MP	78	36	46.2	(x-1, y)	78	100	(x, y)
D.1(b)	PP	95	40	42.1	(x, y+1)	95	100	(x, y)

Image used in R-Table			Fig. D.1(a)			Fig. D.1(b) ($\alpha = -1^\circ$)		
Fig.	Bone	No. Coords	No.	%	Ref	No.	%	Ref
D.1(a)	MP	80	80	100	(x, y)	39	48.8	(x+1, y)
D.1(a)	PP	95	95	100	(x, y)	40	42.1	(x, y-1)
D.1(b)	MP	80	39	48.8	(x-1, y)	80	100	(x, y)
D.1(b)	PP	95	40	42.1	(x, y+1)	95	100	(x, y)

Image used in R-Table			Fig. D.1(a)			Fig. D.1(b) ($\alpha = \frac{1^\circ}{2}$)		
Fig.	Bone	No. Coords	No.	%	Ref	No.	%	Ref
D.1(a)	MP	80	80	100	(x, y)	34	42.5	(x+1, y)
D.1(a)	PP	95	95	100	(x, y)	40	42.1	(x, y-1)
D.1(b)	MP	69	34	49.3	(x-1, y)	69	100	(x, y)
D.1(b)	PP	95	40	42.1	(x, y+1)	95	100	(x, y)

Image used in R-Table			Fig. D.1(a)			Fig. D.1(b) ($\alpha = -\frac{1^\circ}{2}$)		
Fig.	Bone	No. Coords	No.	%	Ref	No.	%	Ref
D.1(a)	MP	80	80	100	(x, y)	43	53.8	(x+1, y)
D.1(a)	PP	95	95	100	(x, y)	40	42.1	(x, y-1)
D.1(b)	MP	80	43	53.8	(x-1, y)	80	100	(x, y)
D.1(b)	PP	95	40	42.1	(x, y+1)	95	100	(x, y)

Table D.4: Generalised Hough Transform open curve orientation results for Fig. D.1.

D.2 T1-Weighted, Gadolinium Enhanced

D.2.1 Data set 2

Data set 2 is derived from a consecutive pair of T1-weighted images (explained in Section 1) of the same finger, taken on the same occasion. Between the scans a contrast agent, Gadolinium (explained in Section 1), was intravenously injected into the patient.

Closed curves

Table D.5 gives the Generalised Hough Transform results for the boundaries in Fig. D.2.

Image used in R-Table			Fig. D.2(a)			Fig. D.2(b)		
Fig.	Bone	No. Coords	No.	%	Ref	No.	%	Ref
D.2(a)	MP	127	127	100	(x, y)	62	48.8	(x-3, y)
D.2(a)	PP	220	220	100	(x, y)	113	51.7	(x-3, y-1)
D.2(b)	MP	122	62	50.8	(x+3, y)	122	100	(x, y)
D.2(b)	PP	234	113	48.3	(x+3, y+1)	234	100	(x, y)

Table D.5: Generalised Hough Transform results for Fig. D.2.

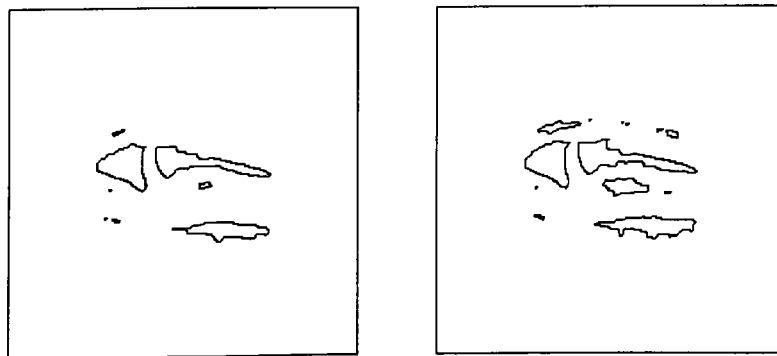


Figure D.2: Bone contours derived from two MRI scan of a PIP joint.

The results in this table indicate that the two bones in the images are misregistered by different amounts. Both bones are displaced by 3 pixels in the x-direction, but the proximal phalanx (explained in Section 1) is also displaced by 1 pixel in the y-direction.

Open curves

Table D.6 gives the Generalised Hough Transform results for open boundaries in Fig. D.2. The results in this table are the same as in the closed curve case.

Image used in R-Table			Fig. D.2(a)			Fig. D.2(b)		
Fig.	Bone	No. Coords	No.	%	Ref	No.	%	Ref
D.2(a)	MP	68	68	100	(x, y)	33	48.5	(x-3, y)
D.2(a)	PP	55	55	100	(x, y)	30	54.5	(x-3, y-1)
D.2(b)	MP	62	33	53.2	(x+3, y)	62	100	(x, y)
D.2(b)	PP	61	30	49.2	(x+3, y+1)	61	100	(x, y)

Table D.6: Generalised Hough Transform results for Fig. D.2.

Orientation Results for Closed Curves

Table D.7 gives the Generalised Hough Transform results for closed boundaries in Fig. D.2 (rotated by α degrees).

Image used in R-Table			Fig. D.2(a)			Fig. D.2(b) ($\alpha = 1^\circ$)		
Fig.	Bone	No. Coords	No.	%	Ref	No.	%	Ref
D.2(a)	MP	128	128	100	(x, y)	61	47.7	(x-3, y+1)
D.2(a)	PP	220	220	100	(x, y)	87	39.5	(x-3, y-1)
D.2(b)	MP	123	61	49.6	(x+3, y-1)			
D.2(b)	PP	234	87	37.2	(x+3, y+1)			
Image used in R-Table			Fig. D.2(a)			Fig. D.2(b) ($\alpha = -1^\circ$)		
Fig.	Bone	No. Coords	No.	%	Ref	No.	%	Ref
D.2(a)	MP	128	128	100	(x, y)	61	47.7	(x-3, y-1)
D.2(a)	PP	220	220	100	(x, y)	79	35.9	(x-3, y-1)
D.2(b)	MP	123	61	49.6	(x+3, y+1)			
D.2(b)	PP	183	79	43.2	(x+3, y+1)			
Image used in R-Table			Fig. D.2(a)			Fig. D.2(b) ($\alpha = \frac{1}{2}^\circ$)		
Fig.	Bone	No. Coords	No.	%	Ref	No.	%	Ref
D.2(a)	MP	128	128	100	(x, y)	64	50.0	(x-3, y)
D.2(a)	PP	220	220	100	(x, y)	111	50.5	(x-3, y-1)
D.2(b)	MP	122	64	52.5	(x+3, y)			
D.2(b)	PP	220	111	50.5	(x+3, y+1)			
Image used in R-Table			Fig. D.2(a)			Fig. D.2(b) ($\alpha = -\frac{1}{2}^\circ$)		
Fig.	Bone	No. Coords	No.	%	Ref	No.	%	Ref
D.2(a)	MP	128	128	100	(x, y)	31	24.2	(x-3, y)
D.2(a)	PP	220	220	100	(x, y)	30	13.6	(x-3, y-1)
D.2(b)	MP	67	33	49.3	(x+3, y)			
D.2(b)	PP	234	111	47.4	(x+3, y+1)			

Table D.7: Generalised Hough Transform closed curve orientation results for Fig. D.2.

Orientation Results for Open Curves

Table D.8 gives the Generalised Hough Transform results for closed boundaries in Fig. D.2 (rotated by α degrees).

Image used in R-Table			Fig. D.2(a)			Fig. D.2(b) ($\alpha = 1^\circ$)		
Fig.	Bone	No. Coords	No.	%	Ref	No.	%	Ref
D.2(a)	MP	68	68	100	(x, y)	33	48.5	(x-3, y+1)
D.2(a)	PP	55	55	100	(x, y)	30	54.5	(x-3, y-1)
D.2(b)	MP	62	33	53.2	(x+3, y-1)			
D.2(b)	PP	62	30	48.4	(x+3, y+1)			
Image used in R-Table			Fig. D.2(a)			Fig. D.2(b) ($\alpha = -1^\circ$)		
Fig.	Bone	No. Coords	No.	%	Ref	No.	%	Ref
D.2(a)	MP	68	68	100	(x, y)	33	48.5	(x-3, y+1)
D.2(a)	PP	55	55	100	(x, y)	30	54.5	(x-2, y-1)
D.2(b)	MP	62	33	53.2	(x+3, y-1)			
D.2(b)	PP	12	7	58.3	(x+2, y+1)			
Image used in R-Table			Fig. D.2(a)			Fig. D.2(b) ($\alpha = \frac{1}{2}^\circ$)		
Fig.	Bone	No. Coords	No.	%	Ref	No.	%	Ref
D.2(a)	MP	68	68	100	(x, y)	33	48.5	(x-3, y)
D.2(a)	PP	55	55	100	(x, y)	30	54.5	(x-3, y-1)
D.2(b)	MP	62	33	53.2	(x+3, y)			
D.2(b)	PP	61	30	49.2	(x+3, y+1)			
Image used in R-Table			Fig. D.2(a)			Fig. D.2(b) ($\alpha = -\frac{1}{2}^\circ$)		
Fig.	Bone	No. Coords	No.	%	Ref	No.	%	Ref
D.2(a)	MP	68	68	100	(x, y)	31	45.6	(x-3, y-1)
D.2(a)	PP	55	55	100	(x, y)	30	54.5	(x-3, y-1)
D.2(b)	MP	49	31	63.3	(x+3, y+1)			
D.2(b)	PP	61	30	49.2	(x+3, y+1)			

Table D.8: Generalised Hough Transform open curve orientation results for Fig. D.2.

D.2.2 Data set 3

Data set 3 comes from a pair of T1-weighted images (explained in Section 1) of the same finger, taken on the same occasion. Between the scans a contrast agent, Gadolinium (explained in Section 1), was intravenously injected into the patient.

Closed curves

Table D.9 gives the Generalised Hough Transform results for the boundaries in Fig. D.3.

Image used in R-Table			Fig. D.3(a)			Fig. D.3(b)		
Fig.	Bone	No. Coords	No.	%	Ref	No.	%	Ref
D.3(a)	MP	122	122	100	(x, y)	56	45.9	(x, y)
D.3(a)	PP	230	230	100	(x, y)	81	35.2	(x, y+1)
D.3(b)	MP	117	56	47.9	(x, y)	117	100	(x, y)
D.3(b)	PP	235	81	34.5	(x, y-1)	235	100	(x, y)

Table D.9: Generalised Hough Transform results for Fig. D.3.

The results in this table show that the middle phalanx (explained in Section 1) in both images are perfectly registered, while the proximal phalanx (also explained in Section 1) is displaced by 1 pixel in the y-direction.

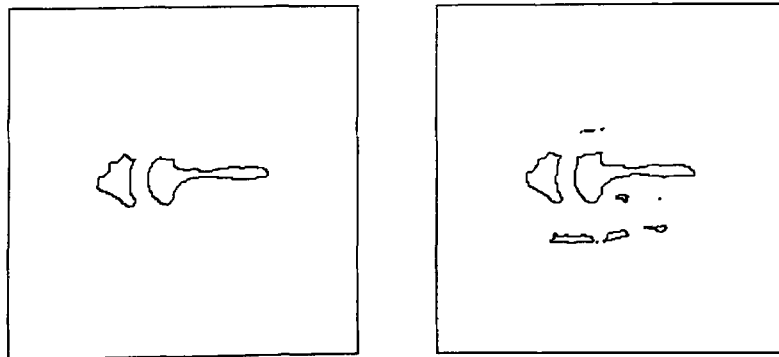


Figure D.3: Bone contours derived from an MRI scan of a PIP joint.

Open curves

Table D.10 gives the Generalised Hough Transform results for open boundaries in Fig. D.3.

Image used in R-Table			Fig. D.3(a)			Fig. D.3(b)		
Fig.	Bone	No. Coords	No.	%	Ref	No.	%	Ref
D.3(a)	MP	69	69	100	(x, y)	33	47.8	(x, y)
D.3(a)	PP	80	80	100	(x, y)	34	42.5	(x, y+1)
D.3(b)	MP	67	33	49.3	(x, y)	67	100	(x, y)
D.3(b)	PP	87	34	39.1	(x, y-1)	87	100	(x, y)

Table D.10: Generalised Hough Transform results for Fig. D.3.

The results in this table are the same as in the closed curve case.

Orientation Results for Closed Curves

Table D.11 gives the Generalised Hough Transform results for closed boundaries in Fig. D.3 (rotated by α degrees).

Image used in R-Table			Fig. D.3(a)			Fig. D.3(b) ($\alpha = 1^\circ$)		
Fig.	Bone	No. Coords	No.	%	Ref	No.	%	Ref
D.3(a)	MP	122	122	100	(x, y)	56	45.9	(x, y+1)
D.3(a)	PP	230	230	100	(x, y)	90	39.1	(x+1, y)
								(x, y)
D.3(b)	MP	117	56	47.9	(x, y-1)			
D.3(b)	PP	235	90	38.3	(x-1, y)			
					(x, y)			

Image used in R-Table			Fig. D.3(a)			Fig. D.3(b) ($\alpha = -1^\circ$)		
Fig.	Bone	No. Coords	No.	%	Ref	No.	%	Ref
D.3(a)	MP	122	122	100	(x, y)	56	45.9	(x, y-1)
D.3(a)	PP	230	230	100	(x, y)	69	30.0	(x, y+1)
D.3(b)	MP	117	56	47.9	(x, y+1)			
D.3(b)	PP	235	69	29.4	(x, y-1)			

Image used in R-Table			Fig. D.3(a)			Fig. D.3(b) ($\alpha = \frac{1}{2}^\circ$)		
Fig.	Bone	No. Coords	No.	%	Ref	No.	%	Ref
D.3(a)	MP	122	122	100	(x, y)	29	23.8	(x, y+1)
D.3(a)	PP	230	230	100	(x, y)	84	36.5	(x, y)
D.3(b)	MP	68	29	42.6	(x, y-1)			
D.3(b)	PP	234	84	35.9	(x, y)			

Image used in R-Table			Fig. D.3(a)			Fig. D.3(b) ($\alpha = -\frac{1}{2}^\circ$)		
Fig.	Bone	No. Coords	No.	%	Ref	No.	%	Ref
D.3(a)	MP	122	122	100	(x, y)	52	42.6	(x, y)
D.3(a)	PP	230	230	100	(x, y)	80	34.8	(x, y)
D.3(b)	MP	117	52	44.4	(x, y)			
D.3(b)	PP	235	80	34.0	(x, y)			

Table D.11: Generalised Hough Transform closed curve orientation results for Fig. D.3.

Orientation Results for Open Curves

Table D.12 gives the Generalised Hough Transform results for open boundaries in Fig. D.3 (rotated by α degrees).

Image used in R-Table			Fig. D.3(a)			Fig. D.3(b) ($\alpha = 1^\circ$)		
Fig.	Bone	No. Coords	No.	%	Ref	No.	%	Ref
D.3(a)	MP	69	69	100	(x, y)	33	47.8	(x, y+1)
D.3(a)	PP	80	80	100	(x, y)	34	42.5	(x, y+1)
D.3(b)	MP	67	33	49.3	(x, y-1)			
D.3(b)	PP	87	34	39.1	(x, y-1)			

Image used in R-Table			Fig. D.3(a)			Fig. D.3(b) ($\alpha = -1^\circ$)		
Fig.	Bone	No. Coords	No.	%	Ref	No.	%	Ref
D.3(a)	MP	69	69	100	(x, y)	33	47.8	(x, y-1)
D.3(a)	PP	80	80	100	(x, y)	34	42.5	(x, y+1)
D.3(b)	MP	67	33	49.3	(x, y+1)			
D.3(b)	PP	87	34	39.1	(x, y-1)			

Image used in R-Table			Fig. D.3(a)			Fig. D.3(b) ($\alpha = \frac{1}{2}^\circ$)		
Fig.	Bone	No. Coords	No.	%	Ref	No.	%	Ref
D.3(a)	MP	69	69	100	(x, y)	26	37.7	(x, y+1)
D.3(a)	PP	80	80	100	(x, y)	34	42.5	(x, y+1)
D.3(b)	MP	53	26	49.1	(x, y-1)			
D.3(b)	PP	87	34	39.1	(x, y-1)			

Image used in R-Table			Fig. D.3(a)			Fig. D.3(b) ($\alpha = -\frac{1}{2}^\circ$)		
Fig.	Bone	No. Coords	No.	%	Ref	No.	%	Ref
D.3(a)	MP	69	69	100	(x, y)	33	47.8	(x, y)
D.3(a)	PP	80	80	100	(x, y)	34	42.5	(x, y+1)
D.3(b)	MP	67	33	49.3	(x, y)			
D.3(b)	PP	87	34	39.1	(x, y-1)			

Table D.12: Generalised Hough Transform open curve orientation results for Fig. D.3.

D.2.3 Data set 4

Data set 4 is derived from four T1-weighted scans (explained in Section 1) of the same finger, on the same occasion. After the first scan a contrast agent, Gadolinium (explained in Section 1), was intravenously injected into the patient. Fig. D.4 illustrate slice 2 and Fig. D.5 illustrate slice 3.

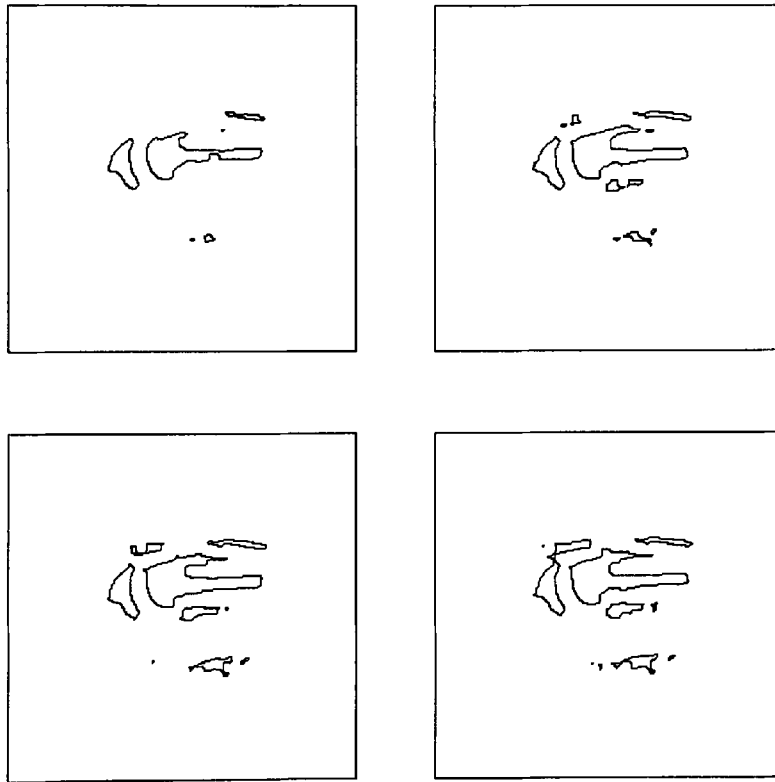


Figure D.4: Slice 2 of a pre- and post-Gadolinium T1-weighted scan.

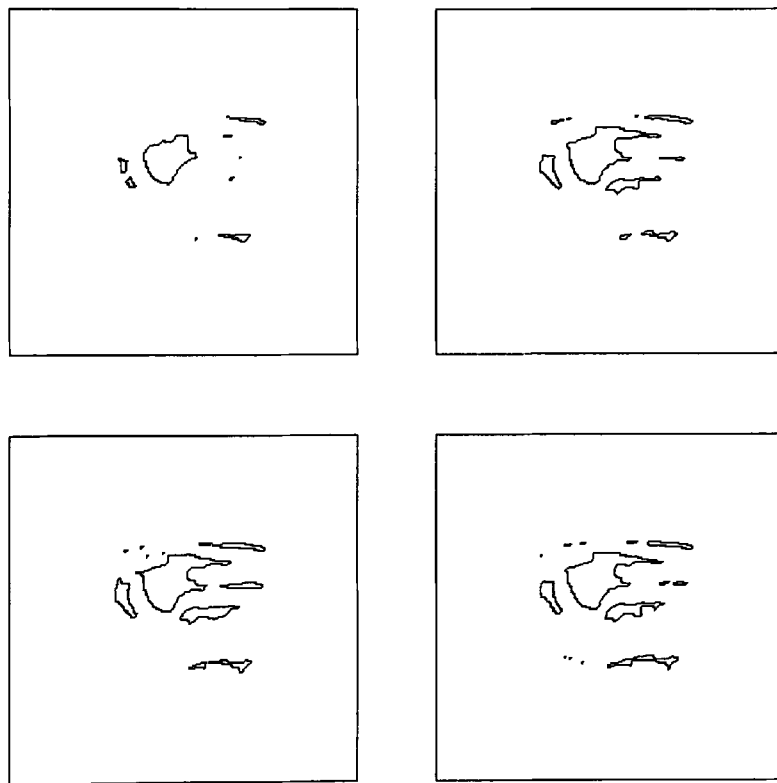


Figure D.5: Slice 3 of a pre- and post-Gadolinium T1-weighted scan.

Closed curves

Tables D.13 and D.14 give the Generalised Hough Transform results for slices 2 and 3 respectively. Fig. D.5(a) required a scale (explained in Section 4.2.3) of 1.5, while Figs. D.5(b) and D.5(d) required scales of $\frac{7}{8}$.

Image used in R-Table			Fig. D.4(a)			Fig. D.4(b)		
Fig.	Bone	No. Coords	No.	%	Ref	No.	%	Ref
D.4(a)	MP	111	111	100	(x, y)	52	46.8	(x, y)
D.4(a)	PP	265	265	100	(x, y)	131	49.4	(x, y)
D.4(b)	MP	112	52	46.4	(x, y)	112	100	(x, y)
D.4(b)	PP	290	131	45.2	(x, y)	290	100	(x, y)
D.4(c)	MP	192	56	29.2	(x, y+1)	45	23.4	(x, y)
D.4(c)	PP	294	107	36.4	(x, y+1)	105	35.7	(x+1, y+1)
D.4(d)	MP	104	59	56.7	(x, y)	49	47.1	(x, y)
D.4(d)	PP	234	87	37.2	(x, y+1)	77	32.9	(x,y)

Image used in R-Table			Fig. D.4(c)			Fig. D.4(d)		
Fig.	Bone	No. Coords	No.	%	Ref	No.	%	Ref
D.4(a)	MP	111	56	50.5	(x, y-1)	59	53.2	(x, y)
D.4(a)	PP	265	107	40.4	(x, y-1)	87	32.8	(x, y-1)
D.4(b)	MP	112	45	40.2	(x, y)	49	43.8	(x, y)
D.4(b)	PP	290	105	36.2	(x-1, y-1)	77	26.6	(x, y)
D.4(c)	MP	192	192	100	(x, y)	68	35.4	(x, y)
D.4(c)	PP	294	294	100	(x, y)	101	34.4	(x, y)
D.4(d)	MP	104	68	65.4	(x, y)	104	100	(x, y)
D.4(d)	PP	234	101	43.2	(x, y)	234	100	(x, y)

Table D.13: Generalised Hough Transform results for Fig. D.4.

The results in Table D.13 show that, initially, the finger is perfectly registered. After the second scan, the finger has started to move and the images are now displaced.

The results in Table D.14 are different to those in Table D.13. This may be due to the fact that these images are not as similar, by eye, as those in slice 2. This dissimilarity is partly a result of the different scales required to try and get images that are similar enough.

Image used in R-Table			Fig. D.5(a)			Fig. D.5(b)		
Fig.	Bone	No. Coords	No.	%	Ref	No.	%	Ref
D.5(a)	MP	69	69	100	(x, y)	23	33.3	(x+1, y+2) (x+2, y+3)
D.5(a)	PP	159	159	100	(x, y)	57	35.8	(x, y)
D.5(b)	MP	86	23	26.7	(x-2, y-3)	86	100	(x, y) (x-1, y-2)
D.5(b)	PP	224	57	25.4	(x, y)	224	100	(x, y)
D.5(c)	MP	67	35	52.2	(x, y+1)	21	31.3	(x+1, y+2)
D.5(c)	PP	213	69	32.4	(x, y+1)	94	44.1	(x, y)
D.5(d)	MP	89	25	28.1	(x, y-1)	38	42.7	(x, y+1)
D.5(d)	PP	226	61	27.0	(x, y)	63	27.9	(x, y)
Image used in R-Table			Fig. D.5(c)			Fig. D.5(d)		
Fig.	Bone	No. Coords	No.	%	Ref	No.	%	Ref
D.5(a)	MP	69	35	50.7	(x, y-1)	25	36.2	(x, y+1)
D.5(a)	PP	159	69	43.4	(x, y-1)	61	38.4	(x, y)
D.5(b)	MP	86	21	24.4	(x-1, y-2)	38	44.2	(x, y-1)
D.5(b)	PP	224	94	42.0	(x, y)	63	28.1	(x, y)
D.5(c)	MP	67	67	100	(x, y)	18	26.9	(x+1, y+1)
D.5(c)	PP	213	213	100	(x, y)	78	36.6	(x, y+1)
D.5(d)	MP	89	18	20.2	(x-1, y-1)	89	100	(x, y)
D.5(d)	PP	226	78	34.5	(x, y-1)	226	100	(x, y)

Table D.14: Generalised Hough Transform results for Fig. D.5.

Open curves

Table D.15 gives the Generalised Hough Transform results for open boundaries in Fig. D.4.

Image used in R-Table			Fig. D.4(a)			Fig. D.4(b)		
Fig.	Bone	No. Coords	No.	%	Ref	No.	%	Ref
D.4(a)	MP	71	71	100	(x, y)	49	69.0	(x, y)
D.4(a)	PP	71	71	100	(x, y)	29	40.8	(x, y)
D.4(b)	MP	76	49	64.5	(x, y)	76	100	(x, y)
D.4(b)	PP	76	29	38.2	(x, y)	76	100	(x, y)
D.4(c)	MP	80	35	43.8	(x, y)	43	53.8	(x, y)
D.4(c)	PP	78	38	48.7	(x, y)	50	64.1	(x, y)
D.4(d)	MP	80	49	61.3	(x, y)	41	51.3	(x, y+1)
D.4(d)	PP	78	32	43.0	(x, y)	34	43.6	(x, y+1)
Image used in R-Table			Fig. D.4(c)			Fig. D.4(d)		
Fig.	Bone	No. Coords	No.	%	Ref	No.	%	Ref
D.4(a)	MP	71	35	49.3	(x, y)	49	69.0	(x, y)
D.4(a)	PP	71	38	53.5	(x, y)	32	45.1	(x, y)
D.4(b)	MP	76	43	56.6	(x, y)	41	53.9	(x, y-1)
D.4(b)	PP	76	50	65.8	(x, y)	34	44.7	(x, y-1)
D.4(c)	MP	80	80	100	(x, y)	34	42.5	(x-1, y-1)
D.4(c)	PP	78	78	100	(x, y)	43	55.1	(x, y)
D.4(d)	MP	80	34	42.5	(x+1, y+1)	80	100	(x, y)
D.4(d)	PP	78	43	55.1	(x, y)	78	100	(x, y)

Table D.15: Generalised Hough Transform results for Fig. D.4.

D.3 Different weights

D.3.1 Data set 5

Data set 5 consists of a set of 3 different-weighted scans (explained in Section 1), Fig. D.6(a), (b), (c). The differently-weighted scans produce images with different contrast. After some manipulation of different scales, most similar boundaries were obtained by scales of $\frac{1}{3}$, $\frac{1}{2}$ and $\frac{3}{4}$ for Fig. D.6(a), (b), (c).

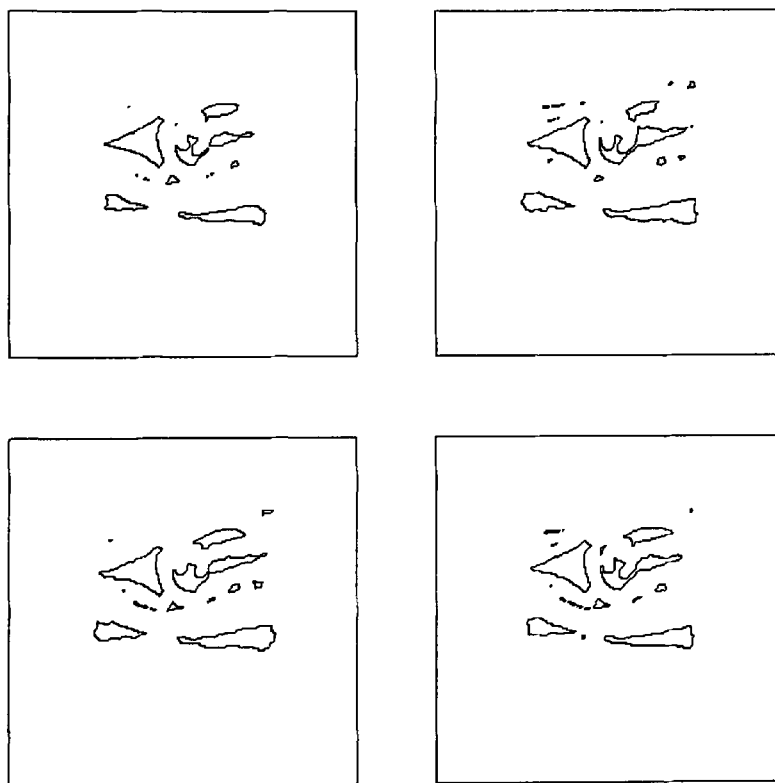


Figure D.6: Bone contours derived from a PD-weighted image.

Closed curves

The Generalised Hough Transform results can be seen in Table D.16.

Image used in R-Table				Fig. D.6(a)			Fig. D.6(b)		
Fig.	Bone	No.	Coords	No.	%	Ref	No.	%	Ref
D.6(a)	MP	143		143	100	(x, y)	52	36.4	(x, y+1)
D.6(a)	PP	98		98	100	(x, y)	36	36.7	(x-1, y)
D.6(b)	MP	149		52	34.9	(x, y-1)	149	100	(x, y)
D.6(b)	PP	198		36	18.2	(x+1, y)	198	100	(x, y)
D.6(c)	MP	151		65	43.0	(x+1, y-1)	54	35.8	(x+1, y-1)
D.6(c)	PP	184		27	14.7	(x, y)	63	34.2	(x+1, y+1)

Image used in R-Table				Fig. D.6(c)		
Fig.	Bone	No.	Coords	No.	%	Ref
D.6(a)	MP	143		65	45.5	(x-1, y+1)
D.6(a)	PP	98		27	27.6	(x, y)
D.6(b)	MP	149		54	36.2	(x-1, y+1)
D.6(b)	PP	198		63	31.8	(x-1, y-1)
D.6(c)	MP	151		151	100	(x, y)
D.6(c)	PP	184		184	100	(x, y)

Table D.16: Generalised Hough Transform results for Fig. D.6(a), (b), (c).

The results for Fig. D.6(a) are very bad due to the proximal phalanx boundary being disconnected. A scale of $\frac{3}{8}$ (Fig. D.6(d)) improves the results as shown in Table D.17.

Image used in R-Table			Fig. D.6(d)			Fig. D.6(b)		
Fig.	Bone	No. Coords	No.	%	Ref	No.	%	Ref
D.6(d)	MP	144	144	100	(x, y)	69	47.9	(x, y+1)
D.6(d)	PP	180	180	100	(x, y)	57	31.7	(x, y)
D.6(b)	MP	149	69	46.3	(x, y-1)	149	100	(x, y)
D.6(b)	PP	198	57	28.8	(x, y)	198	100	(x, y)
D.6(c)	MP	151	49	32.5	(x+1, y-2)	54	35.8	(x+1, y-1)
D.6(c)	PP	184	53	28.8	(x+1, y+1)	63	34.2	(x+1, y+1)

Image used in R-Table			Fig. D.6(c)		
Fig.	Bone	No. Coords	No.	%	Ref
D.6(d)	MP	144	49	34.0	(x-1, y+2)
D.6(d)	PP	180	53	29.4	(x-1, y-1)
D.6(b)	MP	149	54	36.2	(x-1, y+1)
D.6(b)	PP	198	63	31.8	(x-1, y-1)
D.6(c)	MP	151	151	100	(x, y)
D.6(c)	PP	184	184	100	(x, y)

Table D.17: Generalised Hough Transform results for Fig. D.6(d), (b), (c).

It has just been shown that images taken from different-weighted scans require considerable manipulation of the scaling factor in order to produce boundaries that are similar. A different approach would be to use image processing techniques to make the original images more similar before boundaries are derived. One such technique is standardization (explained in Section 4.1.2). Standardizing an image produces a very dark image, as the mean and standard deviation are now 0 and 1 respectively. Contrast stretching the standardized image will re-spread the pixel intensities over the available grey-level range available.

By standardizing and then contrast stretching the differently-weighted images, it is hoped that the resulting images will be similar enough to produce similar boundaries for the Generalised Hough Transform. This process has been tried for the original images in data set 5. Fig. D.7(a), (b), (c) are the boundaries derived from these images. The Generalised Hough Transform results for these boundaries are given in Table D.18.

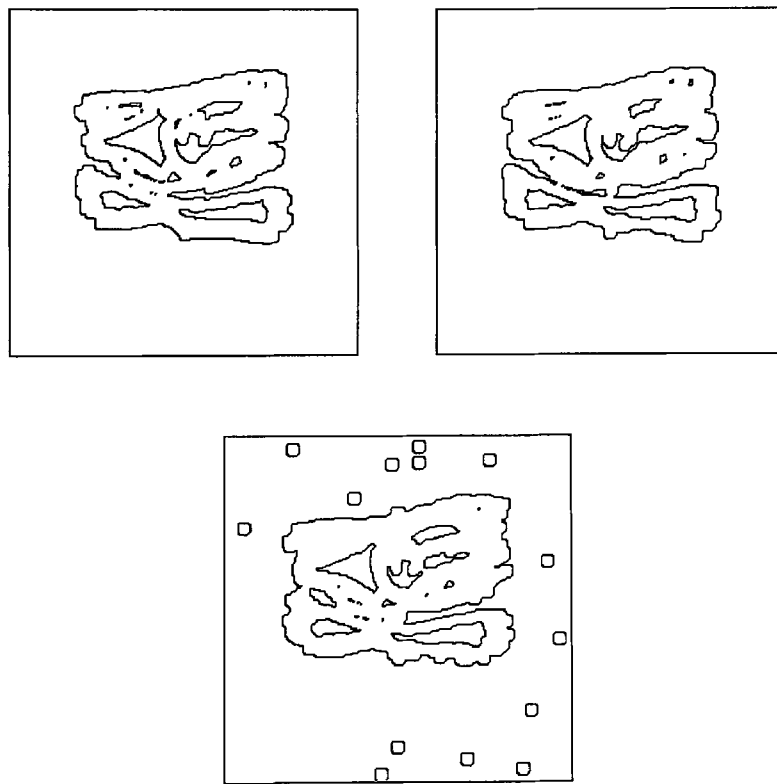


Figure D.7: PD-weighted, normalised and contrast stretched.

Image used in R-Table			Fig. D.7(a)			Fig. D.7(b)		
Fig.	Bone	No. Coords	No.	%	Ref	No.	%	Ref
D.7(a)	MP	156	156	100	(x, y)	73	46.8	(x, y+1)
D.7(a)	PP	170	170	100	(x, y)	55	32.4	(x-1, y-1)
D.7(b)	MP	149	73	49.0	(x, y-1)	149	100	(x, y)
D.7(b)	PP	190	55	28.9	(x+1, y+1)	190	100	(x, y)
D.7(c)	MP	146	47	32.2	(x+2, y)	53	36.3	(x+2, y+1)
D.7(c)	PP	97	26	26.8	(x+1, y)	40	41.2	(x+1, y)

Image used in R-Table			Fig. D.7(c)		
Fig.	Bone	No. Coords	No.	%	Ref
D.7(a)	MP	156	47	30.1	(x-2, y)
D.7(a)	PP	170	26	15.3	(x-1, y)
D.7(b)	MP	149	53	35.6	(x-2, y-1)
D.7(b)	PP	190	40	21.1	(x-1, y)
D.7(c)	MP	146	146	100	(x, y)
D.7(c)	PP	97	97	100	(x, y)

Table D.18: Generalised Hough Transform results for Fig. D.7.

Open curves

(a) Standardized and contrast stretched

Table D.19 gives the Generalised Hough Transform results for open boundaries in Fig. D.7.

(b) Standardized with standard deviation

Table D.20 gives the Generalised Hough Transform results for open boundaries in Fig. D.7.

Image used in R-Table			Fig. D.7(a)			Fig. D.7(b)		
Fig.	Bone	No. Coords	No.	%	Ref	No.	%	Ref
D.7(a)	MP	76	76	100	(x, y)	37	48.7	(x, y+1)
D.7(a)	PP	96	96	100	(x, y)	35	36.5	(x, y)
D.7(b)	MP	69	37	53.6	(x, y-1)	69	100	(x, y)
D.7(b)	PP	112	35	31.3	(x, y)	112	100	(x, y)
D.7(c)	MP	67	25	37.3	(x+2, y)	28	41.8	(x+2, y)
D.7(c)	PP	97	26	26.8	(x+1, y)	40	41.2	(x+1, y)

Image used in R-Table			Fig. D.7(c)		
Fig.	Bone	No. Coords	No.	%	Ref
D.7(a)	MP	76	25	32.9	(x-2, y)
D.7(a)	PP	96	26	27.1	(x-1, y)
D.7(b)	MP	69	28	40.6	(x-2, y)
D.7(b)	PP	112	40	35.7	(x-1, y)
D.7(c)	MP	67	67	100	(x, y)
D.7(c)	PP	97	97	100	(x, y)

Table D.19: Generalised Hough Transform results for Fig. D.7.

Image used in R-Table			Fig. D.7(a)			Fig. D.7(b)		
Fig.	Bone	No. Coords	No.	%	Ref	No.	%	Ref
D.7(a)	MP	68	68	100	(x, y)	34	50.0	(x, y+1)
D.7(a)	PP	109	109	100	(x, y)	33	30.3	(x, y)
D.7(b)	MP	69	34	49.3	(x, y-1)	69	100	(x, y)
D.7(b)	PP	107	33	30.8	(x, y)	107	100	(x, y)
D.7(c)	MP	66	28	42.4	(x+2, y)	29	43.9	(x+2, y+1)
D.7(c)	PP	97	34	35.1	(x+1, y)	35	36.1	(x+1, y)

Image used in R-Table			Fig. D.7(c)		
Fig.	Bone	No. Coords	No.	%	Ref
D.7(a)	MP	68	28	41.2	(x-2, y)
D.7(a)	PP	109	34	31.2	(x-1, y)
D.7(b)	MP	69	29	42.0	(x-2, y-1)
D.7(b)	PP	107	35	32.7	(x-1, y)
D.7(c)	MP	66	66	100	(x, y)
D.7(c)	PP	97	97	100	(x, y)

Table D.20: Generalised Hough Transform results for Fig. D.7.

D.4 Inter Patient Analysis

D.4.1 Data set 6

Data set 6 has been derived from four T1-weighted images from *different* patients. Figs. D.4(a) & D.3(a) are considered as containing a similar pair of boundaries and Figs. D.8 & D.2(a) are considered as containing dissimilar boundaries.

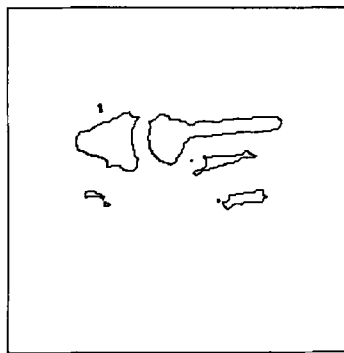


Figure D.8: Bone contours derived from a 2nd MRI scan of a PIP joint.

Closed curves

The Generalised Hough Transform results for the most similar boundaries are displayed in Table D.21, while the Generalised Hough Transform results for the least similar boundaries are displayed in Table D.22.

Image used in R-Table			Fig. D.4(a)			Fig. D.3(a)		
Fig.	Bone	No. Coords	No.	%	Ref	No.	%	Ref
D.4(a)	MP	104	104	100	(x, y)	28	26.9	(x-1, y+14)
D.4(a)	PP	234	234	100	(x, y)	52	22.2	(x-6, y+12)
D.3(a)	MP	122	28	23.0	(x+1, y-14)	122	100	(x, y)
D.3(a)	PP	230	52	22.6	(x+6, y-12)	230	100	(x, y)

Table D.21: Generalised Hough Transform results for Figs. D.4(a) & D.3(a).

Image used in R-Table			Fig. D.8			Fig. D.2(a)		
Fig.	Bone	No. Coords	No.	%	Ref	No.	%	Ref
D.8	MP	165	165	100	(x, y) (x+17, y+15)	27	16.4	(x+16, y+15)
D.8	PP	254	254	100	(x, y)	31	12.2	(x-35, y+24)
D.2(a)	MP	128	27	21.1	(x-17, y-15) (x-16, y-15)	128	100	(x, y)
D.2(a)	PP	220	31	14.1	(x+35, y-24)	220	100	(x, y)

Table D.22: Generalised Hough Transform results for Figs. D.8 & D.2(a).

Open curves

Tables D.23 and D.24 give the Generalised Hough Transform results for open boundaries in Figs. D.4(a) and D.3(a) (considered to be most similar) and Figs D.8 and D.2(a) (considered to be least similar).

Image used in R-Table			Fig. D.4(a)			Fig. D.3(a)		
Fig.	Bone	No. Coords	No.	%	Ref	No.	%	Ref
D.4(a)	MP	74	74	100	(x, y)	24	32.4	(x-1, y+14)
D.4(a)	PP	73	73	100	(x, y)	31	42.5	(x, y+16)
D.3(a)	MP	66	24	36.4	(x+1, y-14)	66	100	(x, y)
D.3(a)	PP	83	31	37.3	(x, y-16)	83	100	(x, y)

Table D.23: Generalised Hough Transform results for Figs. D.4(a) & D.3(a).

Image used in R-Table			Fig. D.8			Fig. D.2(a)		
Fig.	Bone	No. Coords	No.	%	Ref	No.	%	Ref
D.8	MP	68	68	100	(x, y)	22	32.4	(x+6, y+19)
D.8	PP	110	110	100	(x, y)	19	17.3	(x+4, y+12)
D.2(a)	MP	71	22	31.0	(x-6, y-19)	71	100	(x, y)
D.2(a)	PP	80	19	23.8	(x-4, y-12)	80	100	(x, y)

Table D.24: Generalised Hough Transform results for Figs. D.8 & D.2(a).

Appendix E

Poster Abstract

Arthritis & Rheumatism

OFFICIAL PROGRAM

1995 NATIONAL SCIENTIFIC MEETING

October 21–26, 1995
San Francisco, California



AMERICAN COLLEGE OF
RHEUMATOLOGY

Volume 38, No. 9 (Supplement) September 1995

RADIOLOGICAL ASSESSMENT OF ANATOMICAL DAMAGE IN RA: A CONTRIBUTION TO A STANDARDIZED APPROACH IN MULTICENTER STUDIES G.F. Ferrarini¹, F. Pirolo², S. Ferrarini³, O. Della Casa-Alberghini⁴, E. Mancini⁵, G. Pasero⁶, I.RDU Dept Internal Medicine, Lazio, 2 Inst. of Radiology, Rome; 3 Medico Dept, Sandoz P.F., Milan, 4 Inst. of Biometrics, Milan, 5 Chair of Rheumatology, Pisa, Italy

The early RA patient X-rays of hands and feet taken in P-A views at entry and after 12 months, all of the same quality and granulometry, were evaluated under identical scoring conditions, according to 3 different types of reading as single X-rays, randomly ordered in terms of sequence and patient, as paired X-rays for each patient, without knowing their chronological sequence, as ordered X-rays for each patient, i.e. knowing their chronological sequence. The ability of each type of reading to detect differences within patient and between methods was then verified. The X-rays were jointly scored by 3 radiologists according to Larsen-Dale method, the 12 month vs. baseline progression of Erosion Score (PES) i.e. the number of eroded joints being the main variable considered for the analyses.

Variable	Readings	Mean	SD	Lower Quartile	Upper Quartile
PES	single	1.78	3.72	0	4
	paired	1.87	3.07	0	3
	ordered	2.42	3.53	0	4
Comparison of readings		Linear regression line		Test of concordance (H ₀ : r=1)	
		β	r	p	
paired vs single		0.435	0.338	< .001	
paired vs ordered		0.661	0.578	< .001	
ordered vs single		0.540	0.356	< .001	

Conclusions: The paired reading seems to offer a more conservative rating, and for these reasons it appears to be the approach of choice for inferential purposes

1060

TENIDAP (TEN) SLOWS X-RAY DETERIORATION IN RHEUMATOID ARTHRITIS (RA) H.K. Genant¹, Department of Radiology, University of California, San Francisco; D.S. Kirby, E.A. Pickering, L.D. Loose, E.S. Warner, N. Ting², Central Research Division, Pfizer Inc., Groton, CT, 06340

A multicenter double-blind study in disease-modifying antirheumatic drug-naïve (DMARD-naïve) patients with active RA was performed to assess the efficacy and safety of TEN over 2 years vs a nonsteroidal anti-inflammatory drug (NSAID) alone, and a combination of an NSAID with a DMARD. The study included 369 randomized patients, with 126 patients on TEN 120 mg/day, 119 on piroxicam (PIR) 20 mg/day, and 124 on piroxicam 20 mg/day with hydroxychloroquine (PIR-HCQ) 400 mg/day. Posteroanterior X-rays of each hand/wrist were to be obtained at baseline and at weeks 24, 52, and 104, regardless of whether the patient remained in the study. DMARD therapy could be added after week 24 for patients who continued in the study. X-rays were scored by one experienced reader blinded to treatment and sequence using a global modified Sharp and Genant scoring system. Erosions (E) and joint space narrowing (JN) were scored, respectively, in 14 and 13 joints per hand/wrist for a total (T) score of 0-200. ANCOVA analyses were performed on changes from baseline to 24, 52, and 104 weeks for E, JN, and T scores.

Baseline and at least one follow-up X-ray were available for 312 patients (109 TEN, 100 PIR, and 103 PIR-HCQ). All groups showed statistically significant increases in E, JN, and T scores at each time point. Patients with elevated C-reactive protein (CRP) or positive rheumatoid factor (RF) at baseline had greater X-ray deterioration during the study than patients with a normal CRP or negative RF. The TEN group showed approximately 50% less X-ray deterioration than the PIR group, and this difference was statistically significant (p<0.05) for all parameters at 24 and 52 weeks, and for E and T scores at 104 weeks, with E score at 104 weeks also favoring the TEN group (p=0.061). The TEN group also showed less X-ray deterioration than the PIR-HCQ group, although the difference was not statistically significant. After week 24, 35 (25%) PIR and 22 (18%) PIR-HCQ, but only 12 (10%) TEN patients added a DMARD while continuing in the study. The significantly reduced rate of X-ray deterioration seen in TEN-treated vs PIR-treated RA patients, associated with TEN's ability to lower acute phase reactants and provide greater long-term clinical efficacy than PIR alone, provide evidence that TEN is a disease-modifying agent.

Study was sponsored by Pfizer Inc. Dr. H. Genant has received support from Pfizer Inc. All other authors are Pfizer employees.

1061

WRIST PREDOMINANCE IN SERONEGATIVE RHEUMATOID ARTHRITIS: FACT, FICTION OR NATURAL HISTORY?

MJ Plant¹, AA Borg², I Saklatvala³, D Clarke⁴, D Mawer⁵, PT Dawes⁶, University Hospital of Wales, Cardiff; ²Newville Hall Hospital, Abergavenny; ³Staffordshire Rheumatology Centre Stoke-on-Trent, United Kingdom ST6 7AG

It has been suggested that seronegative RA has distinct radiological characteristics, comprising osteoporosis, new bone formation (NBF), tendency to fusion, asymmetry and predominant wrist involvement. We undertook a cross-sectional survey to compare the radiology of seronegative and seropositive disease. IgM and IgA rheumatoid factors (RF) were measured in 101 patients with RA for >5 years. Individual joints on X-rays of hands and feet were scored quantitatively by Larsen's method and were graded for osteoporosis, NBF, sclerosis, malalignment, fusion, cysts, symmetry, joint space narrowing (JSN) and erosion type (marginal, central, surface or resorptive).

IgM RF+ve patients had higher Larsen scores, despite similar age and disease duration. IgM RF+ve patients had more malalignment and JSN (p<0.05) but these parameters were highly correlated with Larsen score (r=0.68). There was no difference in other radiological features. Wrist involvement, expressed as percentage of Larsen score (wrist%), was greater in IgM RF+ve patients. However, it was found that wrist% reduces by 1% for each 10 unit increase in Larsen score, there was no difference in wrist% when corrected for Larsen score.

IgA RF was positive in 28 patients, who had a higher Larsen score (115 vs 106), but this was not significant (p=0.11); there were no differences in radiological features or in wrist%.

		Larsen	wrist%	wrist% corrected for Larsen
IgM RF+ve	n=48	127	30.2%	30.2%
	n=53	96	34.5%	31.2%
		p=0.001		
		p=0.04		
		p=0.3 NS		

Conclusion: Seronegative RA is less severe, but has similar radiological features to seropositive disease. Previously reported wrist predominance is a natural consequence of the fact that percentage wrist involvement decreases with increasing radiological severity.

1062

EIGHT YEAR OUTCOME OF PATIENTS PRESENTING WITH EARLY NON-EROSIVE RHEUMATOID ARTHRITIS

MJ Plant¹, PW Jones², PT Dawes³

Staffordshire Rheumatology Centre, Stoke-on-Trent, ST6 7AG; ²University Hospital of Wales, Cardiff; ³Department of Mathematics, University of Keele.

Longterm outcome of early RA is poorly understood. Although the presence of radiological erosions is a major prognostic indicator, many patients present before erosive damage has occurred. We performed an 8 year review of patients who first presented in 1984 with early, non-erosive RA. Inclusion criteria were: 1) fulfillment of 1958 ARA criteria for probable/definite RA, 2) symptoms prior to presentation of <6yrs, 3) absence of erosive change on X-rays of hands and feet. 125 patients (80 female), aged 18-74yrs, were identified from clinic records; 67 were RF positive; 110 had definite RA and 16 probable RA.

Radiographs were available at 8yrs in 114 patients (91%). 89 patients (71%) were reviewed at a mean of 8 yrs later (range 7.5-12.5); 27 had been lost to follow-up and 10 had died. Cause of death was cardiovascular in 7, cancer in 2 and vasculitis/pneumonia in 1. Eighty-eight patients (70%) developed erosive disease, but 26 (21%) remained non-erosive at 8yrs. Further assessment of this non-erosive group frequently revealed evidence of other diseases. The initial inflammatory polyarthralgia had resolved completely in 8. Osteoarthritis was apparent in 12, and 6 had features of connective tissue disease (2 SLE, 2 Sjogren's syndrome, 2 undifferentiated CTD). Other diagnoses were hypermobility in 2, soft-tissue rheumatism (carpal tunnel syndrome, rotator cuff tendinitis, trochanteric bursitis) in 3, cervical spondylosis in 2 and reactive arthritis in 1. For the cohort as a whole, 46% of those eligible to work became work-disabled; 52% developed rheumatoid deformities; 23% had no active synovitis at follow-up.

Conclusion: 70% of patients presenting with early, non-erosive RA went on to develop erosive disease; 21% remained non-erosive; there was insufficient radiological data in 9% for the non-erosive patients, symptoms resolved completely in 8% but 23% evolved into CTD and 46% showed evidence of alternative rheumatological conditions.

1063

GADOLINIUM-ENHANCED MAGNETIC RESONANCE IMAGING OF THE FINGER JOINTS IN RHEUMATOID ARTHRITIS

MJ Plant, WR Stewart, GP Williams, KBR O'Connor, ST Gorman, H Griffiths, JP Woodcock, BD Williams¹, Departments of Rheumatology, Medical Physics and Bioengineering, University Hospital of Wales, Cardiff, Wales CF4 4XW.

Although synovial inflammation is central to the pathophysiology of RA, currently it can only be assessed indirectly by clinical examination or acute phase response. MRI has the potential to image synovium directly, and as the hand is the main focus of RA, we have developed a high-resolution small-bore scanner to image proximal inter-phalangeal (PIP) finger joints. The scanner comprises a 0.5 Tesla magnet, gradient set and finger coil. Slice thickness is 1.5mm and resolution 0.2mm. Compared to normal, patients with active RA show soft-tissue swelling over the dorsal and palmar aspects of the head of the proximal phalanx, extending proximally. This appears as intermediate signal on T1-weighted images and as high signal on T2-weighted, and is presumed to be synovium because 1) it is in the correct anatomical location, 2) it is seen filling marginal erosions of bone and 3) signal decreases after intra-articular steroid. We have further evaluated the signal response kinetics in various tissues following intravenous Gadolinium-DTPA (Gd) in patients with RA.

10 patients had T1-weighted scans (TR 370ms, TE 25ms) before Gd (0.2ml/kg) and every 3 mins thereafter for 30mins. Regions of interest were selected for synovium, bone and tendon, and the mean MRI signal for each tissue is shown below in arbitrary units. Average time to peak signal for synovium was 7.7min (range 2-16), after which it remained constant up to 30mins.

	Pre-Gd	Post-Gd	Mean % increase	Range
Synovium	562	1923	+340%	10-404%
Bone trabecular	1138	1229	+8%	0-36%
Tendon	261	301	+8%	0-15%

In this system, Gd-enhancement defines normal tissue and so could be extended to quantify degree and extent of synovitis in frequently involved joints in rheumatoid arthritis.

1064

RELATIONSHIP BETWEEN ACUTE PHASE RESPONSE AND RADIOLOGICAL PROGRESSION IN EARLY RHEUMATOID ARTHRITIS DURING DIFFERENT DMARDs

H.A. Cars, A.A.M.E. Stenger, A.J. Slater, R.H. Kuiper, M.A. van Leeuwen, M.H. van Ruiswijk, University Hospital Groningen, P.O. Box 30.001, 9700 RB Groningen, The Netherlands.

A theoretical mathematical model has been established defining the individual relationship between time-integrated C-reactive protein (TI-CRP) values and radiological progression (X-progr) in early RA. Using data of the first 6 months a constant 'K' representing the individual relationship between CRP and X-progr could be calculated. The model appeared to predict accurately the extent of X-progr in patients treated with hydroxychloroquine (HCQ) and/or gold. The present study evaluates this model in patients treated with sulfasalazine (SSZ) and/or methotrexate (MTX).

Methods: 3-year prospective study of 36 DMARD-naïve patients with RA (symptoms < 1 year) with a high risk of X-progr. Patients were treated with HCQ and/or gold (M) (42) or with SSZ and/or MTX (44). Monthly CRP values and 6-monthly Sharp scores of hands and feet were determined. The 'K' values were calculated using data of 0-6 months and 12-24 months for each patient.

Results: Both groups were comparable with regard to initial CRP values and X-scores. The TI-CRP values, the X-progr and the calculated 'K' values over the first 6 months did not differ between the groups. Over 6-24 months the TI-CRP values (p<0.01) and X-progr (p<0.05) were significantly lower in the SSZ-MTX group compared to the HCQ-gold group. However, the 'K' values did not differ between the groups.

Conclusion: There was no influence of the DMARDs studied on the individual relationship between TI-CRP values and X-progr for the calculated 'K' values during the first years of RA. Therefore the model enables an individual interpretation of CRP values in relation to the rate of X-progr independent of the specific DMARD treatment.

Appendix F

IMA paper

Defining a Registration Algorithm for MRI Finger Images

G. P. Williams, P. A. Roach, S. Lloyd

*Division of Mathematics and Computing, University of Glamorgan,
Trefforest, Wales*

W. R. Stewart

*Department of Medical Physics and Clinical Engineering,
University Hospital of Wales, Cardiff, Wales*

Abstract

In many magnetic resonance imaging (MRI) applications, it is necessary to compare regions of interest (ROIs) on different images of the same patient. This comparison is often made difficult when the scanned tissue volume is not in exactly the same three-dimensional location every time. Registration, the accurate alignment of the images through the determination of a transformation from one image space to another, is necessary so that ROIs may be compared correctly.

This paper outlines a new application of registration in the monitoring of rheumatic disease in the proximal interphalangeal joint [1] conducted at the University Hospital of Wales. In particular, registration is required for quantitative comparison of monomodal, serially-acquired images to increase the precision of treatment monitoring. These images correspond to the tissue content of a slice of given thickness of the joint.

We bring to light a number of complications which make identifying suitable transformations to achieve registration difficult. These complications preclude the straightforward application of a standard registration technique and require the development of a bespoke approach. In particular, this paper will show that 2D pixel-based registration is not appropriate for this application. It will go on to examine the factors of this problem which complicate registration and will suggest how suitable transformations may be determined. Characteristics of such transformations will be shown.

1 Introduction

In the Department of Medical Physics and Bioengineering at the University Hospital of Wales, a small bore 1.2 tesla Magnetic Resonance Imaging (MRI) system is used to acquire 2D cross-sectional images of patients' fingers. The images are multi-sliced producing eight images each of which corresponds to

a 1.5 mm thick slice of tissue. The slices are taken in the sagittal plane [2], producing cross sections through the length of the finger.

The brightness of a picture element (pixel) of an MR image reflects the amplitude of the signal. Image pixels take values from a grey-scale of 0 (black) to 4095 (white). The pixels are located by the co-ordinate (x, y) system, where x refers to columns and y refers to rows. The finger images are of size 256×256 pixels with the origin being in the top left hand corner.

This work is currently being applied to MR images of proximal interphalangeal (PIP) joints of patients with Rheumatoid Arthritis (RA). One advantage of MRI is its potential to image synovium directly in the finger joints of patients with RA, which is not possible by other methods such as x-ray imaging. Synovial tissue is a thin lining of the joint which swells under the influence of RA. Active synovial tissue and fluid have a destructive effect on the joint. Bone erosion and cartilage thinning are typical consequences of RA in the PIP joint. A quantitative analysis of synovium will give a measure of disease activity and increase the precision of treatment monitoring with serial images.

Fig. 1 shows a typical finger image from a patient with RA. Of particular interest in this image are: the two bones in the joint (the proximal phalanx and the middle phalanx), the cartilage and the two areas of synovial tissue (synovium dorsal and synovium palmar). Bone erosion caused by active synovium has created a hole in the patient's finger. Active synovium has been seen to be

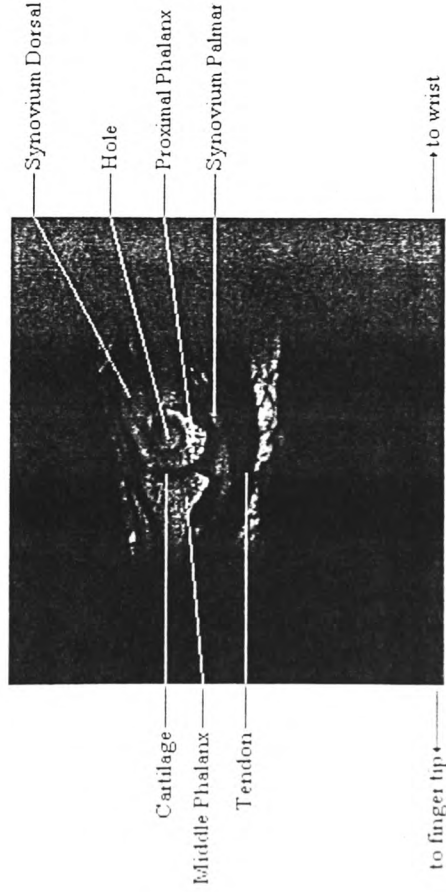


Figure 1. MRI scan of an RA patient.

enhanced when a contrast agent, Gadolinium, was intravenously injected during a sequence of scans [1], where active synovium appears bright on the relatively dark image.

This work is part of a large collaborative project between the University of Glamorgan (UG) and the University Hospital of Wales (UHW). Earlier work in this field produced an extensible image viewer to display the images and to perform various image processing techniques on the images [12]. It is beyond the scope of this paper to detail all the various functions of the viewer.

In Section 2 we explain the particular issues which arise with the registration of MRI finger images. A brief overview of registration is given in Section 3 and the nature of the registration basis is outlined in Section 4. Section 5 discusses various segmentation methods which can be incorporated into registration and Section 6 outlines some new methods we have derived for registering MRI finger images. Finally, Sections 7 and 8 outline our conclusions to this paper and proposed future work.

2 The Problem Statement

To quantify disease activity in a PIP joint at a given time, a measure of active synovium is required from the MR image. This measure can be derived by comparing synovium on different images of the same patient. This comparison is made difficult by the unlikelihood that the area being scanned is in exactly the same three-dimensional location every time. For example, a clinical trial may test the success of a certain drug by periodically scanning the same tissue area. The slices taken in each set of scans will not exactly match across all sets. Another example of the difficulty of comparison is provided when a patient is unable to keep perfectly still during a sequence of scans. Hence, the later scans show some movement when compared to the earlier scans. The movement may affect which cross-sections are imaged for each slice.

Accurate alignment of the images is necessary, so that specific regions of interest (ROIs) may be compared correctly. This is known as registration. This application of registration is monomodal, i.e. we need to register images which originate from a single formation technique, namely MRI.

In this section we bring to light a number of complications which necessitate an application of registration but at the same time make registration difficult.

2.1 Positional Error

Each time a patient inserts their hand into the scanner, it is almost impossible to ensure that their finger is positioned in exactly the same 3D location each time. Imaging different cross-sections each time makes the comparison of ROIs more difficult. The finger's position can differ in any, or all axes, rotationally and in relative angles of articulated joints. This produces an immediate need for registration.

It is unlikely that any method will be found of ensuring that exactly the same cross-sections of the finger are taken each time. Even moulds made of the finger would be inadequate, as the physiology of the treated joint will often change between scan sessions.

2.2 Finger Movement

Finger movement during scanning must be minimised to reduce the number of registration problems. At UIW, a plastic syringe tube is used to aid positioning of the finger. Any excess space in the syringe tube is packed to restrict the amount of movement possible. However, some finger movement can occur in many directions: forwards, backwards, rotational or bending at articulated joints. Even small head or shoulder movement can cause the finger to move. In previous work it was found that very slight movements during scanning affect the images greatly.

In this application, a unique difficulty has arisen from the posture of the patient during the scanning process. The finger is inserted into the scanner giving a forwards thrust (the patients' arm is elevated at 90° to the body). If the patient later relaxes then the constant pressure on the skin holds the skin in place while the internal joint moves backwards. We define this movement as *slippage*.

Other complications for registration include the possibility of tendon relaxation, which could be observed on an image as "movement". Also, small female patients find it easier to insert their hand into the scanner. Conversely, small female patients tend to have short arms and sometimes struggle to position their finger far enough forwards in the scanner. Consequently, the cross-sections taken may not contain all of the ROI necessary for comparison. Finally, over time and with treatment, the shape and size of synovium will change which further complicates the comparison and registration process. This change over time of the pathology and hence image presents the interesting conceptual challenge of how to define a registration in this case.

3 Brief Overview of Registration

As defined by Maurer and Fitzpatrick [3] the term registration is used to mean the determination of a transformation from one space to another. When the transformation has been determined the images are registered. The scope of the work described in this paper is restricted to image spaces only and not physical space.

A transformation is a set of equations that will map the co-ordinates of each point in one image into the co-ordinates of the physically corresponding point in the other image. It is essential that the transformation used for registration is adequate to describe the deformation of the body part under study [4]. This requirement is crucial to this application where changes in shape and size of synovial tissue must be compared and analysed.

Registration is an area of growing interest in many applications of medical image processing. In published reviews [3, 4, 5] the imaging modalities involved include magnetic resonance imaging (MRI), computed tomography (CT), single-photon emission computed tomography (SPECT), positron emission tomography

Monomodal applications are those in which the images to be registered have been acquired from the same modality. Multimodal applications are those in which the images to be registered have been acquired from different modalities. There are many applications of multimodal image registration, examples from [5] include registering MRI images with CT images; PET images with CT/MRI images and SPECT images with CT/MRI images.

This paper is concerned with monomodal MRI registration. The purpose of registering monomodal images is for quantitative comparison, which increases the precision of treatment monitoring with serial images [3].

Medical image registration has been applied to various parts of the anatomy, examples from [5] being (i) head - brain or skull, eye, dental; (ii) thorax - entire, cardiac, breast; (iii) abdomen - general, kidney, liver; (iv) pelvis and perineum; (v) limbs - general, femur, humerus, hand; (vi) spine and vertebrae. No work on registering MRI finger images has yet been found in the literature by the authors.

3.1 Registration Methods

In the literature many registration methods have been tried, including least square fitting, chamfer matching techniques, moment matching, aligning axes, cross-correlation, landmarks and minimising the sum of squared intensities [5]. Other methods use atlases [3], mathematical morphology [6] and Fourier Transforms [7].

Correlation methods have been reported as being suited for monomodal image registration, particularly when comparing serial images of the same patient, for example, when looking for small changes caused by disease [3]. Examples of such methods in the literature are the correlation function, the correlation coefficient, the sum of squares and the sum of absolute values of differences [*ibid*].

Correlation methods try to find the optimum registration method by maximising the similarity between images of the same patient that differ mainly because of different image acquisition conditions and also possibly because of small changes [*ibid*]. Thus, it may seem reasonable to assume that correlation methods should help to determine small changes in synovium, bone erosion and cartilage thinning, all caused by rheumatoid arthritis. The usefulness of such methods are considered in Section 5. Enhancement of active synovium due to a contrast agent (explained in Section 1) may require the introduction of a scaling factor to correct for differences in pixel intensities between images.

Registration methods can be broadly categorized into pixel-based methods and shape-based methods. In Section 4.2 we show how pixel-based methods are not appropriate for this application. Section 5 follows with methods which look for features of the images which characterize the shape and structure of the MRI finger image.

4 Nature of Registration Basis

Image-based registration methods have been divided in the literature into extrinsic methods and intrinsic methods. Extrinsic methods are based on foreign objects being introduced into the image space and intrinsic methods are based on the image information alone [5]. In this section, we give examples of extrinsic and intrinsic methods which have been applied to MRI finger images.

4.1 Extrinsic Methods

Extrinsic methods are aided by objects being added to the patient prior to scanning. For MRI, appropriate non-metal markers with imaging capabilities must be made. Successful extrinsic markers can be viewed easily, can be extracted from images and have potential for automatic detection [4].

Other researchers in this field have tried the use of externally placed markers to aid registration [8]. At UIW, small cylindrical tubes of copper sulphate were attached to a finger prior to scanning. The method is limited in that it has poor accuracy for reproducing the placement of the tubes for each scanning session. Also, internal slippage (explained in Section 2.2) would create movement that would be beyond the markers' contribution for registration. Therefore, extrinsic methods are not appropriate for this application.

4.2 Intrinsic Methods

Intrinsic methods rely on information contained within the images only. In the literature, intrinsic registration methods are divided into 3 groups based on: a set of points or landmarks; the alignment of segmented binary structures; measures computed from the image grey values [5]. The analysis and results of applying segmented binary structures to this work is explained in Section 5.

Establishing corresponding landmarks in two images in many cases can be a rather difficult task. Landmarks are usually established by correlation techniques to find corresponding gross features in two images. However, correlation measures are affected by factors such as noise and image rotation and thus generally yield less precise spatial correspondences between landmarks [9]. In Section 5 we show how features of MRI finger scans have been established for registration purposes instead of landmarks.

Registration methods based on image grey level values require knowledge of a region of interest (ROI) or a landmark in terms of pixel grey levels alone. If tissues or landmarks could be classified or segmented by grey level values only then clearly registration would be a very simple matter.

The graph in Fig. 2 shows average grey levels plus or minus one standard deviation, for rectangles drawn on the finger image in Fig. 1. The rectangles were drawn within the proximal phalanx (PP), the middle phalanx (MP), the synovium dorsal (SD), the synovium palmar (SP), the joint space (JS), the tendon (T) and the crooked hole (H).

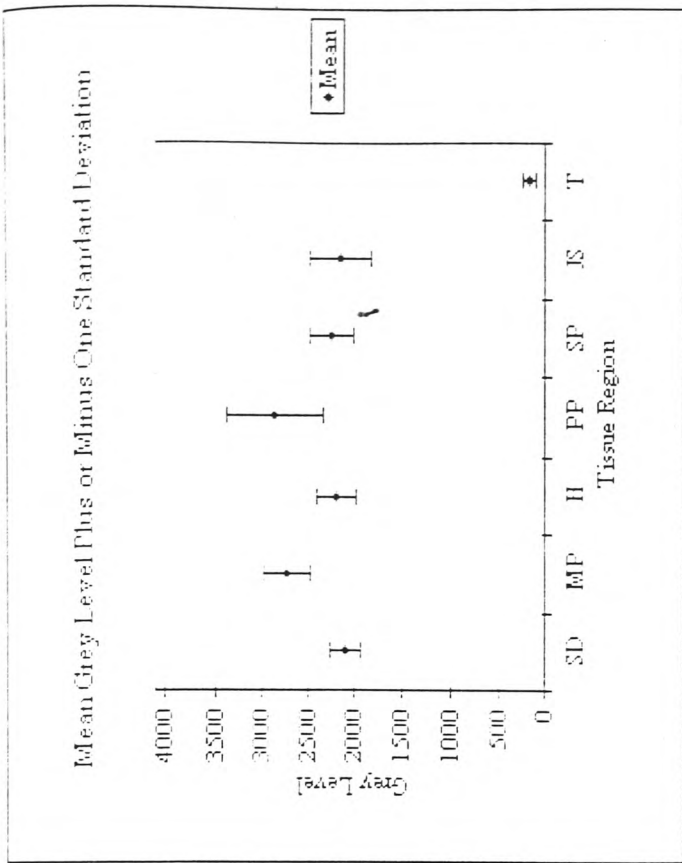


Figure 2. Average grey levels for ROIs taken from an MRI image of an RA patient.

The graph illustrates the fact that for different ROIs, the average grey levels are very similar. Within plus or minus one standard deviation of the mean, many grey levels fall within different tissue regions. The range for each tissue region will show substantially more overlap of grey levels. Thus, defining boundaries for ROIs or landmarks by grey level alone is almost impossible for these sorts of images. Therefore, registration based on image grey levels alone is insufficient for this application. The identification of structural features is also required.

5 Image Segmentation

Segmentation algorithms are generally based on one of two basic properties of grey-level values: discontinuity and similarity. Discontinuity algorithms attempt to partition an image based on abrupt changes in grey-level in the detection of isolated points, lines and edges. Thresholding, region growing, splitting and merging are the principal approaches in similarity detection. These algorithms can be applied to static and dynamic (time varying) images [9].

In this section, we examine various segmentation algorithms to establish a set of features of an MRI finger image that will simplify the registration process.

5.1 Discontinuity Detection

There are three basic types of discontinuities - points, lines and edges. Grey-level discontinuities are most commonly found by edge detection. Therefore, our work so far has concentrated on edges. In this section, we show how classical first and second derivative edge detection techniques have been applied to MRI finger images.

An edge can be defined as the boundary between two regions with distinct grey-level properties [9]. As has already been shown, MRI finger images cannot be segmented in terms of grey level values alone. Usually, when this is the case segmentation techniques are more applicable than edge detection [46d]. However, edge detectors were applied to examine if they could be of any benefit. The results follow in this section.

5.1.1 Gradient Operators

The most common edge detectors are gradient operators. The gradient [9] of an image $f(x, y)$ at location (x, y) is the vector:

$$\nabla \mathbf{f} = \begin{bmatrix} G_x \\ G_y \end{bmatrix} = \begin{bmatrix} \frac{\delta f}{\delta x} \\ \frac{\delta f}{\delta y} \end{bmatrix}$$

Gradient vectors point in the direction of the maximum rate of change of f at (x, y) . In edge detection the magnitude, usually called the *gradient* and denoted by $|\nabla f|$, of this vector is very important.

$$|\nabla f| = \text{mag}(\nabla \mathbf{f}) = [G_x^2 + G_y^2]^{\frac{1}{2}}$$

Much simpler to implement is the commonly practised approximation to the gradient by using absolute values:

$$|\nabla f| \approx |G_x| + |G_y|$$

The simplest way to implement gradient operators is to pass a mask over the image. In this case we use a 3×3 mask. As the mask passes over each 3×3 array of image pixels, calculations are performed for the centre pixel from its nearest neighbours. Choosing an appropriate threshold, T , sends the image to binary.

Examples of gradient operators, where $z_1 \dots z_9$ correspond to a subset of 3×3 pixels, are Sobel:

$$\begin{aligned} G_x &= (z_3 + 2z_6 + z_9) - (z_1 + 2z_4 + z_7) \\ G_y &= (z_7 + 2z_8 + z_9) - (z_1 + 2z_2 + z_3) \end{aligned}$$

$$\begin{bmatrix} -1 & 0 & 1 \\ -2 & 0 & 2 \\ -1 & 0 & 1 \end{bmatrix}$$

and Prewitt:

$$\begin{aligned} G_x &= (z_3 + z_6 + z_9) - (z_1 + z_4 + z_7) \\ G_y &= (z_7 + z_8 + z_9) - (z_1 + z_2 + z_3) \end{aligned}$$

$$\begin{bmatrix} 1 & 0 & 1 \\ -1 & 0 & 1 \\ -1 & 0 & 1 \end{bmatrix} \quad \begin{bmatrix} -1 & -1 & -1 \\ 0 & 0 & 0 \\ 1 & 1 & 1 \end{bmatrix}$$

Note that all the mask coefficients sum to zero, indicating a response of 0 in constant areas, as expected of a derivative operator.

We have applied Sobel and Prewitt edge detectors with binary thresholds to MRI finger images. The aim of an edge detector is to determine some boundary, or shape within the image that would simplify the registration process. However, the created images showed so much information that on their own, they were of little help. Therefore, a simplification algorithm was introduced to reduce the amount of information in the images. By selecting a minimum number of pixels, all horizontal, vertical, and 45° diagonal straight lines of image pixels of length less than the desired minimum were removed from the image. Fig. 4 shows the result obtained when these combined algorithms were applied to the image in Fig. 3. In Fig. 4, we see the beginnings of a display of features to be found in finger images. In particular, the vertical lines that lie either side of the cartilage and the horizontal lines from the proximal phalanx are potential characteristics of a finger image. The diagonal lines which approximate the corners of the bones do not always appear in the segmented images. Finding common, simple features in images of the same patient should ease the search for registration.

Two images showing the same characteristics as in Fig. 4 above can be superimposed (as explained in Section 6) and one image moved through a search space to locate registration by determining the position of maximum "matching" pixels.

5.1.2 Laplacian

The Laplacian [9] of an image is a second order derivative defined as:

$$\nabla^2 f = \frac{\delta^2 f}{\delta x^2} + \frac{\delta^2 f}{\delta y^2}$$

The Laplacian may also be implemented in digital form for a 3×3 region as:

$$\nabla^2 f = 4z_5 - (z_2 + z_4 + z_6 + z_8)$$

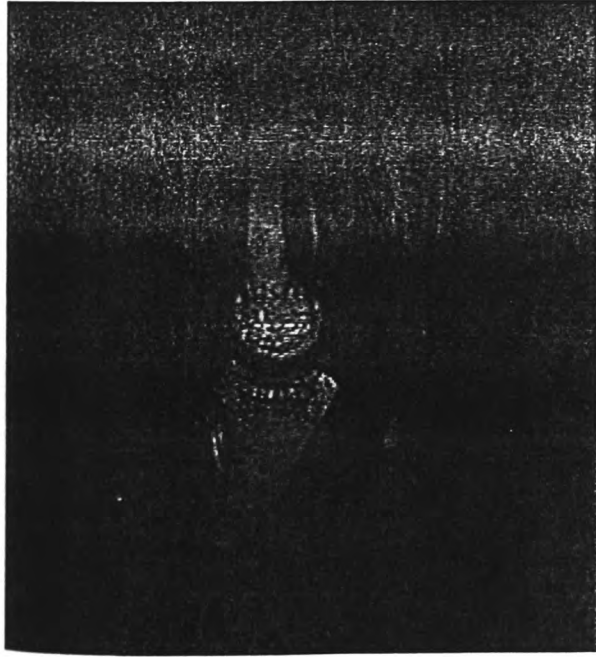


Figure 5. MRI finger scan.

in contrast, making the use of zero crossings alone unreliable. In Section 6 we show some results of post processing of the zero crossings images.

5.2 Similarity Detection

Barnea and Silverman [11] present a class of sequential similarity detection algorithms (SSDAs) which they apply to translational registration.

Let an image S and window W be defined as in Fig. 9. S is an $L \times L$ search area and W an $M \times M$ window, where M is smaller than L . Each $M \times M$ subimage is uniquely referenced by its top left co-ordinates. The parameters L and M must be carefully selected to ensure that a complete subimage is always contained within the search area.

By searching a subset of the allowed range of reference points, translational registration is determined by finding a point (i^*, j^*) which references the most similar subimage to the window W . The choice of M will be crucial in determining the speed of the algorithm as M^2 pixels are processed.

One application of SSDA which we have implemented is the sum of absolute values of differences (SAD) of the corresponding pixels from the subimage and

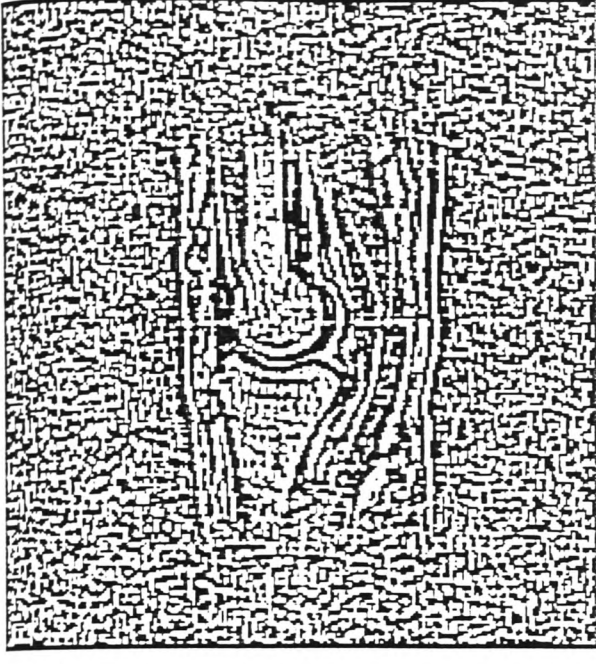


Figure 6. Zero Crossings on Fig. 5.

the window. That is:

$$\|F(i, j)\| = \sum_{i=1}^M \sum_{j=1}^M |S(i, j) - W(i, j)|$$

An extension to SAD is the normalised method, which subtracts the mean of each window from their respective pixel grey levels, i, j :

$$\|F(i, j)\| = \sum_{i=1}^M \sum_{j=1}^M |S(i, j) - S(i, j) - W(i, j) + W|$$

where $S(i, j)$ is the mean grey level of subimage S at reference point (i, j) and W is the mean grey level of window W . The normalised SAD gives the added advantage of ignoring differences of grey levels for different tissue regions on different images. This advantage is particularly useful for Gadolinium enhanced images (as explained in Section 1).

For some local regions the resulting transformations to achieve registration, by eye, looked correct. However, even on pairs of images believed to exhibit relatively little actual finger movement, different local regions from the same images suggested different transformations to achieve registration. Further, when



Figure 7. MRI finger scan.

the algorithm was applied to the image globally, the resulting transformations did not always match the local transformations. Combining transformations from different local regions would mean distorting one image to match the other. Distorting an MRI finger image could result in losing vital information about synovium which is crucial to this application.

6 Superimposing

In this section we explain one method for a registration search in which we derived the basic concept from the search aspect behind SSDA.

We take two images to be registered, an active image, A and a reference image, R . Misregistration is assessed by considering the similarity of the contents of portions of equal size of the two images. A new image, N , is created by superimposing the active image onto the reference image.

The size of the portions can be set with the aid of a rectangle drawn on the active image and automatically copied onto the reference image. As the finger content of our images comprises approximately only a third of the image space, a rectangle is drawn around the finger part of the image only. To reduce computational time further the rectangle can be drawn around selected features.

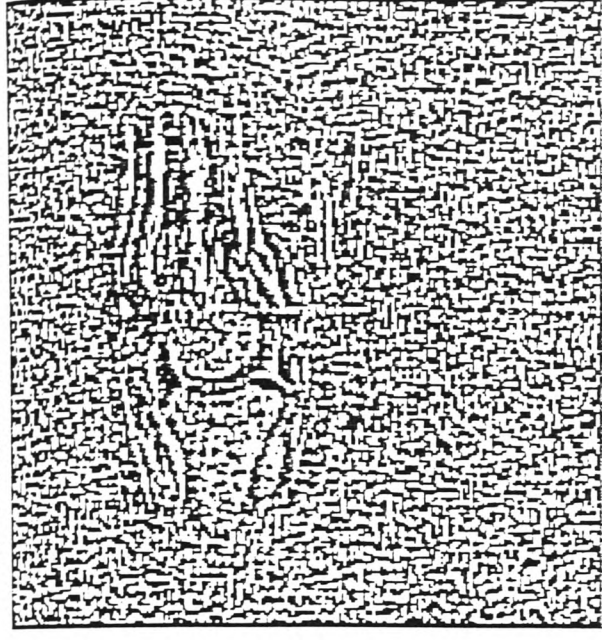


Figure 8. Zero Crossings on Fig. 7.

Each pixel outside the rectangle takes its value from the pixel in the corresponding position in the active image. Within the rectangle pixel values are assigned from the following test:

$$N_{ij} = \begin{cases} A_{ij} & : A_{ij} < R_{ij} \\ Red & : A_{ij} > R_{ij} \\ Blue & : A_{ij} = R_{ij} \end{cases}$$

and the number of (mis)matching pixels are calculated.

The rectangle is moved in the active image within a search procedure to locate the position at which the greatest number of matching pixels occurs. We can also do it manually.

It was thought that a pixel value from a specific tissue region in A would lie within a tolerance of about 20 grey levels of its corresponding pixel in R . On closer examination, however, it was found that within some tissue regions pixel grey levels differed by 500 or more grey levels. To accommodate this, a tolerance, Tol , was introduced to the above test:

$$N_{ij} = \begin{cases} A_{ij} & : R_{ij} - Tol \leq A_{ij} \leq R_{ij} + Tol \\ Red & : A_{ij} < R_{ij} - Tol \\ Blue & : A_{ij} > R_{ij} + Tol \end{cases}$$

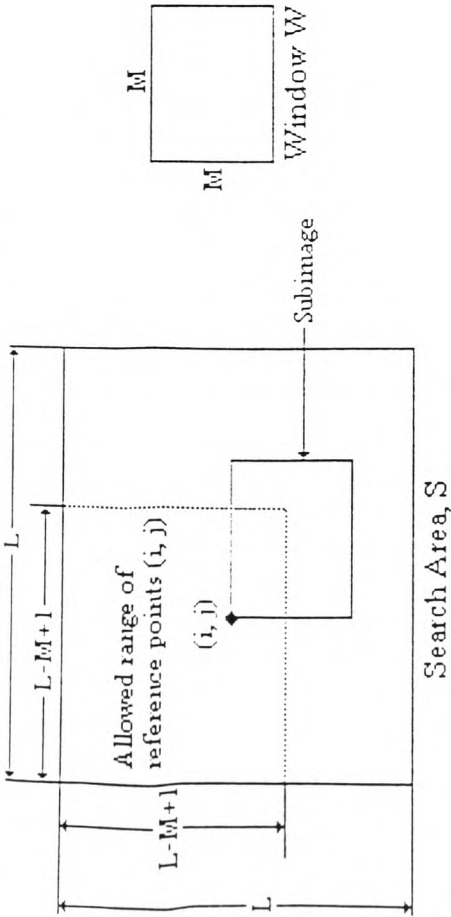


Figure 9. SSDA.

Pixel $A_{i,j}$ is said to match pixel $R_{i,j}$ if pixel $A_{i,j}$ lies within plus or minus the tolerance of $R_{i,j}$. The number of these matching pixels are calculated.

At this stage, issues arose over what would constitute an acceptable tolerance level for registration and how many "matching" pixels warrant the term "registered". On examination, where tolerance levels were increased to 300 or 400, "registration" was possible. This level of tolerance was deemed to be too high and therefore a modified approach was necessary, as described below.

6.1 Combined Methods

The newly developed superimposing method can be used directly on the MRI images, or as a postprocessing registration step on derived images. In this section we show how a combination of edge detectors or zero crossings followed by superimposing can improve registration.

A pair of images obtained by applying the Sobel edge detector with a binary threshold and the simplification algorithm, such as the one in Fig. 4, can be superimposed as above. As the images are binary there is no need for a tolerance level. The algorithms were run on several images. A search was made for the position which yielded the maximum number of matching pixels. In many cases the maximum number of matching pixels gave a position which looked, by eye, to resemble registration. Within the drawn rectangle, the percentage of matching pixels at registration exceeded 90%. However, this measure is not altogether helpful, due to the vast quantity of background pixels in this type of image. Instead the number of matching foreground pixels was calculated. The positions

at which maximum matching pixels were located were the same as previously, although the percentage of matching pixels fell to between 24% and 69%.

The combined approach was also applied to pairs of images produced by applying zero crossings to MRI finger images, such as the ones in Figs. 6 and 8. The speckled nature of these images made it almost impossible to see the detail in the superimposed image well enough for analysis. As an intermediate step, the simplification algorithm, explained in Section 5.1.1, was introduced to simplify the images to make superimposing more meaningful. By selecting a minimum number of pixels, all horizontal, vertical, and 45° diagonal straight lines of image pixels of length less than the desired minimum were removed from the image. If the minimum was too small, too much detail was retained in the image. If the minimum was too large then the curved detail around the finger joint was quickly lost whilst still retaining some unnecessary background information. No optimum value, which would be generally applicable to a range of MRI finger images, could be found to solve both of these.

7 Conclusions

In this paper, we have outlined new research between the University of Glamorgan and the University Hospital of Wales in the use of magnetic resonance imaging to quantify synovium in the finger joints of patients with rheumatoid arthritis. We have shown the need for monomodal registration in the serially-acquired MRI finger scans.

A number of complications have been brought to light which make registration difficult. As has been seen, these complications preclude the straightforward application of a single registration method and require the new development of a bespoke approach.

A number of well-known 2D registration techniques and a newly developed method have been applied to the finger scans. Individually, the techniques gave poor results although the results were improved with combined methods giving the best results to date.

8 Future Work

An extension of this work will be an investigation into the use of registration techniques to match a volumetric set of slices with the possible addition of time as an extra dimension.

A calibration of the MRI scanner will be conducted to determine a measure of error due to noise on the signal. From measures of scanner error, a statistical measure of fit, in registration, will be produced.

References

1. Plant M. J., Stewart W. R., Williams G. P., O'Connor K. B. R., Gorman S. T., Griffiths H., Woodcock J. P., Williams B. D., Gadolinium-enhanced Magnetic Resonance Imaging of the finger joints in Rheumatoid Arthritis. *Arthritis and Rheumatism*, 1995, **38**, No. 9 SS, p. 1063.
2. Rinck Peter A. (Ed.) *Magnetic Resonance in Medicine*. Third Edition. Blackwell Scientific Publications, Oxford, 1993.
3. Maurer Calvin R., Jr., Fitzpatrick J. Michael. (Ed. Maciunas R. J.) *A Review of Medical Image Registration*, in *Interactive Image-Guided Neurosurgery*, Park Ridge IL 1993, pp. 17-44.
4. van den Elsen Petra A., Pol Evert-Jan D., Viergever Max A., Medical Image Matching - A Review with Classification. *IEEE Engineering in Medicine and Biology*, **12**, 1993, pp. 26-39.
5. Maintz J. B. Antoine, Viergever Max A., A Survey of Medical Image Registration. *Medical Image Analysis*, **2**, No. 1, 1998, pp. 1-36.
6. Chen Chu-Song, Hung Yi-Ping, Wu Ja-Ling, Extraction of Corner-Edge-Surface Structure from Range Images Using Mathematical Morphology. *IEEE Trans. Information and Systems*, **E78D**, No. 12, 1996, pp. 1636-41.
7. Fornaro G., Franceschetti G., Image registration in interferometric SAR processing. *IEE Proc. Radar, Sonar Navig.*, **142**, No. 6, 1995, pp. 313-320.
8. Wang Matthew Y., Maurer Calvin R., Jr., Fitzpatrick J. Michael, Maciunas Robert J., An Automatic Technique for Finding and Localizing Externally Attached Markers in CT and MR Volume Images of the Head, *IEEE Trans. Biomedical Engineering*, **43**, No. 6, 1996, pp. 627-637.
9. Gonzalez Rafael C., Woods Richard E., *Digital Image Processing*, Addison-Wesley Publishing Company, 1992.
10. Haralick Robert M., Digital Step Edges. *IEEE Trans. Pattern Analysis and Machine Intelligence*, **PAMI-6**, No. 1, 1984, pp. 58-68.
11. Barnea Daniel I., Silverman Harvey F., A class of Algorithms for Fast Digital Image Registration. *IEEE Trans. Comp.*, **C-21**, No. 2, 1972, pp. 179-186.
12. O'Connor K. B. R., Stewart W. R., Ware J. A., An Interactive Medical Image Processing System based on a Hybrid Computer Architecture. *IEE Colloquium on High Performance Architecture for Real-Time Image Processing*, 14/1 - 14/6, 1995.

Appendix G

Glossary

MP	Middle Phalanx
MRI	Magnetic Resonance Imaging
PD	Proton Density
PIP joint	Proximal Interphalangeal joint
PP	Proximal Phalanx
RA	Rheumatoid Arthritis
RIFF	Resource Interchange File Format
ROI	Region of Interest
SAVD	Sum of Absolute Values of Differences
SMIS	Surrey Medical Instruments
SSDA	Sequential Similarity Detection Algorithm
UHW	University Hospital of Wales

Bibliography

- [Ackland80] Ackland Bryan, Weste Neil, (1980), Real Time Animation on a Frame Store Display System, *Computer Graphics* (Proc. SIGGRAPH 80), **14**, pp. 182-188.
- [Ackland81] Ackland Bryan, Weste Neil, (1981), The Edge Flag Algorithm - A Fill Method for Raster Scan Displays, *IEEE Trans. Computers*, **C-30**, pp. 41-48.
- [Althof97] Althof Raymond J., Wind Marco G. J., Dobbins III James T., (1997), A Rapid and Automatic Image Registration Algorithm with Subpixel Accuracy, *IEEE Trans. Medical Imaging*, **16**, No. 3, pp. 308-316.
- [Amit96] Amit Yali, Kong Augustine, (1996), Graphical Templates for Model Registration, *IEEE Trans. Pattern Analysis and Machine Intelligence*, **18**, No. 3, pp. 225-236.
- [Amit97] Amit Yali, (1997), Graphical Shape Templates for Automatic Anatomy Detection with Applications to MRI Brain Scans, *IEEE Trans. Medical Imaging*, **16**, No. 1, pp. 28-40.
- [Apicella88] Apicella A., Nagel J. H., Duara R., (1988), Fast Multimodality Image Matching, *10th Annual International Conference IEEE Engineering in Medicine & Biology Society*, IEEE Computer Society Press, Los Alamitos, CA, **10**, pp. 414-415.
- [Apicella89] Apicella Anthony, Kippenhan J. Shane, Nagel Joachim H., (1989), Fast multi-modality image matching, *Proc. SPIE Medical Imaging III: Image Processing*, SPIE Press, Bellingham, WA, **1092**, pp. 252-263.

- [Arun87] Arun K. S., Huang T. S., Blostein S. D., (1987), Least-Squares Fitting of Two 3-D Point Sets, *IEEE Trans. Pattern Analysis and Machine Intelligence*, **PAMI-9**, No. 5, pp. 698-700.
- [Ashton97] Ashton Edward A., Parker Kevin J., Berg Michel J., Chen Chang Wen, (1997), A Novel Volumetric Feature Extraction Technique with Applications to MR Images, *IEEE Trans. Medical Imaging*, **16**, No. 4, pp. 365-371.
- [Bailey96] Bailey Robert R., Srinath Mandyam, (1996), Orthogonal Moment Features for Use With Parametric and Non-Parametric Classifiers, *IEEE Trans. Pattern Analysis and Machine Intelligence*, **18**, No. 4, pp. 389-399.
- [Bajcsy83] Bajcsy Ruzena, Lieberman Robert, Reivich Martin, (1983), A Computerized System for the Elastic Matching of Deformed Radiographic Images to Idealized Atlas Images, *Journal of Computer Assisted Tomography*, **7**, No 4, pp. 618-625.
- [Bajcsy89] Bajcsy Ruzena, Kovačič Stane, (1989), Multiresolution Elastic Matching, *Computer Vision, Graphics and Image Processing*, **46**, pp. 1-21.
- [Barnea72] Barnea Daniel I., Silverman Harvey F., (1972), A Class of Algorithms for Fast Digital Image Registration, *IEEE Trans. Computers*, **C-21**, No. 2, pp. 179-186.
- [Bartoo89] Bartoo Grace T., Hanson William A., (1989), Multi-Modality Image Registration Using Centroid Mapping, *11th Annual International Conference IEEE Engineering in Medicine & Biology Society*, **11**, pp. 550-551.

- [Bergevin96] Bergevin Robert, Soucy Marc, Gagnon Herv, Laurendeau Denis, (1996), Towards a General Multi-View Registration Technique, *IEEE Trans. Pattern Analysis and Machine Intelligence*, **18**, No. 5, pp. 540-547.
- [Bookstein91] Bookstein Fred L., (1991), Thin-Plate Splines and the Atlas Problem for Biomedical Images, in Colchester & Hawkes (Eds.) *Information Processing in Medical Imaging*, Springer-Verlag, Berlin, pp. 326 - 342.
- [Borgefors88] Borgefors Gunilla, (1988), Hierarchical Chamfer Matching: A Parametric Edge Matching Algorithm, *IEEE Trans. Pattern Analysis and Machine Intelligence*, **10**, No. 6, pp. 849-865.
- [Bose90] Bose Chinmoy B., Amir Israel, (1990), Design of Fiducials for Accurate Registration Using Machine Vision, *IEEE Trans. Pattern Analysis and Machine Intelligence*, **12**, No. 12, pp. 1196-1200.
- [Bracewell86] Bracewell Ronald N., (1986), *The Fourier Transform and its Applications*, McGraw-Hill, Singapore.
- [Bresenham65] Bresenham, J. E., (1965), Algorithm for Computer Control of a Digital Plotter, *IBM System Journal*, **4**, pp. 25-30.
- [Bydder95] Bydder G. M., (1995), The Mackenzie Davidson Memorial Lecture: Detection of small changes to the brain with serial magnetic resonance imaging, *The British Journal of Radiology*, **68**, No. 816, pp. 1271-1295.

- [Cai96] Cai Jailing, Zhou Shao-Qun, Hopkinson James, Saxena V. Amod, Chu James, (1996), Alignment of Multi-segmented Anatomical Features from Radiation to Images by Using Least Square Fitting, *Medical Physics*, **23**, No. 12, pp. 2069-75.
- [Canny86] Canny John, (1986), A Computational Approach to Edge Detection, *IEEE Trans. Pattern Analysis and Machine Intelligence*, **PAMI-8**, No. 6, pp. 679-698.
- [Chellappa97] Chellappa Rama, Zheng Qinfeng, Burlina Philippe, Shekhar Chandra, Eom Kie B., (1997), On the Positioning of Multisensor Imagery for Exploitation and Target Recognition, *Proceedings of the IEEE*, **85**, No. 1, pp. 120-138.
- [Chen94] Chen Qin-sheng, Defrise Michel, Deconinck F., (1994), Symmetric Phase-Only Matched Filtering of Fourier-Mellin Transforms for Image Registration and Recognition, *IEEE Trans. Pattern Analysis and Machine Intelligence*, **16**, No. 12, pp. 1156-1168.
- [Chen95] Chen Chu-Song, Hung Yi-Ping, Wu Ja-Ling, (1995), Extraction of Corner-Edge-Surface Structure from Range Images Using Mathematical Morphology, *IEICE Trans. Information and Systems*, **E78D**, No. 12, pp. 1636-41.
- [Chiorboli93] Chiorboli G., Vecchi G. P., (1993), Comments on "Design of Fiducials for Accurate Registration Using Machine Vision", *IEEE Trans. Pattern Analysis and Machine Intelligence*, **15**, No. 12, pp. 1330-1332.

- [Cideciyan90] Cideciyan Artur V., Nagel Joachim H., (1990), Multi-modality Image Registration Using The Hough Transform, *Annual International Conference IEEE Engineering in Medicine and Biology Society*, **12**, No. 1, pp. 141-142.
- [Collins92] Collins D. Louis, Peters Terry M., Dai Weiqian, Evans Alan C., (1992), Model based Segmentation of Individual Brain Structures from MRI Data, in Robb, R. A. (Ed.), *Proc. SPIE Visualization in Biomedical Computing*, SPIE Press, Bellingham, **1808**, pp. 10-23.
- [Conger93] Conger Jim, (1993) *Windows API New Testament*, Waite Group Press, California, pp. 643 - 688.
- [Cooley65] Cooley J. W., Tukey J. W., (1965), An Algorithm for the Machine Calculation of Complex Fourier Series, *Math. of Comput.*, **19**, pp. 297-301.
- [Curry90] Curry III Thomas S., Dowdey James E., Murry Jr. Robert C., (1990), *Christensen's Physics of Diagnostic Radiology*, fourth edition, Lea & Febiger, Pennsylvania, USA.
- [Dann88] Dann Robert, Hoford John, Kovacic Stane, Reivich Martin, Bajcsy Ruzena, (1988), Three-Dimensional Computerized Brain Atlas for Elastic Matching: Creation and Initial Evaluation, in Schneider & Dwyer (Eds.), *Proc. SPIE Medical Imaging II*, SPIE Press, Bellingham, WA, **914**, pp. 600-608.

- [Dann89] Dann Robert, Hoford John, Kovačič Stane, Reivich Martin, Bajcsy Ruzena, (1989), Evaluation of Elastic Matching System for Anatomic (CT, MR) and Functional (PET) Cerebral Images, *Journal of Computer Assisted Tomography*, **13**, No. 4, pp. 603-611.
- [Davis97] Davis Malcolm H., Khotanzad Alireza, Flamig Duane P., Harms Steven E., (1997), A Physics-Based Coordinate Transformation for 3-D Image Matching, *IEEE Trans. Medical Imaging*, **16**, No. 3, pp. 317-328.
- [DeCastro87a] De Castro Ercole, Cristini Giuseppe, Martelli Alessandro, Morandi Carlo, Vascotto Marco, (1987), Compensation of Random Eye Motion in Television Ophthalmoscopy: Preliminary Results, *IEEE Trans. Medical Imaging*, **MI-6**, No. 1, pp. 74-81.
- [DeCastro87b] De Castro E., Morandi C., (1987), Registration of Translated and Rotated Images Using Finite Fourier Transforms, *IEEE Trans. Pattern Analysis and Machine Intelligence*, **PAMI-9**, No. 5, pp. 700-703.
- [DeMunck96] De Munck J. C., Dubois E. A., Habraken J. B. A., Verster F. C., Van Herk M., (1996), Automatic Registration of MR and Spect, *Progress in Biophysics and Molecular Biology*, **65**, No. 51, pp. PH203.
- [Dunlavey83] Dunlavey Michael R., (1983), Efficient Polygon-Filling Algorithms for Raster Displays, *ACM Trans. on Graphics*, **2**, pp. 264-273.

- [Elmabrouk99] Elmabrouk A., Aggoun A., (1999), A New Edge Detection Algorithm, *Proc. 2nd IMA Conference on Image Processing: Mathematical Methods, Algorithms and Applications*.
- [Elsen93] van den Elsen Petra A., Pol Evert-Jan D., Viergever Max A., (1993), Medical Image Matching - A Review with Classification, *IEEE Engineering in Medicine and Biology*, **12**, pp. 26-39.
- [Engelstad88] Engelstad Barry L., Meyers H. Joseph, Hanson William A., O'Connell J. William, Taylor Robert C., Bernstein Ralph, (1988), Information extraction from multi-modality medical imaging, *Proc. SPIE Three-Dimensional Imaging and Remote Sensing Imaging*, SPIE Press, Bellingham WA, **902**, pp. 144-149.
- [Foley83] Foley J. D., van Dam A., (1983), *Fundamentals of Interactive Computer Graphics*, Addison-Wesley Publishing Company, Inc., Philippines.
- [Fornaro95] Fornaro G., Franceschetti G., (1995), Image Registration in Interferometric SAR Processing, *IEE Proc. Radar, Sonar and Navigation*, **142**, No. 6, pp. 313-320.
- [Gonzalez87] Gonzalez Rafael C., Wintz Paul, (1987), *Digital Image Processing*, Addison-Wesley Publishing Company, Inc., USA.
- [Gonzalez92] Gonzalez Rafael C., Woods Richard E., (1992), *Digital Image Processing*, Addison-Wesley Publishing Company, Inc., USA.
- [Granlund72] Granlund G. H., (1972), Fourier Preprocessing for Hand Print Character Recognition, *IEEE Trans. Computers*, **C-21**, pp. 195-201.

- [Greiner96] Greiner Russell and Isukapalli Ramana, (1996), Learning to Select Useful Landmarks, *IEEE Trans. Systems, Man and Cybernetics - Part B: Cybernetics*, **26**, No. 3, pp. 437-449.
- [Grimson96] Grimson W. E. L., Ettinger G. J., White S. J., Lozano-Pérez T., Wells III W. M., Kikinis R., (1996), An Automatic Registration Method for Frameless Stereotaxy, Image Guided Surgery, and Enhanced Reality Visualization, *IEEE Trans. Medical Imaging*, **15**, No. 2, pp. 129-140.
- [Haralick84] Haralick Robert M., (1984), Digital Step Edges, *IEEE Trans. Pattern Analysis and Machine Intelligence*, **PAMI-6**, No. 1, pp. 58-68.
- [Hemler94] Hemler Paul F., Sumanaweera Thilaka, van den Elsen Petra A., Napel Sandy, Adler John, (1994), A System for Multimodality Image Fusion, *Seventh Annual IEEE Symposium on Computer-Based Medical Systems*, IEEE Computer Society Press, Los Alamitos, CA, pp. 335-340.
- [Hemler95] Hemler Paul F., Napel Sandy, Sumanaweera Thilaka S., Pichumani Ramani, van den Elsen Petra A., Martin Dave, Drace John, Adler John R., Perakash Inder, (1995), Registration error quantification of a surface-based multimodality images fusion system, *Medical Physics*, **22**, No. 7, pp. 1049-1056.

- [Hemler96] Hemler Paul F., Sumanaweera Thilaka S., van den Elsen Petra A., Napel Sandy, Adler John R., (1996), Quantified registration error versus the accuracy of registered surfaces for a multimodality surface-based registration system, in Loew M. H. and Hanson K. M. (Eds.), *Medical Imaging: Image Processing*, SPIE Press, Bellingham, WA, **2710**, pp. 348-357.
- [Herbin89] Herbin M., Venot A., Devaux J. Y., Walter E., Lebruchec J. F., Dubertret L., Roucayrol J. C., (1989), Automated Registration of Dissimilar Images: Application to Medical Imagery, *Computer Vision, Graphics and Image Processing*, **47**, pp. 77-88.
- [Hinshaw78] Hinshaw W. S., Andrew E. R., Bottomley P. A., Holland G. N., Moore W. S., Worthington B. S., (1978), Display of cross sectional anatomy by nuclear magnetic resonance imaging, *British Journal of Radiology*, **51**, No. 604, pp. 273-280.
- [Holton95] Holton Kerrie S., Taneja Udit, Robb Richard A., (1995), Quantitative validation of 3D image registration techniques, in Loew M. H. (Ed.), *Medical Imaging: Image Processing*, SPIE Press Bellingham, WA, **2434**, pp. 504-519.
- [Junck90] Junck Larry, Moen John G., Hutchins Gary D., Brown Morton B., Kuhl David E., (1990), Correlation Methods for the Centering, Rotation, and Alignment of Functional Brain Images, *The Journal of Nuclear Medicine*, **31**, No. 7, pp. 1220-1226.

- [Kaplan89] Kaplan Isaac L., Swayne Lawrence C., (1989), Composite SPECT-CT Images: Technique and Potential Applications in Chest and Abdominal Imaging, *American Journal Roentgenol*, **152**, pp. 865-866.
- [Kenny90] Kenny P. A., Dowsett D. J., Vernon D., Ennis J. T., (1990), A technique for digital image registration used prior to subtraction of lung images in nuclear medicine, *Physics in Medicine and Biology*, **35**, No. 5, pp. 679-685.
- [Kim96] Kim Seok J., Lee Chae Y., (1996), Modelling and Analysis of the Dynamic Location Registration and Paging in Microcellular Systems, *IEEE Trans. Vehicular Technology*, **45**, No. 1, pp. 82-90.
- [Kovacic89] Kovačič Stane, Gee Jim C., Ching Wallace S. L., Reivich Martin, Bajcsy Ruzena, (1989), Three-Dimensional Registration of PET and CT Images, *11th Annual International Conference IEEE Engineering in Medicine & Biology Society*, **11**, pp. 548-549.
- [Kruggel95] Kruggel Frithjof, Bartenstein Peter, (1995), Automatical Registration of Brain Volume Datasets, in Bizais Y., Barillot C. and di Paola R. (eds.), *Information Processing in Medical Imaging*, Kluwer Academic Publishers, Dordrecht, The Netherlands, pp. 389 - 390.
- [Kuglin75] Kuglin C. D., Hines D. C., (1975), The Phase Correlation Image Alignment Method, *Proc. International Conference Cybernetics & Society*, pp. 163-165.

- [Lavallee95] Lavallée Stéphane, Szeliski Richard, (1995), Recovering the Position and Orientation of Free-Form Objects from Image Contours Using 3D Distance Maps, *IEEE Trans. Pattern Analysis and Machine Intelligence*, **17**, No. 4, pp. 378-390.
- [LeGoualher99] Le Goualher Georges, Procyk Emmanuel, Collins D. Louis, Venugopal Raghu, Barillot Christian, Evans Alan C., (1999), Automated Extraction and Variability Analysis of Sulcal Neuroanatomy, *IEEE Trans. Medical Imaging*, **18**, No. 3, pp. 206-217.
- [Lelieveldt99] Lelieveldt B. P. F., van der Geest R. J., Rezaee M. Ramze, Bosch J. G., Reiber J. H. C., (1999), Anatomical Model Matching with Fuzzy Implicit Surfaces for Segmentation of Thoracic Volume Scans, *IEEE Trans. Medical Imaging*, **18**, No. 3, pp. 218-230.
- [Low91] Low Adrian, (1991), *Introductory Computer Vision and Image Processing*, McGraw-Hill, Cambridge.
- [Maguire86] Maguire Jr. Gerald Q., Noz Marilyn E., Lee Evan M., Schimpf James H., (1986), Correlation Methods for Tomographic Images Using Two and Three Dimensional Techniques, in Bacharach S. L. (Ed.) *Information Processing in Medical Imaging*, Martinus Nijhoff Publishers, Dordrecht, The Netherlands, pp. 266 - 279.
- [Maguire91] Maguire Jr. G. Q., Noz M. E., Rusinek H., Jaeger J., Kramer E. L., Sanger J. J., Smith G., (1991), Graphics Applied to Medical Image Registration, *IEEE Computer Graphics & Applications*, **11**, No. 2, pp. 20 - 28.

- [Maintz96] Maintz J. B. Antoine, van den Elsen Petra A., Viergever Max A., (1996), Evaluation of Ridge Seeking Operators for Multimodality Medical Image Matching, *IEEE Trans. Pattern Analysis and Machine Intelligence*, **18**, No. 4, pp. 353-365.
- [Maintz98] Maintz J. B. Antoine, Viergever Max A., (1998), A Survey of Medical Image Registration, *Medical Analysis*, **2**, No. 1, pp. 1-36.
- [Mamistvalov98] Mamistvalov Alexander G., (1998), n -Dimensional Moment Invariants and Conceptual Mathematical Theory of Recognition n -Dimensional Solids, *IEEE Trans. Pattern Analysis and Machine Intelligence*, **20**, No. 8, pp. 819-831.
- [Mandava89] Mandava Venkat R., Fitzpatrick J. Michael, Pickens III David R., (1989), Adaptive Search Space Scaling in Digital Image Registration, *IEEE Trans. Medical Image*, **8**, No. 3, pp. 251-262.
- [Maurer93] Maurer Jr. Calvin R., Fitzpatrick J. Michael, (1993), A Review of Medical Image Registration, in Maciunas R. J. (Ed.), *Interactive Image-Guided Neurosurgery*, American Association of Neurological Surgeons, Park Ridge, IL, pp. 17-44.
- [Maurer97] Maurer Jr. Calvin R., Fitzpatrick J. Michael, Wang Matthew Y., Galloway Robert L., Maciunas Robert J., Allen George S., (1997), Registration of Head Volume Images Using Implantable Fiducial Markers, *IEEE Trans. Medical Imaging*, **16**, No. 4, pp. 447-462.

- [MedSci98] Osteoporosis: A Review, (1998), *Medical Sciences Bulletin The Internet Enhanced Journal of Pharmacology and Therapeutics*, No. 253.
- [Moshfeghi91] Moshfeghi Mehran, (1991), Elastic Matching of Multimodality Medical Images, *CVGIP: Graphical Models and Image Processing*, **53**, No. 3, pp. 271-282.
- [OConnor98a] O'Connor K. B. R., Stewart W. R., Ware J. A., (1998), An Interactive Medical Image Processing System Based on a Hybrid Computer Architecture, *IEE Colloquium on High Performance Architecture for Real-Time Image Processing*, 14/1 - 14/6.
- [OConnor98b] O'Connor Keith B. R., (1998), *A Medical Image Processing System Based on a Hybrid Computer Architecture*, M.Phil. Thesis, University of Glamorgan.
- [O'Gorman96] O'Gorman Lawrence, (1996), Subpixel Precision of Straight-Edged Shapes for Registration and Measurement, *IEEE Trans. Pattern Analysis and Machine Intelligence*, **18**, No. 7, pp. 746-751.
- [Pearson77] Pearson J. J., Hines Jr. D. C., Golosman S., Kuglin C. D., (1977), Video-rate Image Correlation Processor, *Proc. SPIE Application of Digital Image Processing (IOCC 1977)*, **119**, pp. 197-205.
- [Peli87] Peli Eli, Augliere Reed A., Timberlake George T., (1987), Feature-Based Registration of Retinal Images, *IEEE Trans. Medical Imaging*, **MI-6**, No. 3, pp. 272-278.

- [Persoon77] Persoon E., Fu K., (1977), Shape Discrimination using Fourier Descriptors, *IEEE Trans. Systems, Man and Cybernetics*, **SMC-7**, No. 3, pp. 170-179.
- [Petti94] Petti Paula L., Kessler Marc L., Fleming Terri, Pitluck Samuel, (1994), An automated image-registration technique based on multiple structure matching, *Medical Physics*, **21**, No. 9, pp. 1419-1426.
- [Pettit85] Pettit Frank, (1985), *Fourier Transforms in Action*, Chartwell-Bratt (Publishing and Training) Limited, Bromley, Kent.
- [Plant95a] Plant M. J., Stewart W. R., Williams G. P., O'Connor K. B. R., Gorman S. T., Griffiths H., Woodcock J. P., Williams B. D., (1995), Gadolinium-enhanced Magnetic Resonance Imaging of the finger joints in Rheumatoid Arthritis, *Arthritis and Rheumatism*, **38**, No. 9 SS, p. 1063.
- [Plant95b] Plant M. J., Williams G. P., (1995), Private Communication.
- [Pratt78] Pratt William K., (1978), *Digital Image Processing*, John Wiley & Sons, Inc., USA.
- [Rinck93] Rinck Peter A. (Ed.), (1993), *Magnetic Resonance in Medicine*, Third Edition, Blackwell Scientific Publications, Oxford.
- [Roach94] Roach P., Roberts G., (1994), Computer Vision Lecture Notes, University of Glamorgan.
- [Rogers85] Rogers David F., (1985), *Procedural Elements for Computer Graphics*, McGraw-Hill, United States of America.

- [Rosler87] Rösler R., Schneider H. A., Schuberth R., (1987), Relation between Particle Shape and Profile Fourier Coefficients, *Powder Technology*, **49**, pp. 255-260.
- [Rothe96] Rothe Irene, Süsse Herbert, Voss Klaus, (1996), The Method of Normalization to Determine Invariants, *IEEE Trans. Pattern Analysis and Machine Intelligence*, **18**, No. 4, pp. 366-376.
- [Rycroft98] Rycroft Michael, (1998), *Private communication*.
- [Schalkoff89] Schalkoff Robert J., (1989), *Digital Image Processing and Computer Vision*, John Wiley & Sons, Inc., United States of America.
- [Schwartz96] Schwartz D., Lemoine D., Poiseau E., Barillot C., (1996), Registration of MEG/EEG Data with 3D MRI: Methodology and Precision Issues, *Brain Topography*, **9**, No. 2, pp. 101-116.
- [Singh79] Singh Manbir, Frei Werner, Shibata Tsutomu, Huth Gerald C., Telfer Nancy E., (1979), A Digital Technique for Accurate Change Detection in Nuclear Medical Images - with application to Myocardial Perfusion Studies using Thallium-201, *IEEE Trans. Nuclear Science*, **NS-26**, No. 1, pp. 565-575.
- [Sonka96] Sonka Milan, Hlavac Vaclav, Boyle Roger, (1996), *Image Processing, Analysis and Machine Vision*, International Thomson Computer Press, Cambridge.
- [Stewart2000] Stewart W. R., Williams G. P., (2000), *Private Communication*.

- [Studholme97] Studholme Colin, Hill Derek L. G., Hawkes David J., (1997), Automated Three-dimensional Registration of Magnetic Resonance and Positron Emission Tomography Brain Images by Multiresolution Optimization of Voxel Similarity Measures, *Medical Physics*, **24**, No. 1, pp. 25-35.
- [Taneja94] Taneja Udit, Holton Kerrie S., Camp Jon C., Robb Richard A., (1994), Evaluating the accuracy of three-dimensional image registration algorithms used in multimodal fusion, in *Visualization in Biomedical Computing*, SPIE Press, Bellingham, WA, **2359**, pp. 238-250.
- [Tough84] Tough J. G., Miles R. G., (1984), A Method for Characterizing Polygons in Terms of the Principal Axes, *Computers & Geosciences*, **10**, No. 2-3, pp. 347-350.
- [Tough88] Tough J. G., (1988), The Computation of the Area, Centroid and Principal Axes of a Polygon, *Computers & Geosciences*, **14**, No. 5, pp. 715-717.
- [Turkington93] Turkington Timothy G., Jaszczak Ronald J., Pelizzari Charles A., Harris C. Craig, MacFall James R., (1993), Accuracy of Registration of PET, SPECT and MR Images of a Brain Phantom, *The Journal of Nuclear Medicine*, **34**, No. 9, pp. 1587-1594.
- [vanHerk95] van Herk M., Bruce A., de Munck J., Kwa S., Lebesque J. V., Shouman T., Touw A., (1995), The Use of MRI, CT and Spect Registration for Treatment Planning and Follow-up, *European Journal of Cancer*, **31A**, No. S5, pp. 28-.

- [Venot84a] Venot A., Golmard J. L., Lebruchec J. F., Pronzato L., Walter E., Frij G., Roucayrol J. C., (1984), Digital Methods for Change Detection in Medical Images, in Deconinck F. (Ed.), *Information Processing in Medical Imaging*, Martinus Nijhoff Publishers, Dordrecht, pp. 1-16.
- [Venot84b] Venot Alain, Leclerc V., (1984), Automated Correction of Patient Motion and Gray Values Prior to Subtraction in Digitized Angiography, *IEEE Trans. Medical Imaging*, **MI-3**, No. 4, pp. 179-186.
- [Venot88] Venot A., Devaux J. Y., Herbin M., Lebruchec J. F., Dubertret L., Raulo Y., Roucayrol J. C., (1988), An Automated System for the Registration and Comparison of Photographic Images in Medicine, *IEEE Trans. Medical Imaging*, **7**, No. 4, pp. 298-303.
- [Wallace80] Wallace T. P., Wintz P. A., (1980), Efficient Three-Dimensional Aircraft Recognition Algorithm Using Normalised Fourier Descriptors, *Computer Graphics and Image Processing*, **13**, pp. 99-126.
- [Wang96] Wang Matthew Y., Maurer Jr. Calvin R., Fitzpatrick J. Michael, Maciunas Robert J., (1996), An Automatic Technique for Finding and Localizing Externally Attached Markers in CT and MR Volume Images of the Head, *IEEE Trans. Biomedical Engineering*, **43**, No. 6, pp. 627-637.

- [West96] West Jay, Fitzpatrick J. Michael, Wang Matthew Y., Dawant Benoit M., Maurer Jr. Calvin R., Kessler Robert M., Maciunas Robert J., Barillot Christian, Lemoine Didier, Collignon André, Maes Frederik, Suetens Paul, Vandermeulen Dirk, van den Elsen Petra A., Hemler Paul F., Napel Sandy, Sumanaweera Thilaka S., Harkness Beth, Hill Derek L. G., Studholme Colin, Malandain Gregoire, Pennec Xavier, Noz Marilyn E., Maguire Jr. Gerald Q., Pollack Michael, Pelizarri Charles A., Robb Richard A., Hanson Dennis, Woods Roger P., (1996), Comparison and evaluation of retrospective intermodality image registration techniques, in Loew M. H. and Hanson K. M. (Eds.), *SPIE Proc. MI*, **2710**, pp. 332-347.
- [West99] West Jay, Fitzpatrick J. Michael, Wang Matthew Y., Dawant Benoit M., Maurer Jr. Calvin R., Kessler Robert M., Maciunas Robert J., (1999), Retrospective Intermodality Registration Techniques for Images of the Head: Surface-Based Versus Volume-Based, *IEEE Trans. Medical Imaging*, **18**, No. 2, pp. 144-150.
- [Westermann96] Westermann Birgit, Hauser Rolf, (1996), Non-Invasive 3-D Patient Registration For Image-Guided Skull Base Surgery, *Computers and Graphics*, **20**, No. 6, pp. 793-799.
- [Whitted81] Whitted Turner, (1981), A Software Test-Bed for the Development of 3-D Raster Graphics Systems, *Computer Graphics (Proc. SIGGRAPH 81)*, **15**, No. 3, pp. 271-277.

- [Williams2000] Williams G. P., Roach P. A., Lloyd S., Stewart W. R., (2000), Defining a Registration Algorithm for MRI Finger Images, in Blackledge J. M., Turner M. J. (Eds.), *Image Processing II Mathematical Methods, Algorithms and Applications*, Proc. 2nd IMA Conf. on Image Processing: Mathematical Methods, Algorithms and Applications, 1998, Horwood Publishing, England, pp. 115 - 132.
- [Wong96] Wong Wai-Lip, Hussain Karim, Chevretton Elfy, Hawkes David J., Baddeley Hiram, Maisey Michael, McGurk Mark, (1996), Validation and Clinical Application of Computer-combined Computed Tomography and Positron Emission Tomography with 2-[18F]Fluoro-2-Deoxy-D-Glucose Head and Neck Images, *American Journal of Surgery*, **172**, No. 6, pp. 628-632.
- [Yang96] Yang J., Huang S. C., Mega M., Lin K. P., Toga A. W., Small G. W., Phelps M. E., (1996), Investigation of Partial Volume Correction Methods for Brain FDG PET Studies, *IEEE Trans. Nuclear Science*, **43**, No. 6, pp. 3322-27.
- [Yu89] Yu Joseph Jy-Haw, Hung Biing-Nan, Liou Chone-Lin, (1989), Fast Algorithm for Digital Retinal Image Alignment, *Annual International Conference IEEE Engineering in Medicine and Biology Society*, **11**, pp. 374-375.
- [Zahn72] Zahn C. T., Roskies R. Z., (1972), Fourier Descriptors for Plane Closed Curves, *IEEE Trans. Computers*, **21**, No. 3, pp. 269-281.

- [Zuiderveld89] Zuiderveld Karel J., Romeny Bart M. ter Haar, Viergever Max A., (1989), Fast rubber sheet masking for digital subtraction angiography, in Viergever (Ed.), *Proc. SPIE Science and Engineering of Medical Imaging*, SPIE Press, Bellingham, WA, **1137**, pp. 22-30.
- [Zuiderveld96] Zuiderveld Karel J., Koning Anton H. J., Stokking Rik, Maintz J. B. Antoine, Appelman Fred J. R., Viergever Max A., (1996), Multimodality Visualization of Medical Volume Data, *Computers & Graphics*, **20**, No. 6, pp. 775-791.